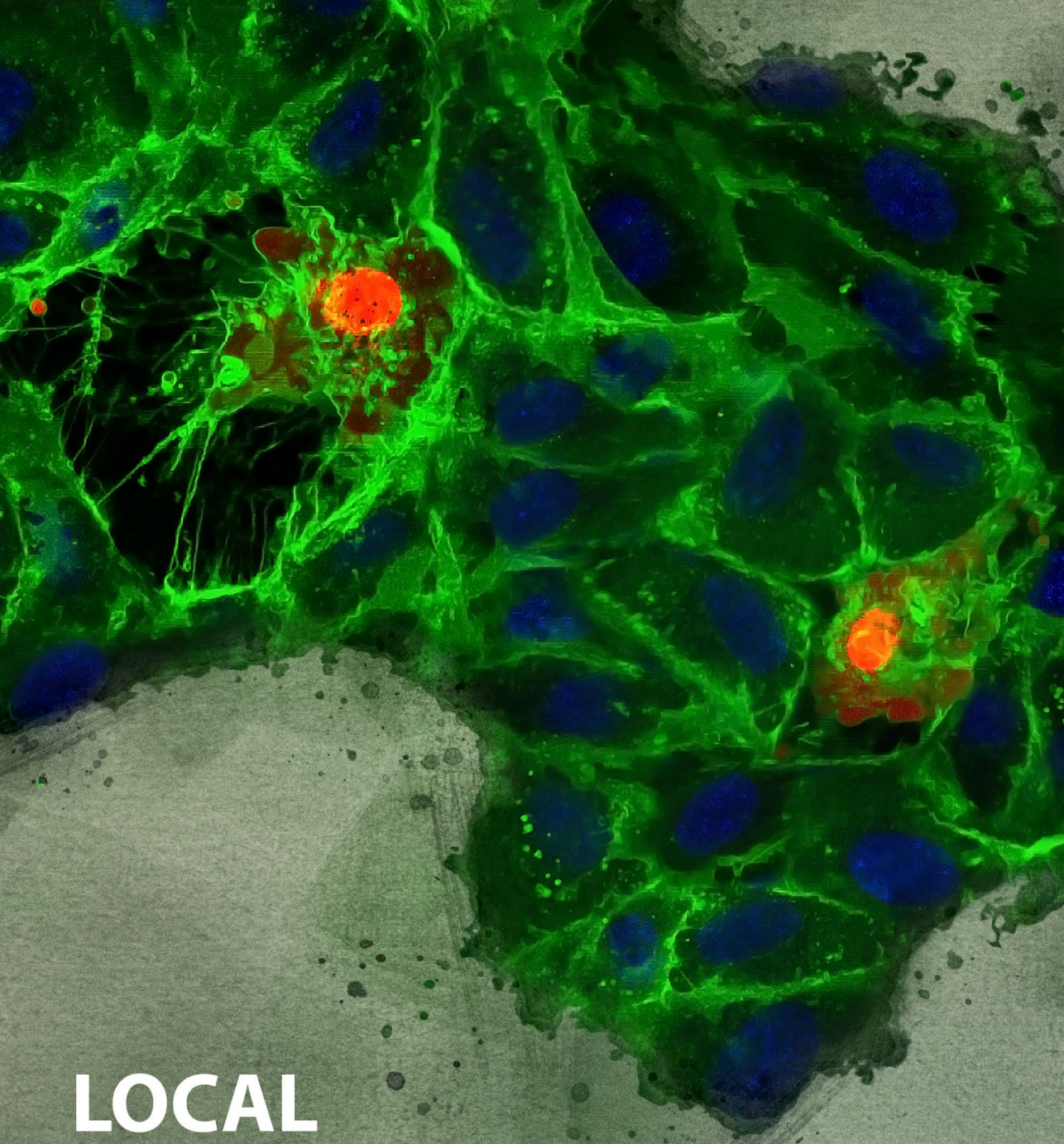

LOCAL DRUG DELIVERY BY MICROBUBBLES

Inés Beekers

Local Drug Delivery by Microbubbles

Dalien Inés Beekers

ISBN
978-94-028-2039-3

Lay-out
Inés Beekers

Cover
Inés Beekers

Print
Ipskamp Printing

An electronic version of this dissertation is available at
`http://hdl.handle.net/1765/125896`

Local Drug Delivery by Microbubbles

Lokale medicijnafgifte met microbellen

Thesis

to obtain the degree of Doctor from the
Erasmus University Rotterdam
by command of the
rector magnificus

Prof. dr. R. C. M. E. Engels

and in accordance with the decision of the Doctorate Board.

The public defence shall be held on
Wednesday the 8th of July 2020 at 13:30 hrs
by

Dalien Inés Beekers

born in Hillegom, the Netherlands

Erasmus University Rotterdam

Doctoral Committee

Promotors	Prof. dr. ir. N. de Jong
	Prof. dr. ir. A. F. W. van der Steen
Other members	Prof. dr. A. B. Houtsmuller
	Prof. dr. A. C. H. Yu
	Prof. dr. A. Bouakaz
Co-promotors	Dr. K. Kooiman
	Dr. ir. M. D. Verweij

This work was supported by the Applied and Engineering Sciences TTW (Veni-project 13669), part of NWO.

The research described in this thesis has been carried out at the Department of Biomedical Engineering, Thoraxcenter, Erasmus University Medical Center, Rotterdam, The Netherlands.

Financial support by the Dutch Heart Foundation for the publication of this thesis is gratefully acknowledged.

Nikon Instruments Europe B.V.

Financial support for the publication of this thesis was graciously provided by:

Mimetas B.V.
Oldelft Ultrasound
Erasmus University Medical Center

Contents

1

Introduction

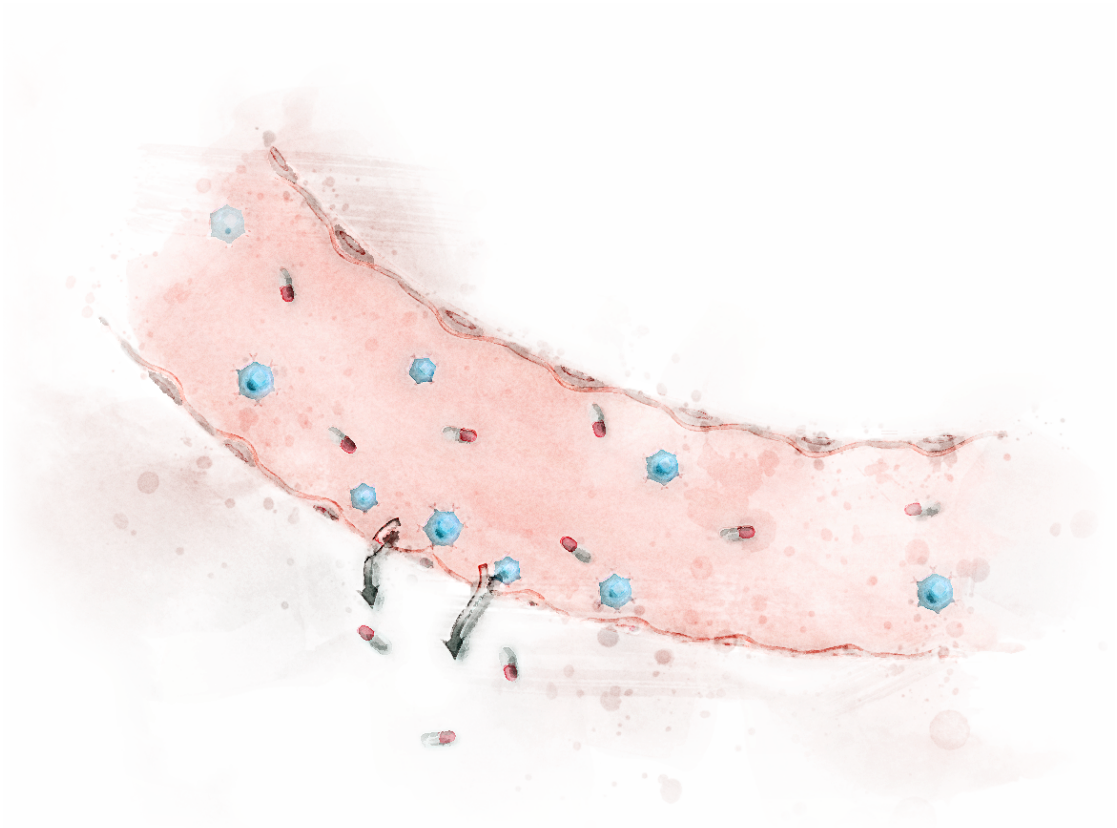

1

1.1. ULTRASOUND IMAGING

Figure 1.1: Prenatal ultrasound image of Inés when she was 13 weeks old.

Medical diagnostic ultrasound is widely used in the clinic for real-time imaging of soft tissues, to capture their anatomy and possible pathological lesions. Ultrasound is mainly known for prenatal imaging (Fig. 1.1), but also commonly used as a diagnostic tool for cardiovascular disease or cancer. Ultrasound imaging refrains from ionizing radiation, is noninvasive, portable, and relatively inexpensive, especially compared to other conventional imaging techniques such as a CT (computed tomography) and MRI (magnetic resonance imaging).

Ultrasound is aptly named; it is *sound* at *ultra*-high frequencies, above the audible range of human hearing (> 20 kHz). Sound is a pressure wave that when traveling through a medium will reflect when it encounters a material interface, just as an echo reflects on the mountains. When the interface is small or the object does not have smooth surface, the pressure wave will be scattered. A reflective or scattering interface is characterized by a change in material stiffness and/or density. Ultrasound imaging exploits these phenomena to identify boundaries, just like dolphins and bats are able to locate prey and identify objects in their surrounding by emitting calls and listening to their echoes (i.e. biosonar or echolocation). In medical ultrasound imaging, a transducer generates ultrasound pulses and receives the returning echoes. These echoes are then reconstructed into an image to identify tissue interfaces in the human body.

1.2. ULTRASOUND CONTRAST AGENTS

Cardiovascular ultrasound imaging is limited by the weak scattering properties of blood. To enhance imaging contrast, ultrasound contrast agents can be used that consist of gas-filled microbubbles with a typical diameter of 1 to 10 µm [1, 2]. These microbubbles are administered intravenously and can circulate for several minutes in the human body. They are too large to extravasate from the vasculature and therefore act as blood-pool markers. The gas core can be stabilized with an albumin, polymer, or phospholipid coating to lower the surface tension and thereby reduce gas dissolution. Additionally, to improve longevity their core consists of a heavy inert gas with low solubility, such as SF_6 or C_4F_{10} [3]. Microbubbles have been in clinical use now for more than three decades as contrast agents for ultrasound imaging [1].

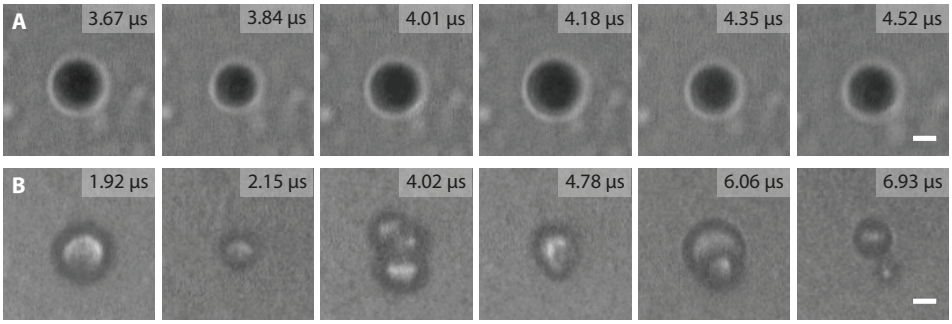

Figure 1.2: Selected frames of Brandaris 128 ultra-high-speed camera recordings. (**A**) Stable microbubble oscillation upon insonification (8 cycles, 1.6 MHz, 20 kPa PNP). (**B**) Inertial microbubble oscillation showing non-spherical oscillation and fragmentation (10 cycles, 2 MHz, 400 kPa PNP). Scale bars are 2 µm.

Gas bubbles are very efficient scatterers of sound. Due to their high compressibility they expand and contract in response to the locally varying ultrasound pressure wave, also known as microbubble oscillation or vibration [4]. Hereby microbubbles can increase scattering by a factor of 10,000, thereby significantly enhancing contrast of the bloodstream compared to the surrounding tissue and liquid [5]. Upon ultrasound insonification at clinically relevant frequencies of more than 1 MHz, microbubbles will oscillate more than a million times per second. Therefore, an optical imaging system with a nanosecond temporal resolution is required to visualize and characterize microbubble oscillation behavior. Currently, there are two ultra-high-speed cameras that can achieve such high frame rates (up to 25 million frames per second, Mfps) with sufficient consecutive frames (up to 128): the Brandaris 128 [6] and the UPMC Cam [7]. These fast-framing cameras are connected to microscopy systems, such that a magnified image of the microbubble is projected on a fast-rotating mirror which projects the image over 128 (or 64 for the UPMC Cam) CCDs (charge-couple devices).

Using these ultra-high-speed cameras, microbubble oscillation behavior has been studied over the past 15 years. The various regimes of acoustic response of a single phospholipid-coated microbubbles could finally be resolved. Upon increasing volumetric oscillations microbubbles present with stable linear spherical oscillations, non-linear spherical oscillations, non-spherical oscillations, up to inertial cavitation leading to microbubble fragmentation or collapse [3, 4, 8]. A microbubble exhibiting linear spherical oscillations recorded with the Brandaris 128 ultra-high-speed camera is shown in Fig. 1.2A. Violent and non-spherical microbubble oscillations are shown in Fig. 1.2B.

1

1.3. MICROBUBBLE-MEDIATED DRUG DELIVERY

In addition to being excellent image contrast enhancers, oscillating microbubbles have the ability to permeabilize biological barriers. This has a great therapeutic potential, since it can thereby locally enhance drug delivery (Fig. 1.3). Local drug delivery to diseased tissue to reduce systematic toxicity remains a main clinical challenge. Upon intravenous administration, drugs circulate through the bloodstream and are delivered systematically to the entire body. On top of that, these intravenously administered drugs need to extravasate from the vasculature in order to reach the tissue of target. However, the vascular endothelium forms a major barrier, blocking up to 98% of small molecule drugs in the blood-brain barrier [9]. Consequently, high drug dosages need to be administered to still achieve the proper efficacy level at the target. Successful drug delivery should maximize drug concentration at the target site, while at the same time reduce the systematic toxicity and development of side effects in the rest of the body. Therefore, locally permeabilizing the vasculature with oscillating microbubbles is a promising novel method to facilitate local enhanced drug delivery [3, 10].

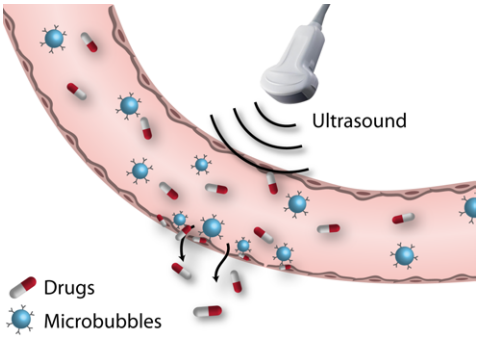

Figure 1.3: Schematic representation of microbubble-mediated vascular drug delivery, showing intracellular uptake in the endothelium and enhanced delivery to the extravascular space.

Microbubble-mediated drug delivery is facilitated either by co-administration of the drugs and microbubbles or by using microbubbles as drug carriers, in which therapeutics are embedded in the microbubble shell or in the gas core [3, 11]. Local release of the therapeutic agent can then be triggered upon ultrasound insonification. Alternatively, drugs can be incorporated in liposomes or nanoparticles that are attached to the surface of the microbubble coating [12]. Microbubbles can also be targeted to specific biomarkers by conjugating ligands to the microbubble coating, such as antibodies, peptides, or glycoproteins [13]. By binding microbubbles to molecules specifically expressed by diseased cells, microbubbles become an ideal theragnostic tool. Molecular imaging can be performed thanks to their ability to enhance contrast in imaging [14], and on top of that, they can enhance drug delivery in the diseased tissue to which they targeted [15, 16].

Current applications of microbubble-mediated drug delivery range from oncology, neurological disorders, to cardiovascular disease [10]. Despite the leaky vasculature in a tumor environment, the elevated interstitial pressure and dense extracellular matrix hinder successful penetration and distribution of therapeutic agents [17].

Microbubbles have shown to improve efficiency of intratumoral drug delivery without adverse effects [18]. The first human clinical trial in 2016 evaluated chemotherapeutic treatment of pancreatic cancer in combination with ultrasound and microbubbles, resulting in decreased tumor size in half of the patients, improved survival, and no additional toxicity [19]. Brain tumors and neurological disorders, such as Alzheimer's and Parkinson's disease, prove extremely difficult to treat because of the limited molecular transport over the blood-brain barrier [20, 21]. In 2001, oscillating microbubbles were reported to enable reversible opening of the blood-brain barrier [22]. More recently, the first preliminary patient studies on non-invasive MRI guided treatment with ultrasound and microbubbles have demonstrated safe and effective opening of the blood-brain barrier [23–25]. Cardiovascular treatment can also be achieved using the forces of the oscillating microbubble itself. For instance, expedited dissolution of thrombi by sonothrombolysis to restore blood flow upon vascular occlusion in ischemic stroke or myocardial infarction [26–29]. Microbubbles can also improve muscle perfusion in patients, to reverse tissue ischemia [30], and can even aid treatment of bacterial biofilm infections through sonobactericide [31].

To better control and tune microbubble-mediated drug delivery to the requirements of each therapeutic application, the underlying biological and physical mechanisms need to be elucidated. In this thesis, we focus on vascular drug delivery, since microbubbles are blood-pool agents and thus are primarily in contact with endothelial cells that line blood vessels.

Drug delivery pathways

Vascular drug delivery can be locally enhanced by increasing the endothelial permeability through three main drug delivery pathways: oscillating microbubbles can perforate the cell membrane (i.e. sonoporation), open intercellular junctions, and stimulate endocytosis [3, 32–34].

An oscillating microbubble can perforate the cellular membrane, also known as **sonoporation** (Fig. 1.4A). This causes a transient opening, through which molecules can passively diffuse in and out of the intracellular space [34]. Commonly, sonoporation is studied by assessing the influx of a model drug such as propidium iodide (PI), since this molecule can only enter a live cell when its membrane has been disrupted. After entering the cell PI binds to DNA and RNA and becomes fluorescent [35].

Sonoporation is believed to be a mechanical effect caused by the forces generated by the oscillating microbubble [33]. The reported oscillation behavior for sonoporation ranges from stable cavitation, inertial cavitation, microbubble jetting, microstreaming, up to actual microbubble penetration into the cell [3]. The size of the membrane pores created upon sonoporation have been reported as small as 1 nm [36] up to > 100 μm^2 [37]. It is hypothesized that the degree of pore formation closely correlates with the

specific microbubble behavior [3]. The size of pores can be either imaged directly with confocal microscopy [37], estimated by a mathematical fit to a quasi-steady-state electro-diffusion model that relates the amount of PI uptake to size of the pore [38], or estimated by measuring the transmembrane current via the patch-clamp technique [39].

Sonoporation has been shown to be transient, pores can sometimes reseal through biological mechanisms or pores can remain open [33]. The resealing capabilities upon sonoporation are closely related to the size of the generated pore [38]. Specifically, pores > 100 μm^2 have shown not to reseal [37]. Resealing times of pores have been reported to range from milliseconds to several seconds. However, for a cell to remain viable, the pores should close within approximately 120 s [40].

The disruption of the cell membrane upon sonoporation has been reported to lead to several bioeffects such as shrinking of the cell [41], formation of blebs [42], alterations in cytoskeletal arrangement [43], changes in cellular proliferation [44], and generation of reactive oxygen species [45]. Moreover, it can lead to the influx and outflux of ions, which results in a disruption of the transmembrane potential [46]. For instance, increase in intracellular calcium (Ca_i^{2+}) can occur because of the influx of free calcium ions through the pore, since the concentration outside the cell is about 10,000-fold higher [47]. Additionally, fluctuations in the Ca_i^{2+} concentration can also be triggered by activation of mechanosensitive ion channels on the cell membrane [48]. The increase in Ca_i^{2+} has been shown to be essential in membrane resealing [49]. However, future studies are needed to explain the different bioeffects and thoroughly correlate sonoporation to microbubble oscillation behavior and the resulting long-term cell fate post-exposure.

Microbubble oscillation can also cause **opening of intercellular junctions** (Fig. 1.4B). As a result, gaps form between adjacent endothelial cells, providing an effective route for molecular delivery to the extravascular space. This pathway has shown increased transport for several hours [33]. It remains poorly understood which underlying mechanisms induce the opening of cell-cell contacts [34]. The oscillating microbubble could be pushing the cells apart [50], the increased shear stress due to microstreaming could be triggering the mechano-sensory channels on the outside of the cell, membrane disruption could be inducing cytoskeletal changes [51], or changes

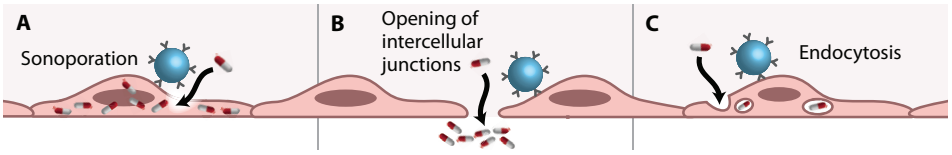

Figure 1.4: The three known pathways of microbubble-mediated drug delivery.

in Ca_i^{2+} could be involved in opening of intercellular junctions [52]. A single example of live cell microscopy has revealed that cell-cell contacts can open within minutes after microbubble oscillation and remain open for tens of minutes [53]. Using electron microscopy, opening of the endothelial cell-cell contacts has been reported *in vivo* in the brain [54] or prostate [55]. In general, there is a clear lack of understanding of the spatiotemporal relationship between microbubble oscillation and endothelial intercellular junction opening [33].

The third known drug delivery pathway triggered by an oscillating microbubble is **endocytosis** (Fig. 1.4C). This active uptake of macromolecules (> 155 kDa) from the extracellular space is a process that occurs naturally, but has been reported to be enhanced upon treatment with ultrasound and microbubbles both *in vitro* and *in vivo* [56, 57]. Because endocytosis is a complex biological mechanism and a long-term response, it is difficult to explore the relationship between endocytosis and the microbubble oscillation behavior [33]. It is believed to be triggered upon enhanced shear stress, membrane deformation due to microbubble oscillation or due to primary radiation forces that push the microbubble into the cell membrane [58], or triggered by other bioeffects, such as the increase in Ca_i^{2+} [59].

Depending on the therapeutic application it will be desirable to achieve either viable enhanced drug delivery or a lethal cellular response. For instance, to improve the efficacy of tumor treatment we want a temporary increase in the permeability of the endothelium to allow the drugs to diffuse out of the vasculature, but no significant long-term damage or cell death of the endothelium itself. The same is desirable for opening of the blood-brain barrier, since we want to enhance drug delivery while avoiding any significant vascular damage. Alternatively, the oscillating microbubble should induce irreversible cell damage to cause cell death when treating cancer cells. This is only possible for specific tumors, such as colorectal cancer [60] and hepatocellular carcinoma [61], since these cancer cells have been reported to invade the vasculature such that microbubbles can actually interact with the cancer cells themselves. Irreversible damage is also desirable when treating thrombi or bacterial biofilm infections.

The relationship between the distinct drug delivery pathways has not been fully elucidated. For safe and controlled clinical use, we need to further unravel the trade-off between efficient drug delivery and cell viability. Additionally, it remains unknown which specific microbubble oscillation behavior is required for each of the drug delivery pathways.

Challenges of *in vitro* studies

Elucidating the microbubble–cell interaction is fundamentally important for controlling and optimizing drug delivery. Therefore, the microbubble oscillation behavior and the cellular response should be studied simultaneously. Until now, concurrent visualization has only been possible using an ultra-high speed camera coupled to a widefield microscope [15, 53, 58, 62]. In these studies, the microbubble behavior was known but the cellular response was imaged at low resolution and sensitivity. Others have visualized the cellular response at high spatial resolution and detector sensitivity using fluorescent confocal microscopy [37, 38, 51, 53, 63, 64]. However, these studies lacked information on the microbubble oscillation behavior that was responsible for the cellular effect. Since microbubble response to ultrasound is variable [65, 66] and cannot be predicted solely on acoustic pressure, the underlying mechanisms of the microbubble–cell interaction could not be fully investigated.

Microbubble-mediated drug delivery studies often focus solely on sonoporation, while for most applications the opening of cell-cell contacts to enhance extravascular delivery has a therapeutic potential that is at least as important. In 2D conventional monolayer studies cells are cultured on a surface which hinders evaluation of drug compound transport across the cell barrier. Hence, we ideally require a 3D cell culture model to study drug extravasation. Additionally, endothelial *in vitro* studies are usually performed under static conditions, although it has been shown that cells grown under flow are less susceptible to sonoporation [67]. To better reproduce the physiological cell behavior in the *in vivo* situation, we require more complex vascular *in vitro* models. The ideal *in vitro* set-up includes flow, soft boundaries, lumen architecture, adequate cell types, and possible co-culture. Freedom in choosing an optimal *in vitro* set-up is limited because it should be both optically and acoustically compatible, in order to visualize the cellular response while being able to predict the ultrasound pressure field upon insonification.

1.4. THESIS OUTLINE

This thesis elaborates on elucidating the underlying mechanism of microbubble-mediated drug delivery. The work ranges from understanding the microbubble oscillation behavior itself, to improving the *in vitro* and optical imaging techniques, to studying the endothelial cell response. In **Chapter 2** we evaluated the vibrational response of bound and non-bound microbubbles. The aim was to identify acoustic parameters that discriminate microbubbles bound to a biomarker from those that are not, to increase specificity of ultrasound molecular imaging. The therapeutic potential of these bound and non-bound microbubbles was investigated in **Chapter 3**. The endothelial cell response was studied with widefield fluorescent microscopy and the microbubble oscillation and clustering behavior was resolved with the Brandaris 128

ultra-high-speed camera. The effect on cell viability of microbubble displacement under various acoustic settings was assessed.

To pursue additional *in vitro* studies an alternative acoustically and optically transparent cell culture platform was required. Therefore, in **Chapter 4** the acoustic propagation into the CLINIcell (Mabio, France) was evaluated by using microbubbles as local pressure sensors. Additionally, to image both microbubble oscillation upon ultrasound insonification and the resulting cellular response, an optical imaging system was developed that can achieve the necessary nanosecond temporal and nanometer spatial resolutions. In **Chapter 5** the unique capabilities of this combined confocal microscope and Brandaris 128 ultra-high-speed camera are demonstrated.

Using the novel capabilities of the developed optical imaging system, in **Chapter 6** the intracellular calcium (Ca_i^{2+}) fluctuations induced by oscillating microbubbles were resolved. The time profiles of Ca_i^{2+} uptake upon sonoporation and propagation of calcium waves to adjacent cells were evaluated. Thanks to the combined optical imaging system, for the first time the necessary microbubble oscillation for the distinct cellular responses was unraveled. Additionally, an in depth study on opening of cell-cell contacts due to sonoporation is presented in **Chapter 7**. The microbubble behavior required for drug delivery was unraveled by investigating the effect of harmonics and asymmetry during oscillation as well as the microbubble location on the cell.

To further control the microbubble response on demand, in **Chapter 8** the physicochemical properties of phospholipid coated microbubbles were investigated. The lipid and ligand distribution in the microbubble coating were resolved with high-axial resolution 4Pi microscopy.

Finally, this thesis presents an organ-on-a-chip cell culture platform to study microbubble-mediated drug delivery in a physiological relevant environment. Using 3D cell culture in the OrganoPlate (Mimetas B.V.) the *in vivo* microcirculation and lumen architecture can be mimicked. In **Chapter 9** we assessed whether controlled microbubble oscillation was feasible in the microfluidic channels of the OrganoPlate. The acoustic propagation was simulated with a 3D finite-element model and experimentally characterized using microbubbles as pressure sensors. Once acoustic compatibility was proved, in **Chapter 10** a cell culture method is presented to culture perfusable endothelial microvessels in the OrganoPlate. To evaluate enhanced endothelial permeability, the barrier integrity was evaluated upon treatment with ultrasound and microbubbles.

2

Vibrational responses of bound and non-bound targeted lipid-coated single microbubbles

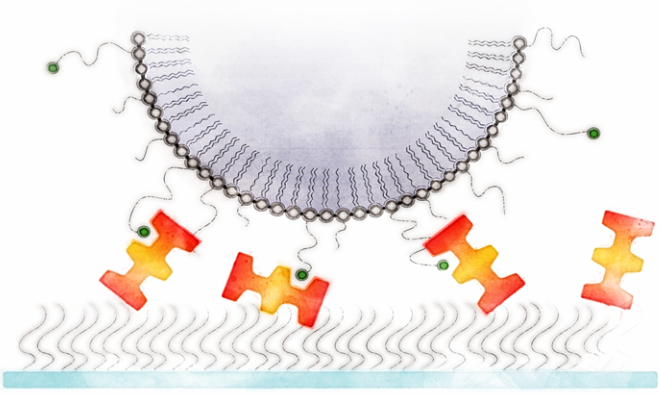

Based on:
Tom van Rooij, **Inés Beekers**, Kirby R. Lattwein, Antonius F. W. van der Steen, Nico de Jong, and Klazina Kooiman, "Vibrational Responses of Bound and Nonbound Targeted Lipid-Coated Single Microbubbles", *IEEE Transactions on Ultrasonics, Ferroelectrics, and Frequency Control*, vol. 64, no. 5, pp. 785-797, 2017 [68].

Abstract

One of the main challenges for ultrasound molecular imaging is acoustically distinguishing nonbound microbubbles from those bound to their molecular target. In this *in vitro* study, we compared two types of in-house produced targeted lipid-coated microbubbles, either consisting of 1,2-dipalmitoyl-*sn*-glycero-3-phosphocholine, C16:0 (DPPC) or 1,2-distearoyl-*sn*-glycero-3-phosphocholine, C18:0 (DSPC) as the main lipid, using the Brandaris 128 ultra-high-speed camera to determine vibrational response differences between bound and nonbound biotinylated microbubbles. In contrast to previous studies that studied vibrational differences upon binding, we used a covalently bound model biomarker (*i.e.*, streptavidin) rather than physisorption, to ensure binding of the biomarker to the membrane. The microbubbles were insonified at frequencies between 1 and 4 MHz at pressures of 50 and 150 kPa. This paper shows lower acoustic stability of bound microbubbles, of which DPPC-based microbubbles deflated most. For DPPC microbubbles with diameters between 2 and 4 μm driven at 50 kPa, resonance frequencies of bound microbubbles were all higher than 1.8 MHz, whereas those of nonbound microbubbles were significantly lower. In addition, the relative radial excursions at resonance were also higher for bound DPPC microbubbles. These differences did not persist when the pressure was increased to 150 kPa, except for the acoustic stability which further decreased. No differences in resonance frequencies were observed between bound and nonbound DSPC microbubbles. Nonlinear responses in terms of emissions at the subharmonic and second harmonic frequencies were similar for bound and nonbound microbubbles at both pressures. In conclusion, we identified differences in vibrational responses of bound DPPC microbubbles with diameters between 2 and 4 μm that distinguish them from nonbound ones.

Index Terms — Biotin-streptavidin, lipid-coating, molecular imaging, nonlinear behavior, targeted microbubbles, ultra-high-speed optical imaging, ultrasound contrast agents.

2.1. INTRODUCTION

Ultrasound contrast agents that consist of targeted microbubbles are emerging in their applications for ultrasound molecular imaging [69–71]. These microbubbles have a ligand attached to their shell by which they can be targeted to a specific biomarker, for example, $\alpha_v\beta_3$ that is expressed on the cellular membrane of endothelial cells in neovasculature [72, 73]. For successful translation of ultrasound molecular imaging to the clinic, two major problems still need to be tackled: 1) producing microbubbles of the same size that also behave identical in an ultrasound field and 2) distinguishing the response of a single targeted microbubble bound to a specific biomarker from a nonbound targeted microbubble. Since microbubbles of the same size can still have

different acoustic properties [65, 74–77], producing monodisperse microbubbles may not necessarily result in microbubbles that have, for example, the same resonance frequency. But if it is possible to determine the acoustic parameters that are specific for bound targeted microbubbles, they may be distinguished from nonbound targeted microbubbles based on their acoustic signal. Several studies investigated the difference in acoustic properties of bound and nonbound microbubbles, but these studies reported conflicting results. In the low frequency range (2 –4 MHz) a shift in resonance frequency was found for microbubbles after binding [78, 79], whereas at 11 and 25 MHz no shift was observed [80]. For the responses at the subharmonic frequency either a change in frequency [80] or no change in amplitude and frequency [81] was reported upon binding. In contrast, for the response at the second harmonic frequency, the results reported in [81] and [82] were in agreement with each other: the amplitude increased for bound microbubbles. Finally, Overvelde *et al.* [79] and Zhao *et al.* [81] found a decrease in the vibrational response at the fundamental frequency for bound microbubbles.

All acoustic studies on bound versus nonbound targeted microbubbles used either physisorption as a method to attach a model biomarker to an artificial surface (membrane or capillary) [78, 79, 81, 82] or had the model biomarker embedded in agarose [80]. Physisorption or physical adsorption relies on electrostatic binding through van der Waals forces between the biomarker and the membrane, but is in fact a very weak bond [83], which can result in detachment of the biomarker from the membrane or capillary. As a result, the biomarker can cover the whole targeted microbubble, including the area that is not directly in contact with the membrane. This was reported in [84] for the model biomarker streptavidin that was physisorbed to an OptiCell membrane. Functionalization of lipid-coated microbubbles with streptavidin changes the properties, such as elasticity [85–87] and acoustic stability [87]. Consequently, the comparisons made in previous studies between bound microbubbles and nonbound microbubbles are in fact a comparison between bound lipid-coated microbubbles covered by streptavidin and nonbound lipid-coated microbubbles, which did not have streptavidin on their shell. In addition, both physisorption and embedding a model biomarker in agarose are far from the *in vivo* situation, where biomarkers are incorporated into the cellular membrane.

We covalently linked a model biomarker to an artificial surface to study the vibrational responses of single bound targeted microbubbles and nonbound targeted microbubbles aiming to find parameters to discriminate them acoustically. Super-resolution confocal laser scanning fluorescence microscopy showed that covalent coupling of the model biomarker streptavidin to a hydrogel prevented the streptavidin to bind to the biotinylated lipid-shell of the microbubble outside the binding area [88]. That study compared the lipid distribution and binding area of two types of targeted lipid-coated microbubbles that were either coated with mainly

1,2-dipalmitoyl-*sn*-glycero-3-phosphocholine, C16:0 (DPPC) which is the main shell component of Definity (Lantheus Medical Imaging, North Billerica, MA, USA) or mainly 1,2-distearoyl-*sn*-glycero-3-phosphocholine, C18:0 (DSPC) which is the main lipid component of SonoVue, Lumason, and BR14 (Bracco Imaging S.p.A., Milan, Italy) [77, 88–92]. It was shown that the lipid distribution was more homogeneous for DPPC-based microbubbles than for DSPC-based microbubbles and that the binding area for DPPC-based microbubbles was significantly larger than for DSPC-based microbubbles [88]. We previously determined the acoustic properties of these DPPC and DSPC-based microbubbles in a setup where the microbubbles were floating against an OptiCell wall (nonbound) [77] and hypothesized that the difference in ligand distribution and binding area could alter the acoustic response after adherence of the microbubble to its molecular target. In this paper, we investigated the vibrational response of in-house produced targeted DPPC-based and DSPC-based microbubbles using the Brandaris 128 ultra-high-speed optical camera [6] when they had bound to a streptavidin-coated hydrogel and compared their responses to those of nonbound microbubbles floating against the hydrogel. We aimed to identify differences in vibrational responses that may be used to discriminate bound from nonbound microbubbles.

2.2. MATERIALS AND METHODS

Microbubble Preparation

Biotinylated lipid-coated microbubbles with a C4F10 gas core (F2 Chemicals Ltd, Preston, UK) were made as previously described [88, 93] by sonication for 1 min. The coating was composed of 59.4 mol% DSPC (P6517, Sigma-Aldrich, Zwijndrecht, The Netherlands) or DPPC (850355, Avanti Polar Lipids, Alabaster, AL, USA), 35.7 mol% polyoxyethylene-40-stearate (PEG-40 stearate, P3440, Sigma-Aldrich), 4.1 mol% 1,2-distearoyl-*sn*-glycero-3-phosphoethanolamine-N-[carboxy(polyethylene glycol)-2000] (DSPE-PEG(2000), 880125, Avanti Polar Lipids); and 0.8 mol% 1,2-distearoyl-*sn*-glycero-3-phosphoethanolamine-N-[biotinyl(polyethylene glycol)-2000] [DSPE-PEG(2000)-biotin, 880129, Avanti Polar Lipids].

A 25 µm-thick polyester membrane was mounted on a custom-made rectangular polyvinylchloride holder (same size as a microscope objective glass) and was custom-coated with a 1-2 µm-thick polycarboxylate hydrogel (XanTec bioanalytics GmbH, Düsseldorf, Germany). For the bound targeted microbubbles, the hydrogel was activated and streptavidin (S4762, Sigma-Aldrich) was subsequently covalently attached to the hydrogel, using the amine coupling kit (K AN-50, XanTec bioanalytics GmbH) according to the instructions of the manufacturer, as previously described [88]. Briefly, streptavidin was dissolved in acetate buffer (2 mM, pH 5.4) (1 mg/mL). After desalting the streptavidin by use of a PD-10 desalting column (GE Healthcare Bio-Sciences), the concentration was determined spectrophotometrically at 570 nm

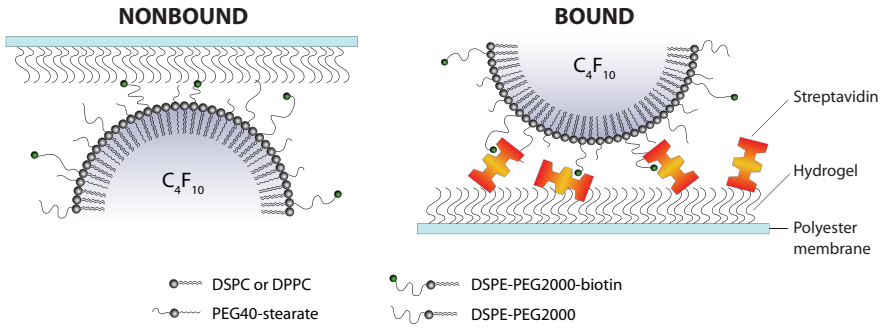

Figure 2.1: Configuration and composition of nonbound targeted microbubbles (left) floating against a hydrogel and targeted microbubbles bound to this hydrogel via streptavidin (right) in the experimental setup (not to scale).

using a Pierce BCA Protein Assay kit (Thermo Scientific) and Thermo Multiskan EX. Three polyester membranes were placed in a 5-Slidemailer (Heathrow Scientific, Northgate, U.K.) with 18 mL of 1 M NaCl + 0.1 M NaB (pH 10) elution buffer (K AN-50, XanTec bioanalytics GmbH), followed by an incubation with 18 mL of 1.6% (w/v) EDC · HCL (K AN-50, XanTec bioanalytics GmbH) in activation NHS/MES buffer (K AN-50, XanTec bioanalytics GmbH), and 18 mL of 33 µg/mL desalted streptavidin in 2 mM acetate buffer at pH 5.2-5.4. Finally, 18 mL of 1 M ethanolamine hydrochloride (pH 8.5) quenching buffer (K AN-50, XanTec bioanalytics GmbH) was used to terminate the reaction. The targeted microbubbles were allowed to adhere to the streptavidin-coated membrane in air-equilibrated phosphate buffered saline (PBS) containing calcium and magnesium (DPBS, 14080, Invitrogen, Thermo Fischer Scientific, Landsmeer, The Netherlands) by flotation for 5 min. Then, the membrane was gently washed three times with air-equilibrated PBS containing calcium and magnesium using a 3 mL plastic Pasteur pipette. For the nonbound targeted microbubbles the hydrogel was treated in the same way, except for the addition of streptavidin. The targeted microbubbles were added below the hydrogel-coated polyester membrane of the custom-made holder and floated up due to buoyancy. The hydrogels with the nonbound targeted microbubbles and bound targeted microbubbles were orientated in the setup as shown in Fig. 2.1.

Microbubble Spectroscopy

The vibrational responses of the bound and nonbound targeted microbubbles were captured using the Brandaris 128 ultra-high-speed camera operated at ~15 million frames/s [6]. Single microbubbles were investigated in Region Of Interest (ROI) mode [94] using the microbubble spectroscopy technique [74] in combination with the exact same setup as in [77], except for a higher magnification microscope objective (60×, NA = 0.9, Olympus, Tokyo, Japan). Briefly, a broadband single element polyvinyl difluoride (PVDF) transducer (25 mm focal distance, f-number 1.1, center frequency 5 MHz, PA275, Precision Acoustics Ltd, Dorchester, UK) transmitted a Gaussian tapered eight-cycle sine wave burst at transmit frequencies swept from 1 to 4 MHz (increment steps of 200 kHz) at a peak-negative pressure (P_A) of 50 or 150 kPa at the focus. The pressures were calibrated with two calibrated PVDF needle hydrophones in a separate measurement beforehand (0.2 mm diameter PA2030 and 1 mm diameter PA1875, Precision Acoustics). The optic focus was aligned with the acoustic focus, to ensure that the microbubble received the intended pressure. The ultrasound was triggered on the second recording of each microbubble to obtain the initial resting diameter and the noise level with our contour tracking algorithm in the first recording. The experiments were conducted at room temperature and the sample was submersed in air-equilibrated PBS containing calcium and magnesium. All microbubbles were exposed to ultrasound within 2 h after addition to the custom-made holder.

Data Analysis

Diameter-time (D-t) curves were obtained using custom-designed image analysis software [74] that determines the vibrational responses as described elsewhere [77]. Briefly, the acoustic stability of the microbubbles was quantified as the difference between the mean diameter of the microbubble in the initial D-t curve (D_0) and the final D-t curve (D_{end}). Next, the asymmetry of the D-t curves was measured as the ratio E/C between the relative expansion E, defined as $(D_{max}–D_0)/D_0$, and the relative compression C, defined as $(D_0–D_{min})/D_0$, of the microbubble. Where D_{max} is the maximum diameter, D_{min} the minimum diameter in the D-t curve, and D_0 the resting diameter before vibration. The E/C ratios were used to classify the asymmetry as: 1) compression-only behavior ($E/C < 0.5$); 2) normal excursion ($0.5 \leq E/C \leq 2$); or 3) expansion-only behavior ($E/C > 2$) [95].

Using the fast Fourier transformation (FFT) the frequency content of the D-t curves was analyzed in terms of the amplitude at the transmit frequency (f_T). These amplitudes were fit to a resonance curve of a linear oscillator by a least-mean-squares method [74, 77] to determine the resonance frequency (f_{res}) of the microbubble. f_{res} was usually located in between two insonifications. The microbubble diameters at these insonifications are known, and the diameter at resonance D_{res} was determined from an interpolation between these two insonifications. The maximum relative radial

excursions (*i.e.*, at f_{res}) were defined as the maximum amplitude of the FFT divided by the corresponding resting diameter of the microbubble [77]. The same approach was used to determine the subharmonic resonance frequencies (f_{sub}) and the second harmonic resonance frequencies, and the corresponding maximum relative radial excursions. Next, the maximum relative radial excursions were transformed into pressures using [65, 77]

$$P_S = -\frac{\rho\, \omega_{res}^2\, R_{res}^2\, \epsilon}{d} \tag{2.1}$$

where P_S is the scattered pressure at a distance d from the microbubble, $\rho = 1 \cdot 10^3$ kg/m^3 is the density of the surrounding fluid (PBS), $\omega_{res} = 2\pi\ f_{res}$ the angular resonance frequency, R_{res} the corresponding radius, and ϵ is the maximum relative radial excursion amplitude. All calculations were performed in MATLAB (The MathWorks Inc., Natick, MA, USA).

Statistics

Shapiro–Wilk tests for normality showed that the data was not normally distributed, so we used nonparametric testing. For comparing the acoustic stability of the microbubbles we used Wilcoxon signed-rank tests. When comparing groups, *e.g.*, bound DSPC and nonbound DSPC, we used Mann-Whitney U tests. Medians and interquartile ranges (IQRs) are reported and were calculated using Tukey's Hinges method. Statistical analyses were performed using SPSS (Statistics 21, IBM Corporation, Armonk, NY, USA) and a p-value < 0.05 was regarded as significant.

2.3. RESULTS

In total, 143 single microbubbles having a D_0 between 1.5 and 10 µm were analyzed. At 50 kPa, 46 bound DPPC microbubbles were insonified; 18 of which were also insonified at 150 kPa. For bound DSPC microbubbles, 43 were insonified at 50 kPa; 15 of which were also insonified at 150 kPa. None of the bound microbubbles detached during the experiments since every microbubble remained within the optic focus. For the nonbound microbubbles we included 26 DPPC and 28 DSPC microbubbles, which were all insonified at both 50 and 150 kPa.

Acoustic Stability

Fig. 2.2 shows an example of a bound DPPC-based microbubble insonified at a pressure of 50 kPa and subsequently at 150 kPa. Comparing D_0 with D_{end} at both pressures shows a clear decrease in diameter. The corresponding ultra-high-speed Brandaris recordings can be found in the Supplementary Material of the online published version of this manuscript [68], as well those of a bound DSPC-based microbubble. Overall, at P_A = 50 kPa, both bound DPPC and DSPC-based

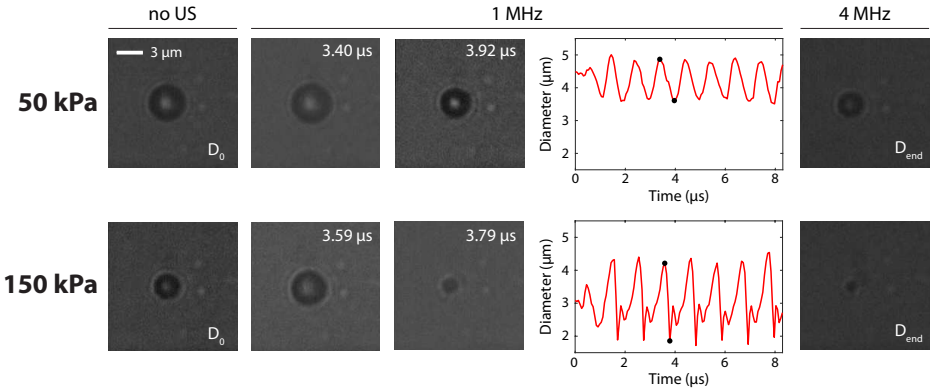

Figure 2.2: Still frames of the Brandaris ultra-high-speed recordings of a bound DPPC-based microbubble insonified at pressures of 50 and 150 kPa (see Supplemental Material of the online published version of this manuscript for the videos [68]). The initial state is indicated with "no US" and D_0 is determined from this recording. At a frequency of 1 MHz, two frames have been selected: one in the expansion phase and one in the compression phase of the oscillation, as also indicated by the black dots in the D-t curves. The curve at a pressure of 150 kPa shows inertial cavitation and thus asymmetric behavior. Acoustic deflation is clearly visible when comparing D_{end}, determined from the 4 MHz recordings, with D_0.

microbubbles deflated significantly more than when they were nonbound (p = 0.0001), as shown in Fig. 2.3. The median size for the bound DPPC microbubbles after insonification was 83% of D_0, while this was 98% for the nonbound DPPC microbubbles. The median size of bound DSPC microbubbles was 93% of D_0 after insonification, whereas nonbound DSPC microbubbles maintained their original size (100% of D_0). At a pressure of 150 kPa, the size difference between bound DPPC and nonbound DPPC microbubbles was not significant. The median diameter after insonification decreased to 53% of D_0 for bound DPPC microbubbles and to 56% for nonbound DPPC microbubbles. In case of DSPC microbubbles, those that had bound deflated more than those that had not (p = 0.004). For the DSPC microbubbles this was 76% for the bound ones and hardly any shrinkage (98% of their initial size) for the nonbound ones. In addition, for both bound and nonbound microbubbles, those based on DPPC deflated more than those based on DSPC at 50 kPa (bound: p = 0.001, nonbound: p = 0.031) and also at 150 kPa (both p = 0.0001).

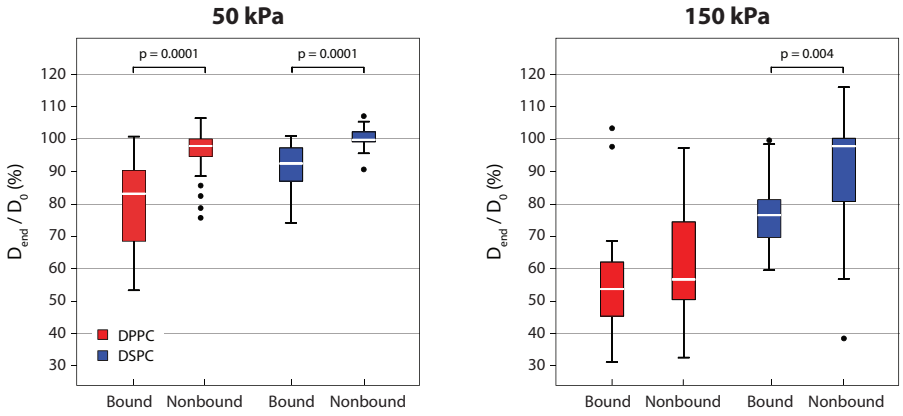

Figure 2.3: Diameter change during ultrasound exposure expressed as D_0/D_{end} for bound DPPC (50 kPa: n = 46, 150 kPa: n = 18), nonbound DPPC (50 kPa: n = 28, 150 kPa: n = 28), bound DSPC (50 kPa: n = 43, 150 kPa: n = 15), and nonbound DSPC microbubbles (50 kPa: n = 26, 150 kPa: n = 26). The filled black circles are outliers.

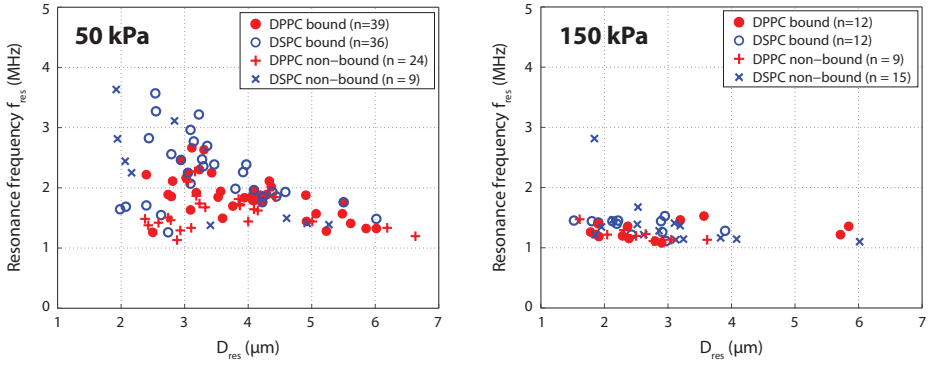

Figure 2.4: Resonance frequencies (f_{res}) of bound DPPC (filled red circles), nonbound DPPC (red crosses), bound DSPC (blue open circles), and nonbound DSPC (blue crosses) microbubbles plotted versus the diameter at resonance (D_{res}) at P_A = 50 kPa (left panel) and P_A = 150 kPa (right panel).

Linear Oscillation Behavior

The resonance frequencies in relation to D_{res} are shown in Fig. 2.4. First of all, at a pressure of 50 kPa the resonance frequencies of bound DSPC microbubbles were similar to those of nonbound DSPC microbubbles. For DPPC-based microbubbles, the resonance frequencies of bound microbubbles were significantly higher than for nonbound DPPC microbubbles (p = 0.045). To further highlight the differences in resonance frequencies between bound and nonbound DPPC microbubbles, we compared the resonance frequencies of those having D_{res} < 4 µm. For larger microbubbles all resonance frequencies were similar, but for microbubbles having

Table 2.1: Resonance frequencies and maximum relative radial excursions provided as median (IQR).

Type	P_A (kPa)	Bound	D_{res} (μm)	F_{res} (MHz)	Maximum relative radial excursion
DPPC	50	Yes	1 - 7	1.85 (1.63 - 2.11)	0.14 (0.11 - 0.18)
			< 4	1.94 (1.83 - 2.25)	0.14 (0.10 - 0.20)
		No	1 - 7	1.50 (1.39 - 1.73)	0.09 (0.06 - 0.13)
			< 4	1.59 (1.40 - 1.77)	0.07 (0.06 - 0.10)
	150	Yes	1 - 7	1.22 (1.18 - 1.37)	0.28 (0.22 - 0.33)
		No	1 - 7	1.20 (1.13 - 1.24)	0.25 (0.18 - 0.28)
DSPC	50	Yes	1 - 7	2.39 (1.98 - 2.78)	0.11 (0.08 - 0.12)
			2 - 4	> 2	0.11 (0.08 - 0.12)
		No	1 - 7	2.63 (2.25 - 3.11)	0.05 (0.03 - 0.13)
			2 - 4	> 2	0.03 (0.02 - 0.04)
	150	Yes	1 - 7	1.43 (1.27 - 1.45)	0.28 (0.23 - 0.35)
		No	1 - 7	1.28 (1.15 - 1.41)	0.11 (0.09 - 0.23)

a D_{res} < 4 μm, the resonance frequencies of bound DPPC microbubbles were significantly higher than for nonbound DPPC microbubbles (p = 0.002). In addition, no overlap was found between the median (IQR) resonance frequencies of bound DPPC microbubbles and nonbound DPPC microbubbles (Table 2.1). In contrast, the resonance frequencies of bound and nonbound DSPC microbubbles were similar for all studied sizes (p = 0.494). The resonance frequencies of bound DSPC microbubbles were significantly higher than those of bound DPPC-based microbubbles at P_A = 50 kPa (p = 0.001), for the nonbound DSPC and DPPC microbubbles no difference was found. All resonance frequencies at a pressure of 150 kPa were similar. The number of microbubbles included in Figs. 2.4 and 2.5 is lower than the total number of studied microbubbles, since some resonance peaks were below or above the measuring range (<1 or >4 MHz); the resonance frequency could therefore not be determined.

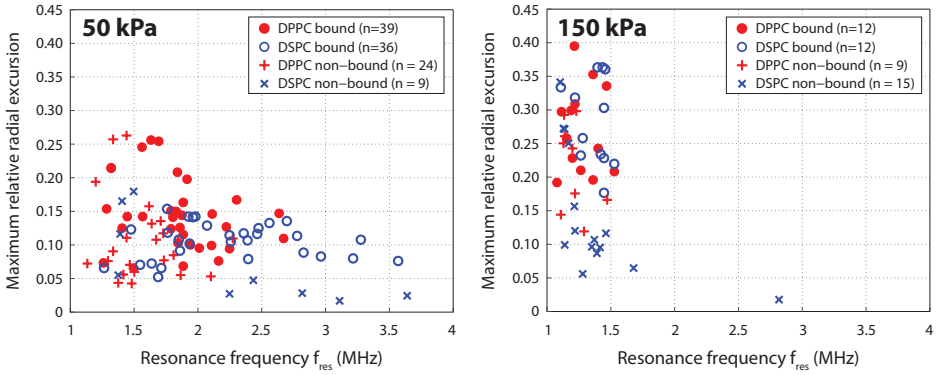

Figure 2.5: Maximum relative radial excursions at the resonance frequency of bound DPPC (filled red circles) nonbound DPPC (red crosses), bound DSPC (blue open circles), and nonbound DSPC (blue crosses) microbubbles plotted versus the resonance frequency (f_{res}) at P_A = 50 kPa (left panel) and P_A = 150 kPa (right panel).

For bound DPPC microbubbles, the maximum relative radial excursions at a pressure of 50 kPa were significantly higher than for the nonbound DPPC microbubbles (p = 0.002, Fig. 2.5, Table 2.1). Although the maximum relative radial excursions of bound DSPC microbubbles were not significantly different from nonbound DSPC microbubbles (p = 0.157) over the whole resonance frequency range, the maximum relative radial excursions for bound DSPC microbubbles were significantly higher for resonance frequencies >2 MHz (p = 0.001). In addition, the maximum relative radial excursions of bound DSPC microbubbles were significantly lower than of bound DPPC microbubbles (p = 0.0001), but similar for the nonbound DSPC and DPPC microbubbles. At a driving pressure of 150 kPa the maximum relative radial excursions of bound and nonbound DPPC microbubbles were similar, but significantly higher for bound DSPC than nonbound DSPC microbubbles (p = 0.001). The maximum relative radial excursions for bound DPPC and bound DSPC-based microbubbles were similar (Fig. 2.5, Table 2.1). For nonbound microbubbles the maximum relative radial excursions were significantly higher (p = 0.03) for DPPC microbubbles than for DSPC microbubbles.

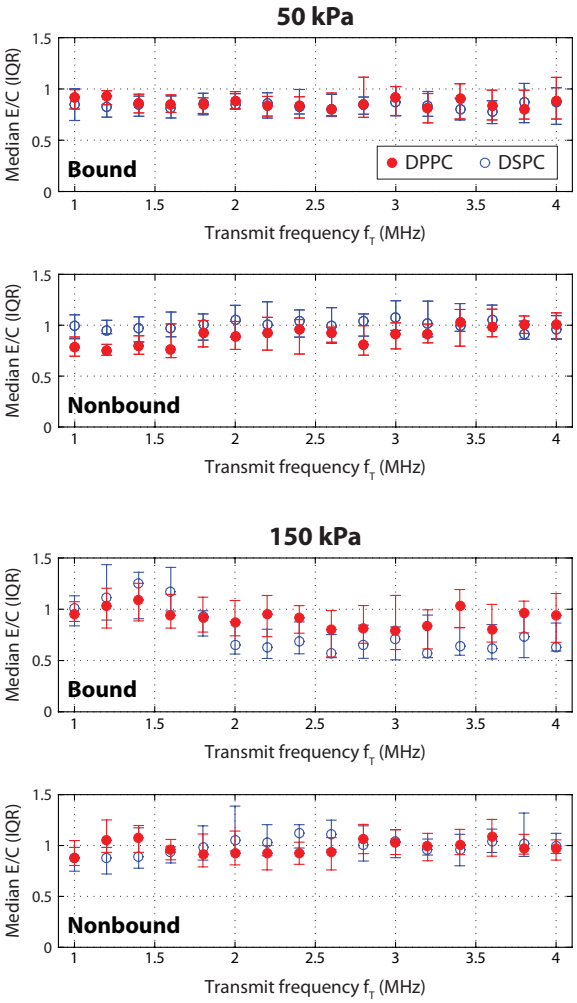

Figure 2.6: Median (IQR) ratio between the relative expansion E and the relative compression C of bound DPPC (50 kPa: n = 37, 150 kPa: n = 18) and bound DSPC (50 kPa: n = 43, 150 kPa: n = 15) microbubbles, and nonbound DPPC (50 kPa: n = 28, 150 kPa: n = 28) and nonbound DSPC (50 kPa: n = 26, 150 kPa: n = 26) microbubbles plotted versus the transmit frequency at P_A = 50 kPa and P_A = 150 kPa.

Nonlinear Oscillation Behavior

The asymmetry of the radial excursions at each transmit frequency was expressed as the ratio between the relative expansion E and relative compression C. At 50 kPa, the median of the radial excursions was compression-dominated with $0.5 < E/C < 1$ for bound targeted microbubbles of both types (Fig. 2.6) at all frequencies. For the nonbound microbubbles the oscillations were mostly symmetric, except

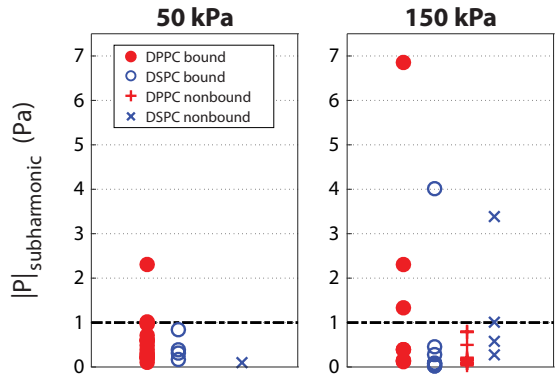

Figure 2.7: Absolute pressures emitted at the subharmonic resonance frequency of bound DPPC (50 kPa: n = 17, 150 kPa: n = 8), bound DSPC microbubbles (50 kPa: n = 7, 150 kPa: n = 7), nonbound DPPC (50 kPa: n = 0, 150 kPa: n = 10), and nonbound DSPC microbubbles (50 kPa: n = 1, 150 kPa: n = 4).

for the frequencies between 1 and 1.6 MHz for which the radial excursions of DPPC microbubbles were compression-dominated. At P_A = 150 kPa the excursion behavior of bound microbubbles at frequencies between 1 and 1.8 MHz ranged from symmetric to expansion-dominated, whereas at higher frequencies the behavior of both microbubble types was compression-dominated. An example of a bound DPPC-based microbubble showing asymmetric oscillations at 150 kPa due to inertial cavitation is shown in Fig. 2.2. The nonbound microbubbles showed mostly symmetric oscillations.

Responses at the subharmonic frequency at a driving pressure of 50 kPa were present in 22 out of 46 (48%) bound DPPC microbubbles and in 7 out of 43 (16%) bound DSPC microbubbles. For both nonbound DPPC and DSPC microbubbles only one (4%) responded at the subharmonic frequency. At the higher pressure of 150 kPa, the number of bound DPPC microbubbles responsive at the subharmonic frequency was similar to that at 50 kPa: 8 out of 18 (44%), but increased to 9 out of 15 (60%) for DSPC-based microbubbles. The number of nonbound microbubbles that responded at the subharmonic frequency increased to 12 out of 28 (43%) for DPPC and 6 out of 26 (23%) for DSPC microbubbles.

For quite some microbubbles a response at the subharmonic frequency was observed in the FFT of the D-t curves. However, to determine the scattered subharmonic pressures using Equation 2.1, the subharmonic resonance frequency f_{sub} is required; f_{sub} could only be determined for the microbubbles shown in Fig. 2.7. Reasons for not being able to determine the subharmonic resonance curve were not enough points for a fit or the peak of the subharmonic resonance curve was below or above the measuring range. Emitted subharmonic pressures at a distance of 2 cm were similar irrespective of binding and the type of lipid coating at each acoustic pressure (Fig. 2.7), but their origin was different. At 50 kPa, of the 17 bound DPPC microbubbles shown in Fig. 2.7, nine had a response at transmit at twice the resonance frequency (T2R with $f_{sub} = f_{res}$ [96, 97]) and four at transmit at the resonance frequency (TR, $f_{sub} = 1/2\ f_{res}$ [76, 96]).

Of the seven bound DSPC microbubbles, three had a clear response at T2R and none had a response at TR. At 150 kPa, of the eight bound DPPC microbubbles seven had a response at T2R and one at TR. Of the seven bound DSPC microbubbles four had a response at T2R and none at TR. In the case of nonbound microbubbles at 50 kPa the only microbubble responsive at f_{sub} was a DSPC microbubble with a response at T2R. At 150 kPa, one out of the ten DPPC microbubbles had a response at T2R and two out of ten at TR. For the four nonbound DSPC microbubbles two had a response at T2R and none at TR. For the other microbubbles responding at f_{sub}, the relation between TR or T2R could not be determined; either because no clear relation was found between the subharmonic and fundamental frequency, or because the fundamental frequency had not been determined since the peak was located outside the measuring range. We assumed a detection limit of 1 Pa (black dashed line in Fig. 2.7) for diagnostic ultrasound scanners, achievable with a typical high-quality transducer for harmonic imaging [98].

At P_A = 50 kPa, about half of both bound DPPC (53%) and bound DSPC (57%) microbubbles responded at the second harmonic frequency. The number of responding nonbound microbubbles based on DPPC was similar (50%), but for nonbound DSPC microbubbles only 1 out of 26 (4%) was responsive at the second harmonic frequency. The number of responsive microbubbles at a driving pressure of 150 kPa increased in all cases: to 14 out of 15 (93%) for bound DPPC, 13 out of 18 (72%) for bound DSPC, 17 out of 28 (61%) for nonbound DPPC, and 8 out of 26 (31%) for nonbound DSPC microbubbles. The median (IQR) pressures emitted at the second harmonic frequency when insonified at 50 kPa were 2.0 (1.0 –2.6) Pa for bound DSPC microbubbles, hence in the same order as the only nonbound DSPC microbubble (3.1 Pa, Fig. 2.8). For bound and nonbound DPPC microbubbles, the emitted pressures were not significantly different (p = 0.351). In addition, the emitted pressures at the second harmonic frequency of bound DPPC microbubbles were higher than those of bound DSPC microbubbles (p = 0.004). At the higher driving pressure of 150 kPa, the emitted pressures were significantly higher (p = 0.017) for nonbound than bound DSPC microbubbles, with median pressures of 28.5 (14.0 –38.1) Pa for nonbound and 3.2 (2.4 –8.4) Pa for bound DSPC microbubbles. The median pressures of the other groups were all similar.

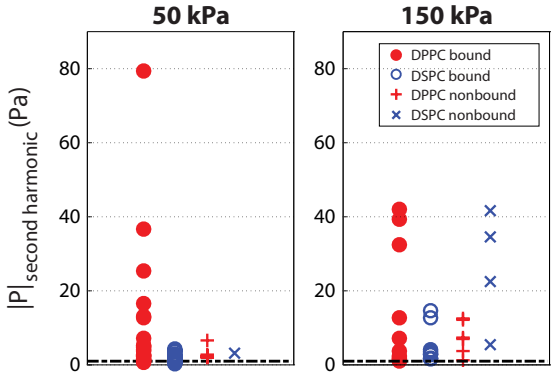

Figure 2.8: Absolute pressures emitted at the second harmonic resonance frequency of bound DPPC (50 kPa: n = 21, 150 kPa: n = 10), bound DSPC microbubbles (50 kPa: n = 19, 150 kPa: n = 8), nonbound DPPC (50 kPa: n = 6, 150 kPa: n = 6), and nonbound DSPC microbubbles (50 kPa: n = 1, 150 kPa: n = 4).

2.4. DISCUSSION

This paper investigated vibrational responses of bound and nonbound microbubbles to identify differences to acoustically discriminate them. For DPPC-based microbubbles with diameters between 2 and 4 µm the resonance frequencies and relative radial excursions were higher than for nonbound DPPC-based microbubbles (P_A = 50 kPa). In contrast, at an insonifying pressure of 150 kPa the relative radial excursions for bound and nonbound DPPC-based microbubbles were similar. Interestingly, at this higher pressure the radial excursions for bound DSPC-based microbubbles were higher than for nonbound DSPC microbubbles, whereas these were similar at 50 kPa. We also found compression-dominated behavior and a higher number of responsive microbubbles at the second harmonic frequency for bound microbubbles, irrespective of the main coating lipid.

Acoustic Stability

Bound microbubbles were acoustically less stable than nonbound microbubbles, irrespective of their main coating component. Further, we found that the acoustic stability for DPPC-based microbubbles was lower than that for DSPC-based microbubbles. This was previously attributed to the shorter acyl chain length of the DPPC lipid than that of the DSPC lipid [77]. This shorter chain results in lower intermolecular van der Waals forces between the different lipids and results in less attraction and cohesion of the microbubble shell [77, 99]. The maximum relative radial excursions of bound microbubbles were higher at the resonance frequency than those of nonbound microbubbles (for DPPC at 50 kPa and DSPC at 150 kPa). This means that the radial excursions after binding were more prominent, which resulted in more shrinkage and therefore a lower acoustic stability. Others have reported lower radial excursions after binding for DSPC-based microbubbles [79, 81], but those studies had not covalently linked their model biomarker to their membrane. As a result,

the biomarker that attached to the microbubble shell increased the stiffness [87] and therefore limits the radial oscillations.

Some nonbound DSPC microbubbles appeared to increase in diameter after insonification at 150 kPa. The microbubbles in which this was observed were all relatively small (<2.5 μm). This apparent increase may be due to small changes in the optic focus due to radiation forces, in combination with the error in the tracking algorithm which was previously estimated to be approximately 10% [74].

Linear Oscillation Behavior

The resonance frequencies for bound DPPC microbubbles were higher than for nonbound DPPC microbubbles at a pressure of 50 kPa for microbubbles with diameters between 2 and 4 μm at resonance. Based on the IQRs, the resonance frequencies of most bound DPPC microbubbles of this size were higher than 1.8 MHz, whereas those of nonbound DPPC microbubbles were lower than 1.8 MHz. In terms of shell properties, a higher resonance frequency is related to an increase in elasticity (*i.e.*, a stiffer shell) by the Marmottant model [100]. It is not likely that the elasticity changes upon binding, but the apparent stiffness may increase due to binding of the microbubble to the biomarker. We may not have found a change in apparent stiffness for DSPC-based microbubbles, because their surface binding area is smaller than for DPPC-based microbubbles as previously determined by our group for the same type of microbubbles and same streptavidin biomarker [88]. Next, the initial elasticity of DSPC microbubbles is already higher than for DPPC microbubbles [77], and it has been shown that the resonance frequencies for DSPC microbubbles did not change after conjugating the relatively heavy molecule streptavidin to the lipid shell, whereas for DPPC microbubbles the resonance frequencies increased [87]. In addition, the resonance frequency exponentially decreases for increasing microbubble size [101]. As a consequence, the difference in resonance frequencies for microbubbles with diameters between 2 and 4 μm is larger than for microbubbles with diameters between 5 and 7 μm [77]. An increase in resonance frequency for bound microbubbles will therefore be more pronounced for smaller than for larger microbubbles. This may explain why the apparent increase in stiffness was only present for bound DPPC microbubbles having diameters between 2 and 4, and not for DSPC microbubbles or larger DPPC microbubbles. At 150 kPa, however, all resonance frequencies appeared the same. The microbubble oscillations at this pressure start off very violently (*i.e.*, inertial cavitation) in the first insonifications between 1 and 1.5 MHz, thereby largely decreasing the microbubble size and shifting its original resonance frequency toward higher frequencies. Since the mechanical index was ~2× lower for the insonifications at the end of the frequency sweep, the resulting relative radial excursions were lower at the new resonant microbubble size. Therefore, the oscillations of the first

insonifications dominated the resonance behavior, leading to an apparent resonance frequency between 1 and 1.5 MHz before shrinkage.

Others have also reported differences in resonance frequencies between bound and nonbound microbubbles. Casey *et al.* [82] reported an increase in resonance frequency for their bound in-house produced biotinylated microbubbles, but for DSPC microbubbles (C_3F_8 gas core and same components as our DSPC-based microbubbles, but unknown ratios) instead of for DPPC-based microbubbles as we report here. Overvelde *et al.* [79] found 30% lower frequencies of maximum response for targeted BG-6438 microbubbles bound to an OptiCell wall than for nontargeted BG-6437 microbubbles floating against the wall at pressures <40 kPa (both bubble types are from Bracco Research S.A., Geneva, Switzerland). The BG-6438 microbubbles were targeted to FITC-BSA using an anti-FITC antibody attached to the microbubble shell using streptavidin-biotin bridging. The main limitation of both studies is the method of attaching the model biomarker streptavidin to the cellulose tube [82] or FITC-BSA to the OptiCell wall [79], namely, by physisorption. As mentioned before, this physisorbed biomarker is likely to bind to the microbubble shell creating a lipid-coated microbubble covered with the model biomarker. These very large and heavy complexes are expected to behave completely different in an ultrasound field than a bare lipid-coated targeted microbubble, as has been shown for microbubbles that were functionalized with streptavidin, depending on the initial stiffness of the microbubble coating [87]. In addition to this, Overvelde *et al.* [79] did not block the OptiCells to prevent unspecific binding in their experiments that compared free BG-6437 microbubbles and BG-6437 microbubbles close to the wall: the latter may have actually bound to the wall. Next to that, the BG-6437 microbubbles did not have anti-FITC antibody attached to their shell, which is not a fair comparison between microbubbles that have bound to the wall and that are floating against the wall. In our present study, the covalent coupling of streptavidin to the hydrogel, and thus the membrane, was established and it was confirmed that no streptavidin was present on the microbubble shell [88].

Nonlinear Oscillation Behavior

For nonlinear contrast-enhanced ultrasound imaging the responses at the subharmonic and second harmonic frequencies are usually exploited [102]. At 50 kPa more bound than nonbound microbubbles responded at the subharmonic frequency, for both the DPPC and DSPC-based coatings. At 150 kPa more microbubbles –both bound and nonbound– were responsive at the subharmonic frequency, but the emitted pressures of single microbubbles were close to or below the assumed detection limit for clinical use of 1 Pa [98]. Based on these results, the subharmonic emissions seem of limited use for nonlinear contrast-enhanced imaging and discrimination of bound from nonbound microbubble based on our experimental conditions. However,

when multiple microbubbles are in close proximity of each other, their subharmonic emissions could be in phase and the resulting cumulative pressure may be higher [80]. This is worth to further investigate, but was outside the scope of this paper.

We found similar amplitudes at the subharmonic frequency for bound and nonbound microbubbles, in line with the findings of Zhao *et al.* [81] for microbubbles with a coating of 82 mol% DSPC, 9 mol% DSPE-PEG(2000), and 9 mol% DSPE-PEG(2000)-biotin [103]. Helfield *et al.* [80] reported similar amounts of bound and nonbound Target-Ready MicroMarker microbubbles that were responsive at the subharmonic frequency, whereas we found more bound microbubbles that responded. The different composition and gas core of Target-Ready MicroMarker likely contributed to these differences. As suggested in [80], the membrane material could have frequency-dependent effects and their results might be biased due to aggregation of microbubbles that may have changed the echogenicity [104]. We previously performed the exact same experiments as described here for nonbound microbubbles in an OptiCell [105]. Indeed, a membrane dependent effect was observed, but was not found to be frequency related. The maximum relative radial excursions of nonbound microbubbles in an OptiCell (both DPPC and DSPC) were 2-2.5 times higher than for nonbound microbubbles floating against the hydrogel. Because the microbubbles may be partly embedded in the polymer-based hydrogel, this can damp the microbubble oscillations and therefore result in lower maximum relative radial excursions.

Another difference between our study and that in [80] is that they coated their cellulose tube with streptavidin using physisorption, with the disadvantage of streptavidin covering the microbubble shell, which may have influenced the amplitude of the subharmonic signal. Indeed, their acoustic measurements showed a 20% higher subharmonic signal of Target-Ready MicroMarker, a streptavidin-functionalized lipid-coated microbubble, when bound to a biotinylated agarose phantom. The difference between the results in [80] and our results presented in this paper might also be due to the used techniques: ultra-high-speed optical imaging versus acoustic measurements. In our setup, we were only able to image the top-view of the microbubble oscillations, whereas acoustic measurements can detect out-of-plane signals as well. If a larger portion of the subharmonic excursions were generated in the perpendicular plane, we might have missed those vibrations with our setup.

Numerical simulations have shown that the subharmonic signal is optimal when the microbubble is insonified at T2R [106]. Experimental validation showed that the threshold for generating TR subharmonic responses is higher than that for T2R subharmonic responses in lipid-coated microbubbles [96, 107]. The absence of DSPC responders at TR may suggest that the threshold for generating TR subharmonic responses is lower for DPPC microbubbles than for DSPC microbubbles, irrespective of them being bound or not. On the other hand, due to the applied frequency range and studied microbubble sizes, the majority of the resonance frequencies were between

1.5 and 3.5 MHz; this limits the possibility to insonify microbubbles at T2R within the frequency range we applied.

The higher second harmonic amplitudes we measured for nonbound DSPC-based microbubbles at 150 kPa are in contrast with results reported by others [78, 82]. The study in [82] used microbubbles similar to our DSPC microbubbles, but with a C_3F_8 core and attachment to a capillary wall using the physisorbed streptavidin as biomarker (f_T = 2 MHz, P_A = 90 kPa). The study in [78] also used DSPC-based microbubbles, with a setup and parameters comparable to those in [82]. Both studies used somewhat lower pressures, but may also have effectively studied bound targeted DSPC-based microbubbles coated with a streptavidin layer, which may explain the different findings. In our study, the emitted pressure amplitudes of bound microbubbles were similar or lower than for nonbound microbubbles and acoustic discrimination based on the second harmonic pressures does therefore not seem feasible.

DSPC versus DPPC for Ultrasound Molecular Imaging Applications

The differences between bound targeted DPPC and DSPC-based microbubbles were not as pronounced as we expected from the differences in shape change upon adherence and their surface binding areas, as previously determined by our group for the same type of microbubbles and same streptavidin biomarker [88]. The most prominent differences we did find were higher acoustic stability for nonbound microbubbles, higher resonance frequencies (for DPPC microbubbles with diameters between 2 and 4 μm) and radial excursions for bound DPPC microbubbles at 50 kPa, and higher amplitudes at the second harmonic frequency for nonbound DSPC microbubbles than for bound DSPC microbubbles at 150 kPa. The lower resonance frequencies for DPPC microbubbles than for DSPC microbubbles were already observed for nonbound DPPC microbubbles [77], and were thus maintained upon binding.

For *in vivo* ultrasound molecular imaging the ideal targeted microbubble: 1) can effectively bind to the biomarker of interest; 2) persists binding to the biomarker after initial binding, *i.e.*, the binding strength is larger than the shear stress induced by the flowing blood; 3) is stable during the course of the ultrasound examination; 4) nonlinearly scatters ultrasound that is microbubble specific; 5) can be discriminated acoustically from nonbound microbubbles; and 6) has the same resonance frequency as the other microbubbles that are injected, *i.e.*, all microbubbles in the population respond in the same way to ultrasound. Concerning the first two points, Kooiman *et al.* [88] favored targeted DPPC microbubbles over DSPC microbubbles because of their larger surface binding area to a streptavidin-coated membrane, their dome shape after binding, and a more homogeneous distribution of fluorescently labeled ligands attached to DSPE-PEG(2000). The more homogeneous lipid distribution

might aid the initial attachment, whereas the larger binding area and difference in shape might be able to better sustain blood shear forces. However, binding of the microbubbles was performed under static conditions and experiments in the presence of flow are required to verify which of the two microbubble types binds best under flow. Based on the acoustic stability (point 3), DSPC-based microbubbles are favored over DPPC-based microbubbles. This also means that the size is better maintained during insonification and the resonance frequency will therefore be more consistent throughout the investigation. In terms of nonlinear scattering of ultrasound (point 4), the maximum relative radial excursions at the subharmonic frequency for both our DPPC and DSPC microbubbles resulted in ~20 dB lower scattered pressures than the second harmonic responses. The subharmonic responses were unpredictable and too low to discriminate bound from nonbound microbubbles. In contrast, the responses at the second harmonic frequency were sufficiently high to be detected, but amplitudes were similar for bound and nonbound microbubbles, or higher for the nonbound ones in terms of DSPC-based microbubbles (point 5). At 50 kPa, bound and nonbound DPPC microbubbles with diameters between 2 and 4 μm at resonance could be separated based on their resonance frequencies: bound DPPC microbubbles had resonance frequencies above 1.8 MHz, whereas those were significantly lower for nonbound DPPC microbubbles. Lastly (point 6), as mentioned in the introduction one of the main challenges for successful translation of ultrasound molecular imaging to the clinic is the production of microbubble populations that have the same acoustic signature. Both the DPPC and DSPC-based microbubbles can have different resonance frequencies and radial excursions although their sizes are similar. Several studies showed that monodisperse lipid-coated microbubble distributions can be produced using flow-focusing devices [108–111]. Kaya *et al.* [109] and Talu *et al.* [111] studied the difference between echo amplitudes of these monodisperse single microbubbles when insonified at a frequency close to resonance, and found a lower standard deviation than for polydisperse microbubbles. Segers and Versluis [112] developed an acoustic sorting chip that separated monodisperse microbubbles based on the radiation force they experienced, which resulted in an overall contrast enrichment of more than 10 dB. This is an important step toward improving the quality of *in vivo* ultrasound molecular imaging, especially if microbubbles with low shell elasticity and a diameter between 2 and 4 μm can be produced to distinguish bound from nonbound microbubbles, as shown in our study. However, this approach is still limited to specific microbubble compositions that can be produced monodispersely by means of flow focusing devices.

Summing up all the aforementioned similarities, differences, advantages, and disadvantages of DPPC and DSPC-based microbubbles, this results in a favor for DSPC-based microbubbles for ultrasound molecular imaging, solely based on a higher acoustic stability. Studying the adherence of the microbubbles under flow

should reveal whether the heterogeneous lipid distribution in the DSPC shell hinders binding. On the other hand, bound DPPC microbubbles (diameters between 2 and 4 μm) at 50 kPa had resonance frequencies higher than 1.8 MHz, whereas those of nonbound DPPC microbubbles were lower than 1.8 MHz. In addition, the relative radial excursions of bound DPPC microbubbles were also higher. When monodisperse DPPC microbubbles with a diameter between 2 and 4 μm are produced, these could acoustically be discriminated based on their resonance frequency.

Limitations and Outlook

Although we aimed to create a more *in vivo*-like setup using covalent biomarker binding versus physisorption, the membrane we used in our experiments was still artificial. The 1-2 μm-thick hydrogel created a softer layer between the microbubble and the polyester membrane, but to have a real *in vivo*-like membrane one would need to develop a material with exactly the same stiffness, viscosity, etc. as an actual cell layer or perform *in vivo* experiments. In addition, *in vivo* one can also study microbubble vibration when microbubbles are in contact with cells and under flow, for which the chorioallantoic membrane model could be used. This model has proven to be useful to study nontargeted microbubble vibration using ultra-high-speed imaging and targeted-microbubble mediated drug delivery [16, 113].

For *in vivo* ultrasound molecular imaging multiple microbubbles may bind in closer range with each other than investigated in this paper. However, the binding range actually depends on the availability of the biomarker on the cell surface, which depends both on the cell type and the biomarker of interest. When the interbubble distance is ≤10 μm, this will cause interaction of the bubbles in terms of secondary Bjerknes forces, and due to the secondary Bjerknes forces a bubble will deform in the direction of their neighboring bubble [114]. Next to that, two similar sized bubbles that are close to each other result in a shift in resonance frequency and therefore a decrease in maximum relative radial excursions [115]. As a consequence, for abundant biomarkers on the cell membrane these observations may counteract the increase in resonance frequency and maximum relative radial excursions we observed for DPPC microbubbles between 2 and 4 μm at 50 kPa. This, however, should first be experimentally verified using a setup comprising of a biomarker distribution that is comparable to the *in vivo* situation. The chorioallantoic model would be a good approach to study this.

2.5. CONCLUSION

This paper shows that binding of in-house produced DPPC-based microbubbles to a streptavidin-coated surface increased the resonance frequencies (for microbubbles with diameters between 2 and 4 μm) and the corresponding relative radial excursions at relatively low pressure (50 kPa). At this pressure, the bound 2 to 4 μm microbubbles resonated above 1.8 MHz, whereas the nonbound 2 to 4 μm DPPC microbubbles were resonant below this frequency. In terms of nonlinear responses, only the responses at the second harmonic frequency of bound DSPC microbubbles at 150 kPa were lower than of nonbound DSPC microbubbles. Our in-house produced DSPC-based microbubbles were acoustically more stable than our DPPC-based microbubbles, which is the major advantage of this type of microbubble for ultrasound molecular imaging applications.

ACKNOWLEDGEMENT

The authors would like to thank R. Beurskens, F. Mastik, M. Manten, and G. Springeling for technical assistance, Dr. T. Kokhuis for valuable discussions (all from the Department of Biomedical Engineering, Thorax Center, Erasmus MC), and Dr. J. L. Raymond for experimental assistance (visiting fellow Whitaker program). They would also like to thank I. Chrifi from the Department of Experimental Cardiology, Thorax Center, Erasmus MC, for the spectrophotometer measurements, and Dr. E. Gedig from XanTec bioanalytics GmbH, Germany, for discussions about the covalent coating of streptavidin to the polyester membranes. The authors are grateful to Prof. Dr. A. L. Klibanov from the University of Virginia, Cardiovascular Division, Charlottesville, VA, USA, for discussions about the microbubble preparation.

3

Viability of endothelial cells after ultrasound-mediated sonoporation

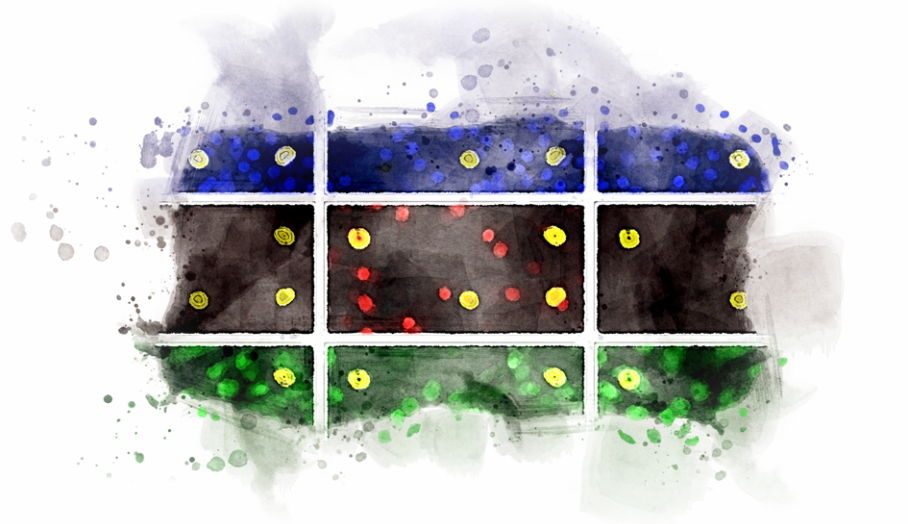

Based on:
Tom van Rooij, Ilya Skachkov, **Inés Beekers**, Kirby R. Lattwein, Jason D. Voorneveld, Tom J. A. Kokhuis, Deep Bera, Ying Luan, Antonius F. W. van der Steen, Nico de Jong, and Klazina Kooiman, "Viability of endothelial cells after ultrasound-mediated sonoporation: Influence of targeting, oscillation, and displacement of microbubbles", *Journal of Controlled Release*, vol. 238, pp. 197–211, 2016 [40].

Abstract

Microbubbles (MBs) have been shown to create transient or lethal pores in cell membranes under the influence of ultrasound, known as ultrasound-mediated sonoporation. Several studies have reported enhanced drug delivery or local cell death induced by MBs that are either targeted to a specific biomarker (targeted microbubbles, tMBs) or that are not targeted (non-targeted microbubbles, ntMBs). However, both the exact mechanism and the optimal acoustic settings for sonoporation are still unknown. In this study we used real-time uptake patterns of propidium iodide, a fluorescent cell impermeable model drug, as a measure for sonoporation. Combined with high-speed optical recordings of MB displacement and ultra-high-speed recordings of MB oscillation, we aimed to identify differences in MB behavior responsible for either viable sonoporation or cell death. We compared ntMBs and tMBs with identical shell compositions exposed to long acoustic pulses (500 - 50,000 cycles) at various pressures (150 - 500 kPa). Propidium iodide uptake highly correlated with cell viability; when the fluorescence intensity still increased 120 s after opening of the pore, this resulted in cell death. Higher acoustic pressures and longer cycles resulted in more displacing MBs and enhanced sonoporation. Non-displacing MBs were found to be the main contributor to cell death, while displacement of tMBs enhanced reversible sonoporation and preserved cell viability. Consequently, each therapeutic application requires different settings: non-displacing ntMBs or tMBs are advantageous for therapies requiring cell death, especially at 500 kPa and 50,000 cycles, whereas short acoustic pulses causing limited displacement should be used for drug delivery.

Index Terms — Ultrasound contrast agents, microbubble behavior, sonoporation, drug delivery, therapy, endothelial cells

3.1. INTRODUCTION

Microbubbles (MBs) are ultrasound (US) contrast agents that consist of gas bubbles with diameters between 1 and 10 μm, which are encapsulated by a stabilizing coating. Non-targeted microbubbles (ntMBs) are clinically used as blood pool agents for contrast-enhanced US imaging in cardiology and radiology [2, 116] and also have therapeutic potential [3, 26]. Targeted microbubbles (tMBs) are promising agents for US molecular imaging and therapy; in particular for diseases that can alter the endothelium, such as cancer and inflammation. The tMBs can adhere to specific disease-associated intravascular biomarkers by the addition of targeting ligands to the MB coating [71, 87].

When MBs are insonified by US, they oscillate due to the acoustic pressure wave [3]. Oscillating MBs can increase cell membrane permeability to facilitate intracellular

drug uptake (sonoporation), stimulate endocytosis, and open cell-cell junctions [3, 32]. Although the exact mechanisms of MB-mediated drug uptake still remain unknown, many studies have attempted to pinpoint the US settings that best stimulate intracellular drug uptake [3, 117]. So far the key findings are: 1) cell membrane pores induced by oscillating MBs can be reversible or irreversible [37]; 2) a MB has to oscillate with sufficient amplitude to induce sonoporation [15]; 3) tMBs stimulate drug uptake better than ntMBs both *in vitro* [118–122] and *in vivo* [123–126]. Recently, it has also been shown that the cell membrane pore size and pore resealing coefficient can be mathematically obtained from real-time observed MB-mediated intracellular drug uptake [38].

While reversible sonoporation likely facilitates cellular drug uptake without causing lethal damage to the cell, irreversible sonoporation is thought to lead to significant cell damage and eventually cell death. Different therapeutic approaches may require reversible or irreversible sonoporation, and a balance is expected between therapeutic effectiveness and cell damage. Hu et al. [37] revealed the size of the created cell membrane pore to be a predictor for reversible or irreversible sonoporation: pores $< 30\,\mu m^2$ successfully resealed within 1 min after insonification, while pores $> 100\,\mu m^2$ had not resealed within 30 min. An established method to study drug uptake by sonoporation relies on the intracellular uptake of the model drug propidium iodide (PI) [15, 16, 38, 58, 127], because this molecule can only pass the cell membrane of a live cell when it has been disrupted. After entering the cell it binds to DNA and RNA and becomes fluorescent [35]. Fan et al. [38] showed that intracellular PI fluorescence intensity directly relates to the amount of PI-DNA and PI-RNA complexes that have formed in the cell. They proposed a model to relate intracellular fluorescence intensity to the size of the created pore and its resealing time, which corresponded well with their experimental *in vitro* results on kidney [38] and endothelial cells [63].

For MB-mediated drug uptake, MB dynamics also have to be considered. The frequency generally used for MB-mediated drug delivery is 1 MHz [3], which means that the MBs oscillate one million times per second. These MB oscillations can only be resolved using an ultra-high-speed camera, capable of recording at least two million frames per second (Mfps) to satisfy the Nyquist sampling criterion [128]. While our group used ultra-high-speed recordings to determine that the relative oscillation amplitude of tMBs had to be above 50% to successfully sonoporate a cell [15] (6× 10 cycles at 1 MHz and 80 – 200 kPa peak negative acoustic pressure), others used high-speed cameras (in the order of a few thousand fps) to reveal that MB displacement is an important contributor to sonoporation-mediated cell death (1.25 MHz, 60 – 600 kPa, pulse repetition frequency (PRF) 10 – 1000 Hz, duty cycles 0.016 – 20%) [129]. MBs displace due to acoustic radiation forces, especially when longer acoustic pulses are used [130, 131]. Long acoustic pulses have sparsely been used in MB-mediated drug delivery studies [56, 132–134], even though one of these studies

reported that 7000 cycles resulted in significantly more luciferase activity than 1000 and 5000 cycles in endothelial cells *in vitro* (2.25 MHz, 330 kPa, PRF 20 Hz, 120 s treatment) [134]. On the other hand, no significant differences between 1000, 5000, and 10,000 cycles were observed; different US pulse lengths thus affected luciferase activity. So far, in depth sonoporation studies on the effect of longer acoustic pulses at different acoustic pressures are lacking, as is the relation between MB oscillation and sonoporation efficiency. In addition, the effect of the same type of ntMBs and tMBs on endothelial cells has never been directly compared *in vitro*. All prior studies comparing ntMBs and tMBs were performed on cancer [118, 120–122] and smooth muscle cells [119], despite that MBs are primarily in contact with endothelial cells when injected intravenously [3, 71].

In this study we used long US pulses (500 – 50,000 cycles) at various pressures (150 – 500 kPa) to investigate how these settings affect US mediated endothelial cell membrane permeability and cell death. In order to properly compare ntMBs and tMBs, we used home-made MBs with identical shell compositions to investigate their effect. The real time observed PI uptake patterns were fit to the previously proposed diffusion model of Fan et al. [38] and additional Principal Component Analysis was used to determine whether cells were reversibly or irreversibly damaged. In combination with high-speed optical recordings of MB displacement and ultra-high-speed recordings of MB oscillation, we aimed to identify MB behavior responsible for viable sonoporation or cell death.

3.2. MATERIAL AND METHODS

Microbubble preparation

Lipid-coated MBs with a C_4F_{10} gas core (F2 Chemicals, Preston, UK) were made by sonication as described previously [16, 93]. The coating of the non-targeted MBs (ntMBs) consisted of 1,2-distearoyl-*sn*-glycero-3-phosphocholine (DSPC; 59.4 mol%; P6517; Sigma-Aldrich, Zwijndrecht, the Netherlands), polyoxyethylene-(40)-stearate (PEG-40 stearate; 35.7 mol%; P3440; Sigma-Aldrich), and 1,2-distearoyl-*sn*-glycero-3-phosphoethanolamine-N-carboxy(polyethylene glycol) (DSPE-PEG(2000); MW 2000; 4.9 mol%; 880125P; Avanti Polar Lipids, Alabaster, AL, USA). Before the experiment, the ntMBs were washed three times using centrifugation for 1 min at 400g. After washing the ntMBs, the size distribution and concentration were measured using a Coulter Counter (n = 3; Multisizer 3; Beckman Coulter, Mijdrecht, the Netherlands). The mean (±standard deviation, SD) diameter of the ntMB was 2.54 (±0.02) μm.

The same components were used for the targeted MBs (tMBs), except 0.8% of DSPE-PEG(2000) was replaced with DSPE-PEG(2000)-biotin (MW2000; 880129C; Avanti Polar Lipids). This allows for adding targeting moieties to the MBs via

biotin-streptavidin bridging as previously described [16, 135]. Briefly, after three washing steps by centrifugation at 400g for 1 min, the concentration of the MBs was measured using a Coulter Counter (n = 3) and 1×10^9 biotinylated MBs were incubated with 20 μg of streptavidin (S4762; Sigma-Aldrich) on ice for 30 min. Following incubation, the streptavidin-conjugated MBs were washed once to remove non-bound streptavidin. Next, 5 μg of biotinylated anti-human CD31-antibody (BAM3567; R&D Systems, Abingdon, United Kingdom) were conjugated to the MB shell, during incubation for 30 min on ice. Following this, tMBs were washed once to remove nonbound antibodies. Directly afterwards the size distribution and concentrations were measured using a Coulter Counter (n = 3) and mean (±SD) diameter for the tMBs was 2.82 (±0.09) μm.

Endothelial cell culture

Human umbilical vein endothelial cells (HUVECs; C2519A; Lonza, Verviers, Belgium) were cultured in EGM-2 medium (CC-3162; Lonza) in T-75 flasks (353,136; BD Falcon Fisher Scientific, Breda, the Netherlands), and maintained in a humidified incubator under standard conditions (37 °C, 5% CO_2). Thereafter the cells were trypsinized using trypsin in EDTA (CC-5012; Lonza) and replated on one side of an OptiCell™(Thermo Scientific, NUNC GmbH & Co, Wiesbaden, Germany). Experiments were performed two days later with 100% confluence of HUVECs in the OptiCell.

Experimental set-up

For visualization of the MBs and HUVECs, the microscopic set-up consisted of a fluorescence microscope (Olympus, Zoeterwoude, the Netherlands) equipped with a 5× objective (LMPlanFl 5X, NA 0.13, Olympus) for the sonoporation and cell viability assays or a 40× objective (LUMPlanFl 40XW, NA 0.80, water immersion, Olympus) to capture MB behavior. For bright-field imaging the sample was illuminated from below via an optical fiber using a continuous light source and for fluorescence imaging a mercury lamp and a suitable set of fluorescent filters were used for the detection of propidium iodide (U-MWG2 filter, Olympus), Hoechst 33342 (U-MWU2 filter, Olympus), and calcein (UMWIB2, Olympus). On top of the microscope three different cameras were mounted: 1) a high sensitivity CCD camera (AxioCam MRc, Carl Zeiss, Germany) for fluorescence imaging, 2) a high-speed Redlake Motion Pro Camera (10K, San Diego, CA, USA), and 3) the ultra-high-speed Brandaris 128 camera [6]. The experimental set-up is illustrated in Fig. 3.1.

For the acoustical set-up, a 1 MHz single-element, focused transducer (focal distance 75 mm; V303; Panametrics-NDTTM, Olympus NDT, Waltham, MA, USA) was mounted in the water bath at a 45° angle below the sample (Fig. 3.1). Each OptiCell was divided into eight equally sized, acoustically non-overlapping sections (19 × 33 mm each; for schematic see Fig. 3.1), which covered the beam area (-6 dB beam width of 6.5 mm)

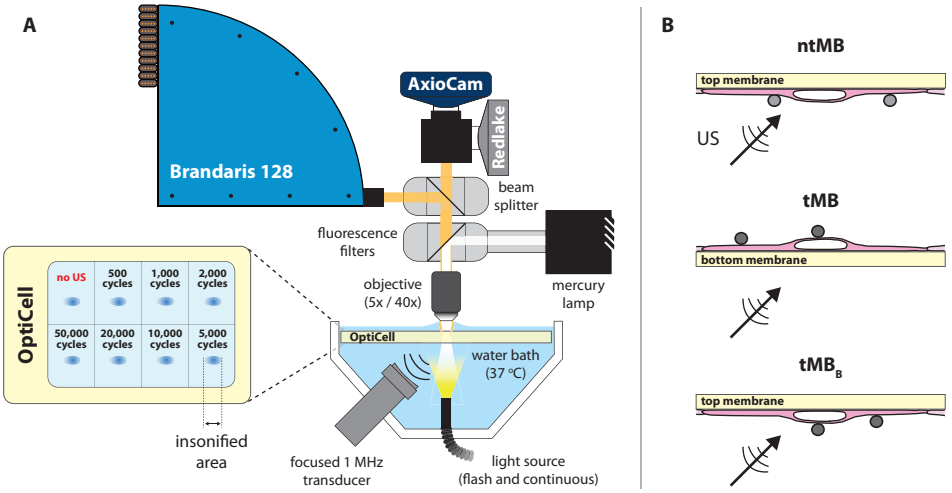

Figure 3.1: Experimental set-up. (**A**) Illustration of the optical imaging systems combined with the acoustical set-up. Brandaris 128 is the ultra-high-speed camera, Redlake the high-speed camera, and AxioCam the fluorescence and bright-field CCD camera. The enlarged OptiCell shows the insonification scheme. (**B**) Orientation of the microbubbles (MBs) with respect to the cells and the direction of ultrasound (US) insonification. Non-targeted MBs (ntMBs) were floating against the cells, targeted MBs (tMBs) were adhered on top of the cells, or tMBs adhered below the cells (tMBB), similar to the ntMB orientation.

at the focus of the transducer, as verified in advance with a calibrated 0.2 mm PVDF needle hydrophone (Precision Acoustics Ltd., Dorchester, UK). The acoustic focus was aligned with the optic focus.

During the experiment, the position of the OptiCell was adjusted to place the center of each subsection in the focal zone. The sample was insonified by a single Gaussian tapered sine wave burst generated by an arbitrary waveform generator (33220A, Agilent, Palo Alto, CA, USA) and amplified using a broadband amplifier (ENI A-500, Electronics & Innovation, Rochester, NY, USA). The peak negative acoustic pressure of the US burst (150, 300, or 500 kPa) was kept constant for the entire OptiCell, whereas the number of cycles in the single US burst (500; 1000; 2000; 5000; 10,000; 20,000; and 50,000) varied per OptiCell subsection (Fig. 3.1). For each OptiCell one of the subsections was used as a control where no US was applied.

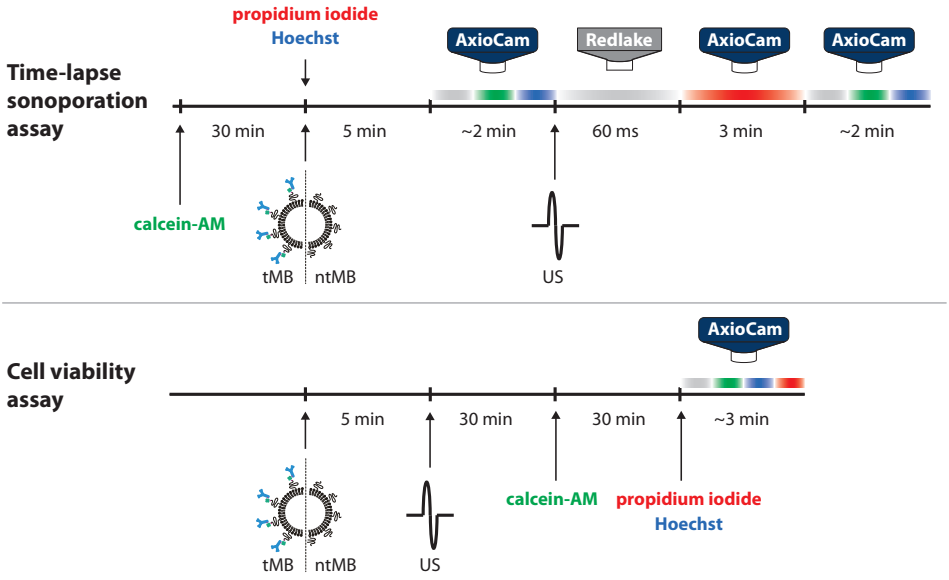

Figure 3.2: Procedural time line (not to scale) for the time-lapse sonoporation and cell viability assays. Arrows indicate when fluorescence dyes or MBs were added, or when US was applied. The cameras show which imaging systemwas used and the colored bars indicate the type of imaging: bright-field (grey), calcein (green), Hoechst (blue), or propidium iodide (red).

Time-lapse sonoporation assay

The time-lapse sonoporation assay was used to monitor sonoporation over time for the different US pressures and number of cycles and is illustrated in Fig. 3.2. First, calcein-AM (C3100MP; Invitrogen; prepared in DMSO (Sigma-Aldrich)) was added to the HUVECs in the OptiCell in a final concentration of 0.25 µg/mL. We used calcein-AM as a live-cell stain as it passively crosses cellular membranes, has high cell retention, and is only converted to fluorescent calcein in living cells [136]. After 30 min of incubation (37 °C, 5% CO_2) of the HUVECs with calcein-AM, we added propidium iodide (PI; final concentration 25 µg/mL; P-4864; Sigma-Aldrich) and Hoechst 33342 (final concentration 5 µg/mL; H3570; Invitrogen, Breda, the Netherlands) to the OptiCell. PI, which is live-cell impermeable, was used to determine the presence and intensity of sonoporation, or disruption of cell membranes, since it only becomes fluorescent when bound to DNA and RNA inside cells [35]. The Hoechst 33342 fluorescent dye was used to stain the nuclei of living and dead HUVECs, as it rapidly diffuses into all cells, binds specifically and quantitatively to DNA, and has low toxicity to viable cells [137]. Since Hoechst is a nonintercalating dye which binds to the minor groove of DNA [138] and PI binds to DNA and RNA by intercalating between the bases [139], no competition between both dyes is expected.

At the same time as PI and Hoechst, $\backsim 10^7$ MBs were added to the OptiCell to obtain a ratio of 1 – 2 MBs per cell. After mixing,we incubated the OptiCell for 5 min at 37 °C,with the cells on the top membrane. This allowed for the MBs to float up and the tMBs to adhere to the cells. The OptiCell was then placed in a 37 °C water bath (Fig. 3.1). For the experiments using tMBs, the OptiCell was placed with the cells on the bottom membrane, so any non-adhered MBs would float away from the cell surface, whereas the OptiCell for the ntMB experiments was placed with the cells on the top membrane to ensure that the ntMBs were floating against the cell membranes. To investigate whether the difference in orientation of tMBs influenced sonoporation outcome, we also performed experiments on tMBs located below the cells (tMB_B, see Supplementary material). The AxioCam was used to take snapshots in brightfield (indicated by the grey bar in Fig. 3.2), and of the fluorescent signals of calcein (green) and Hoechst (blue). Just before US exposure, the Redlake camera was started and ran for 60 ms to completely cover the full US exposure. Consequently, this camera recorded more frames after insonification for the shorter pulses than for the longest pulse. The Redlake camera recorded the MB displacement and clustering at 2000 frames per second (fps). After these 60 ms, the AxioCam recorded the fluorescence intensity change over time for 3 min (1.5 s exposure and 5 s time intervals) caused by cellular PI uptake after US application. At the end of the protocol, snapshots in bright-field and of calcein and Hoechst signal were taken for comparison with the initial situation. This procedure was repeated for each subsection and the experiment was performed in triplicate.

Cell viability assay

For each US setting, cell viability was determined as shown in Fig. 3.2. The same amount of MBs as described in the previous section ($\backsim 10^7$) were added to the OptiCell and left in the incubator (37 °C) for 5 min. Within 3 to 4 min after the US treatment of all eight subsections of the OptiCell, HUVECs were incubated at 37 °C, 5% CO_2. Thirty minutes after the US treatment, calcein-AM was added to the OptiCell and incubated for another 30 min under the same conditions. After the final incubation, PI and Hoechst were added to the OptiCell. This procedure was followed directly with bright-field and fluorescent (calcein, Hoechst, and PI) microscopic examination using the AxioCam (Fig. 3.2). For each condition, five different fields of view were acquired within a 6 mm circle around the center of the insonified area. All experiments were done in triplicate.

Oscillatory behavior of microbubbles

To relate MB behavior to sonoporation, high imaging speeds in the range of a few million frames per second (Mfps) are required. Since these high speeds cannot be achieved using the Redlake camera, we used the Brandaris 128 ultra-high-speed camera [6] in segmented mode [94]. The protocol was similar to the time-lapse sonoporation assay, but the Redlake camera was replaced by the Brandaris 128 camera. The segmented mode of the Brandaris 128 allows for optical recording of long US pulses by dividing the CCD sensor arc into four segments. During each exposure all four segments were illuminated, however only one segment was triggered to transfer the data to the buffer channel. These triggered transfers from the consecutive segments were equally spaced over the time span of the applied US pulse. The start of the acquisition was triggered at a frame rate of 3.85 Mfps, resulting in a corresponding intersegment time of ~ 328 µs. During one US pulse a full recording then captured four equally spaced movies of ~8 µs in bright-field using a Xenon flash source (MVS-7010, Perkin-Elmer Optoelectronics, Wiesbaden, Germany). These settings resulted in a total acquisition time of 1017 µs. The recording time of the ultra-high-speed movies was a few µs longer than the US pulse to ensure that the start and end of the MB oscillations were fully captured. MB behavior was recorded for both tMBs and ntMBs, at 1000 cycles for pressures of 150 and 300 kPa. The number of cycles was limited to 1000 cycles (i.e. 1 ms duration), because the Xenon flash duration could not be extended.

Analysis of fluorescence images

All images acquired with the AxioCam (bright-field and fluorescence) were analyzed using a custom-built plugin for ImageJ [140]. To segment the nuclei, first a composite image of the Hoechst image after insonification and the final PI image was produced, to ensure clear visibility of all nuclei. We chose to use the Hoechst image after insonification, since less cell displacement was expected between this image and the first PI image. The composite image was thresholded using the method of Otsu [141], resulting in a binary image with white nuclei on a black background. A mask of this image was created and watershedding was applied to separate overlapping nuclei. The watershedding algorithm calculates the centers of the nuclei and dilates them until touching another dilated boundary or a white pixel. At the meeting point, a watershed line is drawn. Using the Analyze Particles function, the nuclei and the area of the nuclei were located and stored in the ROI manager. The center of the nuclei was found using the Find Maxima function, added to the ROI manager, and copied to a blank image. Next, the cell borders were automatically segmented using Voronoi tessellation [142] which is a built-in option in the Find Maxima function. Voronoi tessellation is based on the theory that every point p has a distance to another point q that is less than or equal to its distance to any other point r. The lines in a Voronoi diagram are thus equidistant to two points in space (i.e., the cell nuclei) and correspond to the most likely position of

the cell boundaries. The resulting Voronoi segmentation was transformed into a mask and stored in the ROI manager. The ROI manager now contained the center of each nucleus, the area of each nucleus, and the cell borders.

For assessing cell death using the cell viability assay, the number of cells that showed PI uptake on the images without the application of US was analyzed as described above. Next, the number of cells that had taken up PI after receiving US was normalized to the number of cells that had taken up PI in the control sections, to correct for cells that were already dead when the experiment started.

For assessing the dynamic uptake of PI after sonoporation the segmented nuclei and cell borders were overlaid on every frame of the PI fluorescence time-lapse recording after the application of US. The mean signal intensity of PI for each nucleus and each cell was obtained frame by frame. The nuclear PI uptake was used for further analysis because the segmentation of the nuclei was based on intensity thresholding of Hoechst stained nuclei, which is more accurate than the segmentation of cell borders that is based on the highest probability of a cell border being present.

PI model fit and data classification

The temporal PI intensity values in the nuclei were loaded into RStudio (RStudio, Inc., Boston, MA, USA) for further quantification of sonoporation. Fan et al. [38] derived an equation (Eq. 3.1) to model sonoporation dynamics of a single cell, based on the resealing of the created pore and the diffusion rate of PI into the cell.

$$F(t) = \alpha \cdot \pi \mathrm{DC}_0 \cdot \mathrm{r}_0 \cdot \frac{1}{\beta}\left(1 - \mathrm{e}^{-\beta t}\right) \tag{3.1}$$

In Eq. 3.1, $F(t)$ is the fluorescence intensity as a function of time, α is a coefficient that relates the amount of PI molecules to the fluorescence intensity of PI-DNA and PI-RNA. This coefficient is determined by the sensitivity of the fluorescence imaging system. The other parameters are the diffusion coefficient of PI, D, the extracellular PI concentration, C_0, the initial radius of the pore, r_0, the pore resealing coefficient, β, and time, t. The pore size coefficient, $\alpha \cdot \pi \mathrm{DC}_0 \cdot \mathrm{r}_0$, determines the initial slope of the PI uptake pattern and is the scaling factor for the exponential increase. Therefore, a steep initial slope corresponds to a larger pore size. The overall slope follows $F(t) = (\alpha \cdot \pi \mathrm{DC}_0 \cdot \mathrm{r}_0) \cdot \mathrm{e}^{-\beta t}$, in which the pore resealing coefficient β is the time constant that determines the time to reach the asymptotic value of the maximum PI intensity. This asymptotic maximal PI intensity value is given by the inverse relationship between the pore size and pore resealing coefficients (Eq. 3.2):

$$F(\infty) = \frac{\alpha \cdot \pi \mathrm{DC}_0 \cdot \mathrm{r}_0}{\beta} \tag{3.2}$$

Therefore a cell with a high pore resealing coefficient quickly reaches the asymptotic value, resulting from quick resealing of the pore.

To obtain the pore size coefficient, $\alpha \cdot \pi DC_0 \cdot r_0$, and the pore resealing coefficient, β, the PI intensities recorded in the time-lapse sonoporation assay were fit to Eq. 3.1 using a nonlinear least-squares approach. Classification, based on the distributions of both coefficients, was performed using Principal Component Analysis (PCA) [143, 144] on the complete data set (all settings, both ntMB and tMB). We chose PCA because this method captures as much of the variation in the data as possible by computing eigenvectors (for determining the direction in which the data has largest variance) and corresponding eigenvalues (to determine how much variance there is in the data in that direction). The principal components (PCs) are uncorrelated with each other since the eigenvectors are perpendicular to each other. In this data set we chose two PCs because we only used the pore size coefficients and pore resealing coefficients to fit the data to Eq. 3.1. Classification thresholding was applied on the PC with the largest variance, separating the complete data set in two groups. Using these PCs, the cell populations at each different setting were classified. Based on Eq. 3.1, two additional thresholds were chosen to classify the cells that were most likely irreversibly damaged based on very low pore resealing coefficients. In these cells, PI intensities still increased at the end of the time-lapse sonoporation assay (i.e. at 180 s), or for > 120 s. Because pores remaining open for more than 1 min would not close [37], we assumed these pores to most likely result in cell death.

Displacement of microbubbles

Tracking of displacing MBs was implemented in Python™ (v2.7, Python Software Foundation). The recordings on which the tracking was performed were obtained with the Redlake camera and had an isotropic spatial resolution of 0.63 μm/pixel. Gaussian Mixture-based background subtraction [145] was applied to remove all but the displacing MBs from each frame. This was required to correct for illumination fluctuations among the frames and in different regions of the image,which hindered accurate MB tracking. The remaining MBs were tracked using Trackpy [146], an open source blob tracking algorithm, to obtain the trajectory of each displacing MB.

To differentiate between sonoporation due to displacing or non-displacing MBs, the latter were segmented from the AxioCam brightfield images before US application. Since the FOV of the Redlake camera was smaller than that of the AxioCam, only the part of the FOV that overlapped was analyzed. We used the Laplacian of Gaussian (LoG) blob detection algorithm (scikit-image [147]); this algorithm convolves Gaussian kernels of a range of standard deviations with an image. In this way it determines the centroid and diameter of non-displacing MBs, approximated by the standard deviation of the corresponding Gaussian kernel. In order to detect most MBs, their diameters were limited to a range between 1.7 and 5.0 μm, and a 20% overlap was allowed to properly deal with clusters and focal differences.

After locating the displacing and non-displacing MBs, their effect on cellular PI uptake was assessed. For segmentation of the nuclei from the Hoechst images, we also used the LoG blob detection algorithm, which performed best when the range to detect nuclei was limited between 5.0 and 6.7 μm in diameter, and overlapping at most 20%, to separate nuclei with seemingly overlapping borders. Centroids of the segmented cell nuclei were used as seeding points for cell border segmentation using Voronoi tessellation. For segmenting regions with PI uptake in the initial and final frame of the PI stained image sequences, the LoG blob detection algorithm was limited to diameters between 5.0 and 8.3 μm, and allowed 25% overlap. More overlap and larger regions were allowed than for nuclei segmentation since PI can also stain the cytoplasm by binding to RNA. Regions in which PI uptake was detected in both the first and last frame were neglected, because these cells had already taken up PI before US application. Cells were defined as sonoporated when 70% of their equivalent circular diameter overlapped with a region showing PI uptake. This percentage was used to compensate for the overestimation of cellular diameters due to odd shaped cells, e.g. rectangular shaped cells. If a cell's equivalent diameter intersected with 1.25 times a MB diameter (to account for MB expansion) it was considered to be in contact with a non-displacing MB. Similarly, contact with displacing MBs occurred when the cell's full equivalent diameter intersected with a MB's trajectory (the lines connecting a MB between frames, as determined by Trackpy).

The relations between MB displacement and sonoporation outcome at all acoustic settings were visualized using scatter plots and linear fits through these data using a least-squares approach in MATLAB (The MathWorks, Natick, MA, USA).

Statistics

To compare the various acoustical settings, we performed statistical testing using Student's t-tests to identify significantly different outcomes. All statistics were performed using Student's t-tests for independent samples, where a p-value of 0.05 was regarded as significant.

For both sonoporation and cell death, different insonifying pressures were compared at the same number of cycles for both ntMBs and tMBs. One-sided t-tests were used to reveal whether higher pressures at the same number of cycles resulted in more sonoporation and cell death. The same t-tests were performed to verify whether the experimental acoustic settings resulted in more sonoporation than in the control experiments. For comparing sonoporation with cell death, we used 2-sided t-tests to verify whether the percentage of sonoporated cells was different from the percentage of cell death. The effect of ntMBs, tMBs, and tMB_B on the amount of sonoporated cells and on cell death was tested using 2-sided t-tests.

The cells that were classified as non-resealing within 120 s were compared to the cells that were determined as dead by the cell viability assay. We used 2-sided t-tests to verify whether the assumption that both populations were equal was true.

3.3. RESULTS

Sonoporation and cell death

The influence of various acoustic settings on cellular responses, for both ntMBs and tMBs, was evaluated by the amount of sonoporated cells and cell death, as illustrated in Fig. 3.3. The sonoporation and cell death data are presented as the mean of three experiments at the same settings, with a mean (±SD) of 1727 (±338) cells in the FOV for ntMBs and 3104 (±130) cells for tMBs. The amount of injected microbubbles was adjusted accordingly, resulting in 1.9 (±0.8) ntMBs per cell and 1.6 (±0.3) tMBs per cell. No controls are shown for the cell death data, since these were already subtracted at all settings to correct for natural, non-US related, cell death (6.7 ± 1.1%).

The data show that applying higher acoustic pressures and more cycles increased both the number of sonoporated cells (Fig. 3.3A, C) and the number of dead cells (Fig. 3.3B, D). This trend was seen for both ntMBs (Fig. 3.3A, B) and tMBs (Fig. 3.3C, D). However, when statistically comparing the same number of cycles at increasing pressures, the increase in sonoporation at higher acoustic pressure was only significant ($p < 0.05$) for ntMBs with at least 2000 cycles. For tMBs sonoporation at 500 kPa was always higher than at 300 kPa, whereas at 300 kPa at least 10,000 cycles had to be applied to sonoporate more cells than at 150 kPa. Cell death for the same number of cycles at increasing pressures was significantly higher when using ntMBs, in all cases. For tMBs, cell death at 500 kPa was always significantly higher than at 300 kPa. Conversely, when comparing 300 kPa and 150 kPa, cell death was not significantly different between 1000 and 5000 cycles.

The amount of sonoporated cells, in the presence of ntMBs at 150 kPa only resulted in significantly more sonoporation than in control experiments (0.4% sonoporation) when applying 10,000 or 50,000 - cycles (2.0% or 4.7%, respectively). At 300 kPa at least 2000 cycles were required to significantly yield more PI uptake than in the control experiments, whereas at 500 kPa pressure, 1000 cycles were already sufficient. For tMBs, 150 kPa did not result in significantly more sonoporation than in the experiments without US. However, application of 300 or 500 kPa sonoporated significantly more cells than in the control experiments for all cycles considered.

The amount of sonoporated cells was expected to be higher than the amount of dead cells, because cells that are sonoporated can also remain viable. However, for most of the settings we applied, cell death was similar to the amount of sonoporated cells. The settings for which the difference between cell death and sonoporation was significant

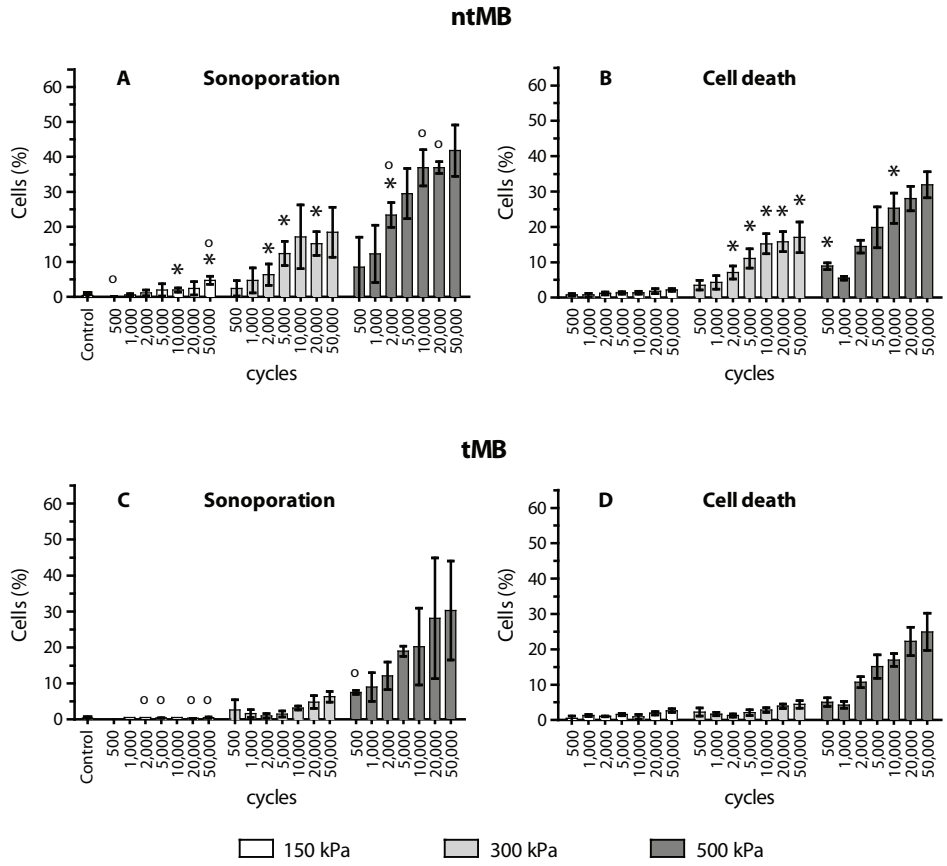

Figure 3.3: Targeted and non-targeted microbubble-mediated sonoporation and cell death after ultrasound exposure at different acoustic pressures (150, 300, and 500 kPa) and number of cycles (500 - 50,000). (**A**) Mean (± SD) percentage of sonoporated cells and (**B**) cell death after insonification of ntMBs. (**C**) Mean (± SD) percentage of sonoporated cells and (**D**) cell death after insonification of tMBs. Results were based on n = 3 repetitions of each experiment. Significant differences ($p < 0.05$) between sonoporation and cell death after US insonification in the presence of ntMB or tMB are indicated by (*). Significantly more sonoporation than cell death is indicated by (o).

are indicated by (o) in Fig. 3.3A and C. Since cell death was assessed from the viability assays —which were performed separately from the sonoporation assays— cell death could even be higher than the amount of sonoporated cells. This was the case for the 150 kPa experiments in the presence of tMBs.

To validate whether ntMBs or tMBs were more efficient in inducing sonoporation and cell death, we statistically compared them for significance. The asterisks (*) in Fig. 3.3 indicate significant differences between ntMBs and tMBs for sonoporation (A) and cell death (B). Although Fig. 3.3A and C may suggest that ntMB more efficiently

sonoporated cells than tMB at 500 kPa using long US pulses, this difference was not significant, probably due to the high standard deviations in the tMB sonoporation experiments. Cell death due to ntMBs was significantly higher for almost all number of cycles at a pressure of 300 kPa, and comparable for all settings at 150 kPa and for most settings at 500 kPa.

Sonoporation-induced PI uptake over time

Before US exposure, bright-field imaging was used to discern MB locations (Fig. 3.4A); the black dots in this figure are the MBs, examples indicated by white arrows. The grey background of the image shows spherical structures; these are the nuclei of the endothelial cells in the monolayer. Fluorescence microscopy established individual cell nuclei locations by Hoechst staining (Fig. 3.4B), cell membrane integrity by the absence of PI fluorescence (Fig. 3.4C), and live cells by the presence of calcein (Fig. 3.4D). After US insonification, less MBs were present because they had dissolved, coalesced, or displaced (Fig. 3.4E). Intracellular PI uptake was observed by increase of fluorescence signal, thus indicating sonoporation (Fig. 3.4G).

Interestingly, when increasing PI signal was observed, Hoechst signal decreased (Fig. 3.4F). Because the segmentation was done on the image after US application, the segmented cell nuclei did not always exactly match the nuclei in the Hoechst image before US (compare panel B and F). In between the recording of these images, there can be small displacements of cells due to the radiation force of the applied US, movement of the MBs, or retraction of cells because of cell-cell contact opening. In cells that had taken up PI, calcein signal was found to decrease (Fig. 3.4H), which has previously been described as an additional measure for sonoporation [38].

The PI time-lapse images (example shown in Fig. 3.4G) were analyzed for all acoustic settings, resulting in time-intensity curves showing the dynamic PI uptake from just after US application, up to 180 s later. The time-intensity curves were fit to the Fan model (Eq. 3.1) and revealed a variety of uptake dynamics. Because PI signal intensity could fluctuate between frames, we chose a robust method that only considered cells as actually sonoporated when the time-intensity curve could be fit to the model with an $R^2 > 0.8$. For $R^2 < 0.8$ the fit was regarded as less reliable, because already dead cells at the start of the experiment without clear increase in PI uptake would also be marked as sonoporated. In Fig. 3.5, four different types of uptake curves are shown corresponding to the numbered cells in Fig. 3.4A. The curves obtained for ntMBs insonified at 500 kPa for 10,000 cycles illustrate the general differences in PI uptake rates found at all other acoustic settings. The red and blue curve reach 90% of the maximum intensity value predicted by the model within 50 s, whereas the green curve reached this 90% value after > 90 s, and the black one did not reach this 90% value within 180 s.

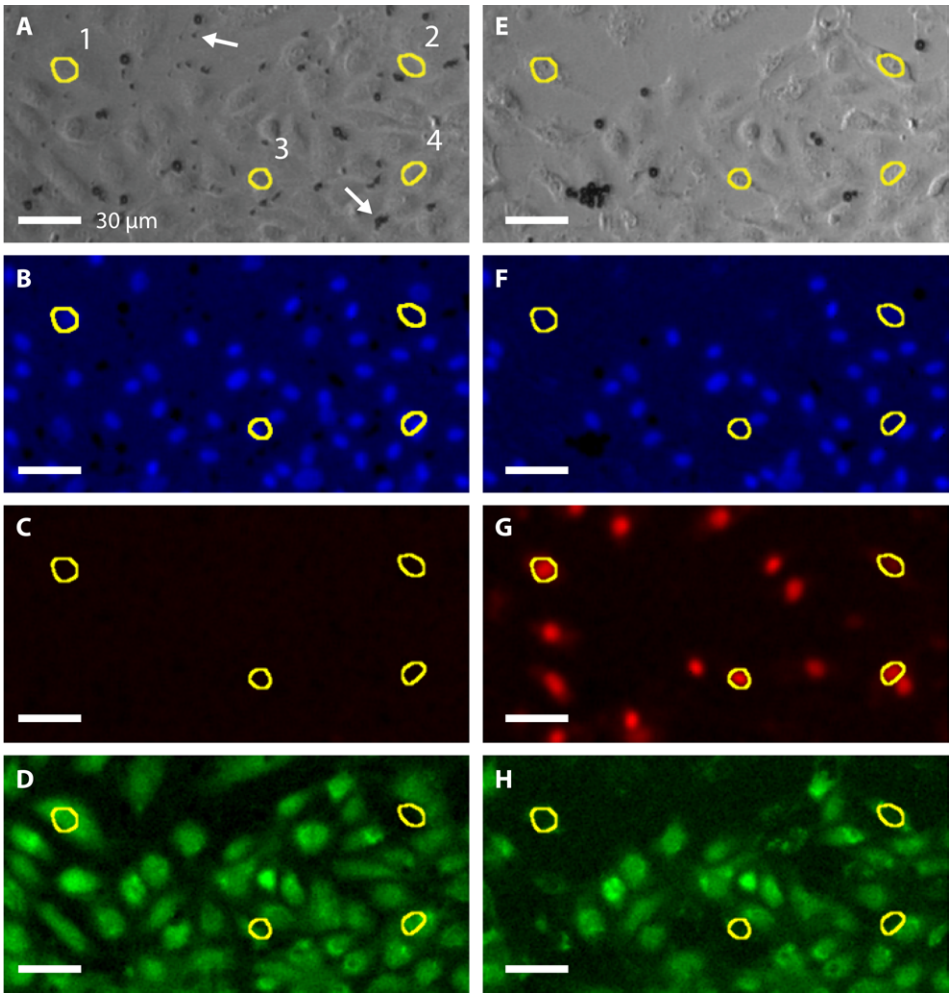

Figure 3.4: Optical recordings of microbubbles and the HUVEC monolayer. (**A**) Bright-field image of ntMB locations (black dots) before US exposure; an example of a single ntMB and a ntMB cluster are indicated by a white arrow. Yellow circles indicate highlighted sonoporated cells. (**B**) Hoechst fluorescence imaging of HUVEC nuclei before US application. (**C**) Fluorescence image of PI uptake before insonification; no uptake was present in the field of view. (**D**) Calcein stained image of live cells before US application. (**E**) Bright-field image after US treatment; ntMBs dissolved, displaced, and clustered. (**F**) Hoechst stained nuclei after US application; signal in sonoporated cells was lower than before US application. (**G**) Fluorescence image of PI signal after US application; red stained nuclei indicate sonoporated cells. (**H**) Calcein stained image after US application; calcein leaked out of some sonoporated cells.

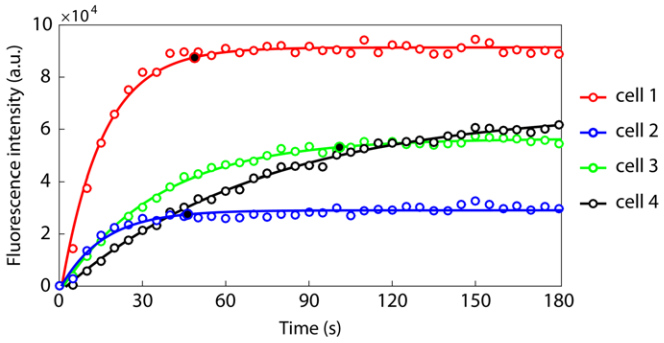

Figure 3.5: PI fluorescence intensity as a function of time up to 180 s after US treatment (colored circles) and fit to the Fan model (Eq. 3.1, solid lines); black circles indicate 90% of theoretical maximum PI intensity that could be reached with the fit parameters. Cells 1 to 4 are marked with yellow circles in panels A-H in Fig. 3.4, and the numbers correspond to those in panel A. US settings: 500 kPa acoustic pressure, 10,000 cycles. Scale bar 30 µm.

PI uptake as a function of pore size and pore resealing coefficients

The pore size and pore resealing coefficients of the cells that resulted in a reliable fit to Eq. 3.1 ($R^2 > 0.8$) were used to classify those cells into groups using PCA. This approach divided the total population of cells into two groups: one with relatively high pore resealing coefficients and relatively low pore size coefficients (Fig. 3.6, blue), and one with relatively low pore resealing coefficient and relatively large pore size coefficients (Fig. 3.6, red). The cells in the blue population had low PI uptake suggesting small pores that sealed quickly, whereas the cells classified as red had high PI uptake suggestive of large pores that sealed slower, but within 120 s. By applying the additional thresholds (based on Eq. 3.1, as described in the Materials and methods section), the cells that were likely to be irreversibly damaged were identified and classified into two separate populations: cells with pores that did reseal, but only after 120 s (Fig. 3.6, green), and cell with pores that did not reseal within 180 s (Fig. 3.6, black).

Influence of acoustic settings on sonoporation-induced uptake and cell death

The impact of the acoustic pressure and the number of cycles in a single burst sine wave on sonoporation-induced PI uptake is illustrated in Fig. 3.7. These graphs show the populations of the time-lapse sonoporation assays classified as high PI uptake cells (red), low PI uptake cells (blue), cells with pores that had not resealed within 120 s (grey, this is the sum of the cells previously classified as green or black), and cell death (yellow) determined from the cell viability assays for each corresponding treatment. The cells with pores that did not reseal within 120 s were expected to be dead, and statistical comparison with cell death indeed confirmed that these two populations

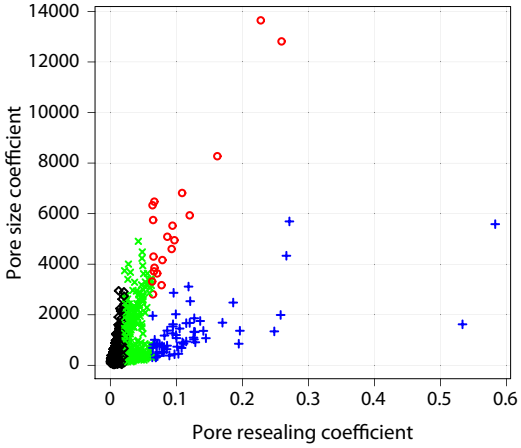

Figure 3.6: Classification of cell populations based on pore size and pore resealing coefficients. This graph originates from the same data set as Fig. 3.4 and shows cells with high PI uptake (red), low PI uptake (blue), cells with pores that resealed within 120 - 180 s (green), and cells with pores that did not reseal within 180 s (black). US settings: 500 kPa acoustic pressure, 10,000 cycles.

were not significantly different except for a few settings, mainly those with very low amounts of sonoporated cells (indicated by (*) in Fig. 3.7). The proportion of cells with low and high PI uptake (blue and red, respectively) significantly increased with increasing pressure, but did not significantly increase when only more cycles were applied. These cells were determined to be reversibly sonoporated and viable. On the other hand, the amount of cells with slow resealing pores (>120 s, grey) and cell death (yellow), continued to increase with increasing pressure and cycles. Only increasing the number of cycles resulted in more cell death, but not necessarily in more cells that were viably sonoporated.

Oscillatory behavior of microbubbles

The ultra-high-speed movies recorded by the Brandaris 128 camera were qualitatively analyzed per segment. For each segment the number of single MBs and the number of MB clusters were counted and classified into four categories: 1) non-oscillating (white), 2) oscillating (dark grey), 3) oscillating with coalescence of MBs (black), and 4) oscillating with separation of MBs (light grey), as illustrated in Fig. 3.8. The time line shows the US signal (for visualization purposes, only 20 cycles are shown in the schematic instead of the 1000 cycles that were actually applied) and the segments of the US pulse at which the ultra-high-speed movies were recorded. The FOV of Brandaris is smaller than that of the AxioCam or Redlake camera, therefore we could only study oscillatory behavior of a subset of MBs.

When ntMBs were insonified at 150 kPa and 1000 cycles, more single MBs were counted than MB clusters. In the first segment about 60% of single MBs oscillated, whereas >90% of MB clusters were oscillating. Towards the end of the US burst, only 25% of single MBs and 60% of MB clusters were still oscillating. From segment a to segment b most coalescence occurred (black). At a pressure of 300 kPa, more ntMBs

oscillated: 75% of single MBs and all MB clusters (Supplemental Video 1 can be found online [40]). The higher pressure ensured that MBs below resonance, i.e. smaller MBs, also started oscillating. In segment a and b, most clusters coalesced into larger clusters that kept oscillating until the end of the US pulse. This higher degree of clustering was probably caused by more displacement of MBs, due to higher acoustic radiation forces. At the end of the pulse, in segment d, the large clusters split into smaller clusters or single MBs.

At 150 kPa less tMBs coalesced than ntMBs. This was hypothesized to be due to less displacement of tMBs, as tMBs were attached and higher forces are needed to dislocate them [114]. Fewer clusters were present for tMBs, but more of them were oscillating (~75% in all segments). At a higher pressure of 300 kPa, the overall trend of oscillating single tMBs and clusters was not very different than that at 150 kPa. This has already been shown in Fig. 3.3 and 3.7 in terms of sonoporation efficiency. However, at 300 kPa more clusters were present and more coalescence occurred (Supplemental Video 2 can be found online [40]).

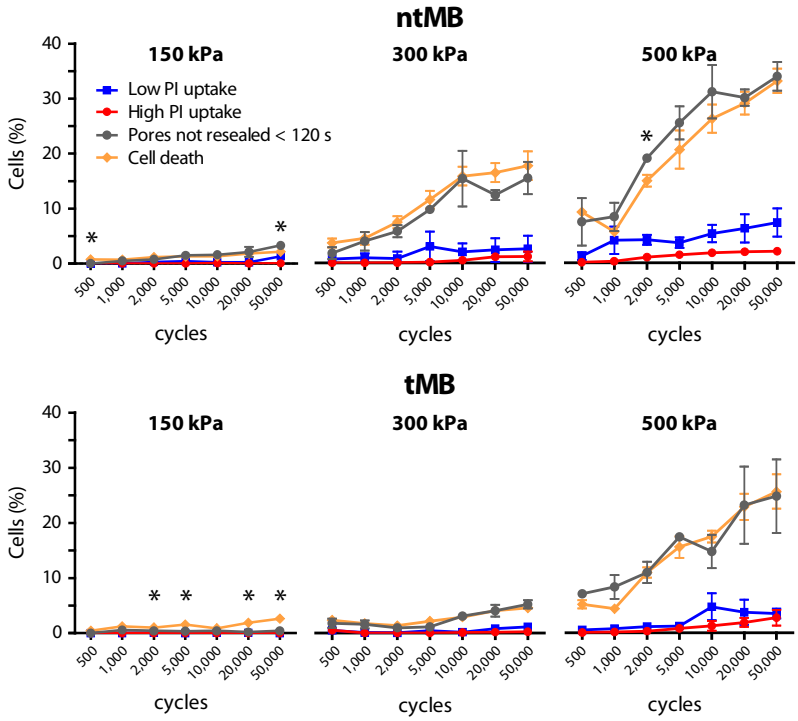

Figure 3.7: Percentage of cell death and cells classified per category by PCA and additional thresholding under various experimental acoustic pressures and cycles. The amount of cells with pores that did not reseal within 120 s (grey line) correlated well with cell death (yellow line) and was only significantly different ($p < 0.05$) at the acoustic settings marked by (*).

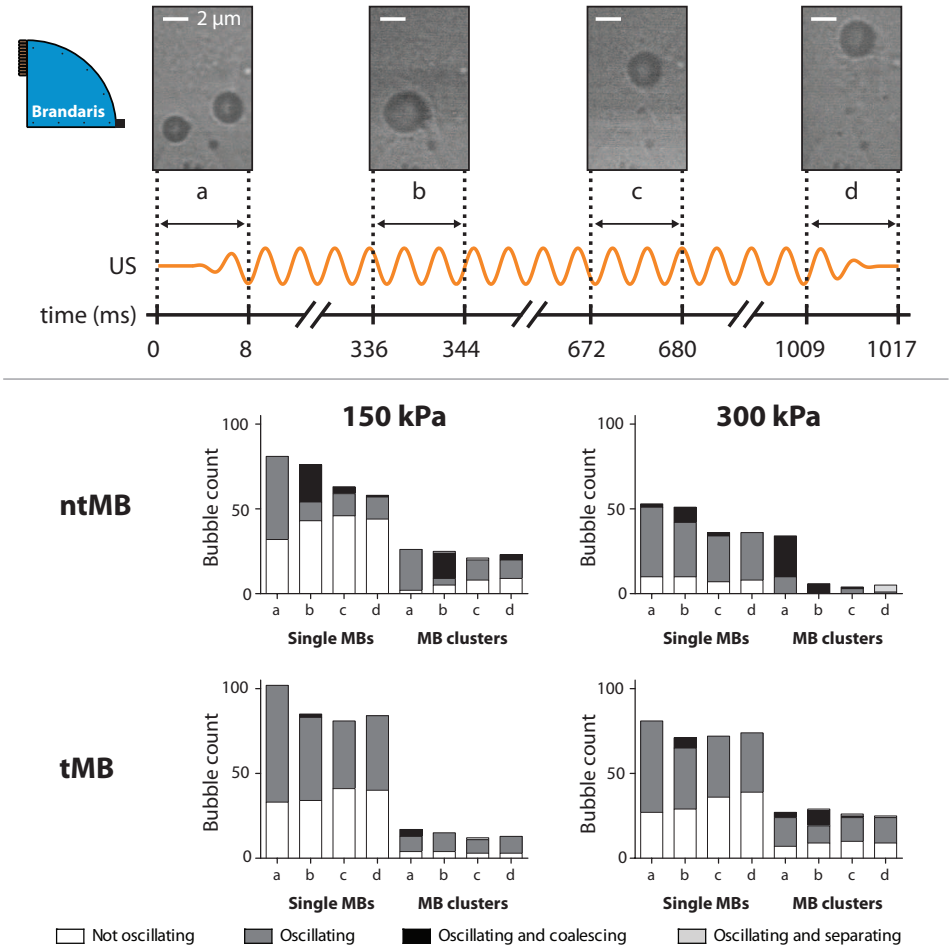

Figure 3.8: Ultra-high-speed imaging of microbubble oscillation behavior. Top: illustration of the segments at which microbubble oscillation was captured and still frames of a recording of tMBs insonified at 300 kPa and 1000 cycles. Bottom: ntMB and tMB oscillation behavior categorized into single MBs and clusters at 150 and 300 kPa insonifying pressure.

Displacement of microbubbles

As described in the previous section, more coalescence and clustering were observed for ntMBs, which was hypothesized to be caused by more displacing ntMBs. For each sonoporated cell, in a subset of the original image (ntMB: ~1100 cells, tMB: ~1700 cells), we determined it to be either in contact with: 1) both non-displacing and displacing MBs (dark grey), 2) a MB that displaced (black), 3) a MB that had not displaced (light grey), or 4) when no MB could be detected nearby the cell (white), as shown by the stacked bars in Fig. 3.9 as percentages of the total amount of sonoporated

cells. The red solid line illustrates the amount of sonoporated cells as a percentage of the total amount of cells in the FOV. This amount was, on average, 2.7% higher than the amount of sonoporated cells shown in Fig. 3.3 and 3.7. This was expected, since the data for those figures only accounted for the cells that fitted properly to the model. Both methods showed the same trends, thus the determination of PI uptake was performed on a representative subset of the full-size AxioCam images.

Overall, most sonoporation was induced by non-displacing MBs (light grey, Fig. 3.9), whereas for ntMBs at 500 kPa and 50,000 cycles both displacing and non-displacing MBs accounted for similar amounts of sonoporation. The use of ntMBs resulted in the highest amount of displacing MBs, which supports the previously stated hypothesis that the higher degree of clustering was due to more displacing MBs. Overall, when comparing the contribution of displacing MBs (dark grey and black in Fig. 3.9) to the amount of sonoporated cells (red line in Fig. 3.9), they followed the same trend.

To relate MB displacement to sonoporation outcome, we compared the two cell classifications: 1) reversibly sonoporated cells that had resealing pores < 120 s (Fig. 3.7, blue and red lines) and 2) irreversibly sonoporated cells (Fig. 3.7, grey line) with a) cells

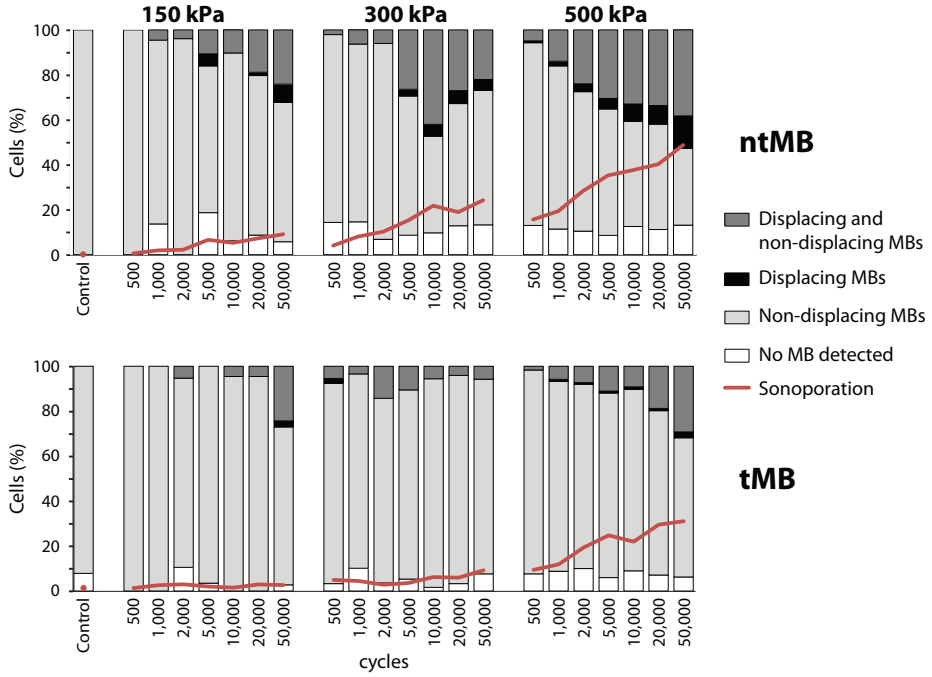

Figure 3.9: Displacement of ntMBs and tMBs under varying experimental acoustic pressures and cycles. For each acoustic setting, the stacked bar graph indicates the percentage of sonoporation caused by displacing MBs, non-displacing MBs, both, or when no MB could be detected. The red line shows the percentage of cells that were sonoporated.

that were sonoporated by displacing MBs (Fig. 3.9, dark grey and black) and b) those that were sonoporated by non-displacing MBs (Fig. 3.9, dark grey and light grey), as shown in Fig. 3.10. The slope of the linear fit shows the ratio of increase between two groups; a ratio of 1 implies that the values are identical and increase proportionally (data follows the line $y = x$).

A proportional increase was found for the amount of irreversibly sonoporated cells and the amount of cells that were sonoporated by non-displacing MBs (slope 1.0 for ntMB in Fig. 3.10A; slope 1.1 for tMB in Fig. 3.10B, both $R^2 = 0.99$). In addition, the amount of sonoporation for cells in contact with non-displacing MBs (Fig. 3.10C and d) increased four times faster than the amount of reversibly sonoporated cells (slope of 3.7 and 4.1, respectively). This strongly suggests that cells in contact with non-displacing MBs were irreversibly damaged.

On the other hand, the amount of sonoporation for cells in contact with displacing ntMBs increased twice as fast as the amount of reversibly sonoporated cells (Fig. 3.10G, slope of 2.1), while still contributing to irreversible sonoporation (Fig. 3.10E, slope of 0.57). This suggests that displacing ntMBs can both induce reversible and irreversible sonoporation. For cells in contact with displacing tMBs the amount of reversibly sonoporated cells increased proportionally (Fig. 3.10H, slope of 1.0). Further, displacing tMBs minimally contributed to irreversible sonoporation (Fig. 3.10F, slope of 0.27). This suggests that displacing tMBs mainly resulted in reversible sonoporation.

The relation between the presence of displacing and non-displacing MBs and the classification of cells was confirmed on a single cell basis, as shown in Fig. 3.11 and Fig. 3.5. Cells 1 and 2 were both reversibly sonoporated due to MBs displacing over their cell membranes, of which cell 1 had high PI uptake and cell 2 low uptake. Cell 1 also had non-displacing MBs in its vicinity, which might be the reason for the higher uptake of PI. Cells 3 and 4 had slow resealing pores (> 120 s) and only non-displacing MBs nearby their cell membranes.

3.4. DISCUSSION

This is the first study that directly compares ntMB and tMB-mediated sonoporation in primary endothelial cells *in vitro* using long acoustic pulses (500 – 50,000 cycles). At 1 MHz and three different acoustic pressures (150 – 500 kPa), we aimed to identify differences in MB behavior responsible for either viable sonoporation or cell death. The real-time observed uptake of PI upon sonoporation was fit using a previously reported diffusion model [38] and subsequently classified using PCA. Cell viability highly correlated with the four different PI uptake patterns derived from this classification. Further, displacing tMBs resulted in viably sonoporated cells, whereas non-displacing tMBs and ntMBs accounted for more cell death.

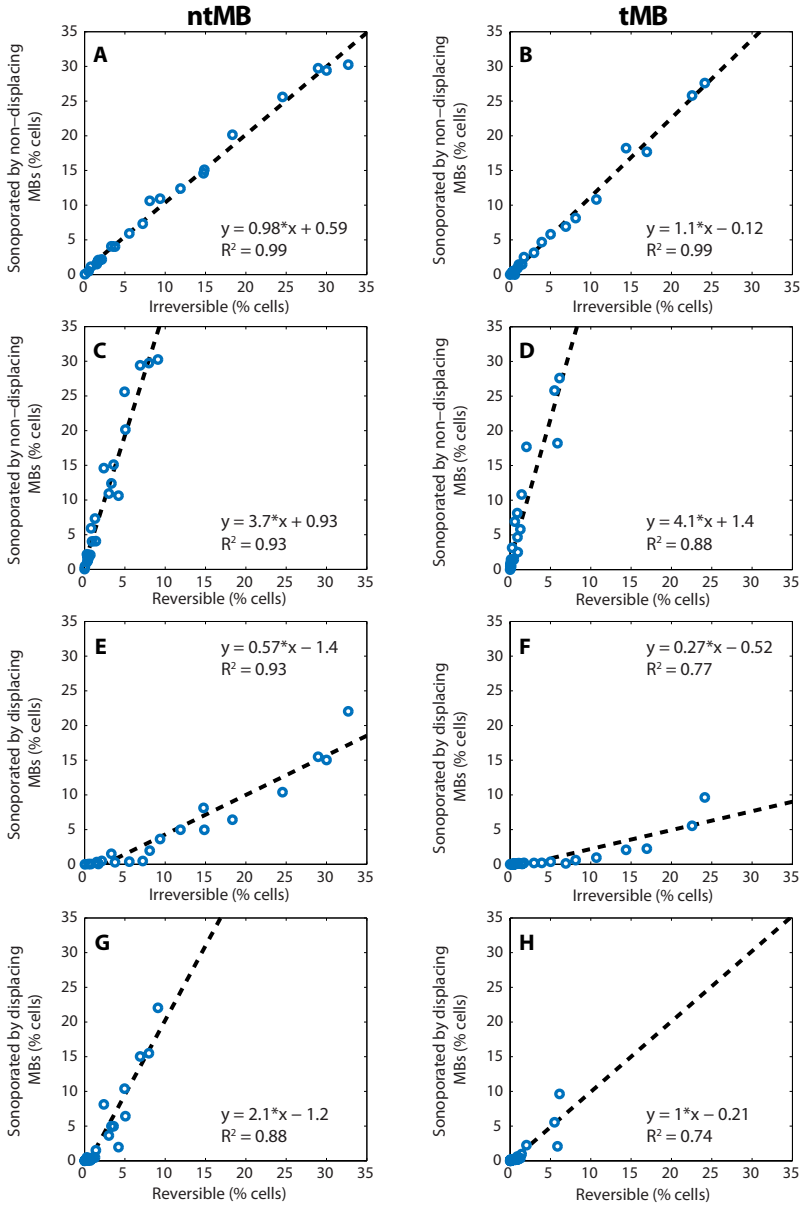

Figure 3.10: Scatter plots visualizing the relation between MB displacement and sonoporation outcome. The slope of the linear fit shows the ratio of increase between each two groups. The circles are the experimental data points at all 21 acoustic settings, the dashed line the linear fit. Irreversible sonoporation is the grey data set from Fig. 3.7; reversible sonoporation is the sum of the red and blue data sets from Fig. 3.7. The equation of the fit and its R^2 are also provided.

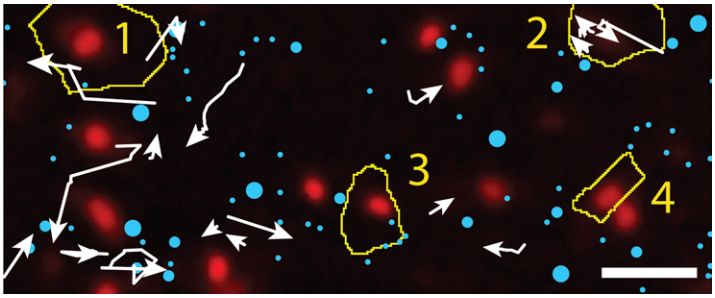

Figure 3.11: Microbubble displacement.White arrows indicate displacing ntMBs and blue filled circles indicate non-displacing ntMBs, overlaid on the same PI stained image as shown in Fig. 3.4G. Cells 1–4 (yellowlines) are the same ones as shown in Fig. 3.4. MB displacement was not correlated to the direction of US application. US settings: 500 kPa acoustic pressure, 10,000 cycles. Scale bar indicates 30 µm.

Cellular response dynamics

Four cell populations with different PI uptake profiles were found for ntMB and tMB-mediated sonoporation at each US setting. The cells that had non-resealing pores within 120 s after US application were irreversibly damaged (Fig. 3.7, grey) as this correlate dwell with cell death (Fig. 3.7, yellow). Further, cells having low PI uptake (Fig. 3.7, blue) and high PI uptake (Fig. 3.7, red) had pores that resealed within 120 s. Other researchers have shown that cells remained viable when pores resealed within a few seconds up to 60 s [37, 58, 148]. However, these studies were not performed on human endothelial cells, but on human fibroblasts [37], bovine endothelial cells [58], and Xenopus oocytes [148]. Enhanced drug uptake up to several hours has also been reported [149, 150], but cells having non-resealed pores for such long periods are not expected to be viable. We therefore believe that the route of model drug uptake in their experiments was most likely not due to pore formation, but possibly stimulated endocytosis. Our results suggest that human endothelial cells showing increasing nuclear PI signal up to 120 s were also viably sonoporated. This may imply that pores open for longer than 60 s can still result in viably sonoporated cells.

Cells that had taken up PI also showed an efflux of calcein, which is another indicator of sonoporation [38]. Next to calcein efflux, those cells also revealed lower Hoechst signals in the fluorescence images taken after US treatment than in those taken before (Fig. 3.4). Since the literature agrees upon non-competitive binding of PI and Hoechst [138, 139], we believe this decrease in signal was caused by Förster resonance energy transfer (also known as FRET) [151]. The emission spectrum of Hoechst (maximum intensity at 461 nm) overlaps with the excitation spectrum of PI (491 – 495 nm); the presence of PI can therefore result in considerable quenching of the Hoechst signal [152]. Hoechst signal intensity was therefore lower in cells that had taken up PI. In addition, the amount of PI uptake was found to be related to the level of quenching; cells 1, 3, and 4 had high PI uptake (Fig. 3.4G) and Hoechst signal was

almost completely quenched (Fig. 3.4F), whereas cell 2 had low PI uptake and less quenching of Hoechst signal.

Influence of oscillation and displacement of microbubbles

Quantitative assessment of the displacement of MBs revealed more PI uptake when more tMBs or ntMBs displaced (Fig. 3.9). We studied the relation between MB displacement and reversibility of sonoporation and found a clear relation between non-displacing MBs and irreversible sonoporation (Fig. 3.10A and B); an increase in sonoporation by non-displacing MBs coincides with a similar increase in irreversible sonoporation. We therefore concluded that irreversible sonoporation was mainly caused by non-displacing MBs, explained by prolonged MB oscillation at the same location on the cell membrane. The relation between displacing MBs and sonoporation is less straightforward. For ntMBs (Fig. 3.10G) the amount of cells sonoporated by displacing ntMBs increased twice as fast as those that were reversibly sonoporated (slope of 2.1), which implies that displacing ntMBs did not only induce reversible sonoporation, but also irreversible sonoporation (Fig. 3.10E). Because longer pulses at higher acoustic pressure cause more displacement, the ntMBs can affect multiple cells or multiple displacing ntMBs can affect a single cell.

For tMBs we found an increase in reversible sonoporation that coincides with a similar increase in sonoporation caused by displacing tMBs (Fig. 3.10H). We therefore conclude that displacing tMBs mainly resulted in reversible sonoporation. The amount of irreversibly sonoporated cells by displacing tMBs is much smaller than for ntMBs (compare Fig. 9E and F). When tMBs detach and displace, they float away from the cells and will not contribute to more sonoporation.

Displacing tMBs resulted mainly in reversible sonoporation, whereas the much larger amount of displacing ntMBs also induced irreversible sonoporation. This may imply that reversibility is only achieved with limited displacement of MBs. Fan et al. [63, 129] concluded that displacement of both ntMBs and tMBs correlated with irreversible sonoporation, while we related displacement to reversibility. This difference may be explained by larger MB displacements in their study, because they used pulsed US (1.25 MHz, 60 – 600 kPa, PRF 10 – 1000 Hz, duty cycles 0.016 – 20%), whereas the single US burst we used resulted in less displacement for the second half of the pulse (Fig. 3.8).

In the high-speed and ultra-high-speed recordings we observed clustering of MBs. Higher pressures enhanced cluster formation, and ntMBs formed more clusters because they displaced more than tMBs. Since the amount of sonoporated cells was similar for ntMBs and tMBs (Fig. 3.3), clustering did thus not result in more sonoporation.

Mannaris and Averkiou [153] were the first to show acoustically that MBs remained oscillating during 1000 acoustic cycles at 100 kPa. Our ultra-high-speed recordings revealed the presence and oscillation of both single MBs and MB clusters at the end of the 1000-cycle US burst at 150 and 300 kPa, albeit that we observed more oscillating MB clusters at the end of the US pulse than single MBs. Chen et al. [154] reported contrasting observations. After 1000 cycles their ultra-high-speed recordings only showed oscillating clusters; no single MBs were present anymore. The most likely cause for these different findings is the high pressure (up to 1.5 MPa) they applied, which resulted in more displacement due to acoustic radiation force [103, 130] and more clustering.

Sonoporation efficiency: ntMB versus tMB

The sonoporation efficiency of ntMB and tMB showed the same trend: higher pressures and more cycles resulted in more sonoporation (Fig. 3.3), as also shown by others [64, 134]. However, for tMBs the amounts of sonoporated and dead cells at 300 kPa were lower than for ntMBs, which is most likely caused by MB displacement or oscillation behavior. Increasing the pressure from 150 to 300 kPa resulted in more displacing ntMBs, but the number of displacing tMBs did not increase (Fig. 3.9). In addition, the ultra-high-speed recordings showed more oscillating ntMBs for increasing pressure, while no change was observed for tMBs (Fig. 3.8). This is caused by functionalization of our tMBs with CD31 antibodies via streptavidin-biotin binding, but we did not add streptavidin nor control-antibodies to our ntMBs, as clinical ntMBs would not have this either. Functionalization of MBs alters shell properties [87] and therefore oscillation behavior [77]. Since our tMBs and ntMBs had identical lipid shells with DSPC as the main lipid, the targeting moieties would result in a higher elasticity and thus a stiffer shell of our tMBs [87]. As a consequence, higher pressures are required for tMBs to obtain the same oscillation amplitude as for ntMBs [3], which likely influences sonoporation efficiency.

The sonoporation experiments with tMBs at 500 kPa and 10,000 to 50,000 cycles showed very large error bars (Fig. 3.3C). Two of the OptiCells in which the experiments were done showed similar uptake percentages, but the amount of sonoporated cells in the third OptiCell was almost twice as high. The underlying cause for this observation is unclear; all cell layers were confluent, the total amount of cells and MB concentration was similar, as well as the average number of MBs per cell. Hence, we can only conclude that sonoporation caused by tMBs is less predictable than by ntMBs.

Our findings, that in general tMBs did not induce higher PI uptake than ntMBs, contradict other *in vitro* studies that report tMBs to be more efficient for drug delivery than ntMBs in a direct comparison. The five reported *in vitro* studies [118–122] all show that the lipid-shell tMBs are 1.1 [122] to 7.7 [118] fold more efficient for drug delivery

than ntMBs. Four out of these five studies describe drug-loaded MBs (with paclitaxel or plasmid DNA), the other one describes co-administration of PI [121]. A direct comparison between our study and the five reported studies is difficult, due to the differences in experimental conditions. None of these studies assessed MB-mediated drug delivery in endothelial cells. Instead, smooth muscle [119] or cancer cells were used. The study that reported the largest difference between ntMBs and tMBs, rinsed the cells to remove free MBs that had not adhered [118]. As a result, the ntMBs would almost all have been washed away, which could explain the large difference. Another study treated cancer cells in suspension [120], whereas we treated a fully confluent monolayer of endothelial cells. Two studies [120, 122] used ntMBs with a different shell composition and smaller mean diameter than their tMBs, which without doubt results in differences in MB behavior [3, 77, 155]. In addition, one study reported that the 5.5 fold higher uptake could only be achieved with 70% confluent cells [119]. Consequently, our results are not supported by other studies, since none directly compared ntMB and tMB-mediated drug delivery in endothelial cells *in vitro*. Several studies reported more efficient drug delivery or transfection *in vivo* for tMBs than for ntMBs [123–126]. Due to blood flow, ntMBs flow by and thus have shorter contact with tissue, thereby making ntMBs less efficient. Inclusion of flow in the *in vitro* experiments is thought to result in more efficient sonoporation for tMB than for ntMB and will be subject for future studies.

Microbubble orientation

We used a different orientation of MBs relative to the cells and US direction for tMBs and ntMBs (Fig. 3.1B and Supplementary material). Therefore, the ntMBs could have been pushed towards the cells by the US, while the tMBs could have been pushed away from the cells. To study whether this influenced sonoporation efficiency, we performed experiments with tMBs in the same orientation as the ntMBs, which we referred to as tMB_B (tMB below cells). Because tMB_B adhered below the cells, non-adhered tMB_B would also be in contact with the cells and could have contributed to sonoporation as well. Higher amounts of non-adhered tMB_B would results in more displacing tMB_B and thus enhance sonoporation. However, since the amounts of tMB_B and tMBs in the FOV were the same (~3100 cells), we can assume that all tMB_B had adhered and that non-adhered tMB_B did not account for the variation in PI uptake.

Sonoporation efficiency for tMB_B seemed higher than for tMBs (compare Fig. 3.3C and Supplemental Fig. 3.1A), possibly caused by MBs that detached during insonification and remained in contact with the cells. In contrast, the configuration for tMBs allowed them to float away after detachment. The sonoporation efficiency, however, was not significantly different to conclude that tMB_B were more efficient than tMBs. To the best of our knowledge, no previously published studies investigated the orientation of MBs relative to the cells and US direction. Others that directly compared the effect of

ntMBs and tMBs either did not mention the orientation [120, 122], had the MBs on top of the cells with US applied from the MB-side [118], or had the MBs below the cells and applied US from below [119, 121].

Experimental considerations

To obtain the amount of sonoporation from the nuclear PI uptake and the associated model fit, we used algorithms implemented in ImageJ and RStudio, whereas a different algorithm in Python was used to obtain sonoporation from PI uptake in the entire cell and its relation to displacing and non-displacing MBs. Although this is not ideal, we chose this approach to optimally utilize the strengths of each method: segmentation (ImageJ) and tracking of moving particles (Python). Since both methods relied heavily on correct detection of cell nuclei, we manually counted the nuclei on the Hoechst images and compared this to the outcomes of the ImageJ and Python algorithms: both detected, on average, only 6% of the nuclei incorrectly (n = 6 images). Since the errors were small, the additional analyses were expected to be comparable as well. Indeed, the segmented cell borders by Voronoi tessellation closely overlapped between the two methods. As already mentioned, sonoporation was slightly higher (2.7% on average) for the tracking method in Python, than for the more robust fitting method using RStudio. This was caused by additional detection of cytoplasmic PI uptake and by cells of which the model could not be fit ($R^2 < 0.8$) to the nuclear uptake profile.

In contrast to the paper by Fan et al. [38], we did not calculate the size of the pores, since not all parameters of our system were known. However, if we would have done this, possible multiple pores in a single cell could still have been detected as one larger pore. In addition, we only included PI uptake in the nucleus because determination of the cell borders was based on probability, whereas the nucleus could be more precisely segmented from the Hoechst images.

On average, 7.4% of sonoporated cells that were found using the tracking algorithm were classified as being sonoporated without the presence of a MB nearby (Fig. 3.9, white). Since control experiments with only MBs showed sonoporation of < 0.9% of all cells, this was not caused by spontaneous uptake of PI, but most likely due to the size of the MBs –only a few pixels in diameter– and the quality of the images. Accurately detecting ntMBs was more difficult due to the optical focus in the corresponding bright-field images; the cells were better in focus, resulting in lower discriminative power between cell structures and MBs. The error for ntMB detection was therefore higher. Manual counting of the number of MBs that was not counted by the algorithm resulted in an average of 9% more MBs per image (n = 9). This is slightly higher than the average amount of sonoporated cells without MBs nearby, because MBs that were in contact with non-sonoporated cells could have also been missed.

Limitations of this study

A limitation to our study is the use of CD31 as the ligand on our tMBs, because this is a constitutively expressed adhesion molecule on endothelial cells [156]. It can therefore not be used *in vivo*, since CD31-tMBs would adhere to the entire vasculature. Also, the MBs circulate within the vasculature *in vivo*, while we performed our studies under static conditions. Flow is expected to have an influence on the sonoporation efficiency, as ntMBs will be taken away by the flow, while tMBs will still adhere to the cells under flow [157]. A higher sonoporation efficiency for tMBs is therefore expected and shown [123, 124, 126] under flow and *in vivo* conditions.

Therapeutic applications

Based on our results, ntMBs exposed to an acoustic pressure of 500 kPa and a pulse length of 1000 cycles would be most beneficial for drug delivery. These settings resulted in relatively high amounts of viably sonoporated cells (Fig. 3.7, blue) and minimal cell death (Fig. 3.7, grey/yellow). For drug delivery, high drug uptake would be most beneficial since higher doses of therapeutics can be delivered (Fig. 3.7, red). Nevertheless, we always observed equal or lower red uptake patterns in comparison to the blue uptake patterns of lower PI uptake, implying there is not one US setting that favors one over the other. On the other hand, for therapeutic applications where high cell death is desired, e.g. cancer therapies, high pressures and long pulses should be applied (e.g., 500 kPa and 50,000 cycles). Both tMBs and ntMBs were shown to effectively kill cells, but ntMBs were more efficient. For therapies requiring sonoporation of specific cells under flow, ntMBs would need to be replaced with tMBs. ntMBs could sonoporate cells as they move along the cells, or when pressed against a thrombus occluding a blood vessel, as in the case of sonothrombolysis [26, 158]. On the other hand, for locally enhanced drug delivery in tumors tMBs are required, since the MBs need to be close to the cell membrane [58, 159]. Hence, the choice of using either ntMBs or tMBs highly depends on the desired therapeutic application.

3.5. CONCLUSION

In depth sonoporation studies on the effect of longer acoustic pulses at 1 MHz at different acoustic pressures revealed a clear relation between sonoporation efficiency and MB behavior. Different patterns of PI uptake derived from the diffusion model and subsequent classification using PCA highly correlated with cell viability. Limited displacement of the MBs enhanced drug delivery and preserved cell viability, while non-displacing MBs were the main contributor to cell death. Longer pulses resulted in more dead cells, but did not result in significant increase in viably sonoporated cells. In addition, the effect of the same type of ntMBs and tMBs to sonoporate endothelial cells was similar *in vitro* under static conditions.

ACKNOWLEDGEMENT

The authors thank Robert Beurskens, Frits Mastik, Michiel Manten, and Geert Springeling from the Department of Biomedical Engineering, Thoraxcenter, Erasmus MC, the Netherlands for technical assistance. This work is financially supported by NanoNextNL, a micro- and nanotechnology consortium of the Government of the Netherlands and 130 partners and by the Dutch Technology Foundation STW (Veni-project 13669), which is part of the Netherlands Organisation for Scientific Research (NWO), and which is partly funded by the Ministry of Economic Affairs. The funding sources were not involved in the study design; neither in the collection, analysis and interpretation of data; nor in writing of the report. NanoNextNL and STW approved the article for publication.

SUPPLEMENTARY MATERIAL

Supplementary data to this article can be found online at `http://dx.doi.org/10.1016/j.jconrel.2016.07.037`.

Orientation of tMBs

For all experiments concerning ntMBs, the cells were on the upper membrane of the OptiCell with the MBs floating against the cells. For the tMB experiments described so far, the cells were on the bottom membrane with the tMBs adhered on top of the cells. In addition to the comparison between ntMBs and tMBs, we also investigated the effect of the orientation of tMBs with respect to the cells and US application. We therefore placed the OptiCell containing tMBs in the same orientation as the experiments on ntMBs, so the cells were on the upper membrane with the tMBs below the cells (tMB_B). These experiments were repeated two times at 500 kPa for all investigated number of cycles with on average 3106 (± 139) cells in the FOV.

The amount of US-induced sonoporated cells with tMB_B was higher than for the control experiments for the four settings with the smallest error bars: 1000; 2000; 10,000; and 50,000 cycles. Although, especially for the longer pulses, tMB_B seemed to more efficiently sonoporate cells than both tMBs and ntMBs, this was not statistically significant for most cycles. Only with 10,000 cycles were tMB_B more efficient than ntMBs (*); and only with 500 cycles were tMB_B more efficient than tMB (o) (Supplemental Fig. 3.1A, $p < 0.05$). Cell death for tMBB was significantly higher than for the tMB_B controls after applying 2000; 5000; 20,000; and 50,000 cycles. In addition, cell death and the total amount of sonoporated cells were significantly different for all experimental settings. For most settings cell death of tMBB was similar to ntMBs or tMBs, except for 1000 cycles with ntMBs (*) and 1000 and 2000 cycles with tMBs (o) as shown in Supplemental Fig. 3.1B. Cell death controls are not shown, since these were subtracted from cell death at the other settings to correct for natural cell death.

Cell classification based on PI uptake patterns showed similar trends for tMB_B as for ntMBs and tMBs, in terms of the amount of cells in each group. However, the cells with non-resealing pores within 120 s (Supplemental Fig. 3.1C, grey) did not correlate with the amount of cell death (Supplemental Fig. 3.1C, yellow), since they were significantly different for all applied settings, possibly of lower statistical power (only n = 2).

As expected, displacement of tMB_B was very similar to the displacement of tMBs (Supplemental Fig. 3.1D and Fig. 3.9), since the binding strength that has to be overcome to displace them is identical.

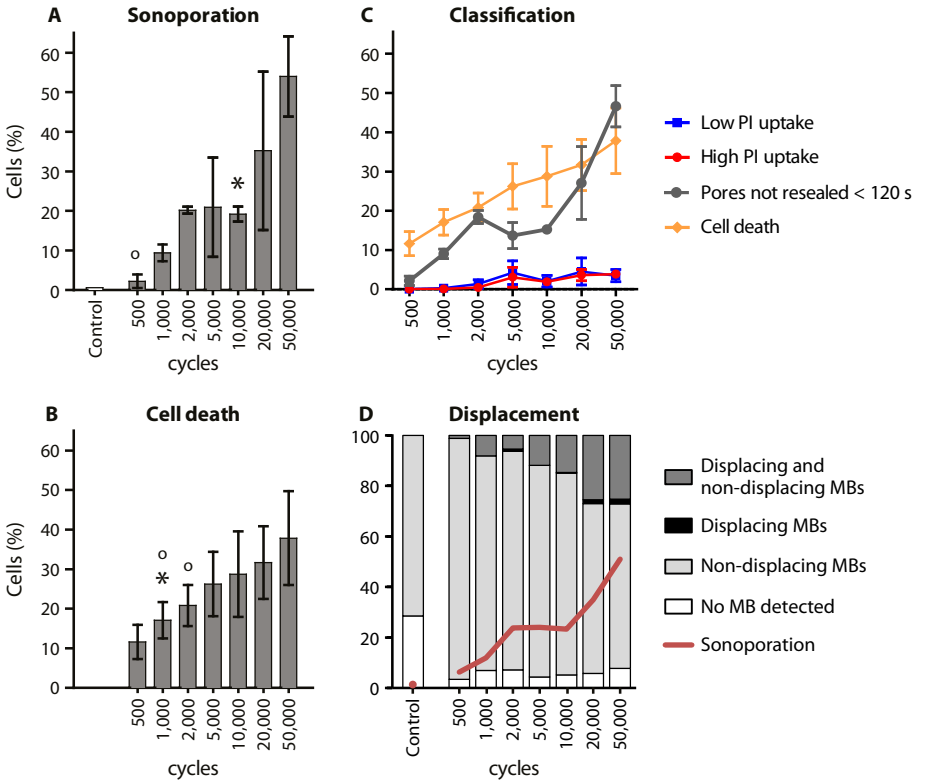

Supplementary Figure 3.1: tMBs adhered below the cells (tMB_B) insonified at 500 kPa. (**A**) Mean (± SD) percentage of sonoporated cells and (**B**) cell death after insonification of tMB_B. Asterisks (*) indicate significant differences between tMB_B and ntMBs, and (o) between tMB_B and tMBs. (**C**) Classification of cells based on their pore size and pore resealing coefficient. The amount of cells with non-resealing pores within 120 s (grey) was significantly different from the amount of dead cells (yellow) for all settings. (**D**) Displacement of tMB_B. For each acoustic setting, the bar graph indicates the percentage of cells that were sonoporated by displacing MBs, non-displacing MBs, both, or when no MB could be detected. The red line shows the percentage of cells that were sonoporated.

4

Acoustic characterization of the CLINIcell

Based on:
Inés Beekers, Tom van Rooij, Antonius F. W. van der Steen, Nico de Jong, Martin D. Verweij, Klazina Kooiman, "Acoustic Characterization of the CLINIcell for Ultrasound Contrast Agent Studies", *IEEE Transactions on Ultrasonics, Ferroelectrics, and Frequency Control*, vol. 66, no. 1, pp. 244–246, 2019 [160].

Abstract

Ultrasound contrast agents consist of gas-filled coated microbubbles that oscillate upon ultrasound insonification. Their characteristic oscillatory response provides contrast enhancement for imaging and has the potential to locally enhance drug delivery. Since microbubble response depends on the local acoustic pressure, an ultrasound compatible chamber is needed to study their behavior and the underlying drug delivery pathways. In this study, we determined the amplitude of the acoustic pressure in the CLINIcell, an optically transparent chamber suitable for cell culture. The pressure field was characterized based on microbubble response recorded using the Brandaris 128 ultra-high-speed camera and an iterative processing method. The results were compared to a control experiment performed in an OptiCell, which is conventionally used in microbubble studies. Microbubbles in the CLINIcell responded in a controlled manner, comparable to those in the OptiCell. For frequencies from 1 to 4 MHz, the mean pressure amplitude was -5.4 dB with respect to the externally applied field. The predictable ultrasound pressure demonstrates the potential of the CLINIcell as an optical, ultrasound, and cell culture compatible device to study microbubble oscillation behavior and ultrasound-mediated drug delivery.

Index Terms — Acoustic characterization, drug delivery, ultra-high-speed imaging, ultrasound contrast agents (UCAs).

4.1. INTRODUCTION

Ultrasound contrast agents (UCAs) are comprised of gas-filled coated microbubbles (1-10 μm in diameter). Upon ultrasound insonification, the microbubbles compress and expand due to the acoustic pressure. This oscillatory behavior is the characteristic microbubble response used in the clinic for contrast enhancement of diagnostic ultrasound imaging. More recently, their potential to locally enhance vascular drug delivery has been demonstrated [3, 32]. Microbubble oscillation upon ultrasound insonification generates local mechanical stress that can increase endothelial cell membrane permeability by pore formation (i.e. sonoporation), opening of cell-cell junctions, and stimulation of endocytosis [3]. However, the underlying mechanisms of these pathways remain unknown.

A better understanding of the microbubble's oscillation behavior can aid the design of UCAs for diagnostic ultrasound imaging. In addition, we need to better understand the microbubble-cell interaction to control the different pathways of ultrasound-mediated drug delivery. Microbubble oscillation strongly depends on the ultrasound insonification, composition of shell and gas core, targeting ligands, microbubble size, production method, and their local environment [3]. Therefore, we require a chamber in which microbubble behavior can be characterized experimentally, with

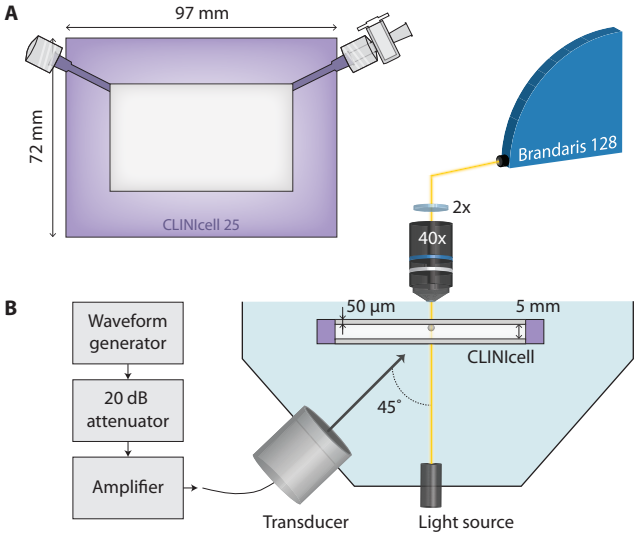

Figure 4.1: (**A**) Sketch of a CLINIcell with a 25 cm^2 cell culture area. (**B**) Schematic representation (not drawn to scale) of the experimental setup to study microbubble oscillation upon insonification using the Brandaris 128 ultra-high-speed camera. The two parallel membranes of the CLINIcell each have a thickness of 50 µm. The microscope was equipped with a 40× water immersion objective and a 2× lens (Olympus, Tokyo, Japan). The insonification scheme was generated by a waveform generator (Tabor 8026, Tabor Electronics, Tel Hanan, Israel), connected to a 20 dB attenuator (Mini-Circuits, Brooklyn, NY, USA) and a broadband amplifier (ENI A-500, Electronics & Innovation, Rochester, NY, USA).

or without cellular interaction, which is both ultrasound compatible and optically transparent. If we quantitatively know how the ultrasound pressure field transmits into the chamber, the microbubble can be insonified in a controlled manner. Optical transparency is essential to image microbubble behavior and cellular response with a microscope. Moreover, the chamber should be suitable for cell culture to study ultrasound-mediated drug delivery *in vitro*.

The OptiCell™ (Nunc, Thermo Fisher Scientific, Wiesbaden, Germany) has been extensively used for both microbubble characterization and drug delivery studies [161]. Since the OptiCell is no longer being manufactured, the CLINIcell® (MABIO, Tourcoing, France) is an interesting alternative imaging and cell culture chamber. It has recently been used to characterize microbubbles [162, 163] and to study ultrasound-mediated drug delivery [164]. However, a thorough acoustic characterization has not been performed yet.

In this study we therefore quantitatively assessed microbubble oscillation in the CLINIcell by performing microbubble spectroscopy using the Brandaris 128 ultra-high-speed camera. The recordings were iteratively processed using our previously reported method [165].

4.2. MATERIAL AND METHODS

The CLINIcell (50 µm membrane, 25 cm^2 area) is a cell culture chamber consisting of two parallel gas permeable polycarbonate membranes, with a separation of 5 mm (Fig. 4.1).

To characterize the acoustic pressure transmitted into the CLINIcell *in situ* and non-invasively, microbubbles were used as pressure sensors, as previously described by us [165]. The CLINIcell was blocked prior to the experiment with 12 mL of 2% bovine serum albumin (BSA) in phosphate buffered saline (PBS) for 1 h, to prevent unspecific microbubble binding to the membranes. Next, it was rinsed three times with PBS before introducing 12 mL of 10^5 microbubbles/mL. We replicated the experimental set-up, ultrasound insonification parameters, microbubble preparation, and experimental data analysis. Briefly, the 1,2-distearoyl-*sn*-glycero-3-phosphocholine (DSPC)-based microbubbles were insonified at 45° incidence angle with a single-element transducer (1-9 MHz bandwidth, 25 mm focal distance, −6 dB beamwidth at 1 MHz of 1.3 mm, PA275, Precision Acoustics, Dorchester, UK). Microbubble spectroscopy [74] was performed by successively insonifying each individual microbubble while sweeping through a range of transmit frequencies (f_T) from 1 to 4 MHz (in steps of 300 kHz). An 8-cycle sine wave burst was applied at 20 kPa external peak negative pressure (PNP), as calibrated in a separate experiment using a 1-mm needle hydrophone. The microbubble oscillation behavior was recorded using the Brandaris 128 ultra-high-speed camera [6] (17 million frames/s) combined with a microscope (80x magnification, BX-FM, Olympus, Tokyo, Japan), as depicted in Fig. 4.1B.

Using custom-designed image analysis software, microbubble oscillation was quantified as the change in radius over time $R(t)$, as previously described [74]. Briefly, the relative excursion was defined as $x(t) = R(t)/R_0 - 1$, with resting radius R_0. The amplitude (x_0) of the relative excursion was defined as the maximum after bandpass filtering $x(t)$ (third-order Butterworth filter, 500 kHz bandwidth, centered at f_T). Next, we determined the acoustic pressure amplitude (P) experienced by the microbubbles by fitting x_0 in an iterative manner [165] to the harmonic oscillator model

$$x_0 = \frac{|P|/(4\pi^2 \rho R_0^2)}{\sqrt{\left(f_0^2 - f_T^2\right)^2 + \left(\delta f_T f_0\right)^2}} \tag{4.1}$$

with $\rho = 10^3$ kg/m^3 being the density of water. The eigenfrequency (f_0) of the microbubble is given by

$$f_0 = \frac{1}{2\pi}\sqrt{\frac{1}{\rho R_0^2}\left[3\gamma P_0 + \frac{2\left(3\gamma - 1\right)\sigma_w}{R_0} + \frac{4\chi}{R_0}\right]} \tag{4.2}$$

with γ = 1.07 the ratio of specific heats for C_4F_{10}, $P_0 = 10^5$ Pa the ambient pressure, σ_w = 0.072 N/m the surface tension in water, and χ the microbubble shell elasticity [74]. The damping coeffcient (δ) is given by

$$\delta = \frac{\omega_0 R_0}{c} + 2 \cdot \frac{4\mu}{R_0^2 \rho \omega_0} + \frac{4\kappa_s}{R_0^3 \rho \omega_0} \tag{4.3}$$

with c = 1500 m/s the speed of sound in water, $\mu = 10^{-3}$ Pa·s the viscosity of water, and κ_s the microbubble shell viscosity [77]. Therefore, with the iterative scheme not only the pressure experienced by the microbubbles in the CLINIcell can be determined, but also the microbubble shell elasticity and viscosity since they are incorporated in f_0 and δ. The results were compared to those of control experiments previously performed in an OptiCell, using an identical experimental set-up [77]. All analyses were performed using MATLAB (The MathWorks, Natick, MA, USA).

4.3. RESULTS

Single microbubbles with resting radius (R_0) from 1.4 to 3.3 μm were recorded upon insonification in the CLINIcell (n=38). Fig. 4.2 shows a typical example of recorded frames and illustrates how the relative excursion amplitude (x_0) was determined. This example also demonstrates that bandpass filtering $x(t)$ removes the low frequency component of compression-only behavior [166], such that the fundamental amplitude is obtained. Fig. 4.3 shows the relative excursion amplitude (x_0) as a function of R_0 for every microbubble when insonified at f_T = 1.6 MHz. The microbubble response was similar in both the OptiCell and CLINIcell, with comparable excursion amplitudes and characteristic resonance behavior for R_0=2.5 μm at 1.6 MHz. The pressure experienced by the microbubble (P) was obtained by iteratively fitting x_0 to the harmonic oscillator model for 30 iterations. Fig. 4.4 shows the frequency dependence of P normalized to the applied external pressure (P_A = 20 kPa PNP). The mean normalized transmitted pressure amplitude from 1 to 4 MHz was similar in both systems: −5.4 dB in the CLINIcell and −5.1 dB in the OptiCell. Moreover, the transmitted pressure showed no clear frequency dependence.

The median shell elasticity (with interquartile range between brackets) obtained by fitting the eigenfrequency f_0 (Fig. 4.5 to equation (4.2) was similar, with χ = 0.32 (0.27) N/m in the CLINIcell and χ = 0.32 (0.25) N/m in the OptiCell. The median shell viscosity obtained from equation (4.3) was also similar in both systems, κ_s = 1.1 (0.5) $\cdot 10^8$ kg/s in the CLINIcell and κ_s = 0.7 (0.4) $\cdot 10^8$ kg/s in the OptiCell.

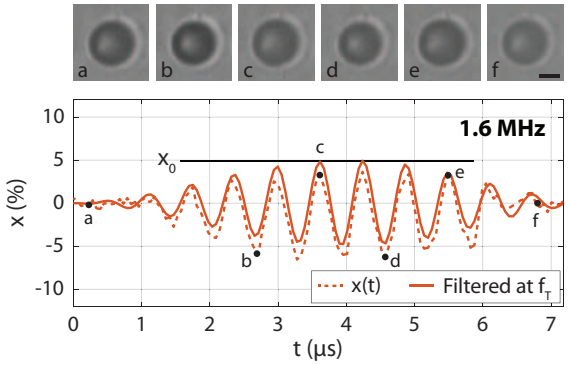

Figure 4.2: Selected frames of a Brandaris 128 ultra-high-speed recording of a single microbubble (R_0=2.4 µm) in the CLINIcell, insonified at f_T=1.6 MHz (2 µm scale bar). The dashed line shows the microbubble's relative excursion x and the black dots indicate the time points of the selected frames. The solid red line shows x bandpass filtered around f_T and its maximum, defined as the relative excursion amplitude x_0 (see Fig. 4.3).

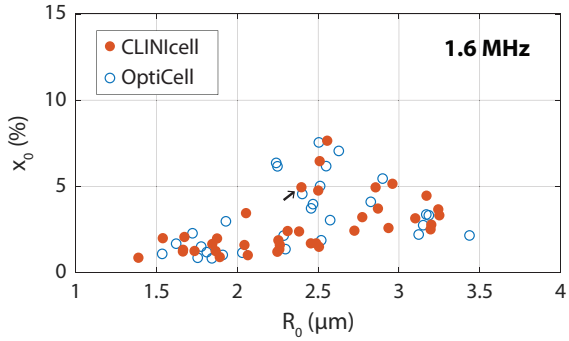

Figure 4.3: Relative excursion amplitude (x_0) of single microbubbles in the CLINIcell (n=38, solid red) and OptiCell (n=30, open blue) as a function of resting radius (R_0) when insonified at f_T = 1.6 MHz. The solid data point indicated by the arrow is shown in Fig. 4.2.

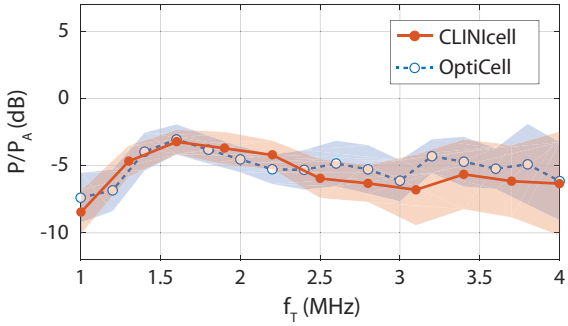

Figure 4.4: Normalized median pressure amplitude derived from microbubble oscillations in the CLINIcell (solid red) and OptiCell (open/dashed blue). The shaded area corresponds to the interquartile range.

4.4. DISCUSSION

The acoustic pressure in the CLINIcell was successfully evaluated using microbubbles as non-invasive pressure sensors, confirming the applicability of our iterative processing method [165]. The pressure amplitude transmitted into the CLINIcell was similar to that of the OptiCell and no clear frequency dependence was observed. The microbubbles oscillated in a controlled manner and their shell parameters remained unchanged. We expect an unaltered focal region of the transmitted ultrasound field,

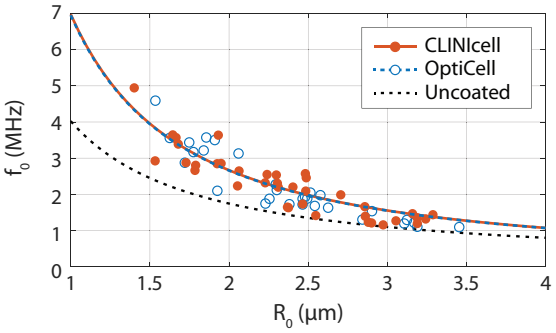

Figure 4.5: Eigenfrequency (f_0) of microbubbles in the CLINIcell (solid red) and OptiCell (open/dashed blue) and the corresponding fit to obtain the shell elasticity. The f_0 of an uncoated microbubble is given by $\chi = 0$ N/m (black dashed line).

since the CLINIcell has two parallel membranes similarly to the OptiCell, in which the focal region remains unchanged [165]. We chose to characterize a CLINIcell with a 50 μm membrane since it is most comparable to the 75 μm membrane of the conventional OptiCell. Also, we assumed that the ultrasound propagation would be affected more by the CLINIcell design with a thicker membrane (125 μm). The surface area available in the CLINIcell (25 cm^2) for cell culture is smaller than in the OptiCell (50 cm^2), while the filling volume remains similar (12 mL versus 10 mL). Therefore, microbubble concentration and cell culture protocols might have to be adjusted.

4.5. CONCLUSION

The pressure amplitude inside the CLINIcell was -5.4 dB on average with respect to that of the externally applied pressure, similarly to the OptiCell. Controlled microbubble behavior was achieved in the CLINIcell and the applied pressure can be corrected for the now quantified pressure drop. This demonstrates the potential of the CLINIcell as an alternative chamber to characterize microbubble behavior and to study ultrasound-mediated drug delivery in an optical, ultrasound, and bio-compatible chamber.

ACKNOWLEDGEMENT

The authors thank Frits Mastik and Robert Beurskens from the Department of Biomedical Engineering, Erasmus MC, for technical assistance during the experiments.

5

Combined confocal microscope and Brandaris 128 ultra-high-speed camera

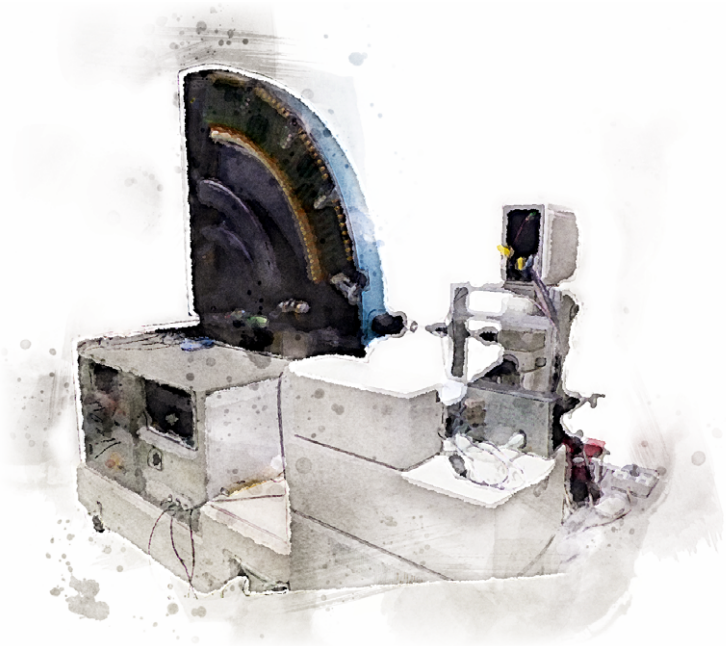

Based on:

Inés Beekers, Kirby R. Lattwein, Joop J. P. Kouijzer, Simone A. G. Langeveld, Merel Vegter, Robert Beurskens, Frits Mastik, Rogier Verduyn Lunel, Emma Verver, Antonius F. W. van der Steen, Nico de Jong, and Klazina Kooiman, "Combined Confocal Microscope and Brandaris 128 Ultra-High-Speed Camera", *Ultrasound in Medicine & Biology*, vol. 45, no. 9, pp. 2575-2582, 2019. [167]

Abstract

Controlling microbubble-mediated drug delivery requires the underlying biological and physical mechanisms to be unraveled. To image both microbubble oscillation upon ultrasound insonification and the resulting cellular response, we developed an optical imaging system that can achieve the necessary nanosecond temporal and nanometer spatial resolutions. We coupled the Brandaris 128 ultra-high-speed camera (up to 25 million frames per second) to a custom-built Nikon A1R+ confocal microscope. The unique capabilities of this combined system are demonstrated with three experiments showing microbubble oscillation leading to either endothelial drug delivery, bacterial biofilm disruption, or structural changes in the microbubble coating. In conclusion, using this state-of-the-art optical imaging system, microbubble-mediated drug delivery can be studied with high temporal resolution to resolve microbubble oscillation and high spatial resolution and detector sensitivity to discern cellular response. Combining these two imaging technologies will substantially advance our knowledge on microbubble behavior and its role in drug delivery.

Index Terms — Bacteria, Confocal microscopy, Drug delivery, Fluorescence microscopy, High-speed imaging, Lipid coating, Microbubble, Sonoporation, Ultrasound, Ultrasound contrast agents.

5.1. INTRODUCTION

To successfully treat diseases, administered drugs need to overcome barriers in the human body that hinder efficient delivery. Currently, high dosages are required because only a fraction of the therapeutic actually reaches the target site. This leads to high toxicity levels in healthy tissue, causing undesirable side effects [168, 169]. However, lipid-coated gas microbubbles (1 - 10 μm) in combination with ultrasound can locally enhance drug delivery, allowing for therapeutics to be delivered efficiently and only to the intended target site. When ultrasound is applied, microbubbles oscillate and thereby permeabilize cell membranes (sonoporation), open intercellular junctions, and stimulate endocytosis [3, 32, 33]. The underlying physical and biological mechanisms enhancing these different pathways are poorly understood. Elucidating the microbubble–cell interaction is fundamentally important for controlling and optimizing drug delivery, and therefore, microbubble oscillation behavior and the cellular response should be studied simultaneously.

To resolve the microbubble oscillation in an ultrasound field of clinically relevant frequencies (MHz), a system with nanosecond temporal resolution is required. Currently, there are two ultra-high-speed cameras that can achieve such high frame rates, up to 25 million frames per second (Mfps) with sufficient consecutive frames:

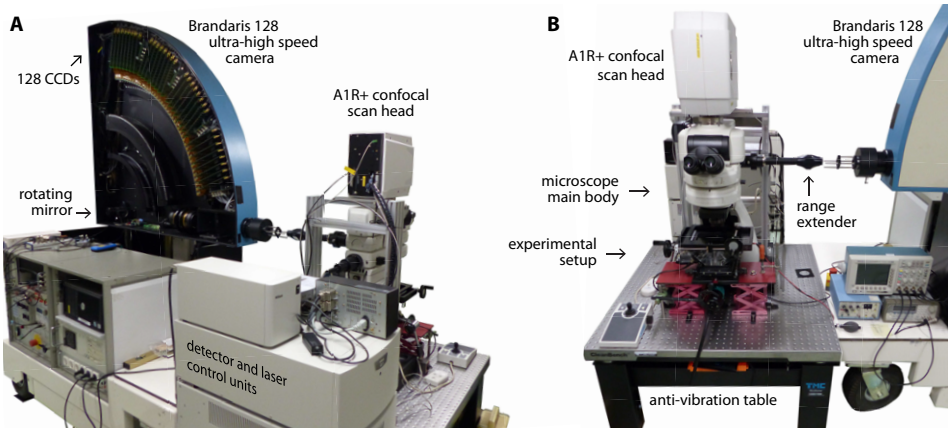

Figure 5.1: Combined confocal microscope and Brandaris 128 ultra-high-speed camera. (**A**) From the back of the system, the inside of the Brandaris 128 casing with the rotating mirror and 128 charge-coupled devices (CCDs) is seen. (**B**) At the front of the system are the confocal microscope and the experimental setup. The range extender facilitates the coupling of the Brandaris 128 to the confocal microscope.

5

the Brandaris 128 [6] and the UPMC Cam [7]. Both cameras have been coupled to an upright microscope (BXFM, Olympus, Tokyo, Japan) for brightfield and widefield fluorescence microscopy. This enables the concurrent visualization of microbubble oscillation and cellular response. Although these systems have been used to study vascular drug delivery [15, 53, 58, 62], imaging resolution showing the cellular response was very poor. Microbubble oscillation leading to bacterial biofilm disruption has been observed at a lower temporal resolution using a 3 Mfps camera [170]. With the use of high-speed cameras, it has been possible to study the microbubble–cell interaction; however, the cellular response was still imaged with poor sensitivity and at a low optical and temporal resolution.

Confocal microscopy allows us to better unravel cellular response, as it provides nanometer spatial resolution, 3D imaging with high axial resolution, and good detector sensitivity for different fluorescent cell labeling. Live confocal microscopy imaging of microbubblemediated drug delivery has revealed a wide-range of cellular effects: pore formation [38] and recovery [37], opening of intercellular junctions [53], endocytosis [64], lipoplex [171] and doxorubicin [12] delivery, changes in reactive oxygen species levels [45], increased bacterial metabolism [172], sonoprinting [173], cytoskeleton disruption [51], and intercalation of model drugs [164]. However, all these studies lack information on the specific microbubble behavior that was responsible for the observed cellular effect, because of the relatively low frame rates of confocal microscopy imaging (<500 fps).

Microbubble response to ultrasound varies a lot, and even equal-sized microbubbles in the same ultrasound field do not respond identically [65, 66, 155]. We need

to gain more insight into microbubble behavior to achieve a more predicable response to ultrasound. To understand how the response is affected by microbubble composition, we want to image both the microbubble oscillation behavior and the coating microstructure [174]. In the past, it has only been possible to image coating microstructure in a static setup, without ultrasound, using, for example, 4Pi high-resolution confocal microscopy [88].

To date, the technological gap has made it impossible to image microbubble oscillation (high temporal resolution) and detailed cellular response (high spatial resolution) in the same field of view of a single sample. To overcome this challenge, we developed a novel optical imaging system by coupling an upright custom-built Nikon confocal microscope to the Brandaris 128 ultra-high-speed camera (Fig. 5.1), which is described in this technical note.

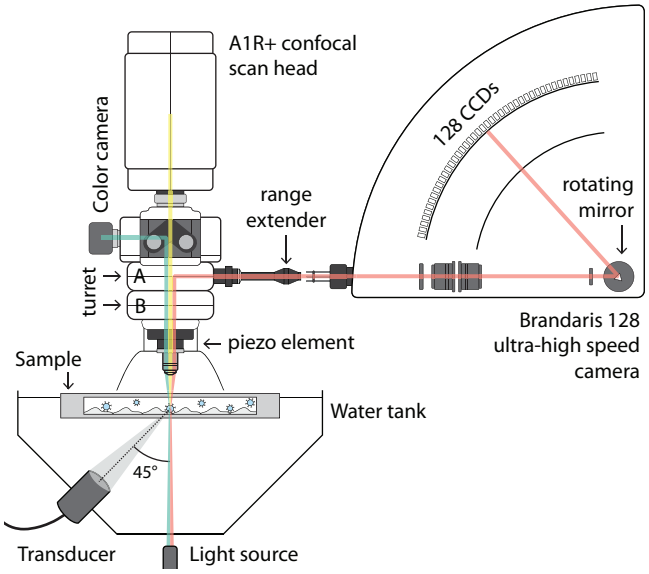

Figure 5.2: Schematic of the light paths to the different imaging output ports (not to scale). The light path goes through the sample, the objective, and the main body of the microscope toward either the color camera (green), the confocal scan head (yellow) or the Brandaris 128 ultra-high-speed camera (red). The light source is used for brightfield and Brandaris 128 imaging. The motorized turret A can place the full mirror in the light path for Brandaris 128 imaging, while turret B can insert the desired filter cubes for widefield fluorescence imaging. The sample can be insonified from below under a 45° angle in a water tank, which can be heated to 37°C. CCDs = charge-coupled devices.

5.2. METHODS

The Brandaris 128 ultra-high-speed camera is a programmable camera with 128 sensitive charge-coupled devices (CCDs) and a fast rotating mirror that sweeps the image over the CCDs, resulting in a minimum interframe time of 40 ns (25 Mfps) [6]. Consecutive 128-frame recordings can be done at an 80 ms interval, with a maximum of 50 consecutive recordings [94]. The brightfield image is 500×292 pixels with 8-bit gray-scale values and a typical resolution of 400 nm [6].

The main body of the confocal microscope is a custom- built upright Eclipse Ni-E microscope (Nikon Instruments, Amsterdam, The Netherlands). By physically removing the conventional base of the main body, the microscope was customized to accommodate the water bath for ultrasound insonification. Microscope modules were chosen to meet our requirements such that the light path (Fig. 5.2) could be directed toward the four different output ports: (i) a binocular (NI-TT-E Motorized Quadrocular Tilting Tube, Nikon Instruments), (ii) a color camera (DS-Fi3, Nikon Instruments) for digital acquisition of brightfield and widefield fluorescence images, (iii) the A1R+ confocal scan head, and (iv) the Brandaris 128 ultra-high-speed camera.

Two motorized turret modules (NI-FLT6-E Mot Epi-fluorescent turret, Nikon Instruments) were incorporated to rotate the desired filters or mirrors into the light path. One turret holds a full mirror to direct the light path toward the Brandaris 128 camera (Fig. 5.2, turret A). The other turret is used for switching between filter cubes for widefield fluorescence imaging (Fig. 5.2, turret B). The four installed filter cubes have the following excitation (Ex), dichroic mirror (DM), and emission (Em) filters: BFP-A with Ex390/18, DM416, and Em460/60; GFP-A with Ex469/35, DM497, and Em525/39; TRITC-A with Ex542/20, DM570, and Em620/52; and Cy5-4040 C with Ex628/40, DM660, and Em692/40 (center wavelength/bandwidth in nanometers; Semrock Inc., Rochester, NY, USA). Widefield fluorescence is performed with a metal halide light source with motorized shutters and neutral density filters (C-HGFIE, Fiber Illuminator Intensilight, Nikon Instruments). During confocal imaging, excitation is achieved with a laser unit (LU-N4, Nikon Instruments) equipped with four lasers (405, 488, 561, and 640 nm; all 15 mW at the output of the fiber tip). The system has a hybrid detector unit (A1-DUG, GaAsP Multi Detector Unit, Nikon Instruments) that includes two gallium arsenide phosphide (GaAsP) photomultiplier tubes (PMTs) and two standard multi-alkali PMTs. The GaAsP PMTs are highly efficient in detecting the 525/50 and 595/50 nm ranges in comparison to the standard multi-alkali PMTs. To create four detection channels, the emitted light is split using three filter cubes. The first filter cube (DM FF495-Di03, Semrock Inc.; Em filter ET450/50 m, Chroma, Bellows Falls, VT, USA) delimits the 450/50 nm channel which is detected by a standard multi-alkali PMT. The second filter cube (DM T560 LPXR, Chroma; Em filter ET525/50 m, Chroma) delimits the 525/50 nm channel, which is detected by a GaAsP PMT. The third filter cube (DM T640 LPXR, Chroma; Em filter ET595/50 m, Chroma; Em ET700/75 m, Chroma)

delimits the 595/50 and 700/75 nm channels, which are detected with a GaAsP PMT and a standard multi-alkali PMT, respectively.

For high-precision focusing and 3D z-stack imaging, the microscope's main body combines two z-scanning devices. First, long ranges (12 mm) can be scanned with the main body's motorized z functionality, which was retained despite the customization. Next, with a piezo element (MCL NANO-F200 N, Mad City Labs Inc., Madison, WI, USA), faster and more precise z-focusing can be performed in a 200 µm range, resulting in improved z-stack imaging. To isolate vibration, the confocal microscope was installed on an active antivibration optical table (74-9090 M Cleanbench top and 12M-424-88 micro-g modular post mount support, Physik Instrumente, Karlsruhe, Germany).

The field of view of the Brandaris 128 camera had to overlap with that of the microscope. Therefore, the Brandaris 128 camera's casing had to be aligned and coupled to the output port of the microscope's main body. This was achieved by fixing a laser pointer on the casing of the Brandaris 128 to project onto a target on the microscope body. Further, to reproduce alignment, the position of both systems with respect to the room was documented using a laser distance measuring tool (GLM 40, Bosch, Stuttgart, Germany). A second requirement was parfocality; that is, the Brandaris 128 and the confocal need to have the same focal plane. To that end, a range extender (XT2 Collimating Emission-Port Adaptor, Photometrics, Tucson, AZ, USA) was inserted in the light path between the output port of the microscope and the Brandaris 128 input port.

When fast switching between confocal imaging and Brandaris 128 acquisition is desired, a Multifunction I/O Device (USB-6000, National Instruments, Austin, TX, USA) can trigger the motorized turret to rotate the full mirror into the light path, temporarily intercepting timelapse confocal imaging to acquire with the Brandaris 128 camera instead. The trigger is given when the rotating mirror in the Brandaris 128 reaches a desired rotation speed. Once the Brandaris 128 acquisition is complete, another trigger is given to remove the mirror from the light path, such that confocal imaging is restored. The confocal recording is intercepted at least for the duration of consecutive Brandaris 128 recordings and the mechanical turret rotation time of 300 ms. The trigger events and turbine speeds are registered in the confocal recording for correct data registration.

The capabilities of the combined Brandaris 128 and confocal microscopy imaging system are demonstrated with three *in vitro* experiments: endothelial drug delivery, bacterial biofilm disruption, and microbubble coating microstructure alterations. The microbubbles used in the experiments were all in-house produced by probe sonication as previously described [88]. Briefly, the main lipid of the coating was 1,2-distearoyl-*sn*-glycero-3-phosphocholine and the microbubbles had a C_4F_{10} gas

core. All images were acquired with a 100× objective (CFI Plan 100XC W, Nikon Instruments) that is chromatic aberration-free infinity (CFI), corrected for field curvature (Plan) and water dipping (W). This objective has a numerical aperture of 1.10; therefore, the resolution achieved with confocal microscopy is 250 nm. The confocal scan speed varies from 0.03 – 1 fps per acquisition channel, depending on the chosen pixel dwell time. By decreasing the field of view, we can image up to 5 fps. From the Brandaris 128 ultra-high-speed recordings, the microbubble radius as function of time was determined using custom-designed image analysis software [74]. During the endothelial drug delivery and biofilm disruption experiments, the sample was inserted in the water tank at 37°C (Fig. 5.2) and insonified with a single-element focused transducer (2.25 MHz center frequency, 76.2 mm focal length, -6 dB beam width at 2 MHz of 3 mm; V305, Panametrics-NDT, Olympus, Waltham, MA, USA). When the microbubble coating was studied, the sample was inserted in the water tank at room temperature and insonified with a single-element broadband transducer (1 to 9 MHz bandwidth, 25 mm focal distance, -6 dB beam width at 1 MHz of 1.3 mm; PA275, Precision Acoustics, Dorchester, U.K.).

5.3. RESULTS

In the first experiment, the response of human umbilical vein endothelial cells to $\alpha_v\beta_3$-targeted microbubbles upon ultrasound insonification was imaged. Acquisition started with confocal microscopy time-lapse imaging (0.65 fps, CFI Plan 100×W objective), revealing the initial state of the cells and the location of the microbubble (Fig. 5.3A). Next, the light path was automatically switched toward the Brandaris 128 to record microbubble oscillation during ultrasound insonification (2 MHz, 250 kPa peak-negative-pressure [PNP], single 10-cycle burst) (Fig. 5.3B). This temporarily intercepted confocal microscopy imaging until the Brandaris 128 recording finished and the light path was switched back. Confocal microscopy imaging proceeded for 3.5 min after ultrasound, monitoring the cellular response (Fig. 5.3C). Uptake of propidium iodide was observed locally around the microbubble (Fig. 5.3C, 00:30 – 00:44), followed by diffusion throughout the cytoplasm and into the nucleus (Fig. 5.3C, 02:25). Moreover, confocal microscopy imaging revealed opening of the intercellular junctions (Fig. 5.3C, 02:25 – 03:50, arrows).

The second experiment started with confocal microscopy time-lapse imaging (0.32 fps, CFI Plan 100×W objective) of a Staphylococcus aureus biofilm. This revealed vancomycin-targeted microbubbles adhered to bacteria (Fig. 5.4A). Confocal time-lapse imaging was temporarily intercepted to record microbubble oscillation with the Brandaris 128 upon ultrasound insonification (2 MHz, 250 kPa PNP, single 10,000-cycle burst). After the Brandaris 128 recording, the light path was switched back and confocal imaging continued for 40 s. Confocal microscopy imaging after insonification revealed microbubbles had clustered (Fig. 5.4C). Moreover,

bacteria detached in the area where microbubbles were originally located, revealing microbubble–mediated disruption of the biofilm (Fig. 5.4C, 0:22, arrows). Toward the end of the confocal recording, partial redisposition of bacteria was observed (Fig. 5.4C, 00:57).

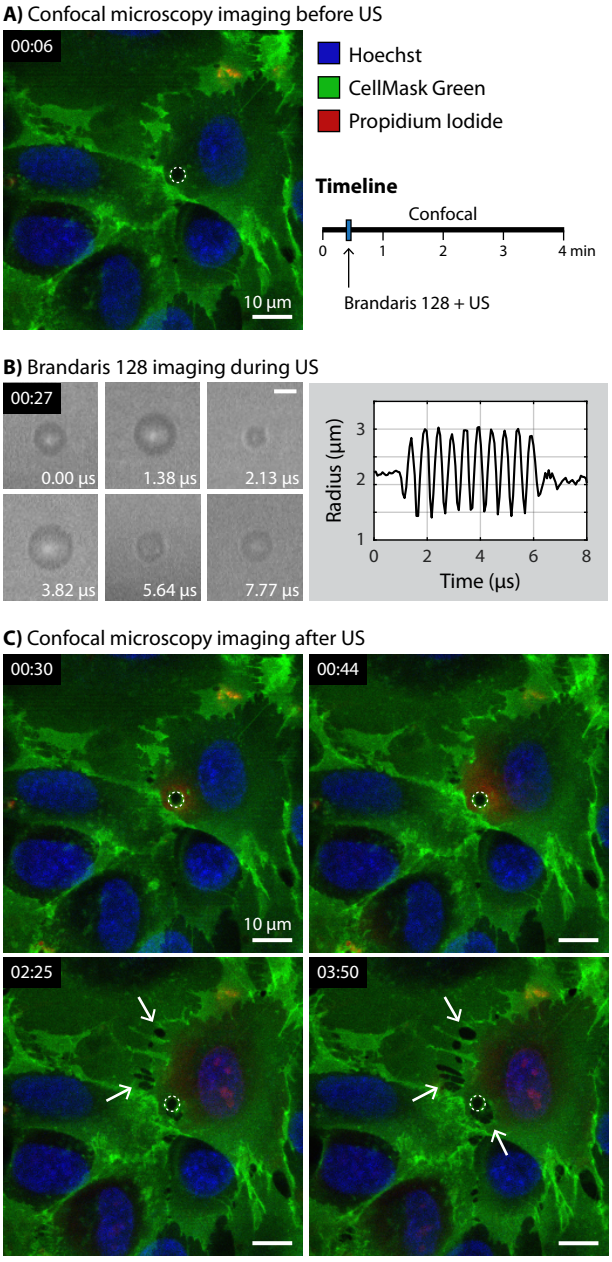

Figure 5.3: Selected frames from time-lapse imaging of microbubble-mediated endothelial drug delivery. Human umbilical vein endothelial cells (Lonza, Verviers, Belgium) were grown in MV2 medium (PromoCell GmbH, Heidelberg, Germany) to confluency for 2 d in a CLINIcell (50 µm membrane; Mabio, Turcoing, France). The cell nuclei were stained with Hoechst (5 µg/mL; Thermo Fisher Scientific, Waltham, MA, USA), the cell membranes with CellMask Green (4 µg/mL; Thermo Fisher Scientific), and sonoporation with propidium iodide (25 µg/mL; Sigma-Aldrich, St. Louis, MO, USA). The dashed line delineates the microbubble. (**A**) Confocal microscopy before ultrasound (US) to image the initial cell state. (**B**) Microbubble oscillation recorded with the Brandaris 128 ultra-high-speed camera (bar = 3 µm) and the microbubble radius as a function of time determined from this recording. (**C**) Confocal microscopy after US to image cellular response. The arrows indicate opening of intercellular junctions.

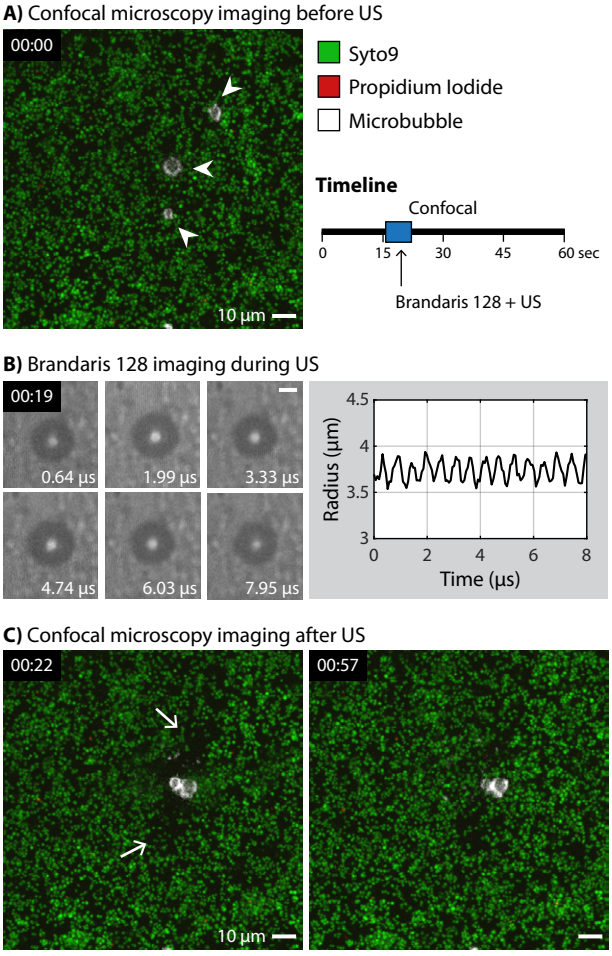

Figure 5.4: Selected frames from time-lapse imaging of microbubble -mediated biofilm disruption. A clinical isolate of *Staphylococcus aureus* (SA25268) was grown in IMDM medium (Thermo Fisher Scientific) for 24 h in an ibiTreat µ-slide (0.8 mm channel height; I Luer; Ibidi GmbH, Martinsried, Germany). The live bacteria were stained with SYTO 9 (4 µg/mL; Thermo Fisher Scientific), the dead bacteria with propidium iodide (25 µg/mL; Sigma-Aldrich) and the microbubble shell with DiD (Thermo Fisher Scientific). (**A**) Confocal microscopy before ultrasound (US) to image the initial biofilm and microbubbles (arrowheads). (**B**) The oscillation of the microbubble located in the center of (**A**) was recorded with the Brandaris 128 ultra-high-speed camera (bar = 3 µm). The microbubble radius as a function of time was extracted from this recording. (**C**) Confocal microscopy after US to image biofilm disruption (arrows).

The third experiment aimed to image the microbubble coating microstructures before and after ultrasound insonification. Before ultrasound, a z-stack was acquired (0.4 µm step size, 31 slices, CFI Plan 100×W objective) of a microbubble that also contained rhodamine-B-1, 2-dihexadecanoyl-*sn*-glycero-3-phosphoethanolamine, triethylammonium salt (rhodamine-DHPE). The 3D image (Fig. 5.5A) revealed that the lipid expanded phase, as stained by the rhodamine-DHPE [175], was distributed in a characteristic honeycomb pattern. Next, Brandaris 128 ultra-high-speed imaging revealed microbubble oscillation (Fig. 5.5B) upon ultrasound insonification (1.4 MHz, 50 kPa PNP, single 8-cycle burst). After ultrasound, another z-stack was acquired revealing structural changes in the microbubble coating (Fig. 5.5C, arrows).

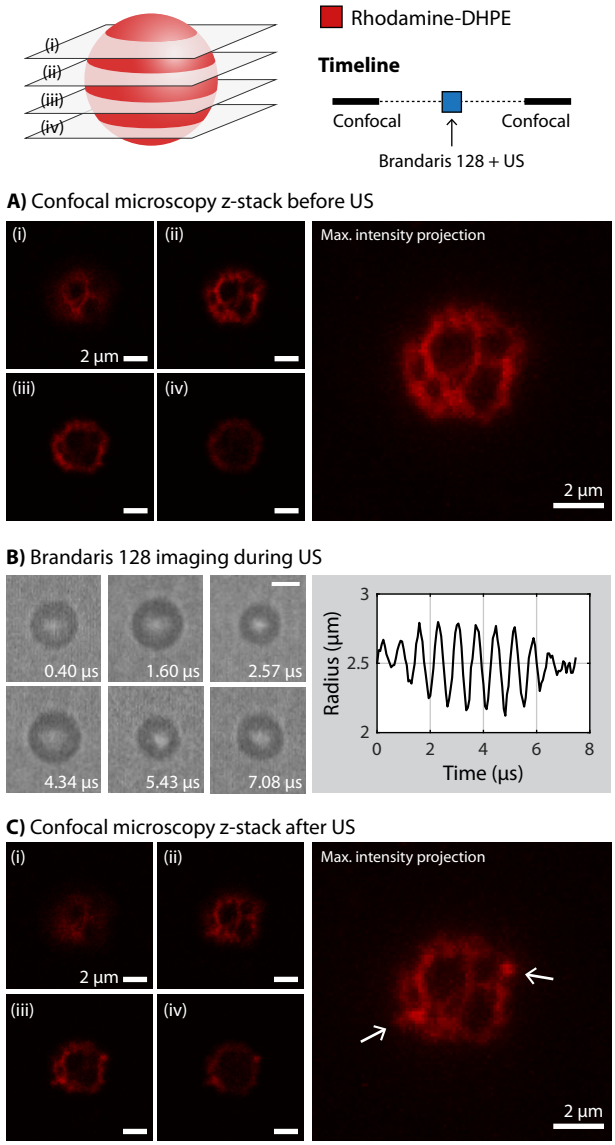

Figure 5.5: Imaging of structural changes in microbubble coating. The lipid-expanded phase was stained with rhodamine-DHPE (0.01 mol%; Thermo Fisher Scientific). Microbubbles were studied in a CLINIcell (50 µm membrane; Mabio). (**A**) Selected z-slices from 3D confocal microscopy (i-iv) and the maximum intensity projection before ultrasound (US). (**B**) Selected frames of the Brandaris 128 ultra-high-speed recording revealing microbubble oscillation (bar = 3 µm) and the resulting microbubble radius as a function of time. (**C**) Selected z-slices (i-iv) and maximum intensity projection after US. The arrows indicate a focal area of increased fluorescence intensity (i.e., hot spot) suggestive of local microbubble shell buckling.

5.4. DISCUSSION

The novel combined confocal microscope and Brandaris 128 ultra-high-speed camera make it possible to study both the cell and microbubble structures with nanometer spatial resolution and the microbubble oscillation with nanosecond temporal resolution, as demonstrated with the three experiments. With this unique device we were able for the first time to relate microbubble oscillation behavior to alterations in cell integrity and microbubble coating microstructures.

Microbubble-mediated endothelial drug delivery (Fig. 5.3) monitored with confocal microscopy provides better detector sensitivity and higher frame rates than the widefield microscope originally coupled to the Brandaris 128. As a result, low and fast changes of local propidium iodide uptake caused by sonoporation can now be detected. This is essential when studying safe drug delivery because low uptakes have been associated with reversible sonoporation and cell viability [40]. Moreover, specific fluorescent cell dyes can now be imaged with high resolution, revealing previously concealed cellular responses. For example, we were able to observe the opening of intercellular junctions using a cell membrane dye (Fig. 5.3C).

The advantage of high-resolution confocal microscopy is also demonstrated when imaging biofilm disruption by oscillating microbubbles (Fig. 5.4). Because of the small size of bacteria ($\backsim$1 μm in diameter), they cannot be well resolved with widefield microscopy. The added value of this new optical system is that we can now distinguish individual bacteria and observe effects on biofilms caused by oscillating microbubbles, while also gaining insight into how microbubbles vibrate nearby a biofilm. Furthermore, the light path switching is quick enough to observe the disruption of the biofilm before redisposition of bacteria occurs (Fig. 5.4C). However, this data set also reveals a drawback of the Brandaris 128 ultra-high-speed camera recordings. Because a maximum of 128 frames can be acquired, it is only possible to partially image the 10,000-cycle microbubble oscillation. Therefore, in this Brandaris 128 acquisition, the microbubble clustering was not observed (Fig. 5.4B) and could only be inferred from the confocal microscopy after ultrasound (Fig. 5.4C).

The developed optical imaging system will be essential not only in understanding ultrasound-mediated drug delivery, but also in designing ultrasound contrast agents. We can finally image how microbubble oscillation behavior affects the structural organization of the coating and vice versa. Although 4Pi microscopy has higher axial resolution and overcomes the signal loss toward the part of the microbubble furthest away from the objective (Fig. 5.5, iv), because of the laser diffraction by the microbubble's gas core, we were able to discern the coating microstructures with the confocal microscope (Fig. 5.5). To date, lipid shedding and buckling of the phospholipid shell caused by microbubble oscillation has been observed only using widefield fluorescence microscopy, at 150,000 fps [176] or 5 Mfps [177]. However, because of the poor axial resolution of widefield microscopy, structural details of the phospholipid shell could not be resolved.

Simultaneous Brandaris 128 and confocal microscopy imaging is not possible with the combined system. This technical limitation remains as the Brandaris 128 requires 100% of the light path to overcome the CCD detection limits. Automatic switching between confocal and Brandaris 128 imaging minimizes the time during which confocal microscopy imaging is interrupted. It is difficult to precisely predict the start of a Brandaris 128 acquisition, as the acceleration of the turbine is variable.

Therefore, confocal microscopy is often interrupted about 2 s before the Brandaris 128 recording starts. During this time no change is expected in the confocal image, because insonification has not taken place yet. As soon as the Brandaris 128 acquisition has completed, during which ultrasound was applied, the full mirror is rotated out of the light path. As a result, the confocal microscope can restore imaging to detect rapid cellular effects with a maximum delay of 300 ms plus the time to scan a confocal frame (which depends on the confocal scan speed chosen). For the endothelial drug delivery example, this corresponded to <1.8 s, and for the biofilm disruption example, this was <3.4 s.

The confocal microscope can image a larger field of view than the Brandaris 128 ultra-high-speed camera. For instance, with the CFI Plan 100×W objective, the field of view of the confocal microscope is 128×128 μm and that of the Brandaris 128 is 45×32 μm. Hence, as seen in Figure 5.4, sometimes microbubbles are observed in the field of view of the confocal microscope, but their oscillation cannot be recorded with the Brandaris 128. Finally, adapting the microscope's main body by removing the conventional base disabled the automatic refocusing capability. Regardless, a desired focus depth can be manually restored because the software is still able to read out the z-position of the objective.

5.5. CONCLUSION

A state-of-the-art optical imaging system was developed by coupling a custom-built confocal microscope to the Brandaris 128 ultra-high-speed camera. Microbubble-mediated drug delivery can now be studied at both high spatial and temporal resolution to evaluate cellular response upon microbubble oscillation. Additionally, changes in microbubble coating structure caused by oscillation behavior can be discerned. With this novel optical imaging system we expect to further elucidate microbubble-mediated drug delivery and advance the development of ultrasound contrast agents.

ACKNOWLEDGEMENT

This work was supported in part by the Applied and Engineering Sciences TTW (Veni-Project 13669), a part of NWO; the Erasmus MC Foundation; the Phospholipid Research Center, Heidelberg, Germany; and the Thoraxcenter of Erasmus MC. The authors thank Gert van Cappellen and Adriaan Houtsmuller from the Erasmus MC Optical Imaging Center; Willem J. B. van Wamel from the Department of Medical Microbiology and Infectious Diseases, Erasmus MC; and Alessandra Scarpellini from Nikon Instruments Europe for the fruitful discussions.

6

High-resolution imaging of intracellular calcium fluctuations caused by oscillating microbubbles

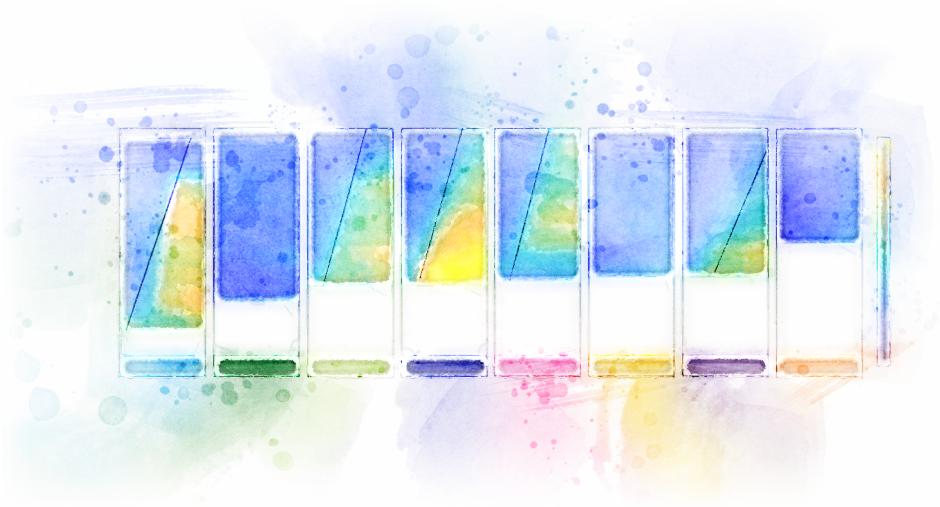

Based on:
Inés Beekers, Frits Mastik, Robert Beurskens, Phoei Ying Tang, Merel Vegter, Antonius F. W. van der Steen, Nico de Jong, Martin D. Verweij, Klazina Kooiman, "High-resolution imaging of intracellular calcium fluctuations caused by oscillating microbubbles", *Ultrasound in Medicine & Biology*, 2020 [178].

Abstract

Ultrasound insonification of microbubbles can locally enhance drug delivery, but the microbubble–cell interaction remains poorly understood. Since intracellular calcium (Ca_i^{2+}) is a key cellular regulator, unraveling the Ca_i^{2+} fluctuations caused by an oscillating microbubble provides crucial insight into the underlying bioeffects. Therefore, we developed an optical imaging system at nanometer and nanosecond resolution that can resolve Ca_i^{2+} fluctuations and microbubble oscillations. Using this system, we clearly distinguished three Ca_i^{2+} uptake profiles upon sonoporation of endothelial cells, which strongly correlated with the microbubble oscillation amplitude, severity of sonoporation, and opening of cell-cell contacts. We found a narrow operating range for viable drug delivery without lethal cell damage. Moreover, adjacent cells were affected by a calcium wave propagating at 15 μm/s. With the unique optical system, we unraveled the microbubble oscillation behavior required for drug delivery and Ca_i^{2+} fluctuations, providing new insight into the microbubble–cell interaction to aid clinical translation.

Keywords — drug delivery, microbubbles, ultrasound, intracellular calcium, sonoporation, cell-cell contact opening, confocal microscopy, high-speed imaging

6.1. INTRODUCTION

Effective disease treatment largely depends on the ability of drugs to overcome barriers imposed by the human body to reach the diseased tissue. The blood brain barrier is almost impermeable for drugs, blocking an estimated ~98% of small molecule drugs, posing a major challenge in the treatment of neurological disorders [9]. Limited drug delivery is also observed –to a lesser extent– in other tissues, e.g. chemotherapy drugs need to extravasate blood vessels and migrate through the extravascular space to reach the tumor [18, 179]. All in all, the vascular endothelium forms a major barrier to localized drug delivery. Consequently, higher drug dosages are prescribed to reach the proper efficacy level but this results in a high systemic toxicity and development of side effects. Therefore, there is a need for a novel method to facilitate efficient drug delivery to diseased tissues and thereby minimize adverse effects.

Vascular drug delivery can be locally enhanced by ultrasound insonification of lipid-coated microbubbles (1 – 10 μm in diameter) [3, 26, 180–182]. These microbubbles are widely used in the clinic to improve contrast in diagnostic ultrasound imaging and additionally have a therapeutic potential. Upon insonification, microbubbles will oscillate and can thereby stimulate the following drug delivery pathways: perforate the cell membrane (i.e. sonoporation), open intercellular junctions, and stimulate endocytosis [3, 32–34]. Moreover, oscillating microbubbles can induce intracellular calcium (Ca_i^{2+}) fluctuations [56, 67, 159,

183–187], which can propagate to adjacent cells within seconds through intercellular signaling mechanisms, causing calcium waves [188]. Since Ca_i^{2+} plays a crucial role in junction integrity, membrane resealing, and intercellular signaling, different Ca_i^{2+} fluctuations and recovery profiles correlate to post treatment cell viability [49, 59, 189].

A better understanding of when cell viability is preserved upon microbubble–mediated drug delivery is required to control the balance between high delivery efficiency and lethal cell damage, and tune this to the requirements of a therapeutic application. Thus far, the specific microbubble-cell interaction necessary for the distinct drug delivery pathways, Ca_i^{2+} fluctuations, and calcium waves remains poorly understood [33]. Elucidating the effect of an oscillating microbubble on the Ca_i^{2+} levels will help unravel the underlying physical and biological mechanisms of microbubble–mediated drug delivery, including the potential downstream biological pathways triggered upon altering Ca_i^{2+} homeostasis. A better understanding of the therapeutic potential of microbubbles will aid development towards safe and efficient widespread clinical use.

Up to now, the microbubble-cell interaction causing Ca_i^{2+} fluctuations has been investigated while focusing on the cellular response. These studies have shown that Ca_i^{2+} fluctuations induced by oscillating microbubbles can remain elevated [183, 184] or return to equilibrium within approximately 180 s [56, 59, 67, 159, 185, 186]. Additionally, these Ca_i^{2+} fluctuations can propagate to adjacent cells via calcium waves, both by means of internal messengers through gap junctions and/or by paracrine signaling through the extracellular space [188]. This intercellular communication can also occur upon an oscillating microbubble, resulting in the delayed Ca_i^{2+} transients in adjacent cells that have been observed in rat cardiomyoblasts [159], Chinese hamster ovary cells [183, 184], and endothelial cells [67].

It remains poorly understood how the spatiotemporal Ca_i^{2+} fluctuations correlate with microbubble oscillation behavior and the different drug delivery pathways. Only for Ca_i^{2+} fluctuations returning to equilibrium, the change in Ca_i^{2+} upon sonoporation has been shown to positively correlate with the final amount of propidium iodide (PI) uptake upon sonoporation, as observed in rat cardiomyoblasts [159]. In human endothelial cells, microbubble-induced Ca_i^{2+} fluctuations have been reported [67, 185], but lacking information on single cell response, microbubble location and behavior, and a direct correlation with sonoporation. Additionally, the observed Ca_i^{2+} fluctuations always returned to equilibrium within ~180 s and calcium waves were only shown for a single example, without further quantification. At present, it remains unknown how the spatiotemporal behavior of Ca_i^{2+} fluctuations relates to microbubble-mediated opening of cell-cell contacts. Live cell microscopy imaging of cell-cell contact opening by an oscillating microbubble has only been reported once before in literature, for a single example and without Ca_i^{2+} imaging [53]. None of the

previous studies were able to resolve the specific microbubble oscillation that induced the Ca_i^{2+} fluctuations and therefore the microbubble-cell interaction was never fully elucidated. Moreover, microbubble-induced Ca_i^{2+} fluctuations have only been imaged at low spatial resolution (widefield microscopy) and at a temporal resolution up to 1.7 fps (frames per second) [184], such that calcium wave propagation was poorly resolved.

To unravel the microbubble-cell interaction mechanisms, we developed a novel optical imaging system consisting of the Brandaris 128 ultra-high-speed camera, to image microbubble oscillation at nanosecond temporal resolution, coupled to a custom-built Nikon A1R+ confocal microscope, to resolve cellular response at nanometer spatial resolution. The endothelial cell response upon insonification of a single targeted microbubble was evaluated by monitoring the spatiotemporal fluctuations of Ca_i^{2+}, uptake of propidium iodide (PI) as a marker for sonoporation, and opening of cell-cell contacts. As a result, the microbubble-cell interaction was studied at both nanosecond and nanometer resolution.

6.2. MATERIALS AND METHODS

Endothelial cell culture

Pooled primary human umbilical vein endothelial cells (HUVECs; C2519A, LOT437550, Lonza, Verviers, Belgium) were cultured in MV2 medium (C22121, PromoCell GmbH, Heidelberg, Germany), supplemented with 1% Penicillin-Streptomycin (15140122, Gibco, Thermo Fisher Scientific, Waltham, MA, USA). The HUVECs were grown to full confluency in T75 flasks (at 37° C and 5% CO_2) in a humidified incubator before detaching them using Accutase solution (A6964, Sigma-Aldrich, St. Louis, MO, USA). The cells were then plated into acoustically characterized CLINIcells [160] (membrane thickness 50 μm; CLINIcell25-50-T, Mabio, Tourcoing, France) and grown for two days into a fully confluent cell monolayer. The medium was refreshed the day after plating. In total, 14 CLINIcells were cultured for experiments with ultrasound and microbubbles, 4 CLINIcells for ultrasound only experiments (i.e. without microbubbles), 3 CLINIcells for sham experiments (i.e. without microbubbles or ultrasound), and 1 CLINIcell for the $\alpha_v\beta_3$-targeted microbubble specificity experiment described below.

Microbubble preparation

Lipid-coated microbubbles with a C_4F_{10} gas core were made by 1 min probe sonication, as described previously [93]. The coating consisted of 1,2-distearoyl-sn-glycero–3-phosphocholine (DSPC; 84.8 mol%; P6517, Sigma-Aldrich), polyoxyethylene-40-stearate (PEG-40 stearate; 8.2 mol%; P3440, Sigma-Aldrich), 1,2–distearoyl–sn–glycero–3–phosphoethanolamine–N–[carboxy(polyethylene glycol)–2000] (DSPE-PEG(2000); 5.9 mol%; PEG6175.0001, Iris Biotech GmbH, Marktredwitz, Germany), and 1,2–distearoyl–sn–glycero–3–phosphoethanolamine–N–[biotinyl(polyethylene glycol)–2000] (DSPE–PEG(2000)–biotin; 1.1 mol%; 880129C, Avanti Polar Lipids, Alabaster, AL, USA). Next, microbubbles were washed three times by centrifugation (400 *g*, 1 min) and counted with a Coulter Counter Multisizer 3 (20 µm aperture tube, Beckman Coulter, Mijdrecht, the Netherlands). To target the microbubbles to the integrin $\alpha_v\beta_3$ (also known as CD51/61), they were functionalized using biotin-streptavidin bridging [135]. Briefly, 6×10^8 microbubbles were incubated on ice for 30 min with 60 µg streptavidin (S4762, Sigma-Aldrich), washed once, and incubated on ice for 30 min with 6 µg of biotinylated anti-human CD51/61 antibody (304412, BioLegend, San Diego, CA, USA), and washed once again. Control microbubbles were produced by substituting the CD51/61 antibody for its biotinylated isotype control (2600520, Sony Biotechnology, San Jose, CA, USA).

$\alpha_v\beta_3$-targeting specificity assays

The expression of $\alpha_v\beta_3$ by HUVEC was evaluated with the following immunohistochemistry assay. The cells cultured in a CLINIcell were fixated for 20 min with 4% formaldehyde, washed three times with PBS, and blocked for 30 min with 5% goat serum (G6767, Sigma-Aldrich). After removing the blocking solution, 2×3 cm pieces were cut from the CLINIcell membrane with cells. These pieces were incubated overnight at 4° C with primary antibody biotinylated anti-human CD51/61 (diluted 1:100, 304412, BioLegend). After washing with 0.5% Tween-20, we blocked again for 30 min with 5% goat serum. Next, the HUVEC were incubated for 60 min with secondary antibody anti-mouse Alexa Fluor 488 (diluted 1:100, A-11029, Thermo Fisher Scientific), washed three times with 0.5% Tween-20 and incubated for 5 min with Hoechst 33342 (5 µg/ml final concentration, H3570, Thermo Fisher Scientific) to stain the cell nuclei. The samples were mounted on a microscope slide in 100 µl of Vectashield Hardset (H-1400, Vector Laboratories, Burlingame, CA, USA). Specificity of the primary antibody CD51/61 was assessed by substituting the antibody for the biotinylated IgG1-κ isotype control (diluted 1:100, 2600520, Sony Biotechnology). The expression was visualized with confocal microscopy (60× objective, A1R+, Nikon Instruments, Amsterdam, the Netherlands). Finally, also the microbubble targeting specificity was assessed by adding either $\alpha_v\beta_3$-targeted microbubbles or control

microbubbles to a CLINIcell (2×10^6 microbubbles/ml) and counting the number of microbubbles bound to the live HUVEC in 20 different fields of view (202 × 143 μm) using brightfield microscopy imaging and a 60× water dipping objective (CFI Plan Apochromat VC 60XC WI, Nikon Instruments).

Experimental set-up

Fig. 6.1 shows a schematic of the developed optical imaging system, consisting of the Brandaris 128 ultra-high-speed camera [6] (up to 25 million frames per second, Mfps) coupled to a custom-built Nikon A1R+ confocal microscope [167]. The integrated experimental set-up for simultaneous imaging and ultrasound insonification is also illustrated in Fig. 6.1, showing the HUVEC cultured on the bottom membrane of a CLINIcell, placed in a water bath at 37° C and insonified from below. A single element focused transducer (2.25 MHz center frequency, 76.2 mm focal length, -6 dB beam width at 2 MHz of 3 mm, V305, Panametrics-NDT, Olympus, Waltham, MA, USA) was mounted in the water bath at a 45° angle, to avoid standing wave buildup. The transducer output was calibrated in a separate experiment using a needle hydrophone (1 mm diameter, PA2293, Precision Acoustics, Dorchester, UK). The ultrasound and optical foci were aligned using a pulse-echo approach and a needle tip located at the optical focal plane [7]. A single 2 MHz and 10-cycle burst was generated by an arbitrary waveform generator (33220A, Agilent, Palo Alto, CA, USA). A broadband amplifier (ENI A-500, Electronics & Innovation, Rochester, NY, USA) was used to obtain peak negative pressures (PNP) of 100, 250, and 400 kPa. These ultrasound settings (MI < 0.3) were chosen to cause stable cavitation, while avoiding jetting and build-up of acoustic streaming. Using a 100× water dipping objective (CFI Plan 100XC W, 2.5 mm working distance, Nikon Instruments), a field of view of 128×128 μm (512×512 pixels, 0.25 μm/pixel) was imaged at 5 frames per second (fps) with the confocal microscopy resonant scanner. The system can automatically switch between confocal microscopy and Brandaris 128 ultra-high-speed imaging by triggering a motorized turret to rotate a full mirror into and out of the light path.

Live cell experimental protocol

For live confocal microscopy imaging, the HUVEC were stained with fluorescent dyes, while remaining in the MV2 culture medium. First, they were incubated for 10 min with 4 μg/ml CellMask Deep Red (C10046, Thermo Fisher Scientific) to stain the cell membrane and 1.8 μM Fluo-4 (F14201, Invitrogen, Carlsbad, CA, USA) to evaluate the intracellular calcium (Ca_i^{2+}) concentration. Then the cells were incubated for 5 min with 2×10^5 microbubbles/ml, 5 μg/ml Hoechst 33342 to stain the nuclei, and 25 μg/ml propidium iodide (PI; P4864, Sigma-Aldrich) as a marker for sonoporation. The cell membrane of viable cells is impermeable for PI. When the cell membrane is compromised, PI enters the cell, binds to DNA and RNA, and becomes

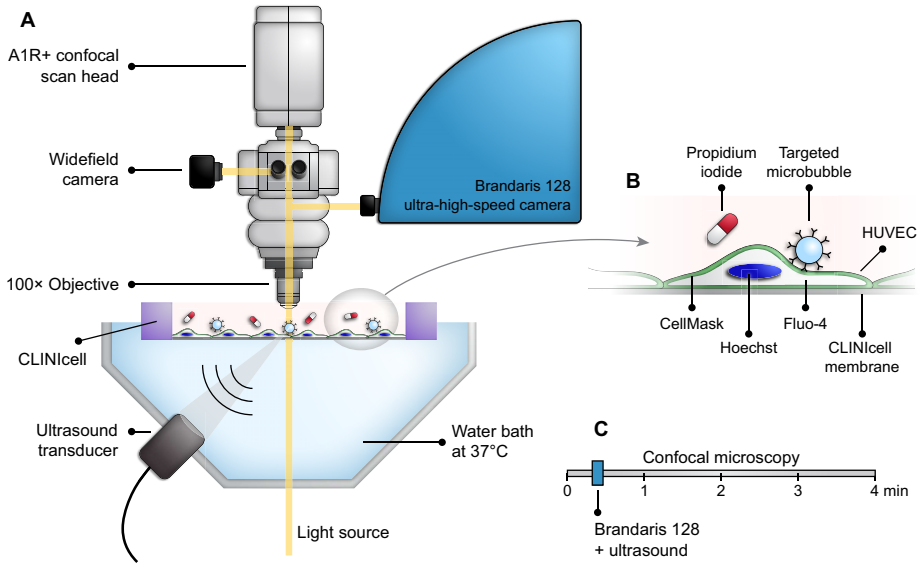

Figure 6.1: Schematic of the experimental set-up (not drawn to scale). (**A**) The optical imaging system consisted of the Brandaris 128 ultra-high-speed camera, an A1R+ confocal microscope, and a DS-Fi3 (Nikon Instruments) color camera for widefield imaging. The HUVEC were cultured on the bottom membrane of a CLINIcell and the top membrane was removed just before inserting the CLINIcell in the water bath at 37° C. Ultrasound insonification occurred under a 45° angle, after alignment of the ultrasound and optical foci. (**B**) The HUVEC nuclei were stained with Hoechst (pseudo-colored in blue), the cell membranes with CellMask Deep Red (pseudo-colored in green), and the intracellular calcium with Fluo-4 (pseudo-colored in white). Propidium iodide (pseudo-colored in red) was added to the medium as a marker for sonoporation. The $\alpha_v\beta_3$-targeted microbubbles were bound to the HUVEC. (**C**) Timeline of the imaging procedure with the combined optical imaging system and ultrasound insonification.

fluorescent [35]. Therefore, PI is often used as a marker for sonoporation to evaluate membrane perforation [38, 40, 43, 53, 58, 127, 190, 191]. During the last incubation step the CLINIcell was turned upside down to allow the targeted microbubbles to float towards the cells to achieve binding. Subsequently, the CLINIcell was turned upright again, such that only the bound targeted microbubbles remained in the focal plane of the cells. The top membrane without cells was cut from the CLINIcell to image with the 100× objective from above. In sham (i.e. without microbubbles and ultrasound) and ultrasound only (i.e. without microbubbles) experiments the same incubation timeline was used, but without adding microbubbles. In each CLINIcell, a maximum of 15 locations spaced by at least 1 cm were imaged within 2 h. At each location, there was only one single targeted microbubble in the field of view. In addition, this targeted microbubble was located on a cell that was completely within the field of view and this cell had a single nucleus that did not overlap with neighboring cells. Confocal microscopy time-lapse imaging was performed during 4 min using the following four channels: (1) Hoechst excited at

405 nm, detected at 450/50 nm (center wavelength/bandwidth), pseudo-colored in blue; (2) Fluo-4 excited at 488 nm, detected at 525/50 nm, pseudo-colored in white; (3) PI excited at 561 nm, detected at 595/50 nm, pseudo-colored in red; and (4) CellMask Deep Red excited at 640 nm, detected at 700/70 nm, pseudo-colored in green. Channel (1) and (4) were imaged simultaneously since there was no spectral overlap. Imaging started before insonification to visualize the initial cell state. Then, the system automatically switched to the Brandaris 128 ultra-high-speed camera to record microbubble oscillation during insonification at ~17 Mfps under brightfield illumination. Once this acquisition was completed, confocal microscopy time-lapse imaging was automatically restored within 500 ms after the Brandaris 128 acquisition to observe the local cellular response during > 210 s.

Brandaris 128 image processing

Microbubble oscillation was quantified using custom-designed image analysis software to determine the change in radius as a function of time [74]. Microbubble oscillation amplitude was defined as the difference between the maximum radius (R_{max}) and the initial radius (R_0; determined from the first 10 frames without ultrasound). The oscillation amplitude thresholds for sonoporation and irreversible Ca_i^{2+} fluctuations were determined by linear discriminant analysis [53].

Confocal microscopy image analysis

The cellular response after ultrasound was evaluated for sonoporation, opening of cell-cell contacts, and Ca_i^{2+} fluctuations. First of all, when the PI intensity increased upon insonification, the cell was classified as *sonoporated*. Secondly, when the CellMask signal showed a gap forming between the cell and its neighbor(s), the cell was classified as undergoing *opening of cell-cell contacts*. Finally, changes in Fluo-4 intensity in the cell were evaluated to classify Ca_i^{2+} fluctuations as described below. To quantitatively assess the local cellular response, custom-built image analysis software was used to manually register the microbubble location and delineate the cell with the targeted microbubble and all its adjacent neighbors. In case of opening of cell-cell contacts, the cell delineation was adjusted as a function of time to account for cell movement. All analyses were performed with MATLAB (MathWorks, Natick, MA, USA).

Quantification of sonoporation

Sonoporation was quantified by the amount of PI uptake to determine the pore size and resealing properties, as mathematically described by Fan et al. [38]. The fluorescence intensity $F(t)$ was defined as the sum of PI fluorescence intensity of all the pixels within the delineated cell area after ultrasound minus the mean PI fluorescence intensity before ultrasound. Using a non-linear least squares approach in MATLAB, the $F(t)$ was fitted to

$$F(t) = \frac{\alpha}{\beta}\left(1 - e^{-\beta t}\right) \tag{6.1}$$

where α is the pore size coefficient and β the pore resealing coefficient. The $F(t)$ reaches an asymptotic value when PI uptake stabilizes, caused by pore resealing. The sonoporated cells were classified as previously described by van Rooij et al. [40]. Briefly, when 90% of the asymptotic value of $F(t)$ was reached in less than 120 s or not, the sonoporated cells were classified as resealing < 120 s or non-resealing, respectively. Cells that resealed within 120 s were additionally classified using Principal Component Analysis into low PI, with small pore sizes and high pore resealing coefficients, and high PI, with large pore sizes and low pore resealing coefficients. Large pores that reseal insufficiently will cause more severe cell damage. To quantify this severity of sonoporation, a pore damage coefficient was defined as the ratio between the pore size coefficient (α) and the pore resealing coefficient (β).

Quantification of intracellular calcium (Ca_i^{2+}) fluctuations

The Ca_i^{2+} fluctuations were quantified based on the relative Ca_i^{2+} level, defined as the mean Fluo-4 fluorescence intensity after ultrasound normalized to the mean Fluo-4 fluorescence intensity before ultrasound, within the delineated cell area. The noise level for Ca_i^{2+} fluctuations was determined from the maximum relative Ca_i^{2+} level in control experiments (sham and ultrasound only). We found that the Fluo-4 intensity could increase up to an average of 30% in control experiments, due to for instance changes in cell loading or shifting of the focal plane. To quantitatively assess the cellular response, a Ca_i^{2+} fluctuation was defined as an increase of the Fluo-4 fluorescence intensity by more than 60% (twice the noise level) during at least 2 s. This corresponds to a relative Ca_i^{2+} level >1.6. This quantification led to the following four classes of Ca_i^{2+} fluctuations: (i) Stable when the relative Ca_i^{2+} level did not increase above the 1.6 threshold during 2 s; (ii) <180s when the relative Ca_i^{2+} level increased above 1.6 during 2 s and decreased below this threshold within 180 s; (iii) >180s when the relative Ca_i^{2+} level increased above 1.6 during 2 s and remained above this threshold after 180 s; and (iv) Clusters when the relative Ca_i^{2+} level increased above 1.6 during 2 s, then quickly dropped, and only a granular-like fluorescence pattern of Ca_i^{2+} remained in the cell.

Quantification of calcium waves

To determine if a calcium wave was induced upon sonoporation, the relative Ca_i^{2+} level in the adjacent cells was monitored in fields of view with a single sonoporated cell (n=55). When the relative Ca_i^{2+} level in an adjacent cell was >1.6 during at least 2 s, this cell was labelled as affected. The fraction of affected cells in a calcium wave is a measure of the extent of disturbance caused by the wave and was defined as the ratio between the number of affected adjacent cells and the total number of adjacent cells. Next, to quantify the speed at which the calcium wave propagated towards adjacent cells, we considered it as a spherical wave propagating outwards from its origin at the microbubble location. In order to do so, the field of view was converted to a spherical coordinate system centered at the microbubble and segmented into radial bands of 1 µm. On average, the field of view was split up in 59 radial bands. The mean relative Ca_i^{2+} level in each radial band was determined for each time frame. This allowed us to quantify the calcium wave propagation in color-coded maps as a function of time and distance from the microbubble. In each radial band, the wave front arrival time was defined as the time at which the relative Ca_i^{2+} level was >1.6 and then remained elevated during at least 2 s. The slope of the linear fit through those arrival times was defined as the calcium wave front speed. Additionally, we evaluated the propagation of Ca_i^{2+} within each adjacent cell. As before, the spherical coordinate system centered at the microbubble was used to partition the field of view into radial bands of 1 µm. However, now the cell delineation of each adjacent cell was used to mask these radial bands. The mean relative Ca_i^{2+} levels in the masked radial bands were determined for each time frame. This resulted in a color-coded map as a function of time and distance from the microbubble for each adjacent cell. The wave front arrival times were again determined and the calcium wave front speed within each cell was obtained. See Supplementary Fig. 6.1 for a stepwise example of this method.

Statistical analysis

Categorical data was tested for significant differences using a Pearson's χ^2-test. Quantitative data (microbubble oscillation amplitude, pore damage coefficient, fraction of affected cells, and calcium wave front speed) were not normally distributed and thus presented in median and interquartile ranges. To test for significant differences the two-sided Mann-Whitney U test was performed. Statistical significant differences were indicated in the graphs with asterisks by using * for $p < 0.05$, ** for $p < 0.01$, and *** for $p < 0.001$. All boxplots were presented with the central line at the median, the box limits at the first and third quartile, and the whiskers ranging from the minimum to the maximum value. A Spearman's rank-order correlation was performed to determine the relationship between the microbubble oscillation amplitude and the fraction of affected cells in a calcium wave. All statistical analyses were performed with MATLAB.

6.3. RESULTS

Cellular response to a single oscillating microbubble

The cellular response to a single $\alpha_v\beta_3$-targeted microbubble (Supplementary Fig. 6.2) upon ultrasound insonification was evaluated (n=108). Selected frames of confocal microscopy and Brandaris 128 imaging are presented in Fig. 6.2, showing three distinct cellular responses caused by an oscillating microbubble. The corresponding confocal microscopy recordings can be found in Supplementary Videos 1, 2, and 3. To better distinguish PI uptake upon sonoporation, the red channel of these confocal microscopy frames is shown in Supplementary Fig. 6.3. Before ultrasound, a single targeted microbubble (arrow, Fig. 6.2) was bound to the central cell in each field of view. Confocal microscopy imaging of the initial cellular state showed that all cells were viable and had an intact cell membrane, indicated by the absence of PI (red channel, Fig. 6.2 and Supplementary Fig. 6.3). There was a similar equilibrium level of Ca_i^{2+} in all cells, as shown by the overall Fluo-4 signal (white channel, Fig. 6.2). Next, the microbubble oscillation was recorded with the Brandaris 128 ultra-high-speed camera during ultrasound and quantified as shown in Supplementary Fig. 6.4. All microbubbles remained bound to the cells during oscillation, since they were still in the same focal plane after ultrasound. After ultrasound, PI uptake (red channel, Fig. 6.2 and Supplementary Fig. 6.3) was observed locally around the microbubble location and then diffused throughout the cell, indicative of sonoporation. The time profiles of the PI intensity upon sonoporation were determined based on the red fluorescent intensity within the cell, normalized to that before ultrasound (panels on the right of Fig. 6.2). The PI intensity was highest in Fig. 6.2C, suggesting that more of this fluorescent marker was able to enter the cell through the pore created in the cell membrane than in Fig. 6.2A and B. Additionally, upon PI influx there was a simultaneous increase in Fluo-4 intensity (white channel, Fig. 6.2) in the sonoporated cell. Successively, the Fluo-4 intensity also increased in adjacent non-sonoporated cells, which is described in more detail in the section *Calcium waves*. Three distinct Ca_i^{2+} fluctuations were observed in the sonoporated cells: (i) Ca_i^{2+} increased upon sonoporation and remained elevated < 180 s, after which it returned to the initial Ca_i^{2+} level (Fig. 6.2A); (ii) Ca_i^{2+} increased upon sonoporation but did not return to the initial Ca_i^{2+} level within 180 s (Fig. 6.2B); (iii) Ca_i^{2+} increased upon sonoporation but quickly decreased and only a clustered pattern of Ca_i^{2+} remained (Fig. 6.2C and Supplementary Fig. 6.5). A high-resolution image of a typical clustered Ca_i^{2+} pattern can be found in Supplementary Fig. 6.5. For each of the Ca_i^{2+} fluctuations, the time profiles of the Fluo-4 intensity are shown in the panels on the right in Fig. 6.2. Finally, the CellMask imaging (green channel, Fig. 6.2) revealed changes in border integrity since gaps (arrowheads, Fig. 6.2) formed between the sonoporated cell and its neighbors, indicative of cell-cell contact opening. Overall, the cellular response upon ultrasound insonification of a microbubble was studied in 108 fields of view.

Intracellular calcium fluctuations upon sonoporation

The oscillating microbubble caused sonoporation in 71% of the cells (77 out of 108 cells) and sonoporation always resulted in a local increase of Ca_i^{2+} (77 out of 77 cells, Fig. 6.3A). When the oscillating microbubble caused no sonoporation, it never induced a local increase of Ca_i^{2+} (n=31, Fig. 6.3A). An increase in Ca_i^{2+} occurs upon pore formation due to a concentration imbalance, since the free calcium concentration is about 10,000-fold lower in the cytosol than outside the cell [47]. Depending on the

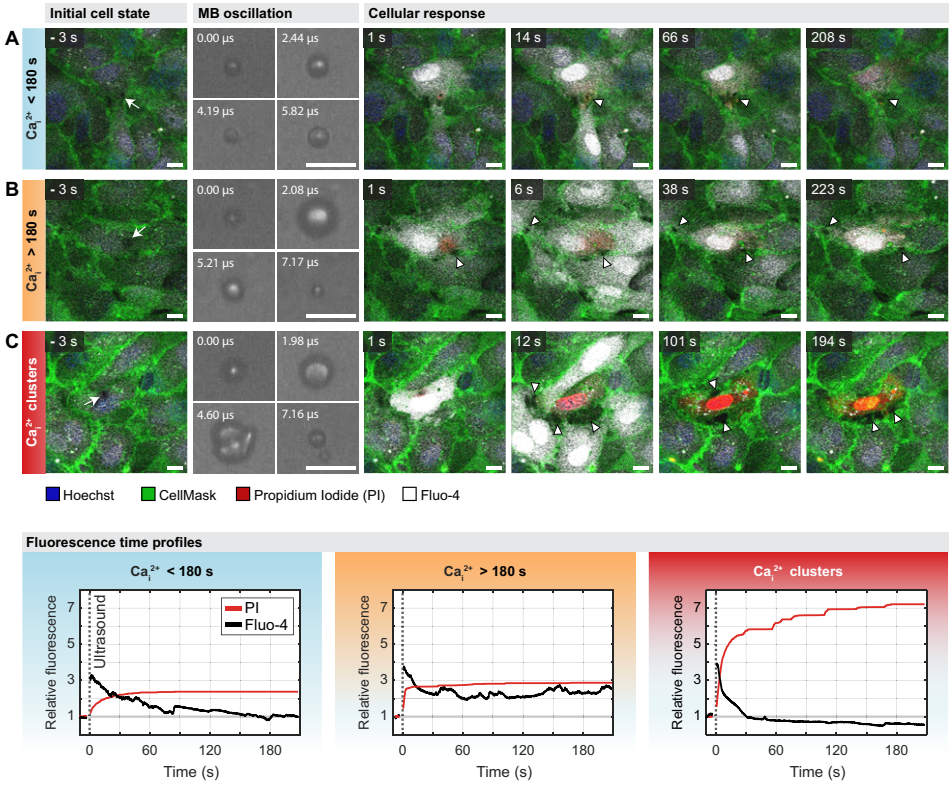

Figure 6.2: Combined Brandaris 128 ultra-high-speed imaging and confocal microscopy. Selected frames of Brandaris 128 imaging and confocal microscopy time-lapse imaging showing a single oscillating targeted microbubble (MB) that induced sonoporation, opening of cell-cell contacts (indicated with white triangles), and intracellular calcium (Ca_i^{2+}) fluctuations. The Ca_i^{2+} fluctuations either (**A**) remained elevated < 180 s, (**B**) remained elevated > 180 s, or (**C**) resulted in a clustered pattern of Ca_i^{2+}. The fluorescence intensity of propidium iodide (PI) and Fluo-4 relative to that before ultrasound are shown in the panels on the bottom. Cell nuclei in blue, cell membrane in green, PI in red, and Ca_i^{2+} in white. The microbubble location was indicated with an arrow in the initial cell state. Scale bars, 10 µm. The corresponding confocal microscopy recordings can be found in Supplementary Videos 1, 2, and 3. To better distinguish PI uptake, see Supplementary Fig. 6.3 for the red channel of confocal microscopy imaging. Radius-time curves of the respective microbubble oscillation can be found in Supplementary Fig. 6.4 and a more detailed image of the clustered pattern can be found in Supplementary Fig. 6.5.

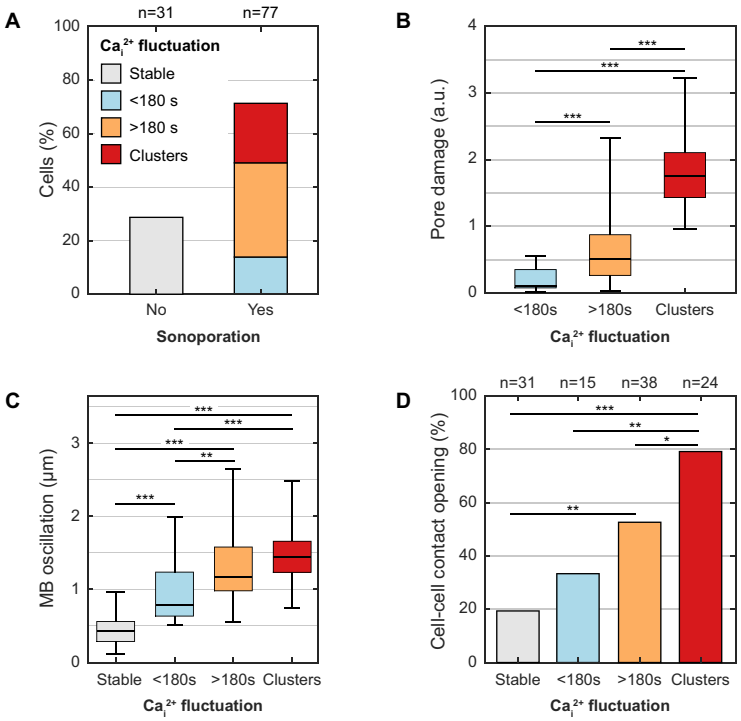

Figure 6.3: Intracellular calcium (Ca_i^{2+}) fluctuations upon sonoporation and cell-cell contact opening. (**A**) Occurrence of sonoporation and the distinct Ca_i^{2+} fluctuations upon an oscillating microbubble. (**B**) Pore damage upon sonoporation for each class of Ca_i^{2+} fluctuations. (**C**) Microbubble oscillation amplitude for each class of Ca_i^{2+} fluctuation. (**D**) Occurrence of cell-cell contact opening upon different Ca_i^{2+} fluctuations. Boxplots show the median and interquartile range and the whiskers extend from minimum to maximum value. Statistically significant differences are indicated with * for $p<0.05$, ** for $p<0.01$, and *** for $p<0.001$.

temporal evolution of the Ca_i^{2+} increase upon sonoporation, the Ca_i^{2+} fluctuations were categorized in the three distinct responses shown in Fig. 6.2. In 19% of the sonoporated cells the Ca_i^{2+} level was elevated < 180 s (n=15), in 49% of the cells Ca_i^{2+} was elevated > 180 s (n=38), and in 31% of the cells Ca_i^{2+} showed clusters (n=24). Sonoporation was never observed in sham (n=36) or ultrasound only control experiments (n=15 at 100 kPa, n=15 at 250 kPa, n=14 at 400 kPa). When there was no sonoporation, in only 1.6% of the monitored cells there was a spontaneous increase in Ca_i^{2+} levels that returned to equilibrium within 180 s (3 out of 216 cells for sham and 5 out of 264 cells for ultrasound only).

For each sonoporated cell, the pore size and pore resealing coefficients are given in Supplementary Fig. 6.6. When the pore created upon sonoporation was small and resealed within 120 s (low PI uptake), the Ca_i^{2+} levels were reversibly altered in 35% of the cells (elevated < 180 s) and Ca_i^{2+} was elevated > 180 s in the remaining 65% of these cells. These small and resealing pores never caused a clustered pattern of Ca_i^{2+}.

However, when pores were large (high PI uptake) or remained open for more than 120 s, the Ca_i^{2+} levels were mainly irreversibly altered since Ca_i^{2+} either remained elevated > 180 s (39%) or clustered (52%) (Supplementary Fig. 6.6). Because large pores with low resealing capabilities cause the most severe damage to a cell, the ratio between the obtained pore size and resealing coefficient was used as a measure for pore damage. The pore damage was significantly higher for Ca_i^{2+} fluctuations that clustered, than for those that remained elevated > 180 s (Fig. 6.3B). Additionally, the pore damage was significantly higher for both these irreversible Ca_i^{2+} fluctuations (> 180 s or clusters) than for those that returned to equilibrium < 180 s (Fig. 6.3B).

The microbubble oscillation amplitude, obtained from the Brandaris 128 ultra-high-speed recordings, ranged from 0.12 up to 2.65 μm upon insonification from 100 to 400 kPa (Supplementary Fig. 6.7). This was predominantly stable cavitation, since only 1 out of 108 microbubbles exceeded the threshold for inertial cavitation (i.e. expansion of at least twice its size during oscillation) [192]. Sonoporation was induced with microbubble oscillation amplitudes above 0.75 μm (n=77, Supplementary Fig. 6.7). As shown in Fig. 6.3C, a higher microbubble oscillation amplitude of > 1 μm was needed to irreversibly alter the Ca_i^{2+} concentration, i.e. when it was elevated for more than 180 s or resulted in clustering. This was significantly larger than the oscillation amplitude required to reversibly alter the Ca_i^{2+}, i.e. when it returned to the initial concentration within 180 s.

Opening of cell-cell contacts

In 46% of the field of view, the oscillating microbubble also induced opening of cell-cell contacts between the cell to which the microbubble was bound and its neighbors. The number of cells in which cell-cell contact opening was observed was significantly higher when the Ca_i^{2+} fluctuation in the sonoporated cell was elevated > 180 s, and even higher upon Ca_i^{2+} clustering (Fig. 6.3D). Opening of cell-cell contacts did not correlate with the amplitude of the microbubble oscillation (Supplementary Fig. 6.7). Ultrasound only without microbubbles did not enhance opening of cell-cell contacts, since that occurred as often in ultrasound only as in sham control experiments without ultrasound (7 out of 36 cells for sham; 8 out of 44 cells for ultrasound only).

Calcium waves

Upon a Ca_i^{2+} fluctuation in the sonoporated cell, an increase in the Ca_i^{2+} concentration was seen to spatially propagate from the sonoporated cell towards adjacent cells (Fig. 6.4A and Fig. 6.5A). This phenomenon is known as a calcium wave, propagating outwards from the microbubble location. By monitoring the Fluo-4 intensity in the adjacent cells, the time profiles revealed a delayed increase in Ca_i^{2+}, about 2 s after microbubble oscillation (Fig. 6.4B and Fig. 6.5B). The increase in Ca_i^{2+} in the adjacent cells was reversible, since it always returned to the equilibrium level within 180 s,

independent of the temporal evolution of the Ca_i^{2+} fluctuation in the sonoporated cell. Not all adjacent cells were equally affected in a calcium wave, some cells had a more delayed response and others were not affected at all. Fig. 6.4A shows selected frames of confocal microscopy time-lapse imaging of a calcium wave that affected 100% of the adjacent cells, since delayed Ca_i^{2+} fluctuations were observed in all cells (Fluo-4

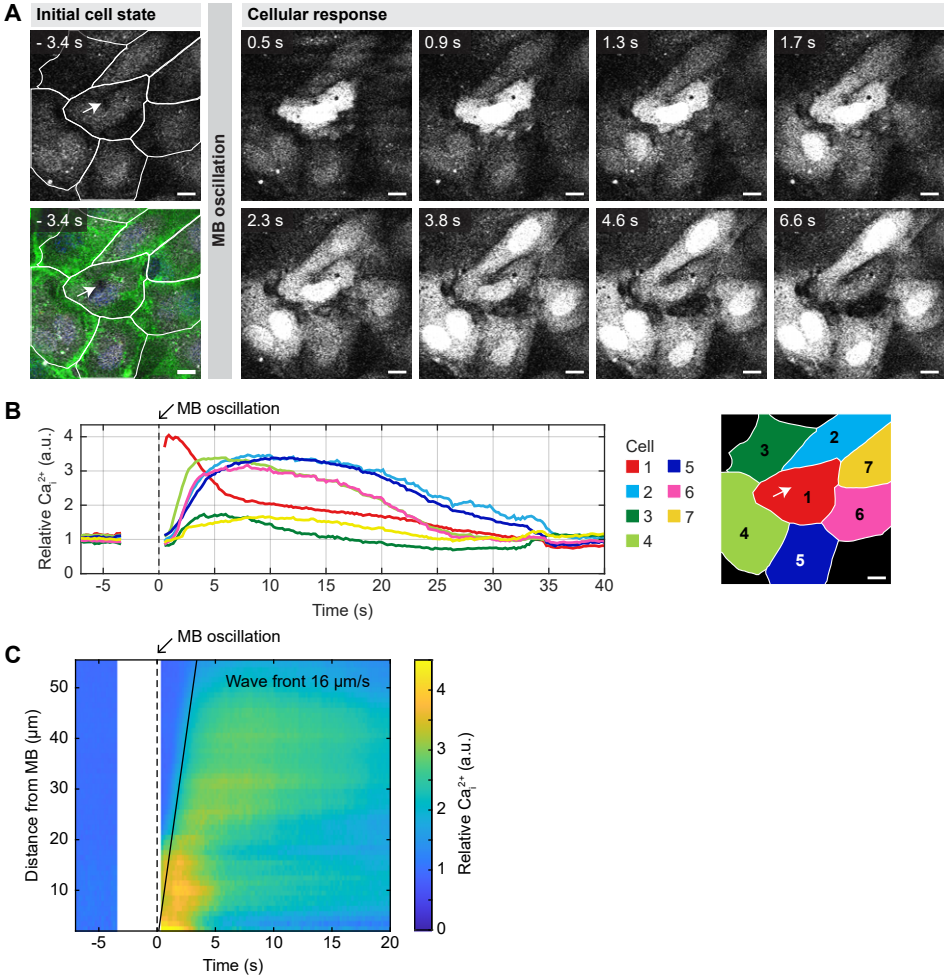

Figure 6.4: Calcium wave to all adjacent cells caused by sonoporation due to an oscillating microbubble (MB). (**A**) Selected confocal microscopy frames of intracellular calcium (Ca_i^{2+}) stained with Fluo-4, corresponding to Fig. 6.2C. The initial cell state shows the microbubble location (arrow) and cell delineation. The microbubble was insonified at 0 s. Scale bars, 10 µm. (**B**) Mean Ca_i^{2+} level in each delineated cell relative to their initial equilibrium state before MB oscillation. Since all adjacent cells showed a Ca_i^{2+} fluctuation, 100% of the cells were affected. (**C**) The resulting space-time diagram of the calcium wave. The relative Ca_i^{2+} level (i.e. normalized to that before ultrasound) is shown as a function of time and the radial distance from the microbubble. The calcium wave front (black solid line) propagated with a speed of 16 µm/s.

time profiles in Fig. 6.4B). Fig. 6.5A shows an example of a calcium wave that only affected a fraction (63%) of the adjacent cells, since delayed Ca_i^{2+} fluctuations were observed in 5 out of 8 cells (Fluo-4 time profiles in Fig. 6.5B). When Ca_i^{2+} clustered in the sonoporated cell, it resulted in a calcium wave propagating to more than half of the adjacent cells in 94% of the cases (Fig. 6.6A). When the severity of the Ca_i^{2+} fluctuation in the sonoporated cell decreased, fewer adjacent cells were affected. Additionally, the fraction of affected cells during a calcium wave positively correlated with the microbubble oscillation amplitude (Spearman correlation coefficient $\rho = 0.6$, $p < 0.001$; Fig. 6.6B).

The calcium wave front, when 100% of the adjacent cells were affected, propagated with a median speed of 15 μm/s (interquartile range 12 – 19 μm/s; n=16; Fig. 6.4C). When calcium wave propagation is considered as a spherical wave, we assume the full field of view is affected. However, when only a fraction of the adjacent cells show an increase in Ca_i^{2+}, the cells in which Ca_i^{2+} remains stable will interfere with adequate quantification of the wave front speed. Therefore, to additionally determine the speed of the *intra*cellular calcium wave, the wave front speed was also quantified within each adjacent cell. The *intra*cellular calcium wave front propagated with a median speed of 12 μm/s (interquartile range 8 – 17 μm/s; n=191; Fig. 6.5C). Since the *intra*cellular wave speed only showed a very weak correlation with the fraction of affected cells (Spearman correlation coefficient $\rho = 0.3$, $p < 0.001$), it suggests that the *intra*cellular wave front speed was independent of the number of cells affected. Finally, there was no statistically significant difference between the propagation speed computed either over the full field of view or within each adjacent cell, i.e. between the *inter*cellular and the *intra*cellular calcium wave propagation speed.

6.4. DISCUSSION

The microbubble-cell interaction necessary for sonoporation, Ca_i^{2+} fluctuations, propagation of calcium waves, and opening of cell-cell contacts was unraveled using the combined Brandaris 128 ultra-high-speed camera and confocal microscope.

By studying the microbubble-cell interaction at ultra-high temporal and high spatial resolution, we found that a microbubble oscillation amplitude > 0.75 μm was needed to induce sonoporation in endothelial cells. This threshold for a 10-cycle pulse is in the range of > 0.72 μm for a 16 cycle pulse or > 1.02 μm for an 8-cycle pulse, as previously reported for 2 MHz [53]. In addition to this, our study showed that sonoporation always resulted in an immediate Ca_i^{2+} influx through the created membrane pore, as was also found for rat cardiomyoblasts [159]. We found that the highest pore damage (large pore size and poor membrane resealing) resulted in the most severe Ca_i^{2+} fluctuations, which also strongly correlated with the microbubble oscillation amplitude. The Ca_i^{2+} fluctuation was reversible (i.e. elevated < 180 s)

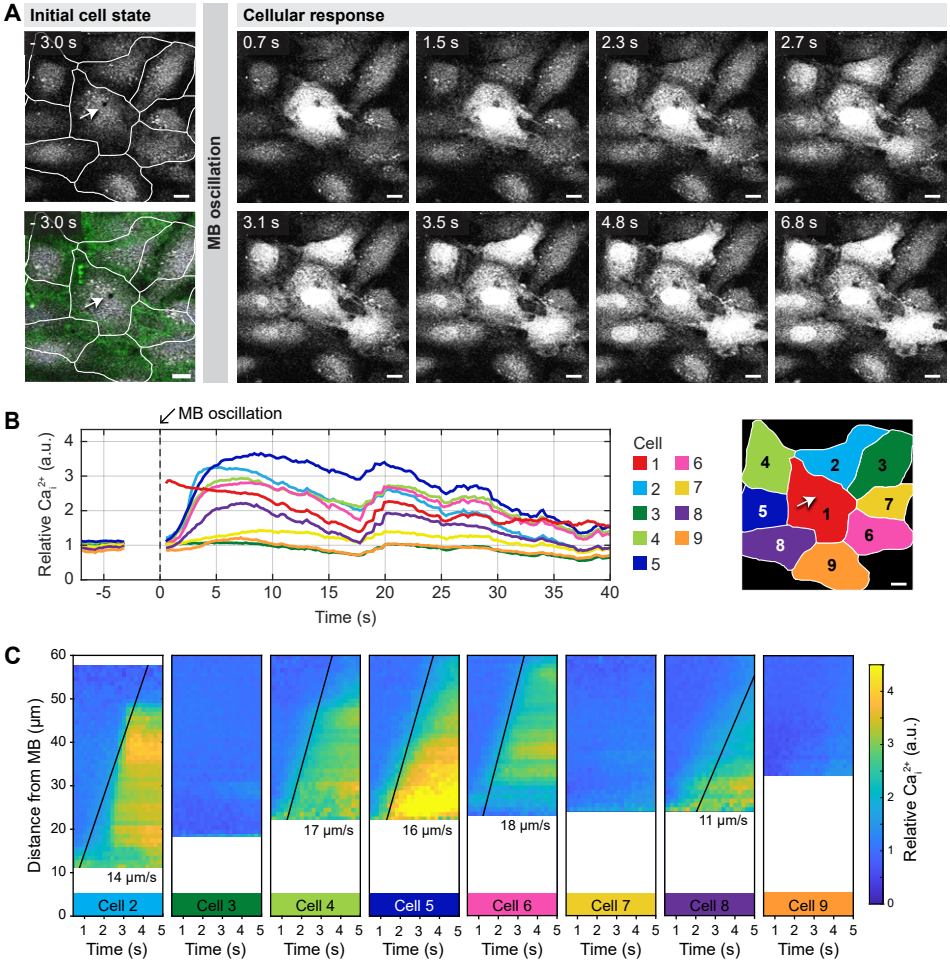

Figure 6.5: Calcium wave to only a fraction of the adjacent cells by sonoporation due to an oscillating microbubble (MB). (**A**) Selected confocal microscopy frames of intracellular calcium (Ca_i^{2+}) stained with Fluo-4. The initial cell state shows the microbubble location (arrow) and cell delineation. The microbubble was insonified at 0 s. Scale bars, 10 µm. (**B**) Mean Ca_i^{2+} level in each delineated cell relative to their initial equilibrium state before MB oscillation. Since five out of eight adjacent cells showed a Ca_i^{2+} fluctuation, 63% of the cells were affected. (**C**) The resulting space-time diagram of the calcium wave in each adjacent cell. The relative Ca_i^{2+} level (i.e. normalized to that before ultrasound) is shown as a function of time and the radial distance from the microbubble. The calcium wave front (black solid line) propagated with a median speed of 16 µm/s.

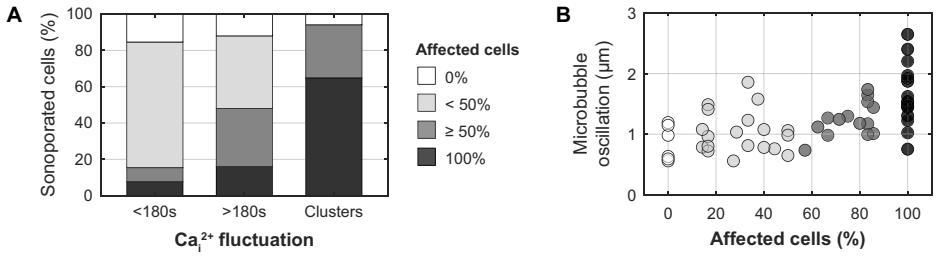

Figure 6.6: Fraction of adjacent cells affected in a calcium wave. (**A**) The fraction of affected cells in a calcium wave induced by each of the distinct Ca_i^{2+} fluctuations in the sonoporated cell. (**B**) Microbubble oscillation amplitude as a function of the fraction of affected cells in a calcium wave.

for oscillation amplitudes < 1 µm, indicating that the cell membrane resealed and normal homeostatic Ca_i^{2+} concentrations were restored. This reversibility suggests cell viability after sonoporation [159]. Reversible Ca_i^{2+} fluctuations have previously been reported in literature, but the necessary microbubble oscillation behavior was never resolved [56, 67, 159, 183–186]. Our results suggest that there is a very narrow band of microbubble oscillation amplitudes, from > 0.75 to < 1 µm, in which cell viability is maintained upon sonoporation. However, it remains to be investigated if the reversible Ca_i^{2+} fluctuation that suggests cell viability on the short-term, cannot trigger long-term cellular responses that for instance interfere in cell proliferation or induce DNA-damage [59, 187, 193].

Upon microbubble oscillation amplitudes > 1 µm we observed an irreversible alteration of the Ca_i^{2+} concentration, since Ca_i^{2+} either remained elevated > 180 s or clustered. Ca_i^{2+} fluctuations that remained elevated > 180 s have also been reported in Chinese hamster ovary cells treated by oscillating microbubbles and were assumed to be caused by unsuccessful membrane resealing [183, 184]. However, in the experimental procedure of these studies by Kumon et al., pore formation was not evaluated to support this hypothesis. In our study, pore formation and resealing were assessed based on PI influx. We observed that even when the pore created upon sonoporation was small and resealed within 120 s (low PI uptake), about 65% of the cells showed irreversible Ca_i^{2+} fluctuations that remained elevated > 180 s (Supplementary Fig. 6.6). Therefore, when Ca_i^{2+} remains elevated it does not necessarily mean sustained membrane damage occurred, but it does indicate the cell is not able to regain homeostatic concentrations after the Ca_i^{2+} overload. Since a highly toxic overload of Ca_i^{2+} can still trigger the onset of biological responses that result in cell death [193], we hypothesize that Ca_i^{2+} levels that are elevated > 180 s are indicative of irreversible cell damage, despite membrane resealing. In other words, membrane resealing is required but not sufficient to preserve cell viability. For the first time, clustering of Ca_i^{2+} was observed upon sonoporation. This characteristic uptake pattern

is likely due to Ca_i^{2+} compartmentalization into cellular organelles that function as Ca_i^{2+} stores [194], such as the endoplasmic reticulum (ER) and mitochondria, and efflux of free Ca_i^{2+} while the pore remains open. It is known that an overload of Ca_i^{2+} will accumulate in the mitochondria which can trigger apoptosis [195, 196]. A flow cytometry study on leukemia cells has shown that oscillating microbubbles can indeed trigger this Ca_i^{2+}-dependent apoptotic pathway [59, 187]. Since Ca_i^{2+} clustering occurred for the highest pore damage coefficients, it is indicative of excessive trauma which might also directly lead to necrosis [59]. A "granular-like fluorescence" has previously been reported when imaging an oxidation-sensitive fluorescent probe (2',7'-Dichlorofluorescein) to study the effect of oscillating microbubbles on reactive oxygen species (ROS). This apparent granulation was suggested to be caused by high levels of ROS in the mitochondria related to the Ca_i^{2+} influx [45].

The Ca_i^{2+} fluctuations spatially propagated within each cell via intracellular calcium waves and among neighboring cells via intercellular calcium waves. These are complex spatiotemporal processes regulated by cellular signaling mechanisms and limited by passive diffusion [188]. Intracellular calcium propagation induced by an oscillating microbubble occurs through two main mechanisms. First of all, upon pore formation external calcium ions diffuse into the cytosol and can trigger a calcium-induced release of Ca_i^{2+} from the ER [193]. Secondly, membrane stress and elevated Ca_i^{2+} levels trigger the production of inositol 1,4,5-trisphosphate (IP3), which diffuses through the cell and also stimulates Ca_i^{2+} release from the ER [188]. At the same time, the intercellular calcium wave leads to a Ca_i^{2+} rise in adjacent cells. However, it is not directly the Ca_i^{2+} that diffuses among cells but the IP3 messenger, as described in detail by Leybaert et al. [188]. Elevated IP3 levels will be transmitted to adjacent cells through gap junctions or through paracrine signaling, by stimulating ATP release into the extracellular space, which in turn stimulates the production of IP3. Both of these processes result in elevated IP3 levels in adjacent cells, which will stimulate Ca_i^{2+} release from the ER, leading to the observed delayed Ca_i^{2+} fluctuations. In our study, some adjacent cells were not affected by the induced calcium wave, suggesting that there were fewer gap junctions for IP3 transmission or less receptors on the cell membrane sensitive to the increase in extracellular ATP to stimulate IP3 production. Additionally, we found that larger microbubble oscillation amplitudes caused a calcium wave that affected more adjacent cells. This is likely due to the creation of a larger pore and hence a more severe Ca_i^{2+} fluctuation that causes a higher production of IP3, so more internal messenger is available to trigger the subsequent pathways for calcium wave propagation. In our study we used Fluo-4 to quantify the relative changes in Ca_i^{2+} using a single imaging channel and normalizing to the initial Ca_i^{2+} levels in each cell. To quantitively compare the Ca_i^{2+} levels between cells, ideally a dual-wavelength ratiometric calcium indicator such as Fura-2 should be used [197]. However, for ratiometric dyes two imaging channels are required. Since there are only four simultaneous imaging channels

available in the confocal microscope, either the nuclei, cell membrane, or uptake of PI could not have been imaged if a ratiometric calcium dye had been used.

The high spatial and temporal resolution of the confocal microscope allowed us to quantify the spatiotemporal evolution of calcium waves as a spherical wave. The *intra*cellular calcium wave front propagated at ~12 μm/s, independent of how many cells were affected, and the *inter*cellular wave front propagated at ~15 μm/s when all adjacent cells were affected. These calcium wave speeds are in agreement with the ~10 – 20 μm/s generally reported in literature for various stimuli and cell types [188], the 17 μm/s estimated in endothelial cells upon force probe stimulation [198], and the 7 – 20 μm/s in Chinese hamster ovary cells upon oscillating microbubbles [184].

Opening of cell-cell contacts was observed upon an oscillating microbubble, causing gap formation between neighboring cells by the disruption of intercellular junctions. This is a clinically relevant therapeutic bioeffect since it can facilitate the extravasation of drug compounds from the vasculature, for instance to overcome the blood-brain barrier [199]. The occurrence of opening of cell-cell contacts was not predictable from microbubble oscillation amplitude. However, it did strongly correlate to the severity of the induced Ca_i^{2+} fluctuation. When an irreversible Ca_i^{2+} fluctuation was induced upon sonoporation there was a significantly higher chance of cell-cell contact opening between the cell and its neighbors. This suggests that cell-cell contact opening is a biological response triggered upon elevated Ca_i^{2+} levels. Membrane stress and elevated Ca_i^{2+} can cause rearrangement of the cytoskeleton, which coupled to the tight junctions might be causing the opening of cell-cell contacts [59, 200]. Rearrangement of the cytoskeleton due to an oscillating microbubble has been reported [51], but it remains to be evaluated if this is associated with an increased occurrence of cell-cell contact opening. Additionally, a rise in Ca_i^{2+} can cause endothelial cell contraction and thereby reduce the cell surface area [189]. This might facilitate quicker resealing of the pore by reducing the pore area and making membrane lipids available to repair the pore. We observed that upon opening of cell-cell contacts the intercellular gaps remained open for > 210 s. The single example previously reported in literature, showed that cell-cell contacts can remain open for tens of minutes [53]. However, they did not correlate this bioeffect to microbubble behavior, sonoporation, or Ca_i^{2+} fluctuations. It remains to be investigated how the long-term recovery of cell-cell contacts correlates to the Ca_i^{2+} fluctuation and calcium wave.

CONCLUSIONS

Using the combined Brandaris 128 ultra-high-speed camera and confocal microscope, we could simultaneously resolve specific microbubble oscillation, sonoporation, Ca_i^{2+} fluctuations, propagation of calcium waves, and opening of cell-cell contacts. Three distinct Ca_i^{2+} uptake profiles were identified upon sonoporation, which propagated to adjacent cells via calcium waves. The distinct Ca_i^{2+} fluctuations strongly correlated with the microbubble oscillation amplitude, the severity of pore damage induced by sonoporation, the occurrence of cell-cell contact opening, and the number of adjacent cells affected in a calcium wave. This novel optical imaging system yields new insights in the microbubble-cell interaction to aid the development of microbubble-enhanced drug delivery.

ACKNOWLEDGEMENT

We thank S.A.G. Langeveld for assistance with microbubble preparation from the Department of Biomedical Engineering and M. Manten and G. Springeling for technical assistance from the Department of Experimental Medical Instrumentation, all from the Erasmus University Medical Center Rotterdam, the Netherlands. The authors would also like to thank R. Verduyn Lunel, E. Verver, and A. Scarpellini from Nikon Instruments Europe for their contribution to development of the optical imaging system. This research was supported by the Applied and Engineering Sciences TTW (Veni-project 13669), part of NWO.

SUPPLEMENTARY INFORMATION

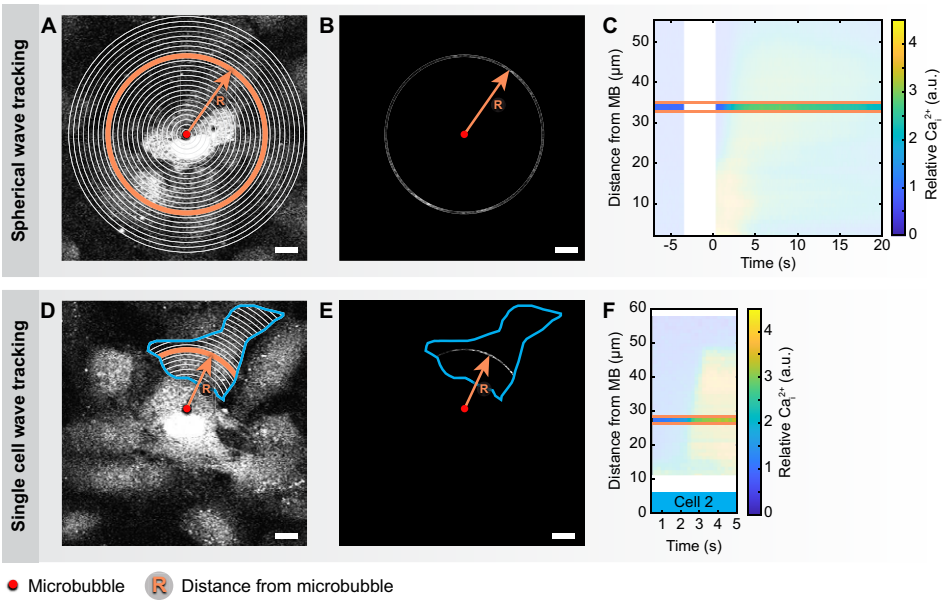

Supplementary Figure 6.1: Tracking calcium wave propagation as a spherical wave phenomenon. (a) The field of view was divided into radial bands of 1 µm centered at the microbubble (MB) location. (**B**) In each radial band the mean intracellular calcium (Ca_i^{2+}) level normalized to before ultrasound was determined. (**C**) The change in relative Ca_i^{2+} in a radial band as a function of time was obtained by repeating the previous step for each time frame. Each radial band was displayed as exemplified by the highlighted band in the color-coded map. By repeating this for each radial band, we obtained a full color-coded map of Ca_i^{2+} levels as a function of time and distance from the microbubble. (**D**) To evaluate the propagation of Ca_i^{2+} within each adjacent cell, the cell delineation was used to mask the radial bands. (**E**) For each cell, the mean Ca_i^{2+} level within each radial band was determined. (**F**) The change in Ca_i^{2+} in each radial band and cell as a function of time was obtained by repeating the previous step for each time frame. Each radial band was displayed as exemplified by the highlighted band in the color-coded map. By repeating this for each radial band, a full color-coded map of Ca_i^{2+} levels was obtained for each cell. Scale bars, 10 µm. The radial bands are not drawn to scale. The example frames in (A, B, and C) correspond to Fig. 6.4 and the examples in (D, E, and F) correspond to Fig. 6.5.

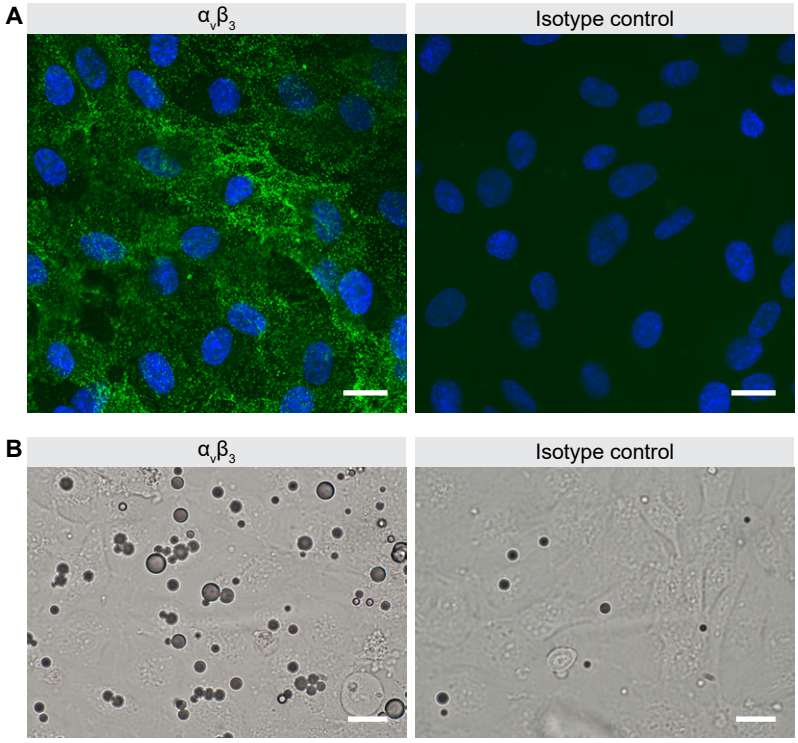

Supplementary Figure 6.2: Expression of the $\alpha_v\beta_3$ integrin and specificity of targeted microbubbles. (**A**) Confocal microscopy images of the immunohistochemistry assay showing the cell nuclei stained with Hoechst (blue) and the antibodies with Alexa Fluor 488 (green). The assay revealed expression of the $\alpha_v\beta_3$ antibody over the entire HUVEC cell membrane. The green fluorescent signal was not observed when the antibody was substituted for its isotype control. (**B**) Brightfield microscopy images of microbubbles bound to live HUVECs. Per field of view, 99.0 (83.8 – 122.3) $\alpha_v\beta_3$-targeted microbubbles adhered to living HUVECs (median with interquartile range between brackets). In contrast, significantly ($p<0.001$) less isotype control microbubbles adhered, with only 9.0 (5.0 – 13.0) observed per field of view. Scale bars, 20 µm.

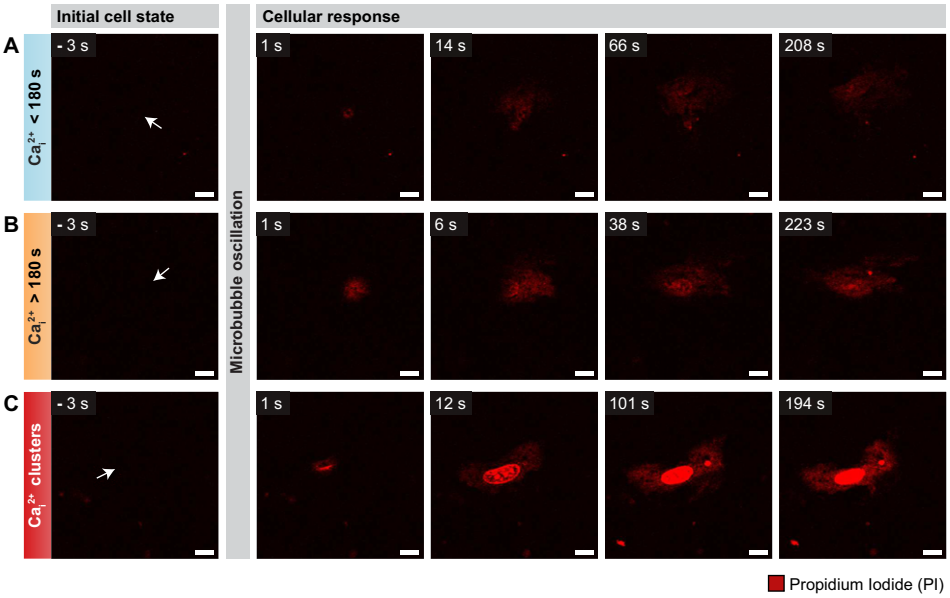

Supplementary Figure 6.3: Selected frames of propidium iodide confocal microscopy imaging. The red imaging channel isolated from the other three channels, showing propidium iodide uptake upon sonoporation. The three examples presented here correspond to the distinct intracellular (Ca_i^{2+}) fluctuations upon sonoporation shown in Fig. 2, were Ca_i^{2+} was either (**A**) elevated < 180s, (**B**) elevated > 180 s, or (**C**) clustered. Scale bars, 10 µm.

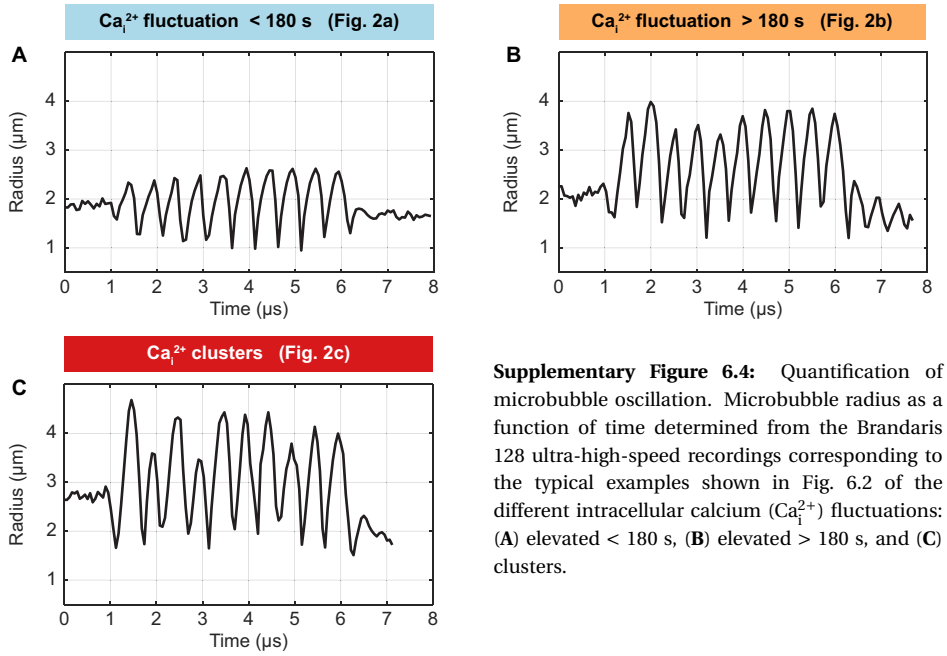

Supplementary Figure 6.4: Quantification of microbubble oscillation. Microbubble radius as a function of time determined from the Brandaris 128 ultra-high-speed recordings corresponding to the typical examples shown in Fig. 6.2 of the different intracellular calcium (Ca_i^{2+}) fluctuations: (**A**) elevated < 180 s, (**B**) elevated > 180 s, and (**C**) clusters.

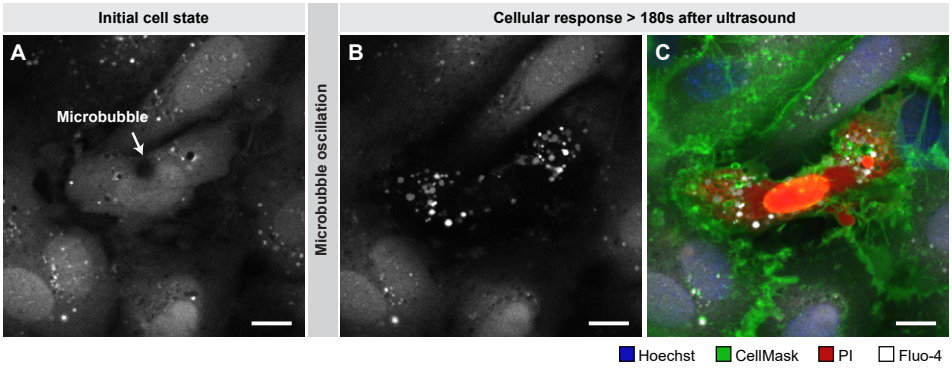

Supplementary Figure 6.5: High resolution imaging of intracellular calcium (Ca_i^{2+}) clusters. Detailed high resolution images of the typical example shown in Fig. 6.2C. High resolution imaging (0.12 µm/pixel, 1024×1024 pixels) was performed with the confocal microscopy Galvano scanner. Scale bars, 10 µm. (**A**) The initial Ca_i^{2+} level before microbubble oscillation shown in the Fluo-4 channel. (**B**) The cellular response > 180 s after microbubble oscillation shown in the Fluo-4 channel. (**C**) Cellular response shown in the merged image of the four imaging channels. The cell nuclei pseudo-colored in blue, cell membrane in green, propidium iodide (PI) in red, and Ca_i^{2+} in white.

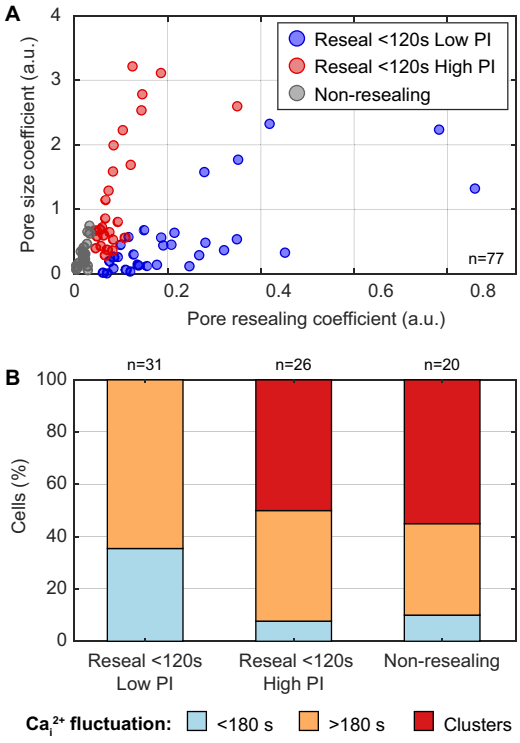

Supplementary Figure 6.6: Pore size and resealing coefficients upon sonoporation. (**A**) The propidium iodide (PI) uptake curves were fit to the mathematical model by Fan et al. [38] and the pore size and resealing coefficients were obtained. The sonoporated cells were classified based on their pore characteristics as described by van Rooij et al. [40] into pores non-resealing within 120 s (gray) or resealing < 120 s with either low PI uptake (blue) or high PI uptake (red). (**B**) The occurrence of different intracellular calcium (Ca_i^{2+}) fluctuations for each sonoporation classification. The Ca_i^{2+} fluctuation was irreversible, i.e. > 180 s or clusters, in 42 out of 46 cells with high PI uptake or non-resealing pores.

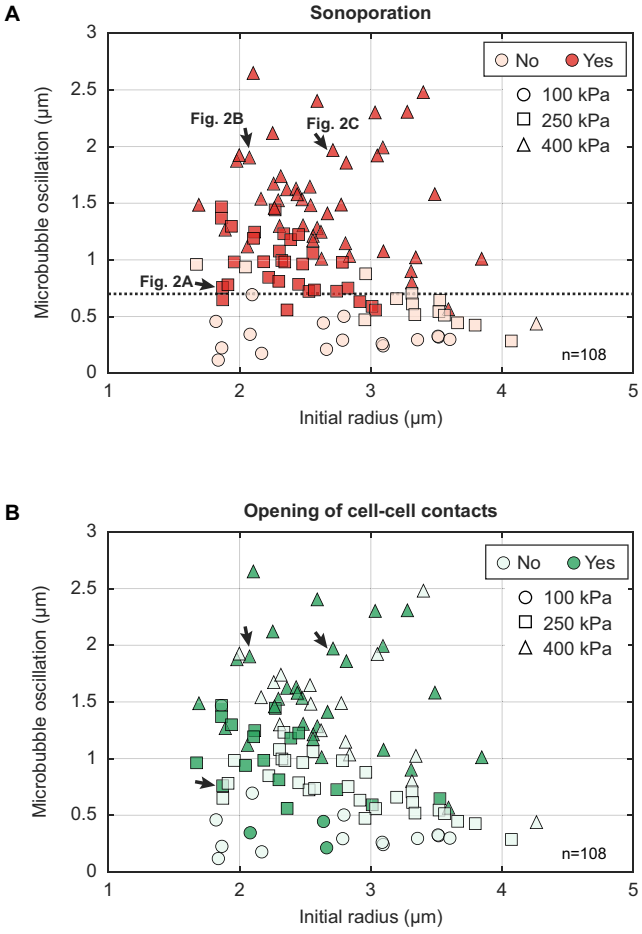

Supplementary Figure 6.7: Microbubble oscillation amplitude for sonoporation and opening of cell-cell contacts. The microbubble oscillation amplitude was determined from the Brandaris 128 ultra-high-speed recordings and defined as the difference between maximum microbubble radius during oscillation and the initial radius. Microbubbles were insonified at peak negative pressures of 100 kPa (n=16, circles), 250 kPa (n=46, squares), or 400 kPa (n=46, triangles). The arrows indicate the data points corresponding to the examples in Fig. 6.2. (**A**) Sonoporation was achieved with a microbubble oscillation amplitude of more than 0.75 µm (dotted line), as determined by linear discriminant analysis. This was independent of the initial microbubble radius. B Opening of cell-cell contacts was achieved without a clear correlation to microbubble oscillation amplitude or initial microbubble radius.

SUPPLEMENTARY VIDEOS

Supplementary videos can be found online at `https://doi.org/10.1016/j.ultrasmedbio.2020.03.029`.

Video 1: Ca_i^{2+} fluctuation less than 180s
The time-lapse confocal microscopy imaging corresponding to the data set shown in Fig. 6.2A. Intracellular calcium (Ca_i^{2+}) increased upon sonoporation and returned to equilibrium within 180 s in the cell to which the targeted microbubble had bound (as indicated by the arrow). Additionally, the Ca_i^{2+} fluctuation resulted in a calcium wave that affected 44% of the adjacent cells. Ultrasound insonification occurred at the 33.4 s timestamp, during which confocal microscopy was temporary intercepted for Brandaris 128 ultra-high-speed imaging of microbubble oscillation. The four separate imaging channels were merged into a pseudo-colored video, shown 10× faster than in real time (at 50 frames per second). Cell nuclei are shown in blue, cell membranes in green, propidium iodide in red, and Ca_i^{2+} in white. Scale bar, 10 μm.

Video 2: Ca_i^{2+} fluctuation more than 180s
The time-lapse confocal microscopy imaging corresponding to the data set shown in Fig. 6.2B. Intracellular calcium (Ca_i^{2+}) increased upon sonoporation and remained elevated for more than 180 s in the cell to which the targeted microbubble had bound (as indicated by the arrow). Additionally, the Ca_i^{2+} fluctuation resulted in a calcium wave that affected 100% of the adjacent cells. Ultrasound insonification occurred at the 7.1 s timestamp, during which confocal microscopy was temporary intercepted for Brandaris 128 ultra-high-speed imaging of microbubble oscillation. The four separate imaging channels were merged into a pseudo-colored video, shown 10× faster than in real time (at 50 frames per second). Cell nuclei are shown in blue, cell membranes in green, propidium iodide in red, and Ca_i^{2+} in white. Scale bar, 10 μm.

Video 3: Ca_i^{2+} fluctuation clusters
The time-lapse confocal microscopy imaging corresponding to the data set shown in Fig. 6.2C. Intracellular calcium (Ca_i^{2+}) increased upon sonoporation and only a clustered pattern of Ca_i^{2+} remained in the cell to which the targeted microbubble had bound (as indicated by the arrow). Additionally, the Ca_i^{2+} fluctuation resulted in a calcium wave that affected 100% of the adjacent cells. Ultrasound insonification occurred at the 33.2 s timestamp, during which confocal microscopy was temporary intercepted for Brandaris 128 ultra-high-speed imaging of microbubble oscillation. The four separate imaging channels were merged into a pseudo-colored video, shown 10× faster than in real time (at 50 frames per second). Cell nuclei are shown in blue, cell membranes in green, propidium iodide in red, and Ca_i^{2+} in white. Scale bar, 10 μm.

7

Opening of endothelial cell-cell contacts due to sonoporation

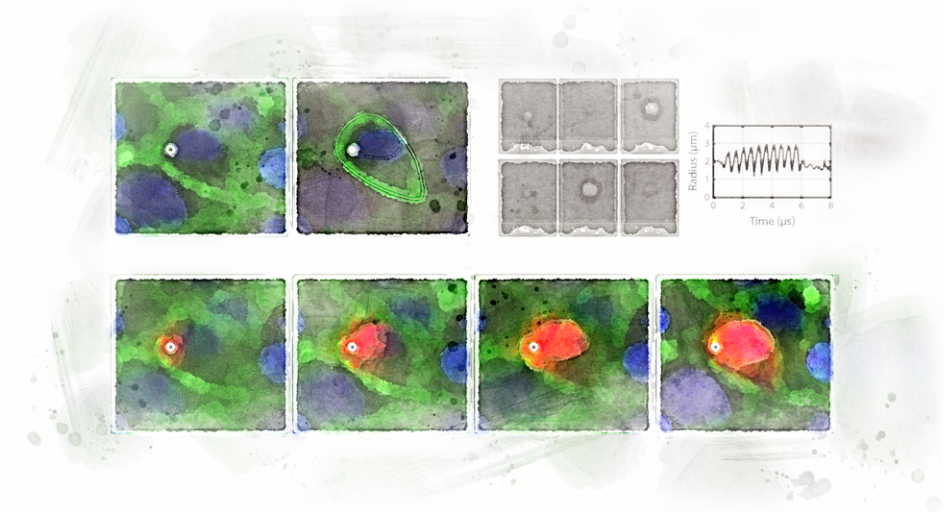

Based on:
Inés Beekers, Merel Vegter, Kirby R. Lattwein, Frits Mastik, Robert Beurskens, Antonius F. W. van der Steen, Nico de Jong, Martin D. Verweij, Klazina Kooiman, "Opening of endothelial cell-cell contacts due to sonoporation", *Journal of Controlled Release*, vol. 322, pp. 426-438, 2020 [201].

Abstract

Ultrasound insonification of microbubbles can locally increase vascular permeability to enhance drug delivery. To control and optimize the therapeutic potential, we need to better understand the underlying biological mechanisms of the drug delivery pathways. The aim of this *in vitro* study was to elucidate the microbubble-endothelial cell interaction using the Brandaris 128 ultra-high-speed camera (up to 25 Mfps) coupled to a custom-built Nikon confocal microscope, to visualize both microbubble oscillation and the cellular response. Sonoporation and opening of cell-cell contacts by single $\alpha_v\beta_3$-targeted microbubbles (n = 152) was monitored up to 4 min after ultrasound insonification (2 MHz, 100 – 400 kPa, 10 cycles). Sonoporation occurred when microbubble excursion amplitudes exceeded 0.7 µm. Quantification of the influx of the fluorescent model drug propidium iodide upon sonoporation showed that the size of the created pore increased for larger microbubble excursion amplitudes. Microbubble-mediated opening of cell-cell contacts occurred as a cellular response upon sonoporation and did not correlate with the microbubble excursion amplitude itself. The initial integrity of the cell-cell contacts affected the susceptibly to drug delivery, since cell-cell contacts opened more often when cells were only partially attached to their neighbors (48%) than when fully attached (14%). The drug delivery outcomes were independent of nonlinear microbubble behavior, microbubble location, and cell size. In conclusion, by studying the microbubble–cell interaction at nanosecond and nanometer resolution the relationship between drug delivery pathways and their underlying mechanisms was further unraveled. These novel insights will aid the development of safe and efficient microbubble-mediated drug delivery.

Index Terms — drug delivery, microbubbles, ultrasound, sonoporation, cell-cell contact opening, high-speed imaging.

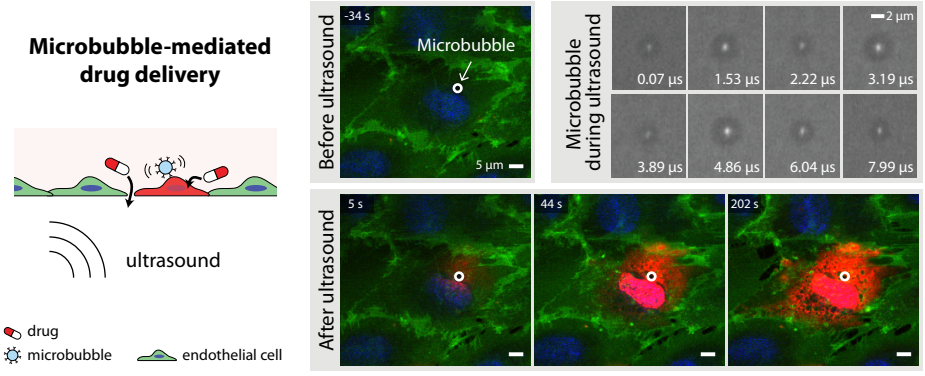

7.1. INTRODUCTION

Life-threatening diseased tissue often lies beyond the vasculature. This means that intravenously administered drugs need to extravasate from the vasculature to reach their intracellular and extravascular targets. The endothelial cells that line the vessel wall are barriers that severely limit local and effective drug delivery necessary for successful treatment. To overcome the challenges these barriers present, drug delivery can be locally enhanced using lipid-coated gas microbubbles (1-10 μm) in combination with ultrasound [3, 32]. These microbubbles are widely used in the clinic to improve contrast in diagnostic ultrasound imaging. When ultrasound is applied, microbubbles will oscillate, which can permeabilize cell membranes (sonoporation), open cell-cell contacts, and stimulate endocytosis [3, 32, 34]. However, the underlying physical and biological mechanisms of the microbubble–cell interaction need to be elucidated. If we can control and predict the different drug delivery pathways, microbubble–mediated drug delivery can be tuned to the requirements of a therapeutic application.

To unravel the underlying mechanisms of the microbubble–cell interaction, one needs to know which microbubble behavior is responsible for which cellular response. Therefore, we need to image both the microbubble oscillation at nanosecond temporal resolution and the ensuing detailed cellular response at nanometer spatial resolution. Until now, concurrent visualization of microbubble oscillation and endothelial cell response has only been possible using an ultra-high-speed camera coupled to a widefield microscope [15, 53, 58, 62]. In these studies, focusing on sonoporation, the microbubble behavior was known but the cellular response was imaged at low resolution and sensitivity. Helfield et al. [53] performed an additional experiment in which they only used confocal microscopy to show sonoporation and opening of cell-cell contacts in a single example. Confocal microscopy has also been used by others to visualize the cellular response at high spatial resolution and detector sensitivity. They investigated sonoporation [37, 51, 64, 171, 202], membrane perforation and recovery dynamics [37], endocytosis [64], sonoprinting [173, 202], lipoplex delivery [171], and cytoskeleton reorganization [51]. However, the studies using confocal microscopy lacked information on the microbubble oscillation behavior that was responsible for the cellular effect. Since single microbubble response to ultrasound is variable [65, 66] even for known acoustic pressures, the underlying mechanisms of the microbubble–cell interaction could not be fully resolved.

Sonoporation has been investigated *in vitro* and in real-time, demonstrating the capability of an oscillating microbubble to create a pore in the endothelial cell membrane [15, 40, 53, 58, 203]. The transient behavior of pore formation and recovery dynamics have been studied with live cell microscopy [37, 38]. Reversible sonoporation can temporarily enhance intracellular drug delivery without cell death.

However, when cell membrane integrity is not restored after pore formation, sonoporation is irreversible and will eventually lead to cell death. Pore resealing times from a few seconds up to 120 s have been reported [37, 40, 148, 203]. Fan et al. [38] showed that upon sonoporation, the amount of fluorescent marker propidium iodide (PI) uptake can be related to the size of the pore and its resealing time. This has been used to quantify the pore dynamics of kidney [38] and endothelial cells [40, 63]. Nevertheless, it remained unknown how microbubble oscillation behavior correlates with the severity of sonoporation, in terms of the pore size and its resealing characteristics. When the microbubble excursion amplitude required for sonoporation was investigated, the cellular response could only be studied at low sensitivity and spatial resolution using widefield microscopy [15, 53].

Opening of cell-cell contacts has been previously observed using live cell microscopy within minutes after ultrasound insonification of a non-targeted microbubble for a single example [53]. The opened cell-cell contacts remained open for tens of minutes, suggesting a prolonged enhanced drug delivery effect of this pathway. In addition, extravasation of drug compounds from the vasculature has been shown, for instance to overcome the blood-brain barrier [20, 199]. It is hypothesized that this cellular response of opening the intercellular junctions is caused by the shear stress from the oscillating microbubbles, the microbubble forces on the cytoskeleton of the cell, and/or the changes in cell morphology due to sonoporation [33]. However, there is still a lack of understanding on how microbubble oscillation behavior causes the opening of cell-cell contacts and whether this is an independent drug delivery pathway or induced upon sonoporation [33].

In this study we aimed to elucidate the missing link between microbubble oscillation behavior and the occurrence of sonoporation and opening of cell-cell contacts in cultured endothelial cells. Microbubbles were targeted to the integrin $\alpha_v\beta_3$ (alpha-v-beta-3), also known as CD51/61, expressed by endothelial cells during angiogenesis [204], which is clinically relevant for cancer and atherosclerosis therapy. Ultrasound at a 2 MHz frequency was applied, commonly used in transthoracic ultrasound [205]. A unique optical imaging system was used consisting of the Brandaris 128 ultra-high-speed camera, to record the microbubble oscillation, coupled to a custom-built Nikon A1R+ confocal microscope, to visualize the cellular response. The cellular response upon insonification of a single targeted microbubble was studied by monitoring uptake of the model drug PI and by assessing opening of cell-cell contacts between adjacent cells. As a result, the microbubble–cell interaction was studied at both nanosecond and nanometer resolution (17 Mfps and 200 nm, respectively).

7.2. MATERIAL AND METHODS

Endothelial cell culture

Primary human umbilical vein endothelial cells (HUVECs) from pooled donors (C2519A, LOT 437550, Lonza, Verviers, Belgium) were cultured in MV2 medium (C22121, PromoCell, Heidelberg, Germany), supplemented with 1% Penicillin-Streptomycin (15140122, Gibco, Thermo Fisher Scientific, Waltham, MA, USA). The HUVECs were grown (at 37 °C and 5% CO_2) in a humidified incubator to full confluency in T75 flasks. Next, they were detached using Accutase solution (A6964, Sigma-Aldrich, St. Louis, MO, USA) and replated on the bottom membrane of a CLINIcell (CLINIcell25-50-T, REF 00106, MABIO, Tourcoing, France) in 12 ml MV2. The CLINIcell is an acoustic compatible cell culture chamber with two gas permeable parallel membranes (thickness 50 µm, surface area 25 cm^2) [160]. The CLINIcells were incubated (at 37 °C and 5% CO_2) for two days to achieve a fully confluent cell monolayer. The HUVECs used in the experiments were between passage numbers 4 and 6.

Targeted microbubble preparation

Lipid-coated microbubbles with a C_4F_{10} gas core were produced in-house by probe sonication for 1 min, as previously described [77, 88, 93]. The coating consisted of 1,2-distearoyl-sn-glycero-3-phosphocholine (DSPC; 84.8 mol%; P6517, Sigma-Aldrich), polyoxyethylene-40-stearate (PEG-40 stearate; 8.2 mol%; P3440, Sigma-Aldrich), 1,2-distearoyl-sn-glycero-3-phosphoethanolamine-N-[carboxy(polyethylene glycol)-2000] (DSPE-PEG(2000); 5.9 mol%; 880125P, Avanti Polar Lipids, Alabaster, AL, USA), and 1,2-distearoyl-sn-glycero-3-phosphoethanolamine-N-[biotinyl(polyethylene glycol)-2000] (DSPE-PEG(2000)-biotin; 1.1 mol%; 880129C, Avanti Polar Lipids). Finally, to fluorescently label the microbubble coating, the lipid dye DiD (1,1'-dioctadecyl-3,3,3',3'-tetramethylindodicarbocyanine perchlorate; D307, Thermo Fisher Scientific) was added before sonication.

The microbubbles were targeted to the $\alpha_v\beta_3$ integrin using biotin-streptavidin bridging, as previously described by others [15, 16, 135, 206–208] with the exception of the type of ligand. Briefly, after washing three times by centrifugation (400 *g*, 1 min) using PBS saturated with C_4F_{10}, the microbubble concentration was determined with a Coulter Counter Multisizer 3 (n = 3) (20 µm aperture tube, Beckman Coulter, Mijdrecht, the Netherlands). Next, 6×10^8 microbubbles were incubated on ice for 30 min with 60 µg of streptavidin (2 mg/ml stock concentration in PBS, S4762, Sigma-Aldrich) and washed. These streptavidin-conjugated microbubbles were incubated on ice for 30 min with 6 µg of biotinylated anti-human CD51/61 antibody (304412, BioLegend, San Diego, CA, USA), followed by a final washing step.

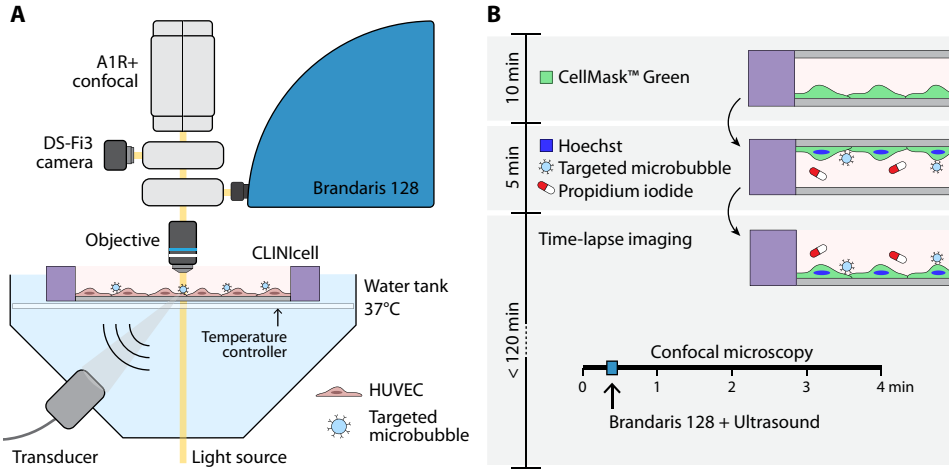

Figure 7.1: Schematic representation of the experimental procedure (not drawn to scale). (**A**) Experimental setup to insonify a CLINIcell under a 45° angle. The optical imaging system combines an A1R+ confocal scan head (Nikon Instruments), with a DS-Fi3 color camera (Nikon Instruments) for widefield imaging, and the Brandaris 128 ultra-high-speed camera. (**B**) Timeline starting with the incubation of HUVECs with fluorescent dyes and targeted microbubbles, followed by time-lapse imaging with the combined optical system.

Experimental set-up

To study the microbubble-cell interaction, a unique optical imaging system was used consisting of the Brandaris 128 ultra-high-speed camera (up to 25 million frames per second, Mfps) [6] coupled to a custom-built Nikon A1R+ confocal microscope (Fig. 7.1A) [167]. With this system high temporal and spatial resolutions can be achieved, required to resolve the microbubble oscillation and cellular response, as explained in more detail by Beekers et al. [167]. For simultaneous imaging and ultrasound insonification, the CLINIcell was inserted into a 37 °C water tank positioned beneath the microscope. A single element focused transducer (2.25 MHz center frequency; 76.2 mm focal length; -6 dB beam width at 2 MHz of 3 mm; V305; Panametrics-NDT, Olympus, Waltham, MA, USA) was mounted in the water tank at a 45° angle, after having been calibrated using a needle hydrophone. The ultrasound and optical foci were aligned such that the cells in the CLINIcell could be both imaged and insonified (Fig. 7.1A). A single 2 MHz and 10-cycle burst was generated by an arbitrary waveform generator (33220A, Agilent, Palo Alto, CA, USA). A broadband amplifier (ENI A-500, Electronics & Innovation, Rochester, NY, USA) was used to obtain peak negative pressures (PNP) of 100, 200, 250, 300, and 400 kPa at the focus.

Experimental protocol

The HUVECs were stained with fluorescent dyes for live confocal microscopy imaging (Fig. 7.1B). They were incubated with CellMask™ Green Plasma Membrane Stain (4 μg/ml final concentration; C37608; Thermo Fisher Scientific) for 10 minutes inside the cell incubator to stain the cell membranes. Next, Hoechst 33342 (5 μg/ml final concentration; H3570, Thermo Fisher Scientific) was added to stain the cell nuclei and PI (25 μg/ml final concentration; P4864, Sigma-Aldrich) was added as a marker for sonoporation. The cell membrane of viable cells is impermeable for PI. When the cell membrane is compromised, PI enters the cell, binds to DNA and RNA, and becomes fluorescent [35]. Therefore, PI is often used as a marker for sonoporation to evaluate membrane perforation [38, 43, 53, 58, 191]. Additionally, CD51/61 targeted microbubbles (2×10^5 microbubbles/ml final concentration) were added and the CLINIcell was incubated during 5 min inside the cell incubator, while turned upside down to allow the targeted microbubbles to float towards the cells to achieve binding (Fig. 7.1B). The CLINIcell was then turned upright again such that only bound targeted microbubbles remained in the focal plane of the cells. Finally, the top membrane without cells was cut from the CLINIcell, making it feasible to image with an objective with a working distance smaller than the 5 mm spacing between the CLINIcell membranes. The same incubation timeline was used for control CLINIcells without microbubbles.

To monitor the cellular response with confocal microscopy, imaging was performed with the following four channels: (1) Hoechst excited at 405 nm, detected at 450/50 nm (center wavelength/bandwidth), (2) CellMask Green excited at 488 nm, detected at 525/50 nm, (3) PI excited at 561 nm, detected at 595/50 nm, and (4) DiD excited at 640 nm, detected at 700/70 nm. Channel 1 and 4 were excited and detected simultaneously because there is no spectral overlap between Hoechst and DiD.

Using a 100× water dipping objective (CFI Plan 100XC W, 2.5 mm working distance, Nikon Instruments), a field of view (FOV) of 74.2 × 74.2 μm (256 × 256 pixels) was scanned at 0.65 frames per second (fps). At each location, time-lapse imaging was performed for 4 min in total (Fig. 7.1B). This 100× objective has a high numerical aperture of 1.10; therefore, we achieve a lateral resolution up to 200 nm and an axial resolution up to 600 nm [209]. To visualize the initial cellular state, confocal microscopy time-lapse imaging started before ultrasound. Within the first minute, the light path was automatically switched from the confocal scanning head to the Brandaris 128 ultra-high-speed camera. The microbubble oscillation was then recorded at approximately 17 Mfps during ultrasound insonification. Once this recording was completed, the light path was switched back towards the confocal scanning head to visualize the cellular response. Since insonification occurred within the first minute, the cellular response upon microbubble vibration was monitored for at least 3 min (Fig. 7.1B).

The area to be imaged was chosen based on the following inclusion criteria: (i) the FOV showed fully confluent cells, such that there were no empty spaces in which an extra cell could have grown and all cells were at least partially attached to neighboring cells; (ii) there was a single targeted microbubble in the FOV; (iii) this targeted microbubble was located on a cell that was completely in the FOV; (iv) this cell had a single nucleus; and (v) this nucleus did not overlap with that of any neighboring cells. Per CLINIcell, a maximum of 15 locations uniformly distributed and spaced by at least 1 cm to avoid overlapping insonification were imaged within 120 min. Additional CLINIcells were used for two types of control experiments: (i) sham, i.e. without microbubbles or ultrasound; and (ii) ultrasound only, i.e. without microbubbles.

Analysis of microbubble oscillation

Microbubble oscillation recorded by the Brandaris 128 ultra-high-speed camera was quantified using custom-designed image analysis software to determine the change in radius as a function of time [74]. The initial radius (R_0) was determined from the first 10 frames without ultrasound. Microbubble excursion amplitude was defined as the difference between the maximum radius (R_{max}) and R_0. The excursion amplitude threshold for sonoporation was determined by linear discriminant analysis and defined as the average over the full microbubble size range [53].

Nonlinear microbubble behavior was studied by assessing the harmonic response. To do so, the frequency spectrum of the radius-time curve was determined using a Fast Fourier Transformation (FFT). Amplitudes were determined within a ±300 kHz bandwidth centered at the subharmonic (1 MHz) and second harmonic (4 MHz) frequencies. The noise levels were defined as the mean amplitude within those bandwidths from the FFT of the radius-time curve before and after oscillation. When the maximum amplitude of the FFT from the radius-time curve during oscillation was at least 6 dB above the mean noise level of all recordings, a microbubble was classified as responsive [155, 177].

Finally, the asymmetry of microbubble oscillation was investigated. This was quantified by the amount of expansion (E) relative to the amount of compression (C). As previously done by others [68, 77, 95, 177, 210], the E/C ratio was defined as $E/C = (R_{max} - R_0)/(R_0 - R_{min})$. Compression-only behavior is characterized by an $E/C < 0.5$, symmetric oscillation ranges from $0.5 \leq E/C \leq 2$, and expansion-only behavior as an $E/C > 2$.

Analysis of confocal time-lapse images

The image analysis aimed at studying the microbubble-mediated drug delivery pathways induced in the "cell of interest", i.e. the cell with a single bound targeted microbubble, which from now on will be referred to as "the cell". From the time-lapse confocal microscopy before insonification, the cell was classified based on the initial state of its contact with adjacent cells. When the cell edge was fully adjacent to the neighboring cells, it was classified as having "full junctions", and when partially adjacent it was classified as having "partial junctions". For the controls without ultrasound, the initial cell state was determined from the first 30 s of time-lapse confocal microscopy. After ultrasound, the cellular response was evaluated by studying two different drug delivery pathways. Sonoporation was assessed based on PI uptake within the cell as described in detail below. Opening of cell-cell contacts was assessed by changes in the cell border integrity to adjacent cells based on CellMask. When a gap, or gaps, formed between the cell and its neighbor(s), the cell was classified as "retracting". Manual classification was performed by two individual users (M.V. and I.B.) for alternating ultrasound settings and experiment days.

To determine the surface area of the cell and the microbubble location, the cell was delineated and the microbubble location was registered. The delineation and registration were performed manually using a custom-built MATLAB (The Mathworks Inc., Natick, MA, USA) routine. After cell delineation, another MATLAB routine was used to automatically segment the corresponding nucleus based on the Hoechst images. The microbubble location was quantified as the distance from the microbubble to the closest cell edge or, alternatively, to the center of the nucleus. The 4 min confocal microscopy time-lapse recording was split between before and after insonification by finding the period of time when the light path was switched towards the Brandaris 128 camera. The resulting sudden loss of CellMask signal in the confocal time-lapse recording was automatically detected using MATLAB. The first confocal frame after ultrasound was defined as $t = 0$.

During time-lapse imaging slight vertical displacements of the CLINIcell can occur within the water tank, caused by, for instance, thermal expansion of the heating element. These small displacements changed the imaging plane, and although the cell was still in the FOV, the focus drift could alter the detected fluorescent intensity. Therefore, the PI intensity in a sonoporated cell can appear to fluctuate. To correct for PI intensity variations caused by focus drift, the CellMask fluorescent intensity was used as a reference. Although CellMask stains the membrane while PI is present in the cytoplasm, it is a valid reference since endothelial cells are very thin, with a mean height of 0.9 μm at the periphery and up to 1.6 μm at the nucleus [211]. Hence, when the membrane is in focus, the cytoplasm is also within the same focal plane (600 nm). For each confocal time-lapse recording, a correction factor was determined as the ratio between the time-dependent CellMask signal and its initial value, both within

the delineated cell. Next, the PI intensity detected upon sonoporation was corrected by this correction factor.

Analysis of PI uptake profiles

Upon sonoporation, the size of the pore created in the cellular membrane is closely related to the amount of PI uptake. Fan et al. [38] mathematically described this by

$$F(t) = \frac{\alpha\pi DC_0 r_0}{\beta}\left(1 - e^{-\beta t}\right). \tag{7.1}$$

The amount of fluorescent intensity $F(t)$ detected in a cell as a function of time is related to the initial pore radius (r_0), for a known diffusion coefficient of the PI fluorescent molecule (D), extracellular PI concentration (C_0), and imaging system dependent calibration coefficient (α). The pore size coefficient ($\alpha\pi DC_0 r_0$)is a measure for the initial pore size, defined by the initial slope of the PI uptake profile and independent of cell size. The stabilization of the fluorescent intensity is quantified by the pore resealing coefficient (β). Since PI molecules bind to both RNA and DNA in the cell cytoplasm and nucleus [35], we were interested in the amount of PI fluorescence within the delineated cell area. The fluorescent intensity $F(t)$ was defined as the sum over the pixels within the cell area after ultrasound minus the mean before ultrasound. Thereby, we corrected for any initial background noise signal (the mean 12-bit pixel intensity, ranging from 0 to 4095, before ultrasound was 150 and increased by an order of magnitude upon sonoporation).

Since PI molecules bind to both RNA and DNA in the cell cytoplasm and nucleus, we were interested in the amount of PI fluorescence within the delineated cell area. The fluorescent intensity $F(t)$ was defined as the sum over the pixels within the cell area after ultrasound minus the mean before ultrasound. Thereby, we corrected for any initial background noise signal (the mean 12-bit pixel intensity before ultrasound is 150 and increased by an order of magnitude upon sonoporation).

Since the light path towards the confocal microscope was temporarily intercepted during insonification, PI uptake could already have started before $t = 0$, i.e. before the confocal light path was restored. In other words, $F(0)$ might not be zero. Therefore, Eq. 7.1 was adapted such that PI uptake started at $t = t_0$ and $F(t_0) = 0$. This changes Eq. 7.1 into

$$F(t) = \frac{\alpha\pi DC_0 r_0}{\beta}\left(1 - e^{-\beta(t-x)}\right). \tag{7.2}$$

Confocal time-lapse imaging was restored within 2 s after ultrasound insonification, hence t_0 ranged from -2 to 0 s. The influx of PI upon pore formation was monitored as

a function of time and the determined $F(t)$ was fit to Eq. 7.2 using a non-linear least squares approach in MATLAB to determine the pore size coefficient ($\alpha\pi DC_0r_0$), the pore resealing coefficient (β), and the starting time of pore formation (t_0). The time t_{90} at which 90% of the asymptotic value, $F(\infty) = \alpha\pi DC_0r_0/\beta$, was reached is

$$t_{90} = \frac{-\ln(1-0.9)}{\beta} + t_0 = \frac{2.3}{\beta} + t_0. \tag{7.3}$$

When t_{90} < 120 s it means PI uptake stabilizes, presumably caused by pore resealing [40]. However, in the case of high PI uptake, the detected fluorescent intensity can also stabilize due to image saturation or DNA/RNA saturation. Although more PI might be entering the cell, this increase can no longer be detected when the pixels are already saturated (i.e. when the 12-bit pixels are at their maximum value of 4095) or when there is no free DNA or RNA left for PI to bind to. In this study, the imaging settings were chosen such that high PI uptake results in image saturation before DNA/RNA saturation. The optimal settings were determined such that the pixels in the nucleus were image saturated when adding 0.1% Triton X-100 (X100, Sigma-Aldrich), which causes non-resealing membrane disruptions leading to DNA/RNA saturation. By doing so, we could easily identify when the fluorescent intensity of PI stabilized by image saturation, since pixels reached their maximum 4095 value, and we avoided the otherwise indiscernible DNA/RNA saturation. Image saturation starts in the cell nucleus, since there the fluorescent intensity is highest because there is more DNA for PI to bind to. Therefore, when 90% of the pixels in the segmented nucleus reached the 12-bit value, the cell was classified as saturated. Based on the pore resealing coefficient and signal saturation, the PI uptake curves were classified in the following three categories: (i) *resealing < 120 s*, i.e. when PI uptake stabilized with t_{90} < 120 s without saturation; (ii) *non-resealing*, i.e. when PI uptake did not stabilize within 120 s (i.e. t_{90} > 120 s); and (iii) *saturated*, i.e. when PI uptake stabilized with t_{90} < 120 s due to image saturation.

Statistical analyses

The occurrence of a cellular pathway was presented in relative frequencies (%). This categorical data was tested for significant differences among groups using a χ^2 test. test. Quantitative data were assumed to be not normally distributed, and therefore presented in median and interquartile ranges and tested for significance using the Mann-Whitney U test. Statistically significant differences were indicated in the graphs with asterisks by using * for p < 0.05, ** for p < 0.01, and *** for p < 0.001. A Spearman's rank-order correlation was performed to determine the relationship between the microbubble excursion amplitude and the pore size coefficient. All statistical analyses were performed using MATLAB.

7.3. RESULTS

Drug delivery pathways

We evaluated the cellular response of 152 cells to a single targeted microbubble upon ultrasound insonification, in 21 different CLINIcells. Additionally, the response of 44 cells was monitored without microbubbles to assess the effect of ultrasound only experiments in four CLINIcells. To control for the experimental procedure, we also evaluated the response of 32 cells during sham experiments in three CLINIcells.

Four distinct cellular responses were observed: no effect, retraction, sonoporation, or sonoporation and retraction. A typical example of a sonoporated cell is shown in Fig. 7.2A, where selected frames of confocal microscopy and Brandaris 128 imaging are depicted. The corresponding confocal microscopy recording is shown in Video 1. Before ultrasound, in Fig. 7.2A(i) a single microbubble (R_0 = 2.00 μm) was located next to the nucleus, no PI was observed in the cell, and the cell-cell contacts were fully adjacent to the neighboring cells. During ultrasound, the microbubble excursion amplitude was determined from the Brandaris 128 recording to be $R_{max} - R_0$ = 0.95 μm (Fig. 7.2A(ii)). After ultrasound, PI uptake was observed at the location of the microbubble and spread throughout the cell over time, meanwhile the cell-cell contacts remained intact (no retraction), as shown in Fig. 7.2A(iii). In Fig. 7.2B, a typical example of sonoporation and retraction induced by the oscillating microbubble is shown. The corresponding confocal microscopy recording is shown in Video 2. Before ultrasound, there was no PI observed in the cell and the single microbubble (R_0 = 1.91 μm) was located next to the nucleus (Fig. 7.2B(i)). The white arrows show the initial cell-cell contacts that were classified as partial junctions. During ultrasound, the microbubble excursion amplitude was $R_{max} - R_0$ = 0.54 μm, as shown in Fig. 7.2B(ii). After ultrasound (Fig. 7.2B(iii)), PI uptake was observed locally around the microbubble and then diffused throughout the cell. After 5 s the cell had already started to retract (white arrowheads in Fig. 7.2B(iii)). Retraction became more severe over the following 3 min. After 202 s, retraction was even observed on the other side of the cell, although it was fully adjacent at that location before ultrasound. In both examples, the PI intensity was brighter in the nucleus than in the cytoplasm, since there is more DNA for PI to bind to in the nucleus.

The occurrence of the four different cellular responses is reported in Table 7.1. The sham and ultrasound only experiments never induced sonoporation. The vast majority (93.4%) of these cells showed no cellular effect at all, independent of acoustic pressure. Retraction was only observed in 6.6% of all cells treated without microbubbles (5 out of 76 cells for both sham and ultrasound only). When treatment consisted of ultrasound insonification of targeted microbubbles, pressure dependence was observed. At 100 kPa PNP, there was no sonoporation induced and still only a small subgroup (3 out of 18 cells) showed retraction. However, for higher pressures the amount of sonoporated cells increased. At 400 kPa PNP, an oscillating microbubble always

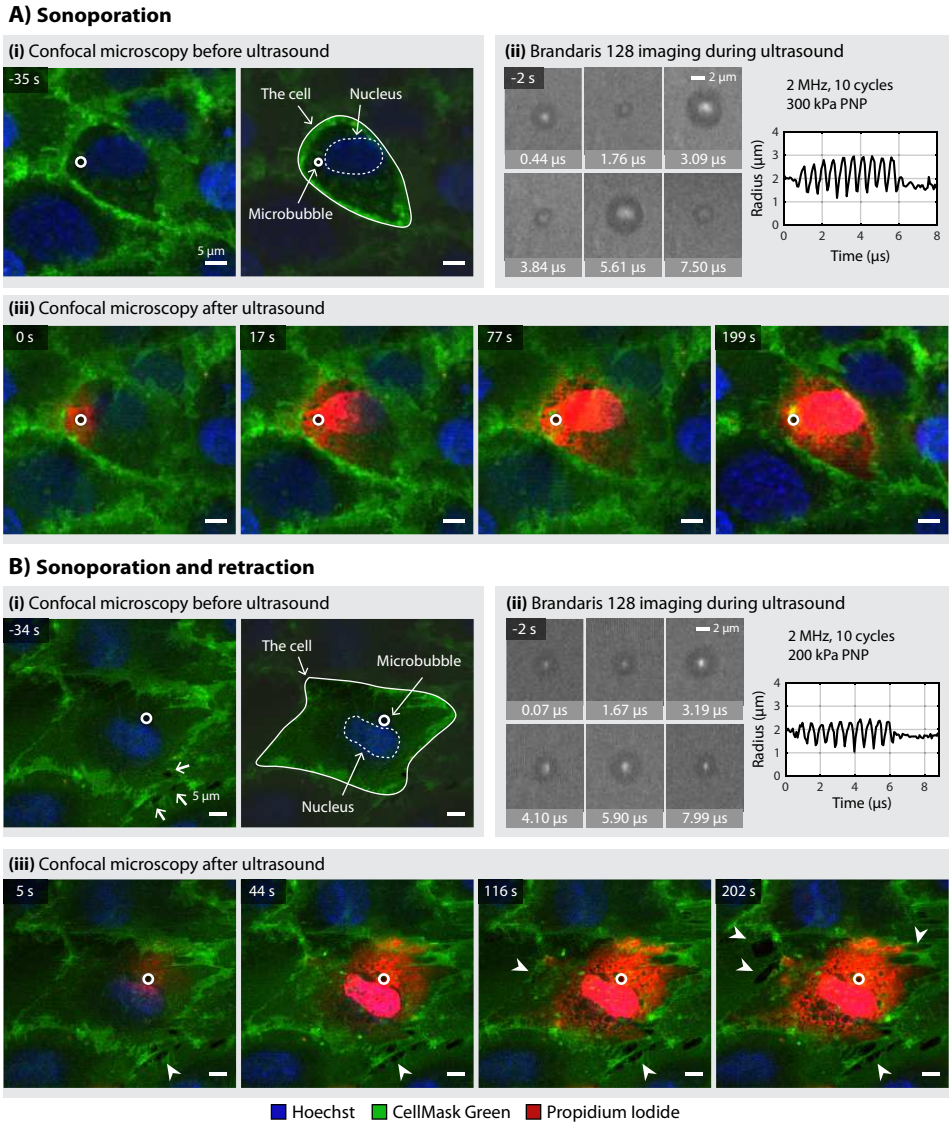

Figure 7.2: Cellular response upon ultrasound insonification of a targeted microbubble imaged with combined confocal microscopy and Brandaris 128 ultra-high-speed imaging. Selected frames are shown of (i) the initial cellular state with cell delineation and segmentation, (ii) the Brandaris 128 recording with the determined microbubble radius as a function of time, and (iii) of the cellular response. (**A**) Sonoporation of a cell that initially had full junctions and remained intact. (**B**) Sonoporation and retraction of a cell that initially had partial junctions. Partial junctions are indicated by the arrows in (i), and retraction is indicated by the arrowheads in (iii).

Table 7.1: Occurrence of cellular effects for sham (i.e. control without microbubbles and ultrasound), ultrasound only, and upon treatment with ultrasound and a targeted microbubble. Values reported as percentage (%) of the total amount of cells evaluated for each setting.

	Sham	**Ultrasound only**					**Ultrasound and targeted microbubble**				
Cellular response (%)	0 kPa n=32	100 kPa n=8	200 kPa n=8	250 kPa n=9	300 kPa n=9	400 kPa n=10	100 kPa n=18	200 kPa n=43	250 kPa n=47	300 kPa n=31	400 kPa n=13
No effect	93.8	100	87.5	88.9	100	90	83.3	62.8	23.4	32.3	0
Retraction	6.3	0	12.5	11.1	0	10	16.7	2.3	21.3	3.2	0
Sonoporation	0	0	0	0	0	0	0	27.9	10.6	41.9	61.5
Sonoporation and retraction	0	0	0	0	0	0	0	7.0	44.7	22.6	38.5

induced sonoporation. There was no clear correlation between retraction and acoustic pressure.

Microbubble oscillation behavior

The microbubbles studied had a mean R_0 of 2.1 μm, ranging from 1.2 μm to 3.7 μm. Insonifying these microbubbles from 100 kPa to 400 kPa PNP resulted in excursion amplitudes ranging from 0.1 μm to 2.2 μm (Fig. 7.3A; see Supplementary Fig. 7.10 for a separate excursion amplitude graph for each studied PNP). The highest excursion amplitudes were observed at R_0 of 2.2 μm and corresponded to the expected resonance size for DSPC-based microbubbles at 2 MHz [77]. All microbubbles were still targeted to the cell after insonification, and the median shrinkage (with IQR, interquartile range, between brackets) of the microbubbles was 92.1% (87.2% – 97.3%), defined as the ratio between the final and initial radius. The excursion amplitudes inducing sonoporation (pink and red) were significantly larger than those where no sonoporation was induced (Fig. 7.3B). Using a linear discriminant analysis, the mean threshold for sonoporation was found to be $R_{max} - R_0 > 0.7$ μm (Fig. 7.3A). However, there was no distinct microbubble excursion amplitude associated with retraction. Since microbubble excursion can also be quantified by considering the minimum radius during oscillation (R_{min}) or relative to R_0, the statistical comparisons between the different cellular responses were also performed for $(R_{max} - R_{min})/R_0$, $R_0 - R_{min}$, and $R_{max} - R_{min}$. The same statistical differences ($p<0.001$) were found between sonoporated and non-sonoporated cells, and the non-significant differences between retracting and non-retracting cells remained.

To evaluate the effect of nonlinear microbubble behavior on drug delivery, we determined if microbubbles exhibited a subharmonic or second harmonic frequency response. The FFT amplitude (mean ± standard deviation) of the subharmonic noise

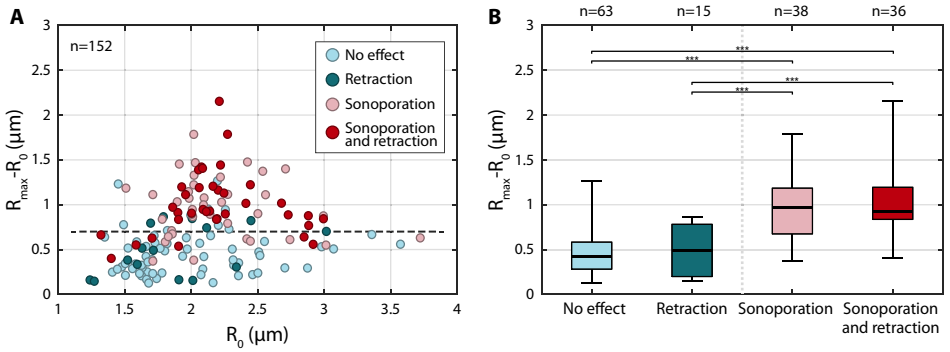

Figure 7.3: Microbubble excursion amplitude ($R_{\max} - R_0$) inducing no cellular effect (light blue), retraction (dark blue), sonoporation (pink), or both sonoporation and retraction (red). (**A**) $R_{\max} - R_0$ as a function of the initial microbubble radius (R_0) for each cellular response. The dashed line indicates the 0.7 µm threshold for sonoporation. (**B**) Median and interquartile range of excursion amplitude for each cellular response. The whiskers range from the minimum to maximum value and statistical significance was indicated with ***p<0.001.

level was 21 ± 13 nm (-18 dB below average fundamental) and that of the second harmonic noise level was 11 ± 6 nm (-23 dB below average fundamental). Only 6 out of 152 microbubbles (4%) had a subharmonic response. The presence of subharmonics did not correlate with a higher occurrence of sonoporation and/or retraction. On the other hand, 105 out of 152 microbubbles (69%) exhibited a second harmonic response, as shown in Fig. 7.4A. Significantly (p<0.01) more microbubbles responded at the second harmonic frequency when sonoporation was induced (49% no effect, 67% retraction only, 84% sonoporation only, 89% sonoporation and retraction). However, the second harmonic amplitude normalized to the fundamental was not higher for microbubbles inducing sonoporation and a second harmonic response was not associated with retraction (Fig. 7.4A).

The asymmetry of microbubble oscillation quantified as E/C is shown in Fig. 7.4B. The recorded microbubbles presented with a full range of E/C ratios, from compression-only behavior (E/C = 0.13) to expansion-only behavior (E/C = 2.15). The E/C resulting in sonoporation was significantly larger than that of microbubbles that did not induce sonoporation (Fig. 7.4B). However, no significant differences were found in E/C for retraction.

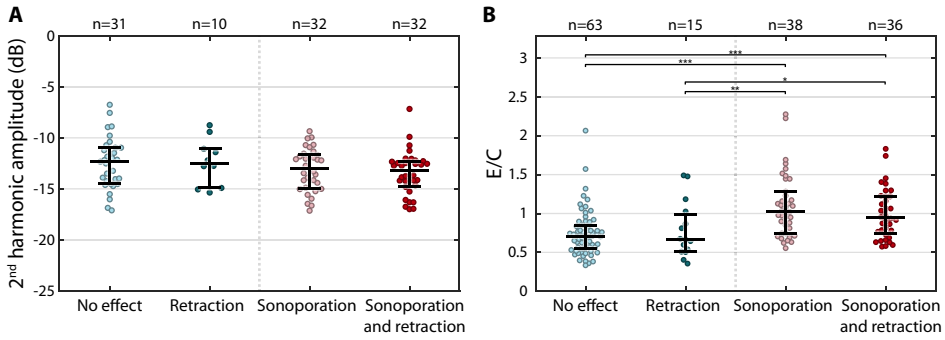

Figure 7.4: Nonlinear microbubble oscillation behavior. (**A**) Second harmonic amplitude normalized to the fundamental for each cellular response. (**B**) Asymmetry of microbubble oscillation quantified as the ratio of expansion over compression (E/C) for each cellular response. The medians and interquartile ranges are overlaid. Statistical significance is indicated with *p<0.05, **p<0.01, and ***p<0.001.

Initial integrity of cell-cell contacts

As described in Section *Analysis of confocal time-lapse images*, the cells were classified into two subcategories based on the integrity of cell-cell contacts before ultrasound: partial junctions (n = 88, Fig. 7.2B) and full junctions (n = 64, Fig. 7.2A). The median (with IQR between brackets) excursion amplitude of microbubbles attached to a cell with partial junctions was 0.65 (0.38 - 0.94) µm and with full junctions 0.65 (0.42 - 1.05) µm. The cells in the control experiments were also classified using the same criteria.

When treated with ultrasound and microbubbles, the occurrence of sonoporation was the same for both cells with partial junctions (48.9%) and with full junctions (48.4%), as shown in Fig. 7.5A. In the case of partial junctions, 65.1% of the sonoporated cells also retracted, while this was only 25.8% of the sonoporated cells with full junctions. For both cell junction subcategories, the sham and ultrasound only treatments never induced sonoporation. In contrast to sonoporation, retraction occurrence was affected by the initial integrity of the cell-cell contacts (Fig. 7.5B). After treatment with ultrasound and microbubbles, retraction occurred significantly (p<0.001) more often when cells initially had partial junctions (47.7%) than when they had full junctions (14.1%) (Fig. 7.5B, US+MB). Sonoporation was only observed in 66.7% of cells with partial junctions that retracted (28 out of 42 cells), whereas almost all cells with full junctions that retracted were also sonoporated (88.9%, 8 out of 9 cells). Retraction without sonoporation in cells with partial junctions was similar for sham (13.3%), ultrasound only (13.6%), and treatment with ultrasound and microbubbles (15.91%). Retraction of cells with full junctions was never observed for the sham and ultrasound only treatments.

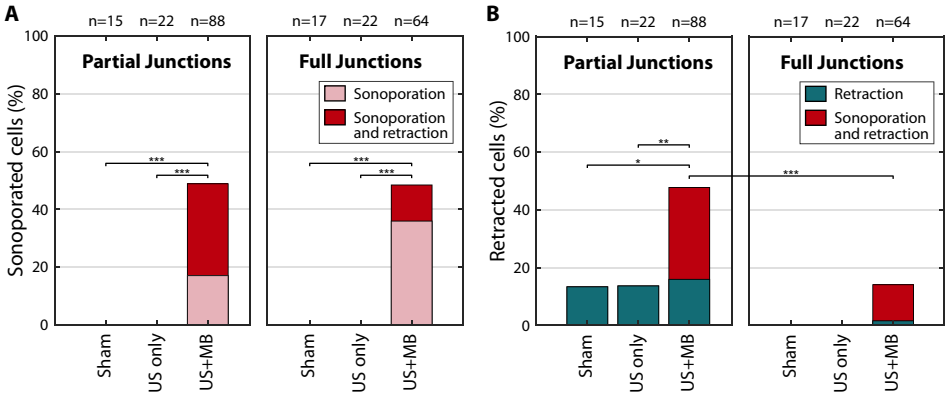

Figure 7.5: The cellular response of cells with partial or full junctions, classified based on the initial integrity of cell-cell contacts. (**A**) Occurrence of sonoporation, with or without retraction. (**B**) Occurrence of retraction, with or without sonoporation. Statistical significance indicated with *p<0.05, **p<0.01, ***p<0.001; US = ultrasound; MB = microbubble.

Cell size and microbubble location

The median (with IQR between brackets) cell area was 908 (725 – 1093) μm^2. There was no significant difference in cell area between the four distinct cell responses, as shown in Fig. 7.6A. Additionally, there was no significant difference in the location of the targeted microbubble on the cell, quantified as the distance from the microbubble to the closest cell edge (Fig. 7.6B)or, alternatively, as the distance from the microbubble to the nucleus. Cells with partial junctions had a median area of 1021 (817 – 1215) μm^2, and therefore were significantly (p<0.001) larger than cells with full junctions, at 794 (621 – 928) μm^2. Also, the median distance of the targeted microbubble to the cell edge was significantly (p<0.001) larger for cells with partial junctions [8.4 (6.4 – 11.1) µm], than for cells with full junctions [6.7 (4.7 – 8.5) µm]. Within these junction subcategories, there was still no significant difference in cell area or distance from the microbubble to the edge between the four cellular responses.

PI uptake profiles

Three typical examples of PI uptake profiles upon sonoporation are shown in Fig. 7.7. In the first example (Fig. 7.7A), the sonoporated cell had a PI uptake profile (Fig. 7.8, blue) that stabilized within 120 s, since 90% of the asymptotic value was reached after 25 s (i.e. t_{90} = 25 s). Signal saturation occurred in only 9.9% of the pixels in the nucleus. Therefore, this cell was classified as “resealing < 120 s”. In the second example (Fig. 7.7B), the PI uptake curve (Fig. 7.8, gray) did not stabilize within 120 s, since t_{90} = 170 s. Signal saturation occurred in 16% of the pixels in the nucleus. Therefore, this cell was classified as “non-resealing”. In the third example (Fig. 7.7C), the PI uptake curve

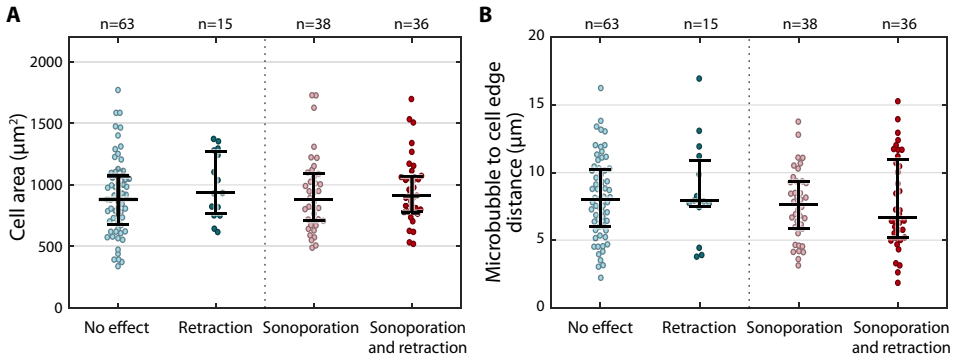

Figure 7.6: Effect of (**A**) cell area and (**B**) microbubble location on the cellular response. The medians and interquartile ranges are overlaid.

(Fig. 7.8, red) stabilized within 120 s, since $t_9 0 = 81$ s. However, 97% of the pixels in the nucleus were saturated, so this cell was classified as "saturated".

The pore size coefficient ($\alpha\pi DC_0 r_0$) and pore resealing coefficient (β) of all sonoporated cells are shown in Fig. 7.9A. The classification based on the resealing time of the pore and the signal saturation in the nucleus separates the cells into three groups. Additionally, the pore size coefficients (median and IQR between brackets) of the saturated class [0.97 (0.68 – 1.73) $\times 10^6$] were significantly (p<0.001) larger than that of the cells classified as resealing < 120 s [0.30 (0.14 – 0.45) $\times 10^6$] or non-resealing [0.18 (0.11 – 0.25) $\times 10^6$]. As shown in Fig. 7.9B, larger microbubble excursion amplitudes correlated with larger pore size coefficients upon sonoporation (Spearman correlation coefficient $\rho = 0.53$, $p < 0.001$). Moreover, the excursion amplitudes (median and IQR between brackets) of the saturated class [1.22 (1.03 – 1.45) µm] were significantly (p<0.001) larger than that of cells classified as resealing < 120 s [0.88 (0.77 – 1.13) µm] or non-resealing [0.89 (0.62 – 1.00) µm]. The microbubble excursion amplitude did not distinguish between resealing or non-resealing pores.

7.4. DISCUSSION

Sonoporation and the opening of cell-cell contacts upon ultrasound insonification of a single targeted microbubble were evaluated. Using high temporal and spatial resolution, we resolved both the microbubble oscillation and the cellular response. Susceptibility to sonoporation and opening of cell-cell contacts clearly depended on microbubble oscillation behavior and the initial state of the endothelial cell. Furthermore, quantification of sonoporation based on cellular PI uptake correlated with microbubble behavior and was used to assess reversibility of sonoporation.

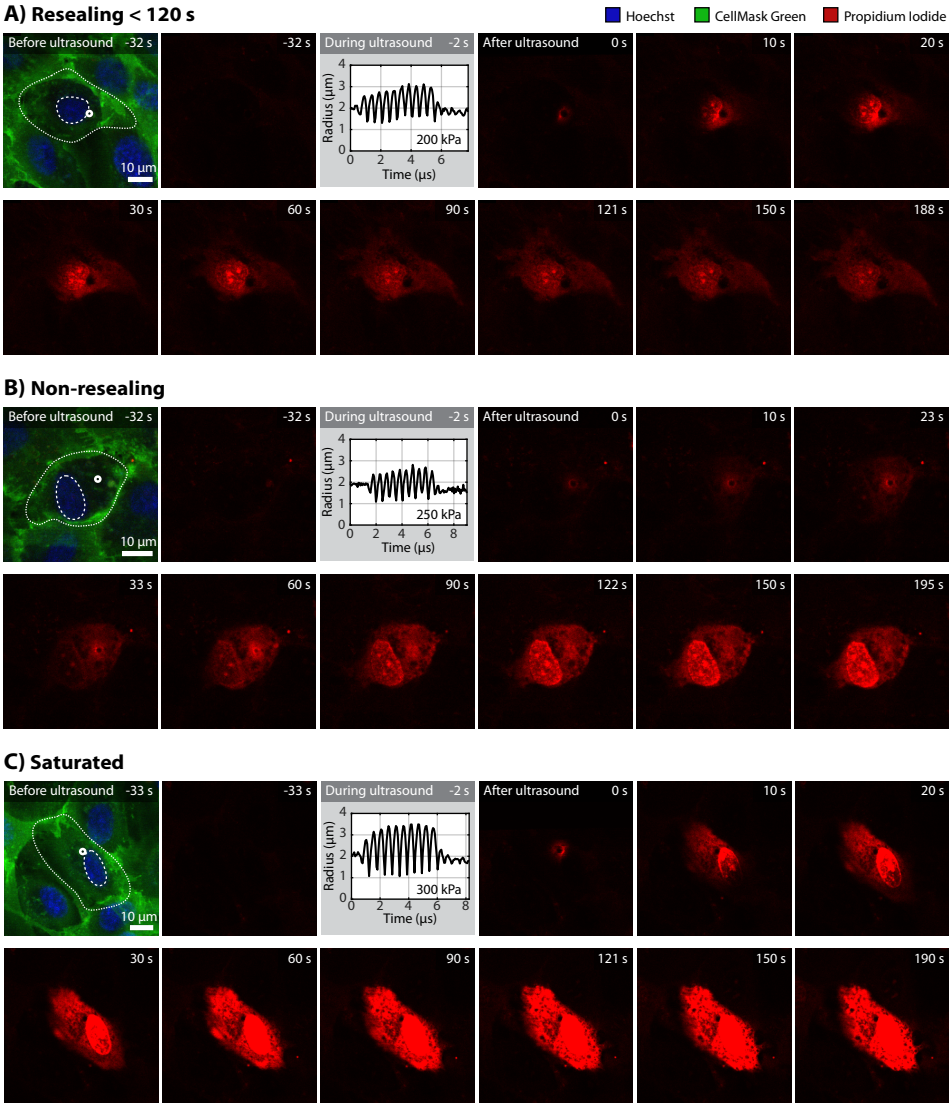

Figure 7.7: Different PI uptake categories upon sonoporation imaged with confocal microscopy. The initial cellular state is shown (composite image of CellMask Green, Hoechst, and PI) with the cell delineation (solid line), nucleus segmentation (dashed line), and microbubble location (white circle). During ultrasound insonification, the change in microbubble radius is shown as a function of time. All other frames show the PI imaging channel only, before and after ultrasound. (**A**) PI uptake classified as resealing < 120 s. (**B**) PI uptake classified as non-resealing. (**C**) PI uptake classified as saturated. The resulting PI uptake curves of each example are shown in Fig. 7.8.

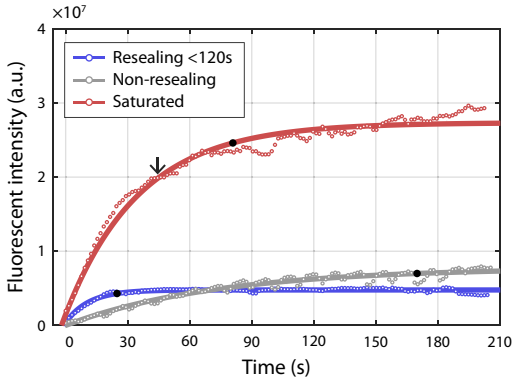

Figure 7.8: Cellular PI uptake curves shown as the fluorescent intensity as a function of time ($F(t)$, circles) and the corresponding fit to the mathematical model of Eq. 7.2 (solid lines). The three examples correspond to those in Fig. 7.7 for each category: resealing <120 s (blue, Fig. 7.7A), non-resealing (gray, Fig. 7.7B), and saturated (red, Fig. 7.7C). The black dots indicate the time t_{90} at which 90% of the asymptotic value was reached (Eq. 7.3). The arrow marks the time at which 90% of the pixels in the nucleus were saturated; a.u. = arbitrary unit.

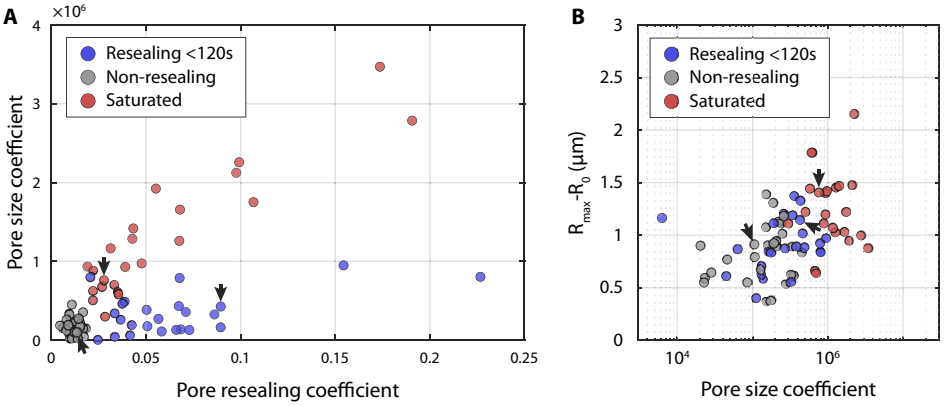

Figure 7.9: Quantification of PI influx upon sonoporation (n=74) and the resulting classification as resealing < 120 s (blue), non-resealing (gray), and saturated (red). The arrows indicate the data points corresponding to the examples in Fig. 7.7 and Fig. 7.8. (The pore size coefficient as a function of the pore resealing coefficient. (**B**) The microbubble excursion amplitude ($R_{max} - R_0$) as a function of the pore size coefficient; a.u. = arbitrary unit.

Microbubble oscillation behavior

The ultra-high-speed recordings of microbubble oscillation revealed that sonoporation correlated with large excursion amplitudes, while there was no direct relationship between microbubble excursion and the opening of cell-cell contacts (Fig. 7.3). Sonoporation was induced for absolute excursion amplitudes $R_{max} - R_0 > 0.7$ µm, similar to the previously found thresholds at 2 MHz of $R_{max} - R_0 >$ 0.72 µm (using 16 cycles) or > 1.02 µm (using 8 cycles) by Helfield et al. [53]. A relative vibration threshold of 0.5 at 1 MHz (with 6× 10 cycles) was reported by Kooiman et al. [15], which corresponds to an absolute threshold of $R_{max} - R_0 > 0.65$ µm (for a mean R_0 of 2.2 µm and symmetric oscillation), similar to our findings.

Microbubbles that induced sonoporation exhibited a second harmonic response more often than those that did not result in sonoporation. Since nonlinear behavior increases with microbubble excursion amplitude [212], this could be inherent to the larger excursions that result in sonoporation. We found no differences in the cellular response when the second harmonic amplitude was normalized to the fundamental (Fig. 7.4A). The E/C ratio was also higher in the case of sonoporation (Fig. 7.4B) only because the expansion phase becomes more dominant with increasing acoustic pressures, and thus excursion amplitudes [100, 166]. Van Wamel et al. [58] hypothesized that cells can better withstand compression than elongation forces, thereby suggesting that compression-only ($E/C < 0.5$) could be more effective in sonoporation. However, in this study we found that nonlinear or asymmetric microbubble behavior itself did not affect the cellular response.

The occurrence of sonoporation or opening of cell-cell contacts was found to be independent of the initial microbubble size for R_0 ranging from 1.24 to 3.72 μm, as previously found by others who studied similar size distributions [15, 53]. However, to achieve high enough excursion amplitudes while insonifying at relatively low acoustic pressures, the microbubble size distribution should match the ultrasound frequency such that microbubbles are insonified at resonance. In this study, microbubbles were insonified at their mean resonance frequency of 2 MHz [77]. We limited our study to a single frequency, since Helfied et al. [53] only showed subtle differences between 0.5, 1, and 2 MHz. The excursion amplitude, i.e. acoustic pressure, plays a more important role than the frequency of oscillation, i.e. the ultrasound frequency (within the clinically relevant range 0.5 to 4 MHz). However, the microbubble–cell interaction upon insonification with longer bursts or repeated treatment remains open for investigation. For instance, when using low acoustic pressures ≤ 200 kPa for longer treatment duration, the stimulation of the mechanosensory channels could possibly induce different drug delivery pathways, such as stimulated endocytosis [33].

The susceptibility to sonoporation or opening of cell-cell contacts was independent of the microbubble's location on the cell (Fig. 7.6B). This is favorable for the clinical applicability, since *in vivo* it would be impossible to control exact microbubble location on the cell membrane. Kooiman et al. [15] also found sonoporation to be independent of microbubble location, albeit based on a manual classification of microbubble positioning for 31 cells. Additionally, drug delivery was also independent of cell area (Fig. 7.6A), and thus all cell sizes seem to be equally susceptible to therapy.

Opening of cell-cell contacts due to sonoporation

Retraction of non-sonoporated cells was observed as often for both the control and ultrasound and microbubble experiments, while the enhanced retraction upon ultrasound and microbubbles only occurred upon sonoporation (Fig. 7.5B). From this we deduce that microbubble-mediated opening of cell-cell contacts only occurred due to sonoporation. Additionally, to open cell-cell contacts the targeted microbubble did not have to be near the cell edge (Fig. 7.6B), although that is often hypothesized [3, 33]. Therefore, our results suggest that the opening of cell-cell contacts is a biological response triggered upon sonoporation, instead of an independent drug delivery pathway mechanically induced by microbubble oscillation. The retraction did not directly correlate to microbubble oscillation behavior (Fig. 7.3) and was strongly affected by the initial cell state (Fig. 7.5B), in contrast to the mechanical induced effect of sonoporation. This reinforces our conclusion that opening of cell-cell contacts is a cellular response mechanism and not directly caused by a microbubble mechanically rupturing the junctions. To the best of our knowledge, this is the first study that investigated the relationship between these two microbubble-mediated vascular drug delivery pathways in real-time and in the same field of view. Live cell imaging showing opening of endothelial cell-cell contacts had only been reported for a single example and without studying its correlation with sonoporation [53].

The initial cell integrity affected the susceptibility to opening of cell-cell contacts, because it occurred significantly more often when cells initially had partial junctions (Fig. 7.5B. About 14% of cells with partial junctions even suffered from retraction in sham and in ultrasound only experiments, independent of the acoustic pressures. This retraction without treatment could be attributed to, for example, the imaging procedure (phototoxicity), the exposure of the CLINIcell to the open air after cutting out the top membrane, or the absence of 5% CO_2. The different susceptibility to microbubble-mediated treatment between partial and full junctions could mean that under physiological conditions that result in intercellular gaps, ranging from 0.3 - 4.7 μm in tumor vasculature [213, 214] or during inflammation [215, 216], the drug delivery pathway of opening cell-cell contacts is induced more often. At the same time, it emphasizes the importance of a realistic model to study the opening of cell-cell contacts. In previous studies, endothelial cell confluency varied from ≈70% to full confluency so not all cells were completely adjacent to their neighbors. Additionally, the integrity of the cell-cell contacts before treatment was not assessed in these previous studies [40, 53, 184]. The only example in literature reporting the opening of endothelial cell-cell contacts was on a not fully confluent monolayer of endothelial cells having partial junctions [53]. In our study, the initial cell integrity was assessed using a CellMask cell membrane dye. However, this dye does not specifically stain for intercellular junctions and can eventually internalize, leading to a poorer co-localization with the plasma membrane. In the current study the

plasma membrane remained well stained throughout the entire 120 min. Now that we observed the importance of the initial integrity of cell-cell contacts, in future studies the integrity of intercellular junctions could be more precisely assessed using specific fluorescent dyes.

A limitation of our study is that cellular response was only monitored up to 4 min after ultrasound insonification. Within that time frame it was not possible to study the recovery of cell-cell contacts, since Helfield et al. [53] showed that cell-cell contacts can remain open for tens of minutes. For long-term effects and recovery studies, the experimental conditions would need to be further optimized to reduce spontaneous retraction. Finally, when translating to *in vivo* studies often extravasation is assessed as a measure for the opening of intercellular junctions [23, 25], without monitoring sonoporation. If extravasation of a fluorescent compound would also be monitored *in vitro* using a different set-up than the CLINIcell, allowing for measurements on the basolateral side of the monolayer, both intracellular delivery by sonoporation and extravascular delivery by opening of intercellular junctions could be quantified. Additionally, since we found that retraction only occurred upon sonoporation, assessing cell membrane permeability and the possible resulting cell death *in vivo* is of great importance.

Transient pore formation

Based on cellular PI uptake upon sonoporation, the transient behavior of pore formation was quantified with the pore size and resealing coefficients, which resulted in three distinct classifications. Cells with pores that resealed within 120 s were assumed to be reversibly sonoporated, while irreversible sonoporation occurred when there was no resealing within 120 s [40]. We found that microbubble excursion amplitudes above 0.7 μm induced sonoporation, and the larger the excursion amplitude the bigger the pore that was created (Fig. 7.9B). This has never been observed before, since it was not possible to image both the microbubble oscillation behavior and detailed cellular response. Although intuitively there should be a higher chance for a small pore to reseal within 120 s, there was no clear correlation between pores resealing < 120 s and the pore size coefficient or microbubble excursion amplitude (Fig. 7.9B). Van Rooij et al.[40] also did not find a correlation between smaller pore size and resealing within 120 s. The intrinsic variability among cells seems to influence membrane resealing more than the microbubble behavior and pore size. Therefore, cellular recovery mechanisms should be further unraveled by studying the underlying resealing mechanisms.

The mathematical model described by Fan et al. [38] considers any PI uptake plateau to be caused by pore resealing. However, we observed that many of the cells that plateau within < 120 s, thus appearing to reseal, actually suffered from a saturated PI signal (Fig. 7.8 and 7.9). Saturation occurred when the pore size was largest. Reversibility of

sonoporation cannot be assessed for the saturation class since the pore might remain open while the corresponding PI increase can no longer be detected. It is unclear if previous studies accounted for PI stabilization due to either image saturation or DNA/RNA saturation [38, 40, 63]. Therefore, it is possible that cells were assumed to be reversibly sonoporated when PI uptake plateaued due to PI saturation. Another difference with a previous study is that we monitored the PI uptake within the entire cell, while van Rooij et al. [40], determined the PI uptake profiles only within the nucleus. Therefore, small pores that quickly resealed might be missed if their PI uptake profiles started in the cytoplasm. In future sonoporation studies the limited dynamic range of an imaging system should be considered. On the one hand, when interested in low uptake, i.e. small pores that quickly reseal, PI signal saturation for the larger pores is often inevitable. On the other hand, when interested in the high uptake, i.e. larger pores that do not or slowly reseal, the imaging settings can be adjusted such that image saturation is avoided while missing the initial and lower PI changes. However, in that case the fluorescent intensity could reach an equilibrium when there is no free DNA or RNA remaining for PI to bind to. Therefore, when avoiding image saturation, one should properly account for DNA/RNA saturation.

In this study we chose to have the cells on the bottom membrane of the CLINIcell to ensure that a targeted microbubble that did not bind would float up. Since the targeted microbubble was located between the objective and the cells, the microbubble gas core caused shadowing, impeding the laser to image directly underneath it (see Fig. 7.7A for an example). With this orientation it was not possible to directly image the created pore. Moreover, the imaging dependent calibration coefficient α (Eq. 7.1 and 7.2) was not determined in this study. Nevertheless, the pore size coefficient provides us with relative sizes because all imaging was performed under the same fluorescent imaging conditions, i.e. with the same α, and using the same extracellular PI concentration (C_0). Another limitation of this study is that reversibility could only be derived from the PI uptake profile. Literature has used two separate experiments to demonstrate the correlation between the occurrence of pore resealing within 120 s and cell viability [40]. However, if both the pore resealing timeline and cell viability were to be studied simultaneously with live cell microscopy, the underlying biological mechanisms leading to cell death could be further unraveled.

7.5. CONCLUSION

Using a state-of-the-art optical imaging system allowed for microbubble-mediated drug delivery to be studied with high sensitivity at short timescales, while also achieving the nanosecond resolution needed to resolve microbubble oscillation. Sonoporation and opening of cell-cell contacts by ultrasound insonification of targeted microbubbles were investigated. We found that larger microbubble excursion amplitudes ($R_{max} - R_0 > 0.7$ μm) correlated with the occurrence and amount of sonoporation, while the opening of cell-cell contacts could not be predicted from microbubble behavior. Microbubble-mediated opening of cell-cell contacts only occurred upon sonoporation and was influenced significantly by the initial cell state. Therefore, our results suggest that opening of cell-cell contacts is a biological response as a consequence of sonoporation, instead of an independent drug delivery pathway. These novel insights will aid the development of safe and efficient microbubble-mediated drug delivery.

ACKNOWLEDGEMENT

This work was supported by the Applied and Engineering Sciences TTW (Veni-project 13669), part of NWO. The authors would like to thank Phoei Ying Tang from the Department of Biomedical Engineering for assistance during experiments and cell culture and Michiel Manten and Geert Springeling from the Department of Experimental Medical Instrumentation for technical assistance, all from the Erasmus Medical Center, the Netherlands.

SUPPLEMENTARY MATERIAL

Supplementary data to this article can be found online at http://doi.org/10.1016/j.jconrel.2020.03.038.

Supplementary Videos

Video 1. Time-lapse confocal microscopy imaging showing sonoporation upon a single oscillating microbubble (corresponding to Fig. 7.2A). Ultrasound insonification occurred at the 32 s timestamp, during which confocal microscopy was temporarily intercepted for Brandaris 128 ultra-high-speed imaging of microbubble oscillation. The pseudo-colored video shows cell nuclei in blue, cell membranes in green, and propidium iodide in red, and is displayed 20× faster than real time (at 13 frames per second).

Video 2. Time-lapse confocal microscopy imaging showing sonoporation and retraction upon a single oscillating microbubble (corresponding to Fig. 7.2B). Ultrasound insonification occurred at the 31 s timestamp, during which confocal microscopy was temporarily intercepted for Brandaris 128 ultra-high-speed imaging of microbubble oscillation. The pseudo-colored video shows cell nuclei in blue, cell membranes in green, and propidium iodide in red, and is displayed 20× faster than real time (at 13 frames per second).

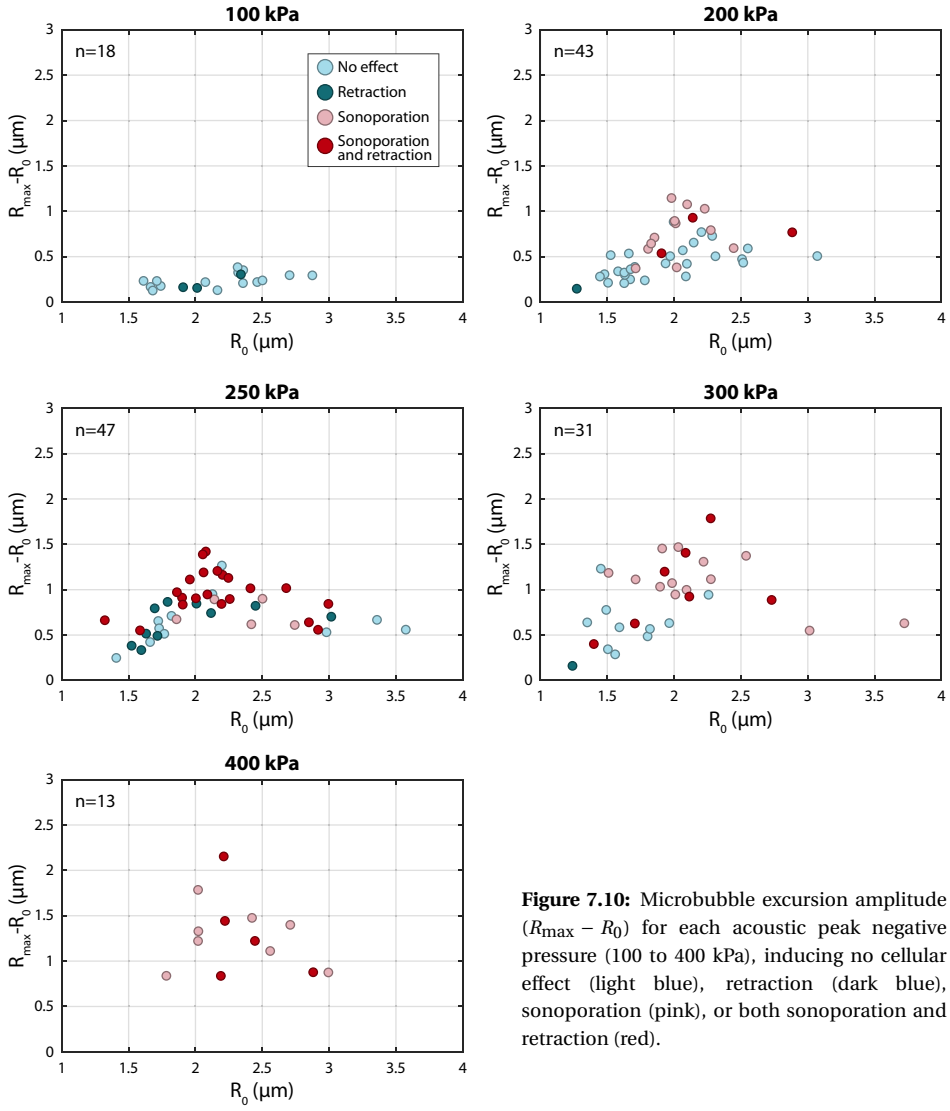

Figure 7.10: Microbubble excursion amplitude ($R_{\max} - R_0$) for each acoustic peak negative pressure (100 to 400 kPa), inducing no cellular effect (light blue), retraction (dark blue), sonoporation (pink), or both sonoporation and retraction (red).

8

Lipid phase and ligand distribution in microbubble coatings

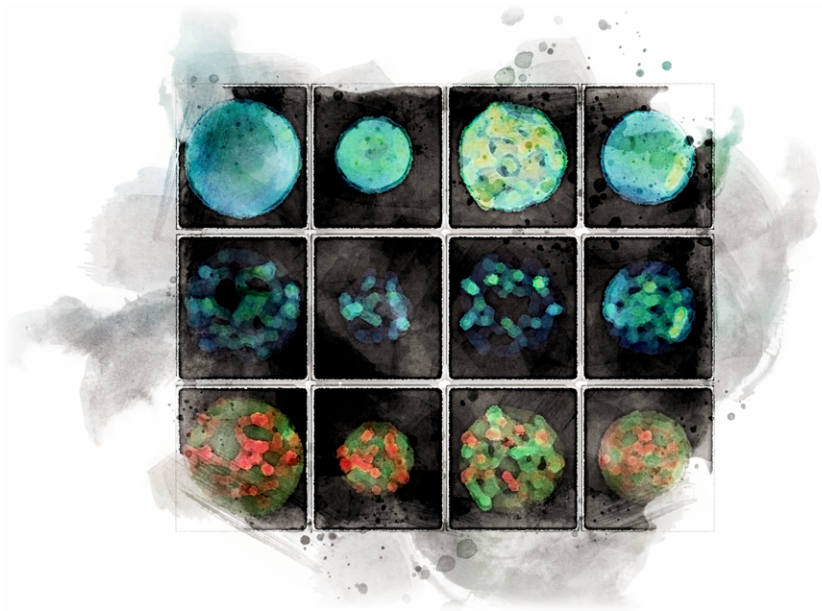

Based on:
Simone A. G. Langeveld, Christian Schwieger, **Inés Beekers**, Jacob Blaffert, Tom van Rooij, Alfred Blume, Klazina Kooiman, "Ligand distribution and lipid phase behavior in phospholipid-coated microbubbles and monolayers", *Langmuir*, vol. 36, no. 12, pp. 3221-3233, 2020 [217].

Abstract

Phospholipid-coated targeted microbubbles are ultrasound contrast agents that can be used for molecular imaging and enhanced drug delivery. However, a better understanding is needed of their targeting capabilities, and how they relate to microstructures in the microbubble coating. Here we investigated the ligand distribution, lipid phase behavior, and their correlation in targeted microbubbles of clinically relevant sizes, coated with a ternary mixture of 1,2-dipalmitoyl-sn-glycero-3-phosphocholine (DPPC) or 1,2-distearoyl-sn-glycero-3-phosphocholine (DSPC), with PEG40-stearate and DSPE-PEG2000. To investigate the effect of lipid handling prior to microbubble production in DSPC-based microbubbles, the components were either dispersed in aqueous medium (direct method) or first dissolved and mixed in organic solvent (indirect method). To determine the lipid phase behavior of all components, experiments were conducted on monolayers at the air/water interface. In comparison to pure DSPC and DPPC, the ternary mixtures had an additional transition plateau around 10-12 mN/m. As confirmed by Infrared Reflection Absorption Spectroscopy (IRRAS), this plateau was due to a transition in the conformation of the PEGylated components (mushroom to brush). While the condensed phase domains had a different morphology in the ternary DPPC and DSPC monolayers on the Langmuir trough, domain morphology was similar in the coating of both ternary DPPC and DSPC microbubbles (1.5 - 8 μm diameter). The ternary DPPC microbubbles had a homogenous ligand distribution and significantly less LC phase area in their coating than the DSPC-based microbubbles. For ternary DSPC microbubbles, the ligand distribution and LC phase area in the coating depended on the lipid handling. The direct method resulted in a heterogeneous ligand distribution, less LC phase area than the indirect method, and the ligand colocalizing with the LE phase area. The indirect method resulted in a homogenous ligand distribution with the largest LC phase area. In conclusion, lipid handling prior to microbubble production is of importance for a ternary mixture of DSPC, PEG40-stearate, and DSPE-PEG2000.

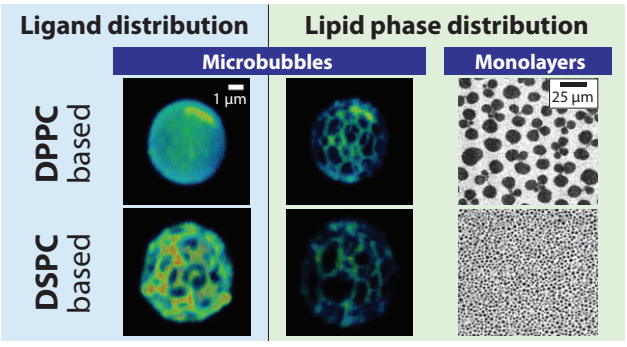

8.1. INTRODUCTION

Microbubbles with a diameter of 1 to 10 μm have been used as ultrasound contrast agents for non-invasive diagnostic imaging of perfusion since they became available for clinical use in the 1990s [218]. When administered intravenously, these microbubbles are too large to extravasate and therefore function as blood pool agents [219]. The gas core of a microbubble compresses and expands in response to ultrasound. This feature not only provides contrast for ultrasound imaging but can also induce bioeffects in nearby cells, resulting in locally enhanced drug delivery [3, 34]. The gas core of the microbubble is usually stabilized by a phospholipid, protein, or polymer coating, which prolongs its lifetime by reducing surface tension and gas diffusion. The coating can be functionalized by incorporating a ligand such that these microbubbles can be targeted to specific biomarkers expressed by cells. Novel targeted microbubbles are being developed for ultrasound molecular imaging of cancer and cardiovascular disease and for therapeutic applications [3, 87, 220, 221]. However, before there can be widespread use of targeted microbubbles in the clinic, a better understanding and control is needed of the acoustic response and targeting, especially the ligand distribution on the microbubble coating.

A common type of coating for clinically approved microbubbles consists of a monolayer of phospholipids and emulsifiers, such as in Definity® (Luminity™ in Europe; coating composition: 1,2-dipalmitoyl-*sn*-glycero-3-phosphocholine (DPPC), 1,2-dihexadecanoyl-*sn*-glycero-3-phosphate (DPPA), and 1,2-dipalmitoyl-*sn*-glycero-3-phosphoethanolamine(polyethylene glycol) (DPPE-PEG5000; MW 5000)) [89], and Lumason® (SonoVue™ in Europe; coating composition: 1,2-distearoyl-*sn*-glycero-3-phosphocholine (DSPC), polyethylene glycol (PEG4000; molecular weight (MW) 4000), and 1,2-dihexadecanoyl-*sn*-glycero-3-phospho-(1'-rac-glycerol) (DPPG)) [90]. Many experimental microbubbles are in-house produced analogues of these clinically approved microbubbles, consisting of a main phospholipid component such as DPPC (C16 tail) or DSPC (C18 tail), and an emulsifier such as polyoxyethylene(40) stearate (PEG40-stearate) and/or 1,2-distearoyl-*sn*-glycero-3-phosphoethanolamine-N-carboxy(polyethylene glycol) (DSPE-PEG2000) [99, 222–224]. For the production of targeted microbubbles, a ligand is typically coupled to DSPE-PEG2000 by biotin–avidin bridging or an alternative method of chemical coupling [87].

Although it is generally assumed that the ligand, that is, DSPE-PEG2000 lipid, covers the microbubble surface uniformly, heterogeneous ligand distributions have been reported for DSPC-based microbubbles coated with binary and ternary mixtures [88, 223]. One study illustrated that the ligand distribution could be altered from heterogeneous to homogenous in microbubbles coated with DSPC and DSPE-PEG2000 (9:1) by different heating–cooling protocols [223].

We have previously shown that the main phospholipid component influences the ligand distribution because for DPPC-based microbubbles the ligand distribution in ternary coating mixtures was homogenous in contrast to a heterogeneous distribution in DSPC-based microbubbles [88]. Increased probability of successful binding of a targeted microbubble is expected when the ligand is distributed homogeneously over the microbubble coating. This is especially important in large vessels where blood flow is high and targeting is more challenging [157]. It therefore remains to be explored if there are other ways to tune the ligand distribution in DSPC-based ternary coated microbubbles.

Next to a homogeneous ligand distribution for optimal targeting, the acoustic response of the microbubble is important for safe and effective use in therapeutic applications [34]. Microbubbles coated with a DPPC-based ternary mixture proved to be less acoustically stable than those coated with a DSPC-based ternary mixture [77]. Both these types of microbubbles show a large variation in their response to ultrasound [68, 77], even when their size distribution is monodisperse [65]. Kim et al. [99] proposed that the acoustical properties of the microbubbles are influenced by microstructures in the coating. Microstructures are formed as a result of the phase behavior and miscibility of the different components [225], and can be influenced by the conformation of the polymer chain for PEGylated components, which can be either in a brush or mushroom state [226]. The degree of phase separation in the microbubble coating was also found to influence the subharmonic response [155].

The phospholipid DPPC can transition from the liquid expanded (LE) to the liquid condensed (LC) phase during monolayer compression [227], whereas the phospholipid DSPC is always in the LC phase at room temperature [228].In addition, the emulsifier PEG40-stearate is known to be in the LE phase only, [222], whereas DSPE-PEG2000 in a binary mixture with DSPC could transition from the LE to LC phase depending on the concentration and surface pressure [229]. Studies using binary lipid mixtures (phospholipid with C18 to C24 tail and PEG40-stearate) demonstrated that microbubble coatings had microstructures with larger domain sizes when they were cooled at a slower rate after production by probe sonication [99]. Another study confirmed LE and LC phase coexistence in binary microbubble coatings (phospholipids with C12 to C24 tail and PEG40-stearate), and domain morphologies varied depending on the cooling rate as well [222].

Next to the lipid phase behavior, microstructures in the microbubble coating are also influenced by the miscibility and conformation (mushroom or brush) of the PEGylated components. The most widely used emulsifiers PEG40-stearate and DSPE-PEG2000 have one and two acyl chains, respectively [224].When microbubbles coated with a binary mixture of DSPC and PEG40-stearate (9:1) were studied with confocal microscopy, no domains were observed in microbubbles smaller than 5 μm [230], suggesting that there was no phase separation. Lozano and Longo concluded

from their phase diagrams of monolayers at an air/water interface that DSPC and DSPE-PEG2000 are immiscible at all relevant pressures because DSPC is always in LC phase, whereas DPPC and DSPE-PEG2000 were miscible in both LE and LC phases [229]. Another study focused on the distribution of DSPE-PEG2000, with a fluorescent ligand attached, in microbubbles (diameter > 10 μm) coated with DSPC and DSPE-PEG2000 (9:1). DSPE-PEG2000, that is, the ligand, was heterogeneously distributed and colocalized with the LE phase as reported for a single example, yet no quantification was performed [223]. Up to now, the ligand distribution and lipid phase coexistence in microbubble coatings have not been quantified simultaneously in individual microbubbles.

A major difference between studies that evaluated microbubbles coated with a binary mixture and those coated with a ternary mixture is the handling of phospholipid components during microbubble production. For binary mixtures, the components were generally dissolved and premixed in organic solvent first, then dried to form a lipid film, and dispersed in aqueous medium before microbubbles were produced [222, 223, 230] (i.e. *indirect method*). For ternary mixtures, the components were generally dispersed directly in aqueous medium before microbubble production [88, 93, 231, 232] (i.e. *direct method*). Based on the effect of cooling rate on microstructures in large microbubbles (>10 μm) after microbubble production [222], we hypothesize that the method of handling the lipids prior to microbubble production may also influence the ligand distribution and/or lipid phase in the coating of microbubbles. The ligand distribution, that is, the location of the ligand on the microbubble surface, is important for the binding probability while the lipid phases are expected to affect the elasticity and viscosity of the coating and thereby influence the acoustical performance.

The main objective of this study was to determine the DSPE-PEG2000 (i.e., ligand) distribution and lipid-phase behavior in microbubbles of clinically relevant sizes (diameter 2 – 8 μm) coated with a ternary mixture of DPPC or DSPC as main component and both PEG40-stearate and DSPE-PEG2000 as emulsifiers. Microbubbles were made by probe sonication after which the ligand distribution and lipid phase behavior in the microbubble coatings were visualized with high axial resolution 4Pi confocal microscopy. In addition, the relationship between the ligand distribution and the lipid phase behavior was investigated by quantifying the co-localization of ligand and LE phase. Previous studies have shown that DSPC-based microbubbles were acoustically more stable than DPPC-based microbubbles [77], but they had a heterogeneous ligand distribution [88]. We therefore also investigated the effect of lipid handling on the ligand distribution in DSPC-based microbubbles. To gain insights into the physicochemical properties of the ternary mixtures, we first focused on characterizing the lipid phase behavior and PEG conformation in monolayers at an air/water interface. Because the phospholipid molecules (1 nm^2)

[233] in the microbubble coating are so much smaller than the total surface area ($0.3 - 0.8 \times 10^8$ nm^2 for microbubbles of 3 – 5 μm diameter), the coating can be regarded as a flat monolayer, despite the spherical shape of the microbubble. Compression isotherms were obtained and were used together with fluorescence microscopy to visualize the lipid phase behavior of the ternary mixtures. Infrared reflection absorption spectroscopy (IRRAS) was performed to determine the phase and conformation of the individual components during monolayer compression.

8.2. MATERIALS AND METHODS

Materials

DPPC, DSPE-PEG2000, and 1,2-distearoyl-*sn*-glycero-3-phosphoethanolamine–N–biotinyl (polyethylene glycol) (DSPE-PEG2000-biotin), as well as the chain deuterated lipids DPPC-d_{62} and DSPC-d_{70} were purchased from Avanti Polar Lipids (Alabaster, Alabama, USA). DSPC and PEG40-stearate were obtained from Sigma-Aldrich (Zwijndrecht, the Netherlands). Perfluorobutane (C_4F_10) was purchased from F2 Chemicals (Preston, UK) and argon gas was purchased from Linde Gas Benelux (Schiedam, the Netherlands). Streptavidin Oregon Green 488 was purchased from BioSynthesis (Louisville, Texas, USA) and Lissamine Rhodamine B 1,2-dihexadecanoyl-*sn*-glycero-3-phosphoethanolamine, triethylammonium salt (rhodamine-DHPE) was purchased from Thermo Fisher (Waltham, Massachusetts, USA).

Monolayer Compression Isotherms

Monolayer compression isotherms were obtained at 20°C with a Langmuir trough (sample trough 6.8 × 80 cm^2) purchased from Riegler and Kirstein GmbH (Berlin, Germany) equipped with movable barriers and a Wilhelmy pressure sensor with a filter paper functioning as pressure probe. The pressure sensor was calibrated prior to each experiment to a surface pressure of 0 mN/m in water and 72 mN/m in air. The temperature was maintained at 20°C by a circulation water bath. The complete setup was placed inside a hood to reduce dust deposition and water evaporation. Monolayers of pure DPPC or DSPC, a binary mixture (composition in mol%: DPPC or DSPC 92.4; DSPE-PEG2000 7.6), or ternary mixture (composition in mol%: DPPC or DSPC 84.8; PEG40-stearate 8.2; DSPE-PEG2000 5.9; DSPE-PEG2000-biotin 1.1) was spread on a surface of phosphate-buffered saline (PBS) as the subphase buffer solution. The binary mixture with 7.6 mol% DSPE-PEG2000 was chosen based on previously published work on microbubbles coated with a binary mixture of DPPC or DSPC (92.4 mol %) and DSPE-PEG2000 (7.6 mol%) [234], having the same molar ratio of 12:1 for the main lipid to DSPE-PEG2000 as the ternary mixtures studied. Chloroform/methanol (9:1 v/v) was used as the spreading solvent [235] and allowed to evaporate for at least 15 min [236] before starting compression with a speed of 2 $\AA^2$

molecule^{-1} min^{-1}. The surface pressure was recorded during compression with a time resolution of 2 s with RUK trough control software (Riegler and Kirstein GmbH).

Monolayer Fluorescence Microscopy

To study the lipid organization with fluorescence microscopy, rhodamine-DHPE (0.01 mol %) was added to the DPPC- and DSPC-based ternary mixtures before spreading the monolayer. Because this dye does not diffuse into the LC phase [175], all dark areas are lipids in the LC phase and all areas with a fluorescent signal are in a more fluid phase, that is, LE phase. The monolayers were spread on a Langmuir trough (sample trough 9.9 × 26 cm^2; Riegler and Kirstein GmbH) and imaged during compression with an Axio Scope A1 Vario epifluorescence microscope (Carl Zeiss MicroImaging, Jena, Germany) equipped with a mercury arc lamp (HXP 120 C) for excitation, a long working distance objective (NEOFLUAR 50×), and a filter/beam splitter set (Zeiss Filter Set 09), which allows excitation between 450 and 490 nm and detection of emitted light above 515 nm. Images were recorded with an EMCCD Camera (ImageEM, C9100-13, Hamamatsu, Herrsching, Germany) and the surface pressure was recorded as described previously.

IRRAS Experiments

On the basis of the isotherms and the fluorescence microscopy images, it is not possible to distinguish the phase state of the individual components in the ternary mixtures. To investigate the phase behavior of the individual components, IRRAS experiments were performed. The use of chain-deuterated phospholipids (DPPC-d_{62} or DSPC-d_{70}) in the ternary mixtures allowed us to distinguish the signal from the PEGylated (CH_2 vibrations) and non-PEGylated (CD_2 vibrations) components. The IRRAS measurements were performed using a Bruker Vector 70 FT-IR spectrometer equipped with a nitrogen-cooled MCT detector and an A511 reflection unit (Bruker Optics, Ettlingen, Germany), placed over a Langmuir trough setup (Riegler and Kierstein GmbH). The sample trough (6 × 30 cm^2) was set up according to the protocol described above. A circular reference trough (3 cm radius) placed next to the sample trough could be brought into the focus of the IR beam by means of a shuttle. Both troughs were filled with PBS as the subphase buffer solution and lipid mixtures were spread in the sample trough as described above. The filling levels of both troughs were kept equal and constant by means of an automated, laser reflection-controlled, pumping system connected to PBS reservoirs. The IR beam was coupled out from the spectrometer and focused by mirrors onto the buffer or film surface at an incidence angle of ϕ = 60°. A KRS-5 polarizer was used to generate perpendicular polarized light. The compression of the monolayer was performed at 2 Å^2 molecule^{-1} min^{-1}. The compression was stopped at several predefined areas per lipid chain, as indicated in Fig. 8.3B,D, to record at least three IRRA spectra

at constant molecular area before the compression was continued. Spectra were recorded with a spectral resolution of 4 cm^{-1} and 160 kHz scanner velocity. One thousand single interferograms were zero-padded with a factor of two and averaged, followed by fast Fourier transformation, resulting in a nominal spectral resolution of 2 cm^{-1}. IRRA spectra were calculated from the reflectivity on the monolayer covered surface (R) and the bare buffer surface (R_0) according to reflection absorption $RA = -\log(R/R_0)$. All IRRA spectra were corrected for atmospheric water vapor absorption using OPUS software (Bruker Optics GmbH, Ettlingen, Germany) and set to a common baseline in a spectral range where no absorptions occurred (4500 – 4600 cm^{-1}). The maxima of the CH_2 (2800 – 2950 cm^{-1}) and CD_2 (2020 – 2270 cm^{-1}) stretching vibrational bands were determined using the standard method of the OPUS software. The peak positions were averaged for spectra recorded at the same lipid molecular area and surface pressure and are presented together with their standard deviation. The presented spectra are averages of all spectra recorded at the same monolayer state. To identify the contribution of the phospholipid headgroups to the transitions, principal component analysis (PCA) [143, 144] was done with the *princomp* function of MATLAB. PCA was chosen to analyze the variation in the data by computing principal components (PC), which can be used to determine the variable responsible for the largest variance in the dataset. Corresponding scores were used to determine the contribution of each spectrum to this main variance. For the analysis, the spectral regions between 1050 and 1300 cm^{-1} for headgroup vibrations and 2020 – 2270 cm^{-1} for CD_2 stretching vibrations were selected from the IRRA spectra recorded at various surface pressures. From both spectral ranges, a linear baseline was subtracted before they were normalized to a vector norm of unity. Subsequently, both subspectra were combined to a single input vector for the PCA, where the wavenumbers were the variables and the surface pressures the conditions. The first principal components and the respective scores are presented in the Results and Discussion section. Scores of the higher principal components did not change systematically with film compression.

Microbubble Production

Biotinylated lipid-coated microbubbles (composition in mol%: DSPC or DPPC 84.8; PEG40-stearate 8.2; DSPE-PEG2000 5.9; DSPE-PEG2000-biotin 1.1) with a C_4F_{10} gas core were made by probe sonication at 20 kHz with a Sonicator Ultrasonic Processor XL2020 at power setting 10 (HeatSystems, Farmingdale, NY, USA) for 10 s as described previously [93]. The coating components were prepared in two different ways. (1) For the direct method, all components were dissolved in PBS with a final concentration of 2.5 mg/mL DSPC or DPPC, 0.625 mg/mL PEG40- stearate, 0.625 mg/mL DSPE-PEG2000, and 0.125 mg/mL DSPE-PEG2000- biotin. Fluorescent dye rhodamine-DHPE (0.01 mol%) was added to study the lipid phase organization in the microbubble coating. (2) For the indirect method, DSPC, PEG-40 stearate,

DSPE-PEG2000, and DSPE-PEG2000-biotin were dissolved in chloroform/ methanol (9:1 vol/vol). The organic solvent was then evaporated with argon gas and the obtained lipid film was dried under vacuum overnight. Finally, the lipid film was dispersed in PBS with a final concentration of 2.5 mg/mL DSPC or DPPC, 0.625 mg/mL PEG40-stearate, 0.625 mg/mL DSPE-PEG2000, and 0.125 mg/mL DSPE-PEG2000- biotin, fluorescent dye rhodamine-DHPE (0.01 mol%) was added, the solution was placed in a sonicator bath for 10 min, and a probe sonicator was used at power setting 3 for 5 min. The three types of microbubbles produced are referred to as "direct DPPC", "direct DSPC", or "indirect DSPC" microbubbles.

Microbubble Fluorescence Imaging

The fluorescent ligand streptavidin Oregon Green 488 was conjugated to the biotinylated microbubbles as described previously by Kooiman et al. [88], allowing us to determine the distribution of DSPE-PEG2000-biotin over the lipid phases in the microbubble coating. Briefly, 0.9 mL microbubble solution was placed in a 3 mL syringe and topped with 2.1 mL PBS saturated with C_4F_{10} for washing by flotation. The subnatant was drained after 45 min, and the microbubbles were resuspended in 0.3 mL PBS saturated with C_4F_{10} and collected. Next, 22.5 µL of streptavidin (2 mg/mL) was added to 0.7-1.0 × 10^8 microbubbles. After incubation on ice for 30 min, the excess streptavidin was washed by flotation, as described above, and resuspended in 0.2 mL of PBS saturated with C_4F_{10}.

A Coulter Counter Multisizer 3 (Beckman Coulter, Mijdrecht, the Netherlands) was used to measure the microbubble size distribution. A 50 µm aperture tube was used for quantification of particles between 1 and 30 µm with a linear spacing between the 256 channels. The size distribution of the samples was evaluated by the span value, which illustrates the width of the distribution, defined as $(d90\% - d10\%)/d50\%$, where $d90\%$, $d10\%$, and $d50\%$ are the microbubble diameters below which 90, 10, and 50% of the cumulative number of microbubbles was found.

After conjugation with streptavidin Oregon Green 488, microbubbles were visualized as described by Kooiman et al. [88]. To reduce Brownian motion, microbubbles were placed in 87% glycerol (v/v in PBS) and visualized using a Leica TCS 4Pi confocal laser-scanning microscope [237]. The 87% was chosen because this has the same refractive index as the quartz glass and glycerol objective of the 4Pi microscope. This high-resolution imaging system has a matched pair of aligned opposing 100× glycerol HCX PL APO objective lenses (Numerical aperture 1.35), increasing the axial resolution up to 90 nm. A 488 nm laser was used for excitation of Oregon Green 488 and a 561 nm laser was used for excitation of rhodamine-DHPE. Image stacks were recorded as y-stacked xz-scans in a green (500 – 550 nm) and red (580 – 640 nm) spectral channel. The software AMIRA (Version 2019.1, FEI, Mérignac Cedex, France) was used to volume-render the image stacks with the "voltex" function.

Microbubble Data Analysis

Custom-developed image analysis software in MATLAB (Mathworks, Natick, MA, USA) was used for quantitative analysis of the 4Pi microscopy data. The ligand distribution was analyzed based on the method described by Kooiman et al. [88]. First, a circle was fitted through the fluorescence intensity maxima of the green channel (Oregon Green 488, 500 – 550 nm) and per xz-slice a region of interest (ROI) was defined in a band of 7 pixels around the fitted circle. Only slices with an ROI radius larger than 75% of the radius in the equatorial plane ROI were included in the analysis. Each of the ROIs was divided into 32 angular parts and the mean fluorescence pixel intensity (I_{part}) was calculated for each of those parts. The I_{part} values were plotted per microbubble as a function of the axial plane and the microbubble circumference in 2D color-coded heatmaps (Supplemental Fig. 8.1A). On average, 30 xz-slices were included per microbubble, resulting in an average of 960 angular parts per microbubble. The median intensity of all the angular parts (I_{median}) was calculated for each microbubble. The image analysis software classified an individual angular part as inhomogeneous when the absolute difference between I_{part} and I_{median} was more than two-third times the value of I_{median} (i.e., $|I_{\text{part}} - I_{\text{median}}| > 2/3 \times I_{\text{median}}$). The percentage of parts classified as inhomogeneous was calculated per microbubble as a measure for the inhomogeneity of the ligand distribution. After this analysis, an adapted version of the software was used to analyze the lipid phase behavior in the red channel (rhodamine-DHPE, 580 – 640 nm). The same xz-slices and ROIs were used as those obtained during the ligand distribution analysis. Again, the ROIs were divided in 32 angular parts and the mean fluorescence pixel intensity ($I_{\text{part-rhod}}$) in each part was calculated. From these, the median part intensity ($I_{\text{median-rhod}}$) was calculated per microbubble and plotted as 2D color-coded heatmaps (Supplemental Fig. 8.1B). The software classified an individual angular part as LC phase when the value of $I_{\text{part-rhod}}$ was less than one-third of $I_{\text{median-rhod}}$ (i.e., $I_{\text{part-rhod}} < 1/3 \times I_{\text{median-rhod}}$) (Supplemental Fig. 8.1C). The LC phase surface area was determined per microbubble in μm^2 and presented as percentage of the total analyzed surface area per microbubble. To study if the ligand colocalized with the parts classified as LC areas, the median fluorescence intensity of the green channel (ligand) was calculated for all parts in LC phase and for those not in LC phase (Supplemental Fig. 8.1D-E). The ratio between these two values was defined as the colocalization ratio.

IBM SPSS Statistics 25 was used to perform statistical analysis. The distribution of the data was assessed using a Shapiro-Wilk test. The data on ligand inhomogeneity was not normally distributed ($p < 0.001$) for all microbubble types. The data on the LC phase area was only normally distributed for direct DPPC ($p = 0.228$), not for direct DSPC ($p = 0.002$) and indirect DSPC ($p < 0.001$) microbubbles. The colocalization ratio was normally distributed (DPPC: $p = 0.168$, DSPC direct method: $p = 0.203$, DSPC indirect method: $p = 0.334$). Therefore, the Mann-Whitney U test was used to test

if the microbubble types had a significant difference in inhomogeneity of the ligand distribution and LC phase area. For the colocalization ratio a regular t-test was used to analyze the differences between the microbubble types. Differences were regarded as significant at p-value < 0.01.

8.3. RESULTS AND DISCUSSION

Monolayer Compression Isotherms

The results of the Langmuir trough experiments are presented in Fig. 8.1. All curves are representative of the results from three or more experiments. In accordance with literature [227, 229], there was a clear difference between the isotherms of pure DPPC (Fig. 8.1A, black line) and DSPC (Fig. 8.1C, black line) as DPPC had a transition from the LE to LC phase at a surface pressure (π) of ~ 5 mN/m, whereas DSPC did not form an LE phase and therefore underwent a direct gaseous to LC phase transition. The binary mixture with 7.6 mol% DSPE-PEG2000 was chosen based on previously published work on microbubbles coated with a binary mixture of DPPC or DSPC (92.4 mol%) and DSPE-PEG2000 (7.6 mol%) [234]. For DPPC in mixtures with PEGylated compounds, we observed two transitions (Fig. 8.1A,B). The transition from the LE to LC phase of DPPC occurred almost at the same surface pressure in the binary mixture (DPPC/DSPE-PEG2000), whereas it was slightly shifted to a lower pressure in the ternary mixture containing PEG40-stearate. This shift to a lower surface pressure is due to the long stearoyl chain of the PEG40-stearate increasing the stability of an LC phase. In the binary mixture, a second transition at ~10 mN/m was observed (Fig. 8.1B, orange line). In the ternary mixture with a higher content of PEGylated components, the second transition moved to ~12 mN/m (Fig. 8.1B, blue line). For DSPC in mixtures with PEGylated lipid components, we observed phase transition plateaus only at ~10 mN/m (Fig. 8.1B, blue line, binary mixture) and ~12 mN/m (Fig. 8.1D, blue line, ternary mixture), simliar to the second transition in DPPC-based mixtures (Fig. 8.1C,D, orange and blue lines). Again, the transition pressure increased with the increasing content of PEGylated components. As the transition ≥10 mN/ m is independent of the type of phospholipid, we assume that it is due to the so-called mushroom to brush transition of the PEG chains attached to the lipid headgroups [238–240]. Theoretical calculations of the mushroom to brush transition [241] for the binary mixture in this study is 45 $\mathring{A}^2$ (lipid chain)$^{-1}$ (see Supplemental Fig. 8.2 which is in agreement with the experimental findings of 30 – 60 $\mathring{A}^2$ (lipid chain)$^{-1}$. For the ternary mixture, the calculated mushroom to brush transition is 87 $\mathring{A}^2$ (lipid chain)$^{-1}$ (see Supplemental Fig. 8.2 which is only slightly higher than the experimentally observed 60 –80 $A_M/\mathring{A}^2$ (lipid chain)$^{-1}$. The difference could be explained by the polydispersity of the PEG40-stearate [242] because a decrease in chain length lowers the Flory radius.

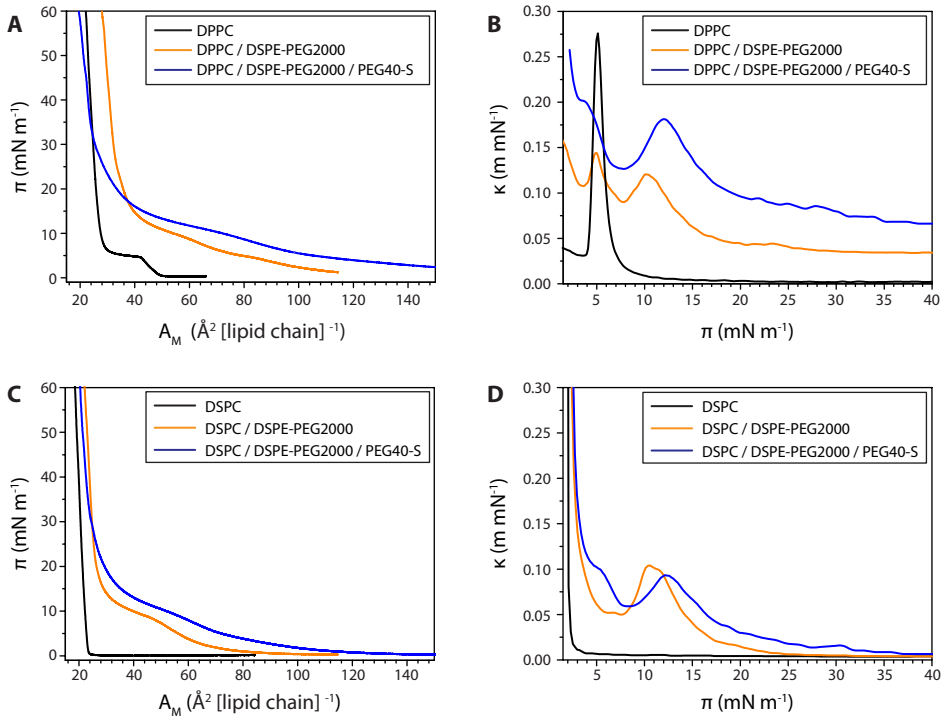

Figure 8.1: Langmuir isotherms of pure, binary (92.4:7.6 mol%), and ternary (84.8:7.0:8.2 mol%) mixtures with (A) DPPC or (C) DSPC as main lipid components and DSPE-PEG2000 and/or PEG40-stearate (PEG40-S) as additional components. (**A**,**C**) Surface pressure (π) as a function of the area per molecule (A_M). (**B**,**D**) Derived compressibility (κ) as a function of the surface pressure (π) where the peaks indicate transition plateaus. Representative curves are shown of at least three repeated experiments.

8

The isotherms of the binary mixtures presented here are in agreement with literature for the same binary mixtures [229, 243]. By contrast, another study on binary mixtures of DSPC with DSPE-PEG2000 or PEG40-stearate (9:1) found that the mixture with DSPE-PEG2000 had an isotherm similar to that of pure DSPC, while the binary mixture with PEG40-stearate had an extra transition plateau around 35 mN/m [230]. This was attributed to expulsion of material from the monolayer, sometimes referred to as squeeze-out [222].However, in the present study, we observed no squeeze-out plateau in the ternary mixtures that contained PEG40-stearate. This may be explained by the differences in concentration of PEG40- stearate (10 vs 8 mol%) and the addition of DSPE-PEG2000 as the third component.

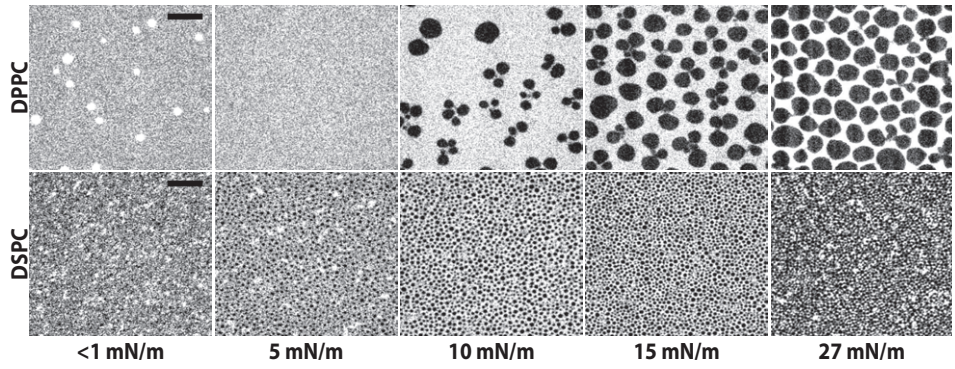

Figure 8.2: Fluorescent micrographs of monolayers of ternary mixtures containing DSPE-PEG2000 (7.0 mol%), PEG40-stearate (8.2 mol%), and either DPPC (84.8 mol%, top row) or DSPC (84.8 mol%, bottom row) at various surface pressures, taken during monolayer compression. Scale bars (black) represent 25 μm and apply to all images.

Monolayer Fluorescence Microscopy

Fluorescent micrographs of monolayers containing ternary mixtures with DSPC or DPPC at different surface pressures during compression are shown in Fig. 8.2.The DPPC containing mixture was homogenous with some bright spots at the starting surface pressure (< 1 mN/m). These bright spots could be due to the coexistence of gaseous and LE phases, with the fluorescent lipid dye enriched in the LE phase spots. With the increasing surface pressure, the bright fluorescent spots disappeared and at 5 mN/m the fluorescent dye was homogenously distributed, indicating that all components were in the same phase, namely, the LE phase. Above 5 mN/m, dark domains of LC-phase lipids appeared and grew larger as the compression of the monolayer advanced. Initially, these dark domains were clustered like flower petals connected to a central point (Fig. 8.2, DPPC 10 mN/m). As the surface pressure increased, the LC domains separated and the interdomain region became brighter because a fixed amount of fluorescent dye was distributed over a smaller surface area. These micrographs show the same morphology of dark domains as in previously published micrographs on a binary mixture of DPPC and PEG40-stearate (9:1)[222]. Interestingly, the dark LC domains containing mainly DPPC did not form the characteristic bean- or propeller-like shapes with defined chirality as observed for pure DPPC [244, 245]. This seems to be an indication that the LC phase is not pure DPPC but contains some achiral PEG40-stearate or DSPE-PEG2000, thus preventing the formation of chiral domains.

A major difference between DPPC- and DSPC-based mixtures is the presence of LC domains in the DSPCcontaining monolayer at low surface pressures (< 1 mN/m). This is consistent with the isotherms of pure DSPC where a direct transition from

the gaseous phase to LC phase is observed. Interestingly, in the DSPC mixture there appeared to be three phases at low surface pressures (< 1 – 5 mN/m). Previous work on bilayers has indeed shown that three-phase co-existence can occur in a ternary mixture of DSPC with 1,2-dioleoyl-sn-glycero-3-phosphocholine and cholesterol [246]. With the increasing surface pressure, the dark LC domains grew larger. However, the size of the LC domains at different surface pressures is much smaller than in the DPPC containing monolayers. The size of LC domains is dependent on the line tension between the LC domains and the surrounding phase and the excess dipole density in the LC domains [244, 247, 248]. The latter effect leads to a repulsion between the domains and prevents the domain growth driven by the line tension. The DSPC-containing LC domains probably have a larger excess dipole density with respect to the surrounding gaseous phase, than DPPC-containing LC domains with respect to the surrounding LE phase, which prevents further LC domain growth of DSPC. High excess dipole density leading to small LC domains has been reported for DMPC/DSPC monolayers containing 60 mol% DSPC [247] and for DSPC monolayers containing 1 – 9 mol % DSPE-PEG2000 [249]. The transition around 10 mN/m that was identified in the isotherms was less apparent in the fluorescence micrographs. With increasing surface pressure, the most noticeable change was an increase in the relative surface area of the LC domains, indicating that the surrounding LE phase is being compressed without molecules transitioning into the LC phase. This suggests that a transition in the headgroup region occurs instead, namely a mushroom-brush transition of the PEG chains in the aqueous phase.

IRRAS Experiments

Fig. 8.3 shows the results of the IRRAS experiments we performed to attribute the different transition plateaus of the isotherms to specific phase transitions. The position of the methylene stretching vibrational bands in the IRRA spectra is dependent on the phase state of the respective lipid, with a downshift in their wavenumbers being indicative for an LE to LC transition [250–252]. The stretching vibrations of the CD_2 groups of the deuterated lipids are well separated from the CH_2 stretching vibrations of the PEGylated components and any other vibrational bands, allowing separate analysis of the phase state of the main phospholipid component and the PEGylated components (Fig. 8.3A,C). Isotherms of pure DPPC-d_{62} and DSPC-d_{70} were measured to confirm that deuteration had only little effect on the lipid phase behavior (Supplemental Fig. 8.3, compared to Fig. 8.1A,C). However, the LE to LC phase transition of pure DPPC-d_{62} shifted to slightly higher surface pressure, that is, toward the second transition detected for DPPC-based ternary mixtures, resulting in a slight overlap of both transitions. Nevertheless, IRRA spectra of the monolayers of ternary mixtures containing DPPC-d_{62} showed a transition from LE to LC phase concomitant with the plateau (at ~12 mN/m) in the isotherm (Fig. 8.3B). In contrast, no DSPC-d_{70} molecules were found in the LE phase, indicating a direct transition

from the gaseous to the LC phase (Fig. 8.3D, blue and orange line). The position of the CD_2 stretching vibrational bands at low wavenumbers throughout the examined compression range indicates that DSPC-d_{70} is already in the LC phase at high molecular areas. This unambiguously shows that the transition plateau we found around ~10 – 12 mN/m is not due to a phase transition of DSPC itself and must thus be caused by a reorganization of the PEGylated components, probably the mushroom to brush transition of the PEG chains [229]. The CH_2 stretching vibrations of the PEGylated components were analyzed as well (Supplemental Fig. 8.4B,D). However, because of low signal, we only have data from surface pressures above 12.5 mN/m; thus, we cannot distinguish the transition that occurs below this surface pressure. The CH_2 vibrational bands arise from the CH_2 groups in the chains and in the headgroups of the PEGylated components, mainly PEG40-stearate, with the majority of the CH_2 groups being located in the PEG groups of PEG40-stearate and DSPE-PEG2000. However, because the conformation of the CH_2 groups in the flexible PEG chains is not well defined, their contribution to the CH_2 stretching vibrational band is broad and the band position is still dominated by the vibrations of the higher ordered lipid acyl chains. The CH_2 vibrational bands of pure DPPC before and after transition can be used as a reference for characteristic LE and LC phase wavenumbers (Supplemental Fig. 8.5). The CH_2 bands in the ternary mixtures were observed at a wavenumber characteristic for neither an LC nor an LE phase, but in between; namely, at 2852 cm^{-1} (symmetric CH_2-vibration) and 2922 cm^{-1} (antisymmetric CH_2-vibration) (Supplemental Fig. 8.4B,D). This suggests that part of the PEGylated molecules was in the LE phase and part was in the LC phase. When comparing the CH_2 vibrational bands of the PEGylated molecules to the CH_2 vibrational band of pure DPPC during transition, the observed wavenumbers ($\tilde{\nu}$) suggest that the majority (about 60%) of the PEGylated lipids are still in LE phase (Supplemental Fig. 8.5). In case of the DSPC-based ternary mixtures, the LE phase is consequently formed only by the PEGylated molecules, whereas in the DPPC-based mixtures the LE phase contains DPPC and/or PEGylated molecules.

To identify the contributions of the lipid headgroups to the transitions, we performed PCA on the IRRA spectra in the region of the PO_2 and C–O stretching vibrations (symmetric and antisymmetric; Fig. 8.3A,C, label d and e), originating from the headgroup attached PEG chains (1050 – 1300 cm^{-1}), and the CD_2 stretching vibrations, originating from the acyl chains (2020 – 2270 cm^{-1}) (Fig. 8.4). This type of analysis identifies the main variances in the spectra during compression of the mixed monolayers and attributes them to different spectral regions, influential in the reorganization of different molecular moieties. The extent of these variations is expressed in first principal component (PC1) scores (Fig. 8.4A, C). In the here presented analysis, these scores change systematically with the surface pressure, with a pronounced step at about 10 mN/m. This corroborates our finding that both

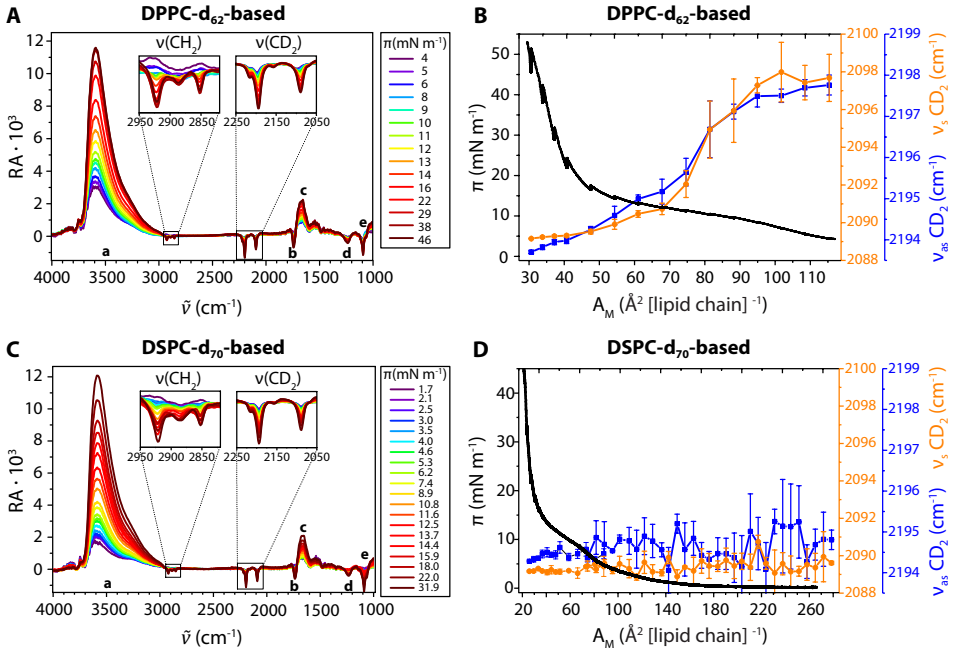

Figure 8.3: Spectra obtained by IRRAS of a monolayer composed of the ternary mixture (**A**) DPPC-d_{62} / DSPE-PEG2000 / PEG40-stearate (84.8:7.0:8.2 mol%) and (**C**) DSPC-d_{70} / DSPE-PEG2000 / PEG40-stearate (84.8:7.0:8.2 mol%), reflection absorption ($RA = -\log_{10}(R/R_0)$) as a function of wavenumber ($\tilde{\nu}$) for different surface pressures (π). CH_2 and CD_2 stretching bands are zoomed in; other bands are labeled: (a) OH stretching, (b) C=O stretching, (c) HOH bending, (d) PO_2 antisymmetric stretching, (e) PO_2 symmetric stretching and C–O stretching. (**B**,**D**) surface pressure (π) as a function of area per lipid chain (A_M) (black curve, left y-axis); wavenumbers of symmetric (orange line and symbols, right y-axis) and antisymmetric (blue line and symbols, right y-axis) CD_2 stretching vibration of the (B) DPPC-d_{62}-based or (D) DSPC-d_{70}-based ternary mixtures. Note the wider area range in (D) as compared to (B). Wavenumbers of the CH_2 stretching vibrational bands are given in Supplemental Fig. 8.3.

mixed monolayers show a transition when compressed above this surface pressure. Interestingly, the reason for this transition is different in DPPC-d_{62} containing and DSPC d_{70} containing monolayers, as can be deduced from the PC1 depicted in Fig. 8.4B,D. The DPPC-d_{62} containing monolayer spectra show simultaneous changes in the CD_2 stretching vibrational region and in the region of the headgroup vibrations. This suggests that both the acyl chains and the PEGylated headgroups contributed to the transition. In contrast, for the DSPC-d_{70} containing monolayer, spectral changes corresponding to the transition were only identified in the head group region because the PC1 (red line in Fig. 8.4D) shows variations in the spectral range of the PO_2 and C–O stretching vibrations but is essentially zero in the range of the CD_2 stretching vibrations. With this finding, the transition in the ternary mixtures containing DSPC

can clearly be attributed to reorganizations in the PEGylated headgroups, presumably a PEG mushroom to brush transition.

To verify that the changes in the headgroup region are not only due to the phospholipid phosphate groups but contain contributions of PEG chain reorganization, we repeated the IRRAS compression experiment and PCA with a pure $DPPCd_{62}$ monolayer (see Supplemental Fig. 8.6). Comparison of the first principal components shows a lower PC1 in the range of the headgroup vibrations for pure $DPPCd_{62}$, indicating that only

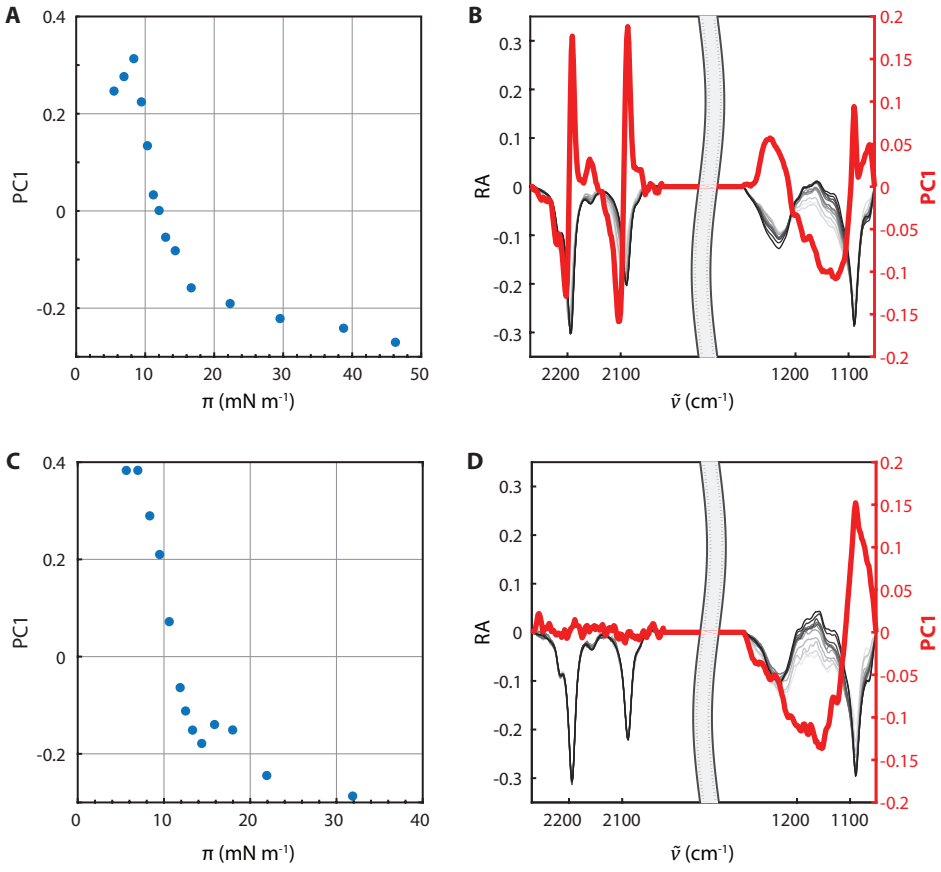

Figure 8.4: PCA of IRRA spectra recorded during the compression of a PL / DSPE-PEG2000 / PEG40-stearate (84.8:7.0:8.2 mol%) mixed monolayer, where PL = DPPC-d_{62} (**A** and **B**) and DSPC-d_{70} (**C** and **D**). IRRA spectra were simultaneously analyzed in the range of the headgroup vibrations (1050 – 1300 cm^{-1}) and the CD_2 stretching vibrations (2020 – 2270 cm^{-1}) after separate vector normalization in the two respective ranges (gray lines in (B and D); low surface pressures (light gray) to high surface pressures (dark gray)). Panels (A and C) show the scores of the first principal components (PC1) as function of the surface pressure (π). Panels (B and D) show the reflection absorption (RA, gray lines, left y-axis) and PC1 score (red lines, right y-axis) as a function of the wavenumbers ($\tilde{\nu}$).

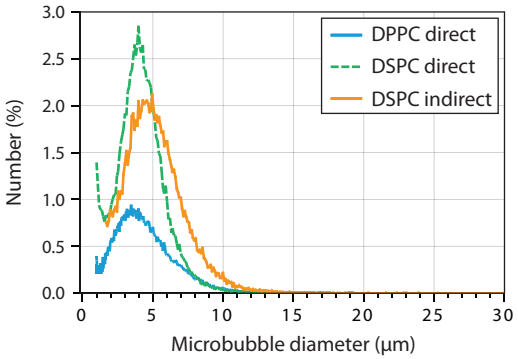

Figure 8.5: Number weighted size distribution of DPPC direct (blue line, n=1 batch), DSPC direct (green dashed line, n=1 batch), and DSPC indirect (orange line, representative for n=2 batches) microbubbles with ternary coating composition containing DSPE-PEG2000 (7.0 mol%) and PEG40-stearate (8.2 mol%) as additional components.

phosphate reorganization would not be sufficient to explain the variations in the above presented spectra. Thus, we conclude that PEG chain conformational changes must be involved in the transitions of the monolayers containing ternary mixtures of DSPE-PEG2000 and PEG40- stearate with DPPC or DSPC.

All experiments described above were performed at the air/ buffer interface. However, during microbubble production, C_4F_{10} gas is added to the air and the phospholipids are dispersed in PBS saturated with C_4F_{10} gas. Recently published work demonstrates how the LE to LC transition of DPPC was shifted to higher surface pressures in the presence of C_6F_{14} in the gas phase [253]. Another study showed a shift of the LE to LC transition to higher surface pressures in a binary mixture of DPPC with 5 mol% DSPE-PEG2000, in the presence of C_6F_{14} in the subphase and air in the gas phase [254]. Taking this into consideration, the influence of a fluorinated hydrocarbon in the gas phase on the isotherms cannot be excluded, meaning that the isotherms would be slightly shifted to higher transition pressures.

8

Microbubbles

Fig. 8.5 shows the number weighted size distribution of the streptavidin-conjugated microbubbles. The number-weighted mean diameter was 3.6 µm for direct DPPC microbubbles, 4.2 µm for direct DSPC microbubbles and 5.17-5.22 µm (n=2 batches) for indirect DSPC microbubbles. The volume weighted mean diameter was 6.6 µm for direct DPPC microbubbles, 6.4 µm for direct DSPC microbubbles, and 7.9-8.4 µm (n=2 batches) for indirect DSPC microbubbles. Direct and indirect DSPC microbubbles had a similar size distribution (span 1.0), whereas the direct DPPC microbubbles were more polydisperse (span 1.4). The size distributions of the direct microbubbles are in agreement with previously published work [88]. The indirect method resulted in slightly larger DSPC microbubbles than direct DSPC microbubbles but did not affect the polydispersity.

Ligand Distribution in Microbubbles

The lipid phase and ligand distribution in the microbubble coating were imaged for direct DPPC (n = 50, 2 batches), direct DSPC (n = 47, 3 batches), and indirect DSPC microbubbles (n = 46, 2 batches) of 1.5 – 8 μm in diameter. Typical examples of the different types of microbubbles are shown in Fig. 8.6. The ligand distribution, representative for the DSPE-PEG2000 distribution, is shown in the left column, the LE phase stained with rhodamine-DHPE in the middle column, and a composite of both signals is displayed in the right column. The calculated ligand distribution inhomogeneity is shown in Fig. 8.7. In concurrence with our previous study [88], the direct DPPC microbubbles had a mostly homogenous ligand distribution (Fig. 8.6A and 8.7),while there was a large variability in ligand distribution for the direct DSPC microbubbles ranging from heterogeneous with areas where the ligand was either lacking or enriched (Fig. 8.6D), to a more homogenous ligand distribution (Fig. 8.6G). Nevertheless, the indirect DSPC microbubbles all had a homogenous ligand distribution (Fig. 8.6J and 8.7). No correlation was found between microbubble size and ligand inhomogeneity. A previous study, which focused on phase separation in phospholipidcoated microbubbles processed with different heating-cooling regimes, showed that the ligand was distributed heterogeneously in slowly cooled microbubbles and homogenously in rapidly cooled microbubbles [223]. These microbubbles were coated with a binary mixture of DSPC and DSPE-PEG2000 (9:1) and made by mechanical shaking. In the present study, we investigated no heating-cooling regimes, yet we found that a different handling of phospholipids before microbubble production could also result in a more uniform ligand distribution.

Lipid Phase Distribution in Microbubbles

In all types of direct and indirect microbubbles, the lipids were phase separated resulting in dark domains (i.e. LC phase) and bright inter-domain regions (i.e. LE phase), when studying the fluorescence of rhodamine-DHPE (Fig. 8.6B, E, H, K). Although the LC domains in the DPPC- and DSPC-based ternary mixture monolayers had different morphologies (Fig. 8.2), the LC domains in the microbubble coatings were similar for all types of microbubbles. Fluorescent dyes have been used before to examine domain formation in microbubbles coated with binary mixtures of DPPC and DSPC with PEG40-stearate or DSPE-PEG2000, with a diameter larger than 10 μm [99, 222–224, 230]. In these studies, the microstructures in the microbubble coating were tuned by varying the cooling rate after microbubble production or by varying the pure lipid to PEGylated molecule ratio. To the best of our knowledge, the present study is the first to include microbubbles coated with a ternary mixture and of clinically relevant sizes, namely, 1.5 – 8 μmin diameter.

The domain morphology of microbubbles coated with a ternary mixture presented here resembles that of microbubbles (diameter > 5 μm) coated with a binary

mixture of DSPC and PEG40-stearate or DSPE-PEG2000 (9:1), despite the use of different fluorescent dyes and microbubble production methods [99, 223]. Others imaged phase separation with epifluorescence or confocal microscopy, in contrast to the highresolution 4Pi confocal microscopy that was used for this study. Previous studies reported that no domain formation was observed in microbubbles with a

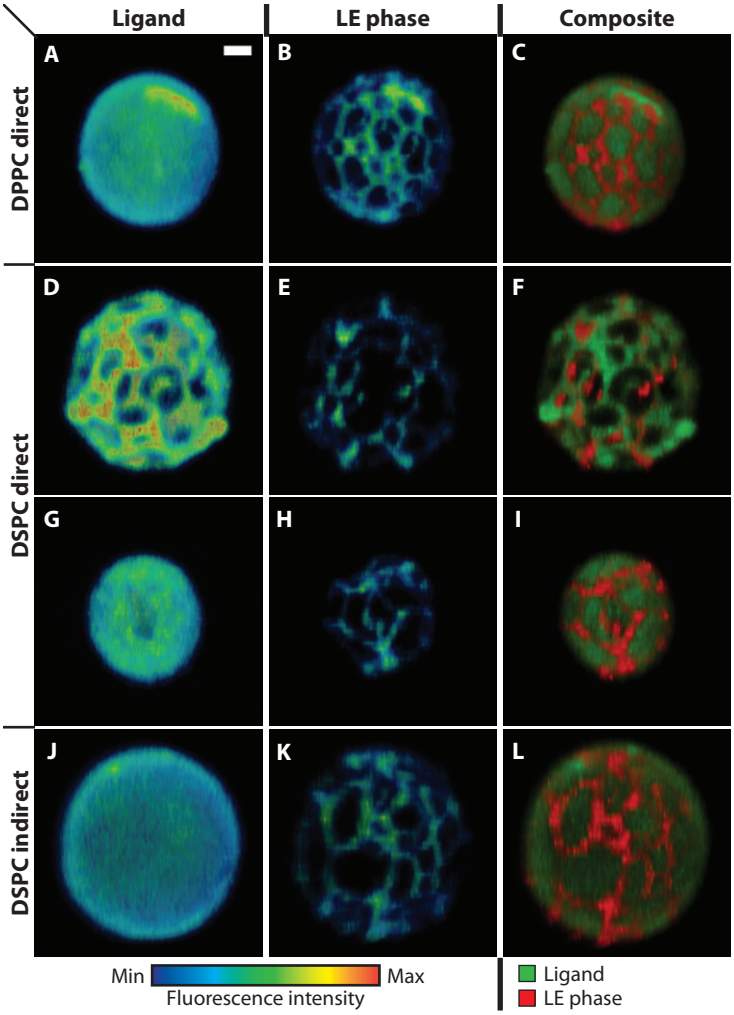

Figure 8.6: Selected views of 4Pi confocal microscopy y-stacks of direct DPPC (**A–C**, diameter (d) = 4.7 µm), direct DSPC (**D–F**, d = 4.9 µm; **G–I**, d = 3.4 µm), and indirect DSPC microbubbles (**J–L**, d = 5.3 µm) with ternary coating composition containing DSPE-PEG2000 (7.0 mol%) and PEG40-stearate (8.2 mol%) as additional components. The images show the ligand distribution (A, D, G, J; Oregon Green 488), LE phase (B, E, H, K; rhodamine-DHPE), and composite view (C, F, I, L). Scale bar is 1 µm and applies to all images. Full 3D reconstructions of these examples are provided as Supplemental Videos 1–4.

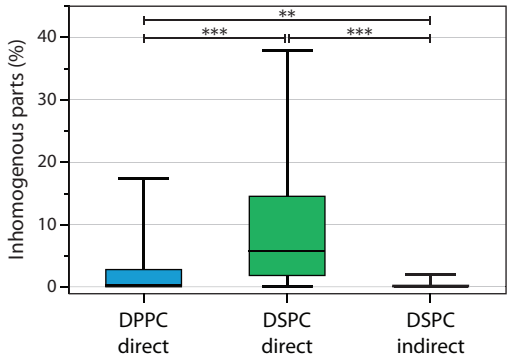

Figure 8.7: Parts classified as inhomogeneous (%) in the ligand distribution of direct DPPC (n=50), direct DSPC (n=47) and indirect DSPC (n=46) microbubbles with ternary coating composition containing DSPE-PEG2000 (7.0 mol%) and PEG40-stearate (8.2 mol%) as additional components. Boxplots show the median, interquartile range and have whiskers from minimum to maximum. Statistical significance was indicated with $^{**}p < 0.01$, $^{***}p < 0.001$.

binary mixture of DSPC and PEG40-stearate (9:1) smaller than 5 µm, even though domains smaller than 5 μm^2 were observed in microbubbles larger than 5 µm [230]. However, all microbubbles analyzed for the present study (1.5 – 8 µmdiameter) had condensed domains in the coating. This is likely due to phase separation of the three components: the main lipid component DPPC (in LE/LC phase), or DSPC (in LC phase), PEG40-stearate in LE phase, and DSPE-PEG2000 in LC or LE phase. Microbubbles were mounted in 87% glycerol for 4Pi high-resolution imaging. Monolayer studies at the air/water interface showed that glycerol in the subphase had no effect on the phase behavior below the transition temperature [255]. In our study, glycerol was added after microbubble production and the sample was kept at room temperature during imaging experiments. We therefore assume that the glycerol did not have an effect on the molecular structure of the lipid microbubble coating.

The rhodamine-DHPE fluorescence intensity ($I_{\text{part-rhod}}$) and the surface area classified as LC phase were plotted as a function of the axial plane and the corresponding circumference (Fig. 8.8A, B). The LC area fraction is presented in Fig. 8.8C as the percentage of the total surface area analyzed per microbubble. The mean percentage of LC area was significantly lower for the direct DPPC microbubbles than for both types of DSPC microbubbles. This was expected because DSPC is always in the LC phase, according to our monolayer results presented above and literature [228]. The direct DSPC microbubbles had a significantly smaller LC phase area than the indirect DSPC microbubbles. Because DSPC is always in the LC phase and the other PEGylated components were the same, there must be a difference in the localization of these PEGylated components causing the differences in LC area between direct and indirect DSPC microbubbles. No correlation was found between microbubble size and LC phase area. These results indicate that the lipid handling affects the phase separation between different components. Previous studies that investigated domain characteristics focused mainly on the effect of cooling rates in microbubbles coated with binary mixtures of DSPC with PEG40-stearate [99, 222], yet the microbubbles in

those studies were much larger (>20 µm diameter) than the microbubbles investigated here.

The right column of Fig. 8.6 shows composites of the lipid phase and ligand distribution in the microbubble coating. For the direct DPPC and indirect DSPC examples, the green fluorescent ligand is distributed homogenously over the fluorescently stained LE phase and the LC phase (Fig. 8.6C, L). For the direct DSPC microbubbles, two examples are shown to illustrate the variability within this group: heterogeneous distribution where the ligand is colocalized with the LE phase (Fig. 8.6F) and homogenous ligand distribution similar to the other types of microbubbles microbubbles (Fig. 8.6I). Colocalization of the DSPE-PEG2000 with the LE phase has been reported before for a single example of a ~20 µm diameter microbubble coated with a binary mixture of DSPC and DSPE-PEG2000 (9:1) without quantification [223]. In our study, we quantified the colocalization between the LC phase (no rhodamine-DHPE fluorescence) and DSPE-PEG2000, the component where

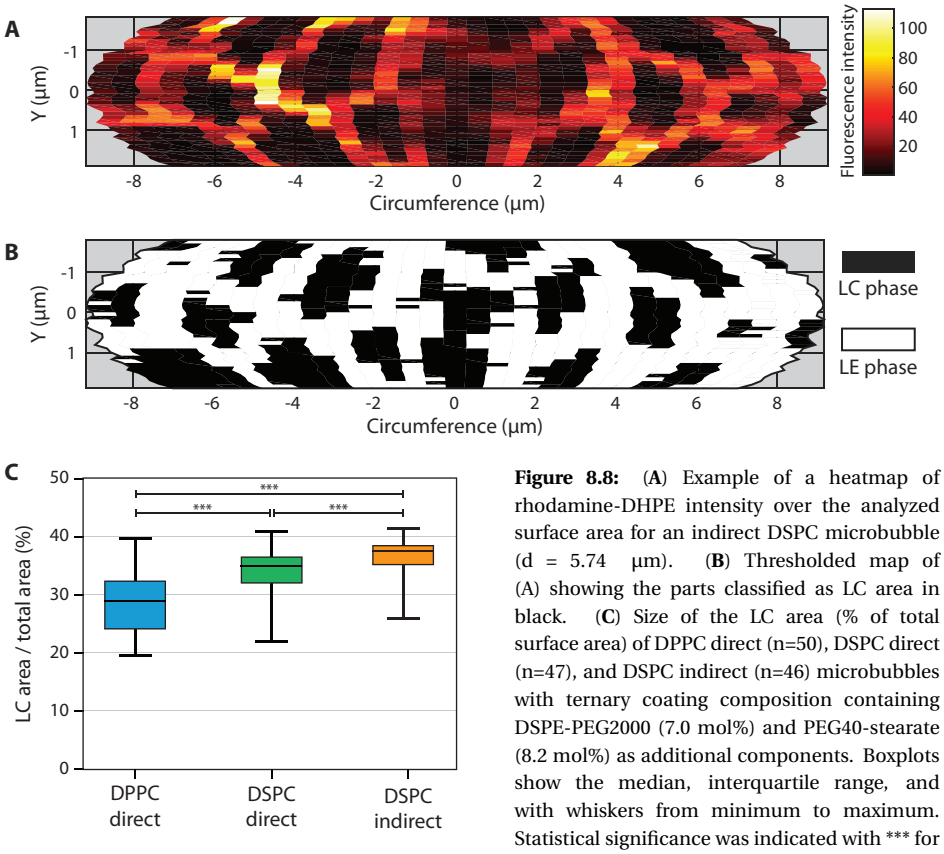

Figure 8.8: (**A**) Example of a heatmap of rhodamine-DHPE intensity over the analyzed surface area for an indirect DSPC microbubble (d = 5.74 µm). (**B**) Thresholded map of (A) showing the parts classified as LC area in black. (**C**) Size of the LC area (% of total surface area) of DPPC direct (n=50), DSPC direct (n=47), and DSPC indirect (n=46) microbubbles with ternary coating composition containing DSPE-PEG2000 (7.0 mol%) and PEG40-stearate (8.2 mol%) as additional components. Boxplots show the median, interquartile range, and with whiskers from minimum to maximum. Statistical significance was indicated with *** for $p < 0.001$.

the fluorescent ligand Oregon Green 488 is attached to, which is presented in Fig. 8.9A. For the direct DPPC and indirect DSPC microbubbles, the mean colocalization ratio was approximately 1, indicating that the amount of DSPE-PEG2000 in the LC phase domains was equal to the amount of DSPE-PEG2000 in the interdomain region. The colocalization ratio was significantly lower for the direct DSPC microbubbles, indicating that there was less DSPE-PEG2000 in the LC phase domains than in the interdomain regions. For these direct DSPC microbubbles, there was a negative correlation between the percentage of inhomogeneity in the ligand distribution and the colocalization ratio (Fig. 8.9B). This suggests that in microbubbles with a heterogeneous ligand distribution, the ligand was depleted in the LC domains.

Based on the differences that we found in LC area and ligand distribution, between the direct and indirect DSPC microbubbles, we expect that the DSPE-PEG2000 component is either excluded from preformed LC domains (for direct method, Fig. 8.6D-F, Supplemental Video 2) or equally distributed over the LE and LC phase (for inidrect method), depending on the phospholipid handling prior to the microbubble production. This is in accordance with the IRRAS results, indicating that the PEGylated components were distributed over both the LE and LC phase, whereby we assume that the monolayer at the air/buffer interface was in thermodynamic equilibrium. With the indirect method for microbubble production, all components were dissolved and mixed in organic solvent. After evaporation of the solvent, the dried film of mixed lipids was dispersed in PBS buffer using a sonicator bath and a probe sonicator at low power. With the direct method, in contrast, the components were each dispersed in PBS buffer without use of sonication and then mixed together. Therefore, it is likely that the lipids in the precursors of the microbubbles, that is, in the liposomes and micelles [256], were more uniformly mixed with the indirect method than with the direct method. The lipids spontaneously self-assemble around the newly formed gas microbubbles during probe sonication [257, 258], likely through membrane spreading [259]. In other words, the indirect DSPC microbubbles are more in equilibrium than the direct DSPC microbubbles. This is in contrast to previous studies on monolayers at the air/water interface, which found that DSPC and DSPE-PEG2000 were immiscible at all surface pressures [229].

For a fair comparison, the 4Pi confocal microscopy experiments were performed at room temperature, in accordance with all microscopy studies on lipid and ligand distribution on microbubble coatings. However, when developing microbubbles for *in vivo* applications, experiments at body temperature will be more translatable to human applications. Another important aspect for *in vivo* applications is the ligand distribution, because a more homogenous distribution could result in higher targeting efficiency. While the homogenous ligand distribution makes direct DPPC microbubbles a good candidate for *in vivo* applications, they are acoustically less stable than direct DSPC microbubbles [77]. Our studies now show that homogenous

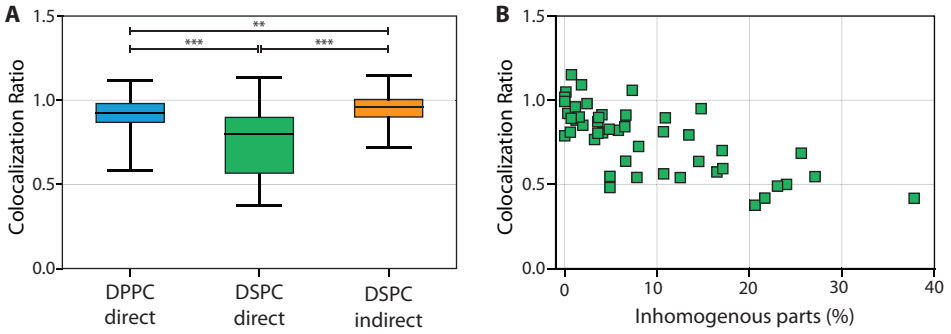

Figure 8.9: (**A**) Colocalization ratio of direct DPPC (n=50), direct DSPC (n=47), and indirect DSPC (n=46) microbubbles with ternary coating composition containing DSPE-PEG2000 (7.0 mol%) and PEG40-stearate (8.2 mol%) as additional components. Boxplots show the median, interquartile range, and with whiskers from minimum to maximum. Statistical significance was indicated with ** $p < 0.01$, *** $p < 0.001$. (**B**) Colocalization ratio as a function of the parts classified as inhomogeneous (%) ligand distribution for direct DSPC microbubbles (n=47).

ligand distributions are also possible for DSPC-based microbubbles. Future studies on the acoustical behavior of indirect DSPC microbubbles may give insight into the effect of LC area and ligand homogeneity on the acoustical stability, diversity in response to ultrasound, and efficacy to enhance molecular imaging and local drug delivery in a safe and effective way.

8.4. CONCLUSIONS

We investigated the ligand distribution and lipid phase state in microbubbles coated with a ternary phospholipid-based mixture of clinically relevant sizes. For better understanding of the lipid phases, we studied the lipid phase behavior in monolayers at the air/water interface of the same ternary mixtures that coated the microbubbles. Isotherms showed that DPPC had a transition from LE to LC phase during monolayer compression at ~5 mN/m, which shifted to lower surface pressures in mixtures with DSPE-PEG2000 only or DSPE-PEG2000 and PEG40-stearate. In contrast, DSPC was always in the LC phase, also in the binary and ternary mixtures we studied. All binary and ternary mixtures had a transition plateau around 10 – 12 mN/m. As confirmed by IRRAS, this plateau was due to a conformational transition (mushroom to brush) in the PEGylated components. Based on 4Pi high-resolution imaging, direct DPPC microbubbles had a homogenous ligand distribution, with a significantly smaller LC phase area than the DSPC-based microbubbles. The lipid handling prior to microbubble production influenced both the ligand distribution and the LC phase area in the DSPC-based microbubbles. Microbubbles made by the direct method had a heterogeneous ligand distribution, while the ligand colocalized with the LE phase

area. Microbubbles made by the indirect method had a significantly larger LC phase area and homogenous ligand distribution. By controlling the ligand distribution and microstructures in the microbubble coating, we can better understand the underlying mechanisms of targeting. This will lead to tailored microbubble formulations for specific clinical applications.

ACKNOWLEDGEMENT

The authors are grateful to Prof. A. L. Klibanov from the University of Virginia, Cardiovascular Division, Charlottesville, Virginia, USA for discussions about the microbubble preparation. The authors thank the Erasmus Optical Imaging Centre of Erasmus MC for use of their facilities, and Dr. Gert van Cappellen and Alex Nigg for their help.

Funding

This project was supported in part by the Phospholipid Research Center, Heidelberg, Germany; and the Thoraxcenter of Erasmus MC. C.S. and A.B. thank Deutsche Forschungsgemeinschaft (DFG) for financial support through the grant FOR1145.

SUPPORTING INFORMATION

The Supporting Information is available free of charge at https://pubs.acs.org/doi/10.1021/acs.langmuir.9b03912.

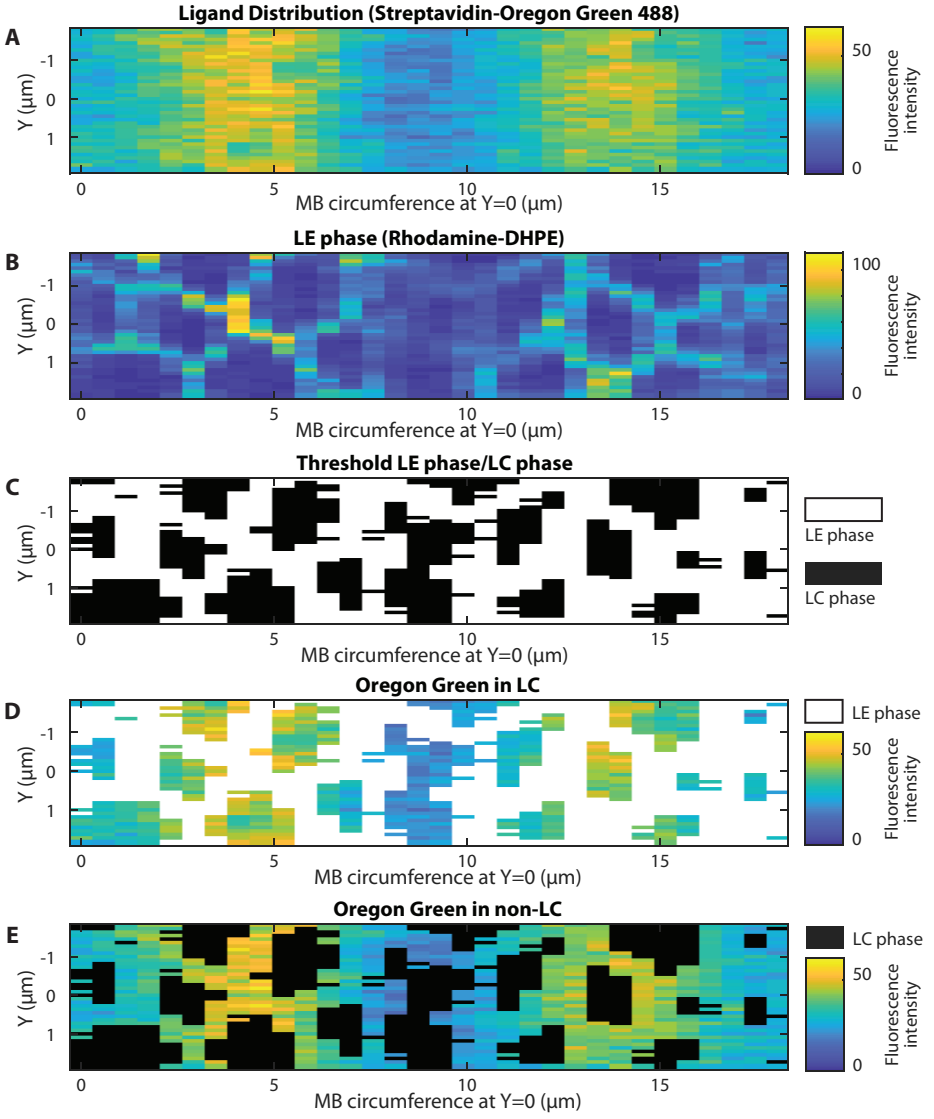

Supplementary Figure 8.1: Typical example of 2D heatmaps of an indirect DSPC microbubble with a diameter of 5.7 µm. Mean fluorescence pixel intensity (I_{part}) of **A**) the ligand (Streptavidin-Oregon Green 488) and **B**) the LE phase (rhodamine-DHPE). **C**) Thresholded image with LC phase area in black and inter-domain region in white. Masked image of ligand fluorescence intensity in **D**) LC phase area (median 34.26) and **E**) inter-domain region (median 34.13, colocalization ratio 1.00).

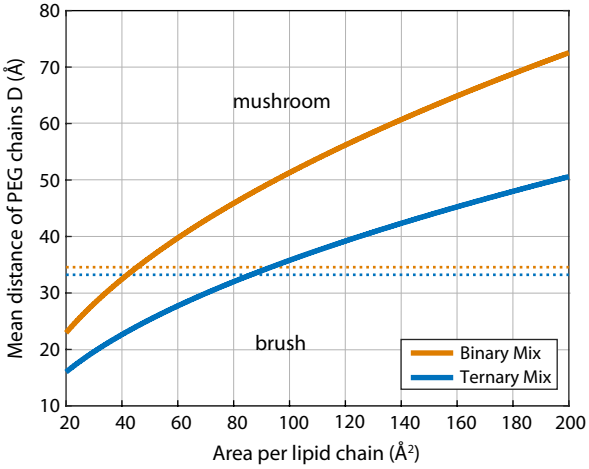

Supplementary Figure 8.2: Theoretical calculation of the mushroom to brush transition for the binary and ternary mixture. The solid lines are the calculations using Equation 2, $D = \sqrt{A_{\text{lipid}} / m}$ from Abou-Saleh et al. [241], where D is the mean distance between PEG chains, A_{lipid} the area occupied per lipid chain, and m the mole fraction of PEG / lipid chain. For the binary mixture (orange solid line), an m of 0.038, i.e. 7.6 mol% PEG / (2·100) lipid chains, was used while this was 0.0781 for the ternary mixture (15 mol% PEG / (2·85 + 2·7 + 1·8) lipid chains) (blue solid line). The dotted lines show the Flory radius calculated from Equation 1, $R_F = aN^{3/5}$ from from Abou-Saleh et al. [241], where R_F is the Flory radius of the grafted PEG, a the size of the monomer (=0.35 nm), and N is the number of monomers per chain. For the binary mixture (orange dotted line), an N set to 2000 / 44 (mean molecular weight of the Polymer chain / monomer molecular weight), while for the ternary mixture (blue dotted line), which contains PEG chains of slightly different length a weighted average of N = 44.24 was used (8/15·40 + 7/15·(2000/44)). The mushroom to brush transition is predicted where dotted and solid lines intersect, i.e. where the mean PEG chain distance becomes smaller than the Flory radius.

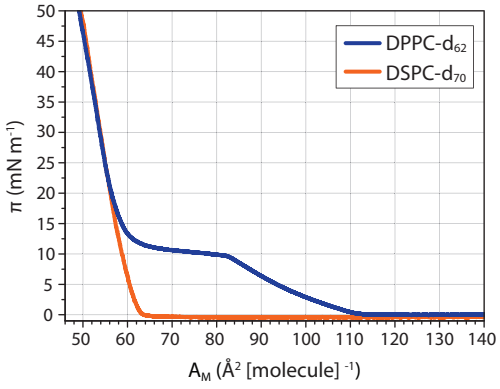

Supplementary Figure 8.3: Compression isotherms of pure DPPC-d_{62} and DSPC-d_{70} at the air/water interface. Graph of surface pressure (π) as a function of the area per molecule (A_M). Experiments performed at 20°C.

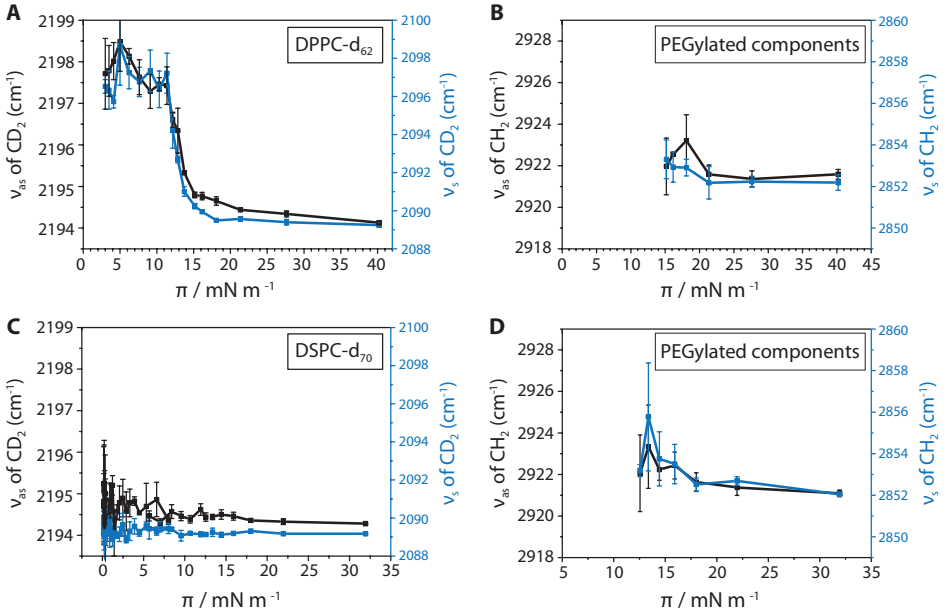

Supplementary Figure 8.4: Wavenumbers ($\tilde{\nu}$) of antisymmetric (ν_{as}) and symmetric (ν_s) CD_2 (**A**, **C**) and CH_2 (**B**, **D**) stretching vibration of the ternary mixtures DPPC-d_{62} / DSPE-PEG2000 / PEG40-stearate (A, B) and DSPC-d_{70} / DSPE-PEG2000 / PEG40-stearate (C, D) (84.8:7.0:8.2 mol%) as function of the surface pressure (π). Note the difference in x-axis of 3A, 3B, 3C, and 3D.

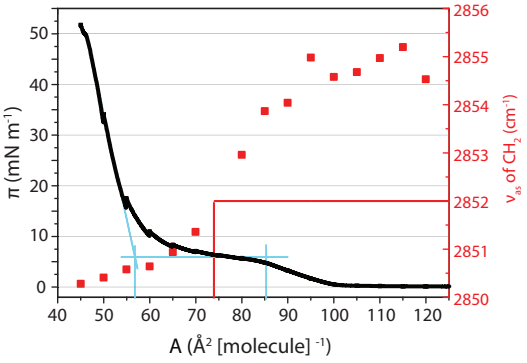

Supplementary Figure 8.5: Compression of a pure DPPC monolayer with simultaneous recording of the compression isotherm (black line, left y-axis) and IRRA spectra. Wavenumbers of antisymmetric CH_2 stretching vibrations (ν_{as} of CH_2) are shown as red symbols (right y-axis). The blue perpendicular lines indicate the limits of the LE to LC phase transition plateau. The phase transition pressure is marked with a blue horizontal line at ca. 6 mN/m. The position of ν_{as} at 2852 cm^{-1} (marked with a red line) is indicative for a partly ordered monolayer state with LE and LC phase co-existence, where the majority of the lipids is still in the LE state and the minority in the LC state. The LE/LC ratio as estimated from the position in the transition plateau was approximately 1.5 (or 60% of the lipids are in LE, 40% are in LC).

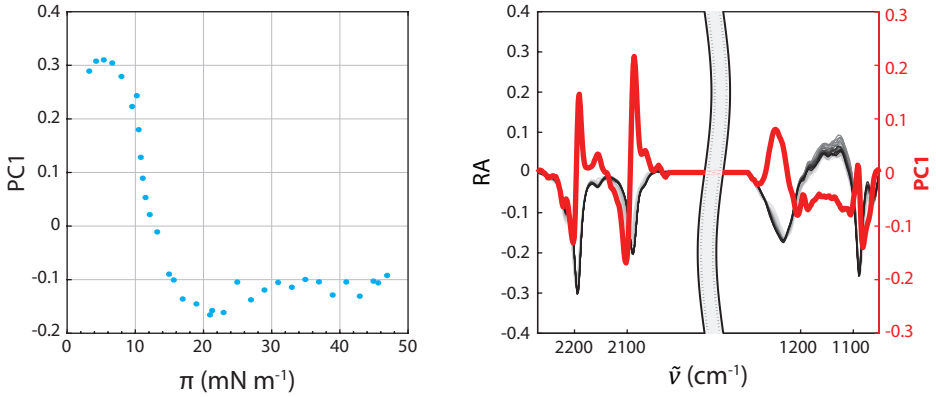

Supplementary Figure 8.6: Principal component analysis of IRRA spectra recorded during the compression of a pure DPPC-d_{62} monolayer. IRRA spectra were simultaneously analyzed in the range of the headgroup vibrations (1050 – 1300 cm^{-1}) and the CD_2 stretching vibrations (2020 – 2270 cm^{-1}) after separate vector normalization in the two respective ranges. The left panel shows the PC1 scores as function of the surface pressure (π). The right panel shows the reflection absorption (RA) as a function of the wavenumber (ν) for different surface pressures (low – light grey, to high – dark grey, left y-axis), and the PC1 as a function of the wavenumbers ($\tilde{\nu}$) (red line, right y-axis).

Supplemental Videos

Video 1. 3D render of direct DPPC microbubble (diameter = 4.7 µm) coated with DPPC, PEG40-stearate, and DSPE-PEG2000 (85:8:7).

Video 2. 3D render of direct DSPC microbubble (diameter = 4.9 µm) coated with DSPC, PEG40-stearate, and DSPE-PEG2000 (85:8:7).

Video 3. 3D render of direct DSPC microbubble (diameter = 3.4 µm) coated with DSPC, PEG40-stearate, and DSPE-PEG2000 (85:8:7).

Video 4. 3D render of indirect DSPC microbubble (diameter = 5.3 µm) coated with DSPC, PEG40-stearate, and DSPE-PEG2000 (85:8:7).

9

Acoustic characterization of the OrganoPlate

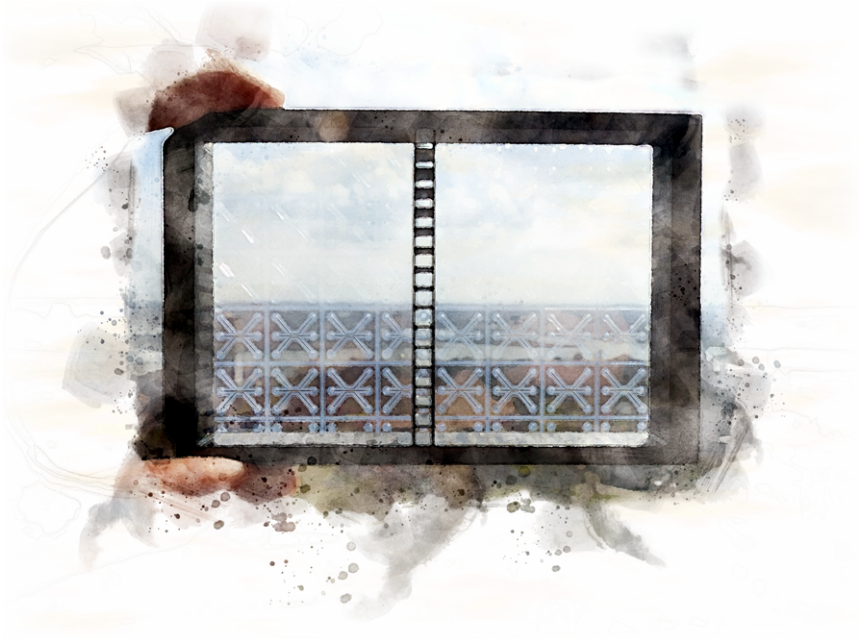

Based on:

Inés Beekers, Tom van Rooij, Martin D. Verweij, Michel Versluis, Nico de Jong, Sebastiaan J. Trietsch, and Klazina Kooiman, "Acoustic Characterization of a Vessel-on-a-Chip Microfluidic System for Ultrasound-Mediated Drug Delivery", *IEEE Transactions on Ultrasonics, Ferroelectrics, and Frequency Control*, vol. 65, no. 4, pp. 570-581, 2018 [165]

Abstract

Ultrasound in the presence of gas-filled microbubbles can be used to enhance local uptake of drugs and genes. To study the drug delivery potential and its underlying physical and biological mechanisms, an *in vitro* vessel model should ideally include 3D cell culture, perfusion flow, and membrane-free soft boundaries. Here, we propose an organ-on-a-chip microfluidic platform to study ultrasound-mediated drug delivery: the OrganoPlate. The acoustic propagation into the OrganoPlate was determined to assess the feasibility of controlled microbubble actuation, which is required to study the microbubble-cell interaction for drug delivery. The pressure field in the OrganoPlate was characterized non-invasively by studying experimentally the well-known response of microbubbles and by simulating the acoustic wave propagation in the system. Microbubble dynamics in the OrganoPlate were recorded with the Brandaris 128 ultra-high speed camera (17 Mfps) and a control experiment was performed in an OptiCell, an *in vitro* monolayer cell culture chamber that is conventionally used to study ultrasound-mediated drug delivery. When insonified at frequencies between 1 and 2 MHz, microbubbles in the OrganoPlate experienced larger oscillation amplitudes resulting from higher local pressures. Microbubbles responded similarly in both systems when insonified at frequencies between 2 and 4 MHz. Numerical simulations performed with a 3D finite element model of ultrasound propagation into the OrganoPlate and the OptiCell showed the same frequency dependent behavior. The predictable and homogeneous pressure field in the OrganoPlate demonstrates its potential to develop an *in vitro* 3D cell culture model, well-suited to study ultrasound-mediated drug delivery.

Index Terms — Acoustic characterization, acoustic wave modeling, drug delivery, microfluidics, organ-on-a-chip, ultrasound contrast agents.

9.1. INTRODUCTION

Ultrasound contrast agents consist of coated gas microbubbles with diameters ranging from 1-10 μm and are widely used to improve the contrast of organ perfusion in diagnostic ultrasound imaging. Upon ultrasound insonification, microbubbles compress and expand due to the acoustic pressure wave. This oscillatory behavior is the characteristic microbubble response which provides contrast enhancement for imaging. Recent studies also demonstrate the potential of oscillating microbubbles to locally enhance vascular drug delivery [3, 32]. Although the exact mechanism of delivery is unknown at present, there are three known pathways for ultrasound-mediated drug delivery [3]: 1) formation of pores in the cell membrane, termed sonoporation [32, 58]; 2) stimulation of endocytosis [56]; and 3) opening of cell-cell junctions into the extravascular tissue [54]. To study these pathways and

elucidate the mechanisms, the *in vitro* endothelial cell model ideally includes 3D cell culture, perfusion flow, and soft boundaries in the absence of rigid membranes. Since microbubble behavior strongly depends on the underlying substrate [8, 79, 260], the soft boundaries of an *in vivo* blood vessel need to be optimally reproduced. To achieve physiological relevant cell behavior, 3D cell culture and flow are required to mimic microcirculation, lumen architecture, and spatial distribution [261–263].

Ultrasound-mediated drug delivery studies commonly use an OptiCell (Nunc, Thermo Fisher Scientific, Wiesbaden, Germany) [12, 15, 40, 53, 64, 159, 264]. This parallel plate chamber limits cell culture to conventional monolayers on rigid boundaries and static conditions. In order to incorporate flow, others have used a commercially available microchannel flow set-up (μ-Slide, Ibidi GmbH, Munich, Germany) [67, 127]. Additionally, a biologically and acoustically compatible device was developed by Carugo *et al.* [265] for monolayer cell culture under flow. So far, these *in vitro* models may include physiological relevant flow, but are unfortunately still limited to cell monolayers and rigid boundaries. Vessel-on-a-chip cell culture in a microfluidic device better reproduces the *in vivo* physical architecture of a vessel [266]. Ideally, a high throughput is desired, cell culture biocompatible materials, a standardized manufacturing process, and optical and chemical access to both the apical and basolateral side of the vessel. To add functionality for ultrasound-mediated drug delivery, we propose to use the OrganoPlate® [267] (Mimetas B.V., Leiden, the Netherlands) to study the drug delivery pathways enhanced by microbubbles upon ultrasound insonification.

The OrganoPlate is an organ-on-a-chip platform with up to 96 microfluidic channel networks incorporated into a standard 384-well microtiter plate (Fig. 9.1). The 4003400B OrganoPlate used here contains 40 microfluidic networks, consisting of three adjacent microchannels allowing for 3D cell culture, perfusion, soft boundaries, and co-culture. The adjacent microchannels are separated by phaseguides: capillary pressure barriers that are used to guide fluid flow and pattern extracellular matrices. The diffusion distances are shortened through the use of capillary pressure barriers instead of membranes or walls and allows for direct cell-cell interactions [268]. Intricate cell models can be developed in the OrganoPlate; such as 3D neuronal networks [269], intestinal epithelium tubes [270], and a functional hepatocyte liver model [271]. In this paper, we propose to use the OrganoPlate in combination with ultrasound for the first time. Since the microchannels are incorporated between two glass plates and separated by polymer walls, here we investigate how ultrasound propagates into the OrganoPlate.

The aim of this study was to assess whether controlled microbubble oscillation is feasible in the OrganoPlate. Since microbubble response is dictated directly by the ultrasound pressure wave, the acoustic propagation into the OrganoPlate was characterized. Because of the small dimensions of the microchannels, the pressure

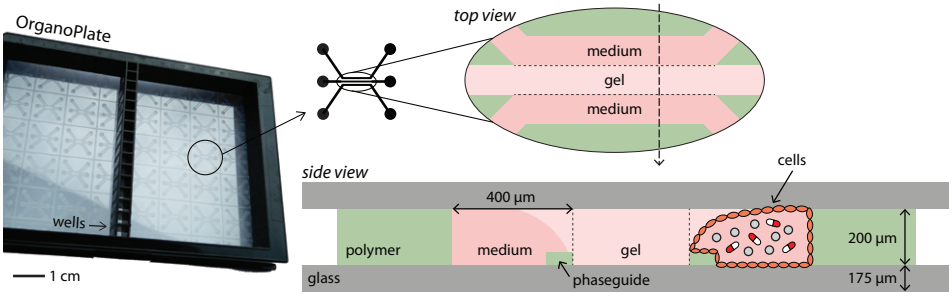

Figure 9.1: The modified OrganoPlate, revealing the microfluidic structure after removing most of the wells (black plastic) of the standard 384-well microtiter plate. The scale bar indicates the dimensions of the picture. The top view shows the three adjacent microchannels: two for medium perfusion and one for gel (i.e. extracellular matrix), allowing for culture against soft boundaries. The arrow indicates the direction of the side view. The side view shows the microchannels encased between two glass plates (gray), bound by polymer walls (green), and separated by polymer phaseguides (green). The meniscus-pinning effect [268] caused by the phaseguides results in a curved gel as soft boundary. The side view also illustrates the desired 3D *in vitro* set-up with cultured endothelial cells (orange) which can be perfused with microbubbles (gray spheres) and therapeutic agent (red/white). (Not drawn to scale.)

field inside the OrganoPlate could not be measured using a hydrophone without altering the ultrasound field. To characterize the pressure *in situ* and non-invasively, microbubbles were used as pressure sensors. The pressure was determined from the well-known microbubble response upon insonification, which requires characterization of the microbubble shell parameters. Since these microbubble shell parameters depend on the pressure itself [272], [273], a new iterative method was introduced that both determined the pressure field to which the microbubbles were exposed and their corresponding shell parameters. In order to do so, individual microbubbles in the OrganoPlate were recorded during ultrasound insonification using the Brandaris 128 ultra-high speed camera [6]. Microbubble spectroscopy [74] was performed by successively insonifying each individual microbubble while sweeping through a range of transmit frequencies, f_T, from 1 to 4 MHz. To characterize the ultrasound propagation, the pressure amplitude experienced by the microbubbles inside the OrganoPlate was obtained from the experimental data. The results were compared to those of control experiments performed in a conventional OptiCell, using an identical experimental set-up [77]. Additionally, a 3D finite element model was developed to simulate the acoustic propagation, to study the spatial distribution of the pressure field and to compare it with the experimental data.

9.2. MATERIAL AND METHODS

The OrganoPlate

The OrganoPlate® (Mimetas B.V., 4003400B) is a microfluidic system consisting of 40 chips developed for 3D cell culture [267]. In the case of a 3-lane design, each chip consists of three adjacent microchannels that can be accessed through their corresponding in- and outlets. The adjacent microchannels are separated by phaseguides [268], which are 100 µm × 50 µm (w × h) in size. As illustrated in Fig. 9.1, cells cultured adjacent to a microchannel with extracellular matrix can grow into a 3D perfusable microvessel. The 400 µm × 200 µm × 2200 µm (w × h × l) microchannels are incorporated between two 175 µm thick borosilicate glass plates (Fig. 9.1). The three microchannels are bound between two polymer walls (400 µm wide; Fig. 9.1). The OrganoPlate was modified to ensure compatibility with our experimental set-up. The standard wells of the 384-well microtiter plate were cut out, leaving only a single column of wells in the middle of the OrganoPlate, as depicted in Fig. 9.1. Removing the wells allowed for visualization of the microchannels using an upright microscope and insonification from below at a 45° incidence angle while submersed in water, thereby minimizing the reflections of the incident ultrasound wave with the microscope objective, as schematically depicted in Fig. 9.2.

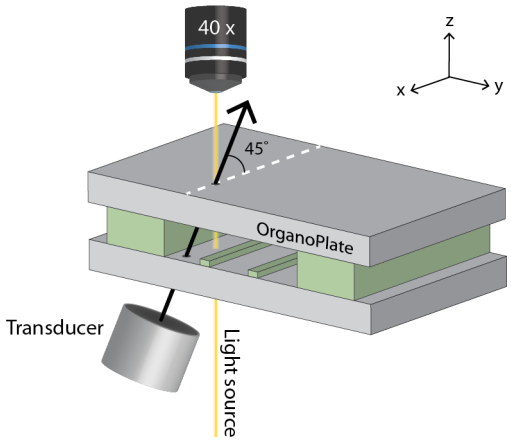

Figure 9.2: Schematic of the experimental set-up to study microbubble oscillation upon ultrasound insonification under a 45° incidence angle. The optical and ultrasound foci are located just beneath the upper glass plate of the OrganoPlate. The entire set-up was submersed in water. (Not drawn to scale.)

Microbubble Preparation

Biotinylated lipid-coated microbubbles with a C_4F_{10} gas core and a DSPC (1,2-distearoyl-sn-glycero-3-phosphocholine)-based shell were made by sonication for 10 s, as previously described [77, 88, 93]. The microbubbles were passively washed by flotation in a 3 mL syringe with a one-way tap by leaving them to stand on the lab bench. After 45 min, the subnatant was drained through the one-way tap and the microbubbles were resuspended in 1 mL of phosphate buffered saline (PBS) saturated with C_4F_{10} and drained into an Eppendorf tube. The microbubbles were diluted to a concentration of approximately $3 \cdot 10^6$ microbubbles/mL in PBS as determined by a Coulter counter Multisizer 3 (n=3) (Beckman Coulter, Mijdrecht, the Netherlands) using a 50 µm aperture tube, allowing for quantification of microbubble diameters of 1-30 µm.

Experimental Set-up

Microbubble oscillations were studied in the OrganoPlate replicating the ultrasound settings by van Rooij *et al.* [77]. Briefly, a single element broadband transducer (1-9 MHz bandwidth, 25 mm focal distance, −6 dB beamwidth at 1 MHz of 1.3 mm, PA275, Precision Acoustics, Dorchester, UK) was used for insonification at a 45° incidence angle while submersed in water (Fig. 9.2). The transducer output was calibrated in a separate experiment using a needle hydrophone (1 mm diameter, PA2293, Precision Acoustics). To perform microbubble spectroscopy measurements, we insonified single microbubbles with transmit frequencies (f_T) ranging from 1 to 4 MHz, in steps of 300 kHz, using an 8-cycle sine wave burst. The first and last cycles were Gaussian tapered (variance $\sigma^2 = 1.1/f_T^2$). Measurements were performed at 20 kPa peak negative pressure (PNP) in the focus, as calibrated in water. The optical and ultrasound foci were aligned and situated just below the upper glass plate of the OrganoPlate, where the microbubbles were located.

In the present study, microbubbles were introduced into the OrganoPlate by pipetting 6 µL of microbubble suspension on the inlet of a microchannel. They were insonified at room temperature within 2 h. Their oscillation behavior was recorded using the Brandaris 128 ultra-high speed camera at approximately 17 million frames per second [6], using a microscope (BX-FM, Olympus, Tokyo, Japan) with a 40× water immersion objective (LUMPlanFl, Olympus) and a 2× lens (Olympus). The first recording was performed in absence of ultrasound to image the initial microbubble size, followed by 11 recordings with ultrasound sweeping through the different transmit frequencies. The time between recordings was 80 ms. Recorded microbubbles were separated at least 0.7 mm to avoid multiple insonifications at the same location due to the finite -6 dB beamwidth of the transducer. In total, data from 12 different microchannels was evaluated.

Experimental Data Analysis

Microbubble oscillations were quantified using custom-designed image analysis software to determine the change in microbubble radius as a function of time (R-t curve) [74]. The relative excursion, $x(t)$, was determined as $R = R_0(1 + x)$, with R_0 the resting radius. To study the oscillations at the transmit frequency a 3$^{\text{rd}}$ order Butterworth bandpass filter was applied to $x(t)$, centered at f_T with a 500 kHz bandwidth. The maximum amplitude of the filtered signal was defined as the relative excursion amplitude, $x_0(f_T)$.

The relationship between the relative excursion amplitude, $x_0(f_T)$, and the acoustic pressure amplitude experienced by the microbubble, P, was determined. In principle, microbubbles insonified at low enough acoustic pressures behave as linear oscillators [192, 274]. Therefore, the amplitude x_0 of the relative excursion $x = x_0 \sin(\omega_T t)$ can be described by the expression for a harmonic oscillator [74]:

$$x_0 = \frac{F_0}{\sqrt{\left(\omega_0^2 - \omega_T^2\right)^2 + (\delta \omega_T \omega_0)^2}} \tag{9.1}$$

with $\omega_0 = 2\pi f_0$ where f_0 is the eigenfrequency of the system, $\omega_T = 2\pi f_T$ with f_T the transmit frequency that drives the oscillation, and δ the total damping coefficient. F_0 is the amplitude of the forcing term $F(t) = F_0 \sin(\omega_T t)$ and is given by $F_0 = |P|/(\rho R_0^2)$ [3], with $\rho = 10^3$ kg/m^3 the density of water. The eigenfrequency f_0 of the system is:

$$f_0 = \frac{1}{2\pi} \sqrt{\frac{1}{\rho R_0^2} \left[3\gamma P_0 + \frac{2\left(3\gamma - 1\right)\sigma_w}{R_0} + \frac{4\chi}{R_0} \right]} \tag{9.2}$$

with $\gamma = 1.07$ the ratio of specific heats for C_4F_{10}, $P_0 = 10^5$ Pa the ambient pressure, $\sigma_w = 0.072$ N/m the surface tension, and χ the elasticity of the microbubble shell as obtained from the linearized microbubble dynamics equation [74]. The total damping coefficient includes the sound reradiated by the microbubble, a contribution by liquid viscosity, a thermal contribution assumed equal to the viscous contribution [192], and the effect of the shell viscosity [77]:

$$\delta = \frac{\omega_0 R_0}{c} + 2 \cdot \frac{4\mu}{R_0^2 \rho \omega_0} + \frac{4\kappa_s}{R_0^3 \rho \omega_0} \tag{9.3}$$

with $c = 1500$ m/s the speed of sound in water, $\mu = 10^{-3}$ Pa·s the viscosity of water, and κ_s the microbubble shell viscosity. Finally, the relative excursion amplitude x_0 in (9.1) can be rewritten as a function of the acoustic pressure amplitude and transmit frequency:

$$x_0 = \frac{|P|/(4\pi^2 \rho R_0^2)}{\sqrt{\left(f_0^2 - f_T^2\right)^2 + \left(\delta f_T f_0\right)^2}} \tag{9.4}$$

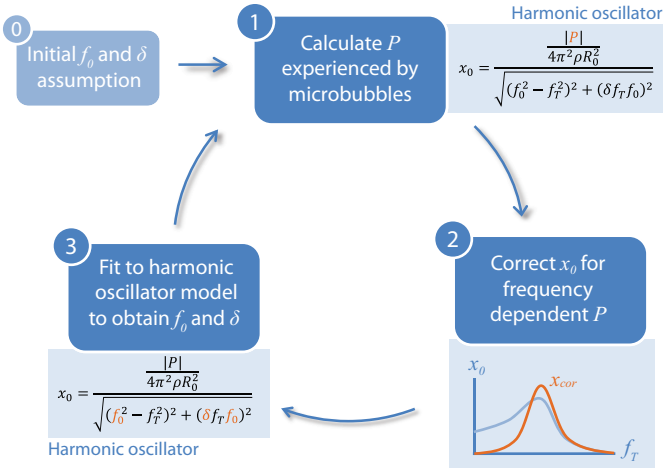

Figure 9.3: Schematic of the iterative method to fit the relative excursion amplitude (x_0) to the harmonic oscillator model (9.4) to determine the pressure amplitude (P) and the microbubble shell parameters, incorporated in the eigenfrequency (f_0) and damping coefficient (δ). Step 1 is repeated for each transmit frequency (f_T) and step 2 and 3 for each microbubble. The parameters determined in each step are shown in orange.

where f_0 and δ depend on the microbubble shell as given in (9.2) and (9.3). Hence, in the linear regime, we can predict the relative excursion amplitude of a microbubble if we know the pressure amplitude, the transmit frequency, and the microbubble's resting size, shell elasticity, and shell viscosity. Equivalently, if we know x_0 and R_0 we can determine the pressure experienced by the microbubble from the experimental data, either in the OrganoPlate or in the OptiCell, when the shell elasticity and viscosity are known.

The shell properties of DSPC-coated microbubbles were determined by van Rooij *et al.* [77] by fitting microbubble excursion to the response of a linear oscillator, at 20 kPa PNP in an OptiCell. However, to account for the variability among microbubble size, shell properties, and the change in shell elasticity with pressure [272], [273], shell characterization was incorporated in our analysis with a new iterative method consisting of three steps, as described below and visualized in Fig. 9.3.

Step 0: Initial Conditions

The initial conditions for the eigenfrequency (f_0) and damping (δ) of each microbubble were chosen by assuming the general shell properties by van Rooij *et al.* [77]. For each microbubble, f_0 was determined using (9.2), the corresponding R_0, and $\chi = 0.26$ N/m [77]. Using (9.3), δ was determined with the R_0 of each microbubble and

a logarithmic fit through the relationship between viscosity and microbubble radius of $\log_{10}(\kappa_s) = 0.188 \cdot R_0 - 8.838$ [77].

Step 1: Calculate $P(f_T)$ experienced by microbubbles
With the initial conditions, R_0, and the known relative excursion amplitudes $x_0(f_T)$, the pressure amplitude experienced by each microbubble was calculated according to the harmonic oscillator model (9.4) (Step 1 in Fig. 9.3). This first step was repeated for every f_T from 1 to 4 MHz and resulted in a frequency dependent pressure, $P(f_T)$, experienced by the microbubbles. To characterize the acoustic propagation into the system, the pressure inside the microchannel was normalized to the applied pressure, $P^* = M(P)/P_A$, with M(P) the median P experienced by microbubbles when insonified at f_T and the applied pressure P_A (20 kPa PNP). When P^* is represented in decibel (dB), it is defined as $20 \cdot \log_{10}(P^*)$.

Step 2: Correct x_0 for the frequency dependent $P(f_T)$
In order to determine the microbubble shell parameters a standard spectroscopy dataset is required, consisting of x_0 as a function of f_T for each microbubble while insonified at uniform pressure amplitude [74]. However, since the pressure in the microchannels found in Step 1 is frequency dependent, $P^*(f_T)$, the microbubbles experienced a different pressure at different f_T. We therefore corrected the relative excursion amplitude for the frequency dependent pressure, $x_{cor} = x_0/P^*(f_T)$ (Step 2 of Fig. 9.3).

Step 3: Fit to harmonic oscillator to obtain shell properties
The corrected relative excursion amplitude, x_{cor}, was fitted to the model of a harmonic oscillator (9.4) by a least-mean-squares method to determine f_0 and δ for every microbubble (Step 3 in Fig. 9.3). This third step resulted in a specific f_0 and δ for each individual microbubble, accounting for the variability of shell properties among them.

Using the specific properties of each individual microbubble, the pressure amplitude experienced by each microbubble was recalculated, returning to the first step of the iterative scheme (Step 1 in Fig. 9.3). In total, 30 iterations were carried out to stabilize the obtained P^*, f_0, and δ. The same data analysis was also performed on the R-t curves obtained by van Rooij *et al.* [77] in an OptiCell (n = 30 microbubbles). All analyses were performed using MATLAB (The MathWorks, Natick, MA, USA).

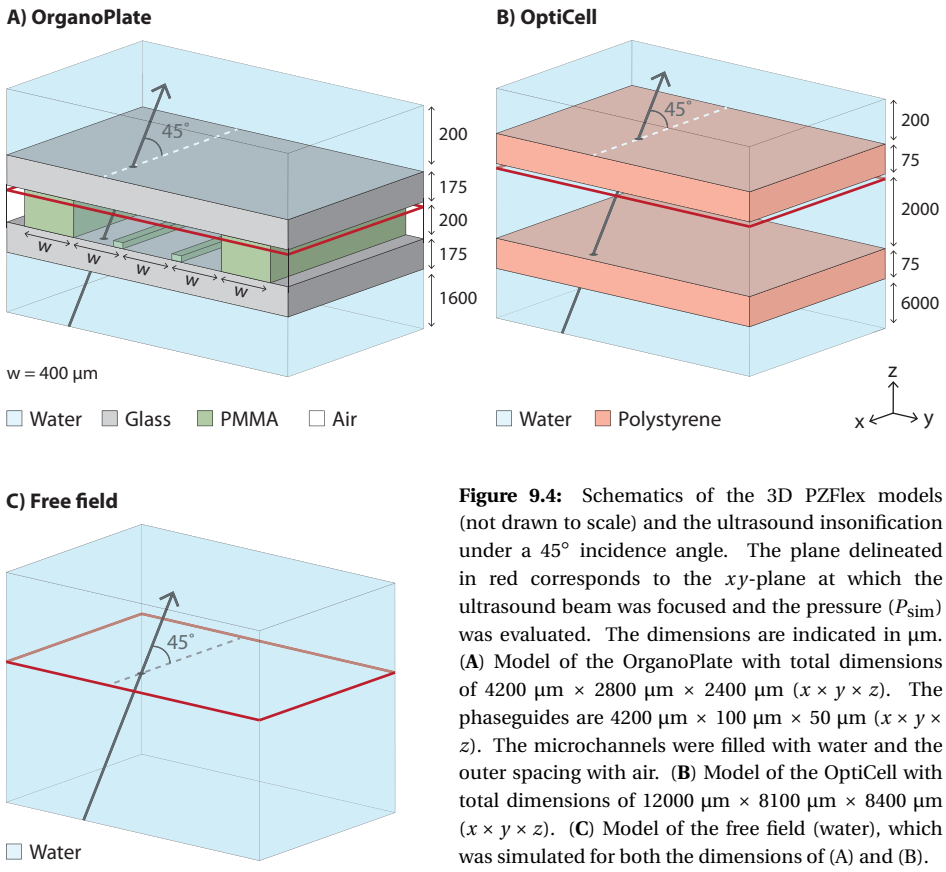

Figure 9.4: Schematics of the 3D PZFlex models (not drawn to scale) and the ultrasound insonification under a 45° incidence angle. The plane delineated in red corresponds to the xy-plane at which the ultrasound beam was focused and the pressure (P_{sim}) was evaluated. The dimensions are indicated in µm. (**A**) Model of the OrganoPlate with total dimensions of 4200 µm × 2800 µm × 2400 µm ($x \times y \times z$). The phaseguides are 4200 µm × 100 µm × 50 µm ($x \times y \times z$). The microchannels were filled with water and the outer spacing with air. (**B**) Model of the OptiCell with total dimensions of 12000 µm × 8100 µm × 8400 µm ($x \times y \times z$). (**C**) Model of the free field (water), which was simulated for both the dimensions of (A) and (B).

Finite Element Model

A 3D wave propagation model was set up in PZFlex (PZFlex LLC, CA, USA), a time domain finite element package. Three different models were simulated: the OrganoPlate, the OptiCell, and the free field in water. The models are shown in Fig. 9.4 and the software implementation can be found in the Supplementary Material.

The model of the OrganoPlate included the glass plates, polymer walls, and phaseguides separating the microchannels, as shown in Fig. 9.4A. The acoustic material properties of PMMA were used to approximate the properties of the polymer walls and phaseguides. The acoustic material properties of borosilicate glass and PMMA are given in Table 9.1. To replicate the insonification conditions of the experimental set-up, the entire OrganoPlate was submersed in water and the three adjacent lanes of the microfluidic network were filled with water. The ultrasound pressure wave originated from a curved disk with the same ratio of curvature radius to diameter as the PA275 transducer (25 mm curvature radius and 23 mm diameter). A

Table 9.1: Acoustic material properties compiled from literature: borosilicate glass [275], [276], PMMA [277], and polystyrene [278].

	Borosilicate glass	PMMA	Polystyrene
Density (g cm^{-3})	2.51	1.20	1.05
Longitudinal velocity (m s^{-1})	5710	2757	2400
Shear velocity (m s^{-1})	3467	1400	1150
Longitudinal attenuation (dB cm^{-1} MHz^{-1})	0.25	1.64	0.35
Shear attenuation (dB cm^{-1} MHz^{-1})	0.8	0.75	1.3

sine wave burst of 8 cycles and unit amplitude was emitted from below at an incidence angle of 45° (Fig. 9.4). The transmit frequency was varied between 1 and 4 MHz. The geometrical focus was located in the middle of the medium channel just beneath the surface of the glass plate, corresponding to the location of the microbubbles during the experiment. The grid size was at least 15 elements per wavelength. The OptiCell was modeled by two polystyrene (Table 9.1) parallel plates, each with a thickness of 75 µm and separated by 2 mm [159], see Fig. 9.4B. The same insonification set-up was simulated for the OptiCell, but now with the ultrasound focus located just below the upper polystyrene plate. To assess the acoustic transparency of both the OrganoPlate and the OptiCell, the wave propagation in the free field was evaluated in the same grid and for the same ultrasound settings (Fig. 9.4C). For all simulations both the longitudinal and shear wave components of the pressure wave propagation were calculated.

The finite element model provides time domain information on the pressure wave propagating through each element. The simulated pressure amplitude (P_{sim}) was defined as the median of the rectangular windowed envelope of the time varying pressure and evaluated in the xy-plane just below the upper glass plate or the polystyrene membrane (Fig. 9.4). We defined $P^*_{sim} = 20 \cdot \log_{10}(P_{sim}/P_{ref})$, normalizing P_{sim} with respect to the maximum pressure amplitude obtained in the free field (P_{ref}), in other words, at the focus when transmitted at the same frequency in water. In the interest of comparing the modeled pressure wave propagation to the experimental data, the median and interquartile range (IQR) of P^*_{sim} were determined in a region equivalent to the field of view around the focus (100 µm × 100 µm).

9.3. RESULTS

Microbubble Oscillation Behavior

Single microbubbles with R_0 from 1.4 to 3.1 μm were insonified and recorded in the OrganoPlate (n = 29). The size range was similar to that previously recorded in the OptiCell (n = 30) [77]. A selection of typical frames of a recorded microbubble in the OrganoPlate are shown in Fig. 9.5, for f_T = 1.6 MHz. Examples of the determined x_0 as a function of R_0 are shown for f_T = 1.0 MHz (Fig. 9.6A), 1.6 MHz (Fig. 9.6B), and 2.8 MHz (Fig. 9.6C). Although variations in response between microbubbles of similar size were observed in the spread of the data points, at f_T = 1.0 and 1.6 MHz the typical x_0 in the OrganoPlate was larger than that in the OptiCell. On the other hand, at f_T = 2.8 MHz, x_0 was similar in both the OrganoPlate and the OptiCell.

By iteratively fitting x_0 to the harmonic oscillator model, the microbubble shell parameters and P experienced by the microbubbles were obtained. The normalized median pressure (P^*) experienced by the microbubbles is shown in Fig. 9.7. The change of P^* for increasing number of iterations at f_T = 1.6 MHz is shown in Fig. 9.7A. The iterative method clearly stabilizes within 30 iterations for both the OrganoPlate and the OptiCell. The frequency dependence of P^* is shown in Fig. 9.7B. The pressure transmitted into the OrganoPlate was larger than in the OptiCell for f_T from 1 to 2 MHz, with mean P^* = 4.7 dB in the OrganoPlate and P^* = −5.0 dB in the OptiCell. The mean P^* from 2 to 4 MHz was similar in both systems: −6.1 dB in the OrganoPlate and −5.1 dB in the OptiCell. In contrast to the OptiCell, the OrganoPlate showed a clear frequency dependent behavior. The χ (with IQR between brackets), obtained by fitting f_0 (Fig. 9.8) to equation (9.2), was similar in both the OrganoPlate and the OptiCell, χ = 0.36 (0.35) N/m and χ = 0.32 (0.25) N/m, respectively. The median κ_s (IQR) was also similar, $\kappa_s = 1.1\ (0.6) \cdot 10^{-8}$ kg/s in the OrganoPlate and $\kappa_s = 0.7\ (0.4) \cdot 10^{-8}$ kg/s in the OptiCell.

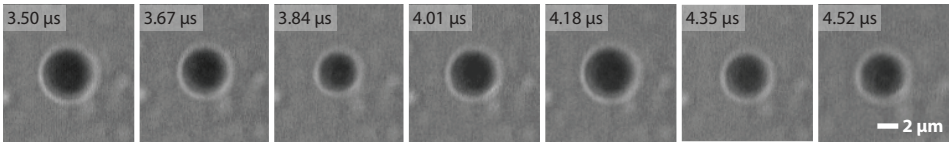

Figure 9.5: Selected frames of a Brandaris 128 ultra-high speed camera recording of a microbubble oscillating in the OrganoPlate (R_0 = 2.18 μm) when insonified at f_T = 1.6 MHz and 20 kPa PNP.

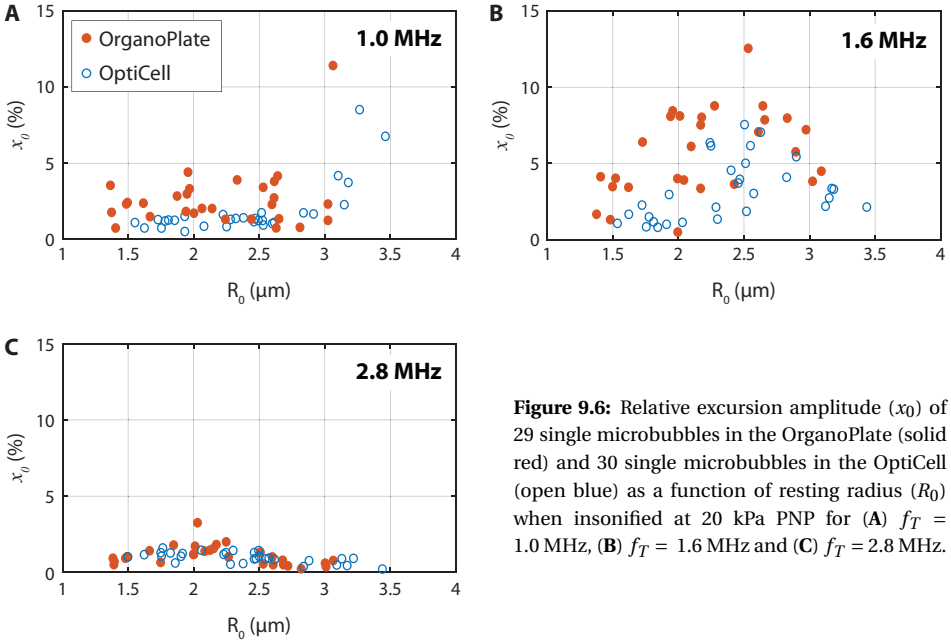

Figure 9.6: Relative excursion amplitude (x_0) of 29 single microbubbles in the OrganoPlate (solid red) and 30 single microbubbles in the OptiCell (open blue) as a function of resting radius (R_0) when insonified at 20 kPa PNP for (**A**) f_T = 1.0 MHz, (**B**) f_T = 1.6 MHz and (**C**) f_T = 2.8 MHz.

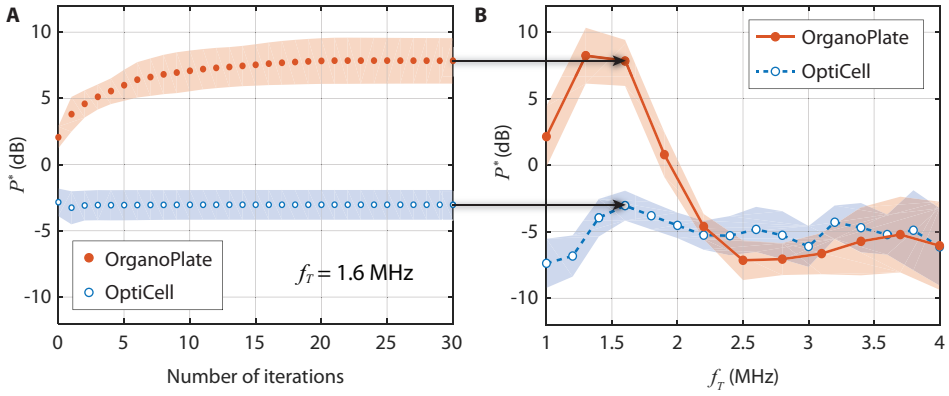

Figure 9.7: Normalized pressure (P^*) experimentally determined in the OrganoPlate (solid red) and OptiCell (open/dashed blue). The shaded area corresponds to the IQR. (**A**) Progress and stabilization of P^* with increasing number of iterations, when insonified at f_T = 1.6 MHz. (**B**) The final P^* obtained at iteration 30, as a function of f_T. The arrows indicate the final P^* as plotted in (A).

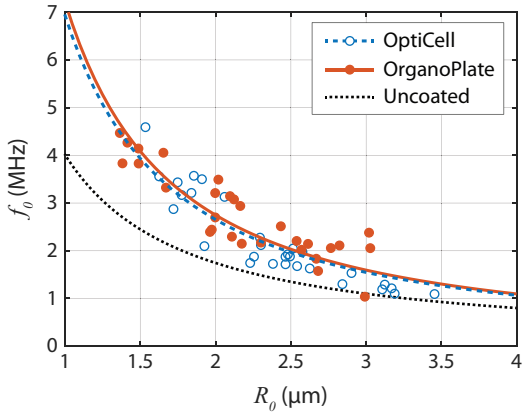

Figure 9.8: Eigenfrequency (f_0) of microbubbles in the OrganoPlate (solid red circles) and OptiCell (open blue circles) and the corresponding fit to (9.2), in order to obtain the average shell elasticity. The f_0 of an uncoated microbubble is given by $\chi = 0$ N/m (black dotted line).

Finite Element Model

The acoustic pressure as a function of time was simulated in water, in the OrganoPlate, and in the OptiCell; see examples depicted in Fig. 9.9. At all f_T, the acoustic pressure in water was evaluated as a reference for the free field and showed a clear start and end point of the pressure wave. In addition, the peak amplitude was constant at 20 kPa PNP over all 8 cycles, with the exception of transient behavior in the first and last pulse.

At f_T = 1.0 MHz (Fig. 9.9A), the pressure amplitude in the OrganoPlate was larger than that in the free field, with P_{sim} = 26 kPa, homogeneous over all cycles, and 15% persisted after the intended 8 cycles due to reverberations. At f_T = 1.6 MHz (Fig. 9.9B), the pressure wave in the OrganoPlate was similar to that in water; the pressure amplitude was P_{sim} = 22 kPa, homogeneous over all cycles, and only 7% of P_{sim} was observed after the intended pulse. At f_T = 2.8 MHz (Fig. 9.9C), the pressure amplitude in the OrganoPlate was only P_{sim} = 14 kPa, but maintained its homogeneity among cycles and 6% of P_{sim} remained. On the other hand, in the OptiCell the pressure amplitude was lower than that in the free field for all f_T. While the pressure was maintained homogeneous over all cycles, the amount of P_{sim} persisting after the intended 8-cycle pulse increased from 8% at f_T = 1.0 MHz up to 30% at 2.8 MHz.

Fig. 9.10 shows examples of the distribution of P^*_{sim} in the free field, the OrganoPlate, and the OptiCell at f_T = 1.0 MHz (Fig. 9.10E, B, and H), f_T = 1.6 MHz (Fig. 9.10F, C, and I), and f_T = 2.8 MHz (Fig. 9.10G, D, and J). The pressure wave was incident under 45° from the positive x-axis, as schematically illustrated in Fig. 9.10A. The pressure field in water had a clear elliptical focus with a smaller −6 dB area for higher transmit frequencies (Fig. 9.10E-G). Inside the OrganoPlate the elliptical focus was clearly changed; the redistribution of the pressure field shifted the maximum towards the right-hand side of the intended focus (positive y-axis). The normalized pressure

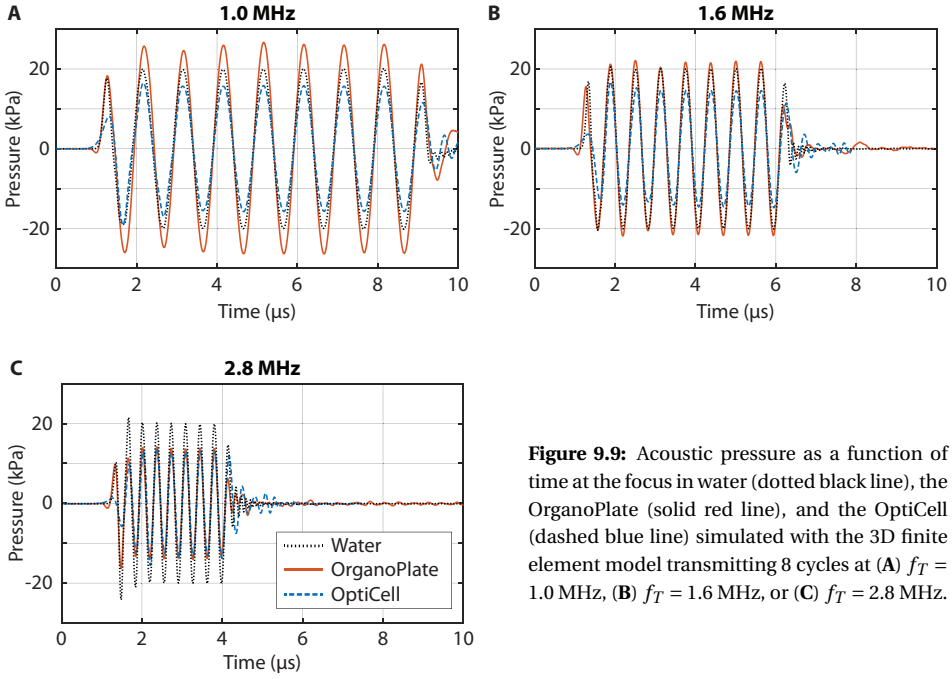

Figure 9.9: Acoustic pressure as a function of time at the focus in water (dotted black line), the OrganoPlate (solid red line), and the OptiCell (dashed blue line) simulated with the 3D finite element model transmitting 8 cycles at (**A**) f_T = 1.0 MHz, (**B**) f_T = 1.6 MHz, or (**C**) f_T = 2.8 MHz.

amplitude when transmitting at 1.0 MHz was 5.3 dB at the maximum and 2.3 dB in the focus (Fig. 9.10B), while 2.9 dB at the maximum and 0.7 dB in the focus for 1.6 MHz (Fig. 9.10C). At 2.8 MHz, it decreased to −0.4 dB at the maximum and −3.2 dB in the focus (Fig. 9.10D). Finally, the pressure distribution in the OptiCell was only slightly more elongated in the direction of propagation than in the free field and the pressure amplitude was at least −2.7 dB lower than P_{ref} (Fig. 9.10H-J).

The frequency dependence of the simulated pressure normalized to the free field is shown in Fig. 9.11, for both the OrganoPlate and the OptiCell. For f_T between 1 and 2 MHz, the mean P^*_{sim} in the OrganoPlate was higher than in the OptiCell (1.6 dB and −2.8 dB respectively). For f_T from 2 to 4 MHz, the mean P^*_{sim} in both systems was similar, with −4.0 dB in the OrganoPlate and −3.8 dB in the OptiCell. For comparison, the P^* obtained experimentally (Fig. 9.7B) is also shown in Fig. 9.11.

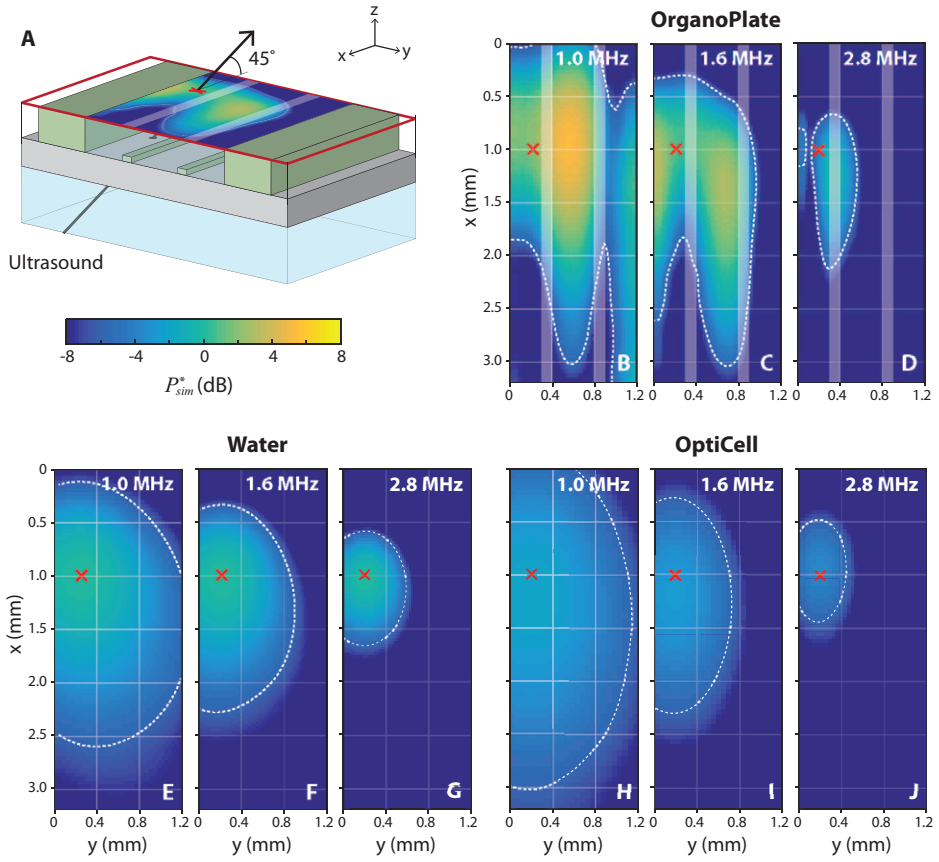

Figure 9.10: Normalized pressure (P^*_{sim}) in the xy-plane at the axial focus simulated with the 3D finite element model, obtained by normalizing the pressure amplitude (P_{sim}) to the maximum pressure amplitude when transmitted in water (P_{ref}). The -6 dB contours are indicated by the white dashed line, the ultrasound geometrical focus by the red cross, and the phaseguides of the OrganoPlate by the white bands. (**A**) Schematic of the OrganoPlate illustrating the xy-plane (delineated in red) at which P^*_{sim} was determined and the ultrasound incidence direction. This example shows P^*_{sim} at f_T = 1.6 MHz. The P^*_{sim} in the OrganoPlate is shown at (**B**) f_T = 1.0 MHz, (**C**) 1.6 MHz, and (**D**) 2.8 MHz; in water at (**E**) f_T = 1.0 MHz, (**F**) 1.6 MHz, and (**G**) 2.8 MHz; and in the OptiCell at (**H**) f_T = 1.0 MHz, (**I**) 1.6 MHz, and (**J**) 2.8 MHz.

9.4. DISCUSSION

To the best of our knowledge, the OrganoPlate has never been used before in combination with ultrasound. Moreover, no information was available on acoustic propagation into the microchannels, which is essential to understand and predict microbubble behavior. The small dimensions of the microchannels in the OrganoPlate do not allow direct measurements of the pressure field using a hydrophone without disturbing the ultrasound field. We therefore assessed the feasibility of controlled

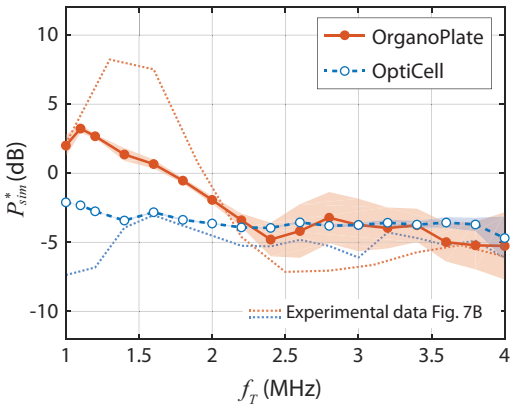

Figure 9.11: Normalized pressure (P^*_{sim}) at the focus in the OrganoPlate (red solid line) and OptiCell (blue dashed line) as a function of f_T, simulated with the 3D finite element models. The shaded area represents the IQR. The dotted lines show the mean P^* obtained experimentally, as shown in Fig. 9.7B.

microbubble behavior in the OrganoPlate by experimentally studying microbubble oscillation and modeling the pressure wave propagation. We found that the pressure wave successfully propagated into the microchannels of the OrganoPlate and resulted in a predictable microbubble oscillatory response.

Microbubble behavior upon ultrasound insonification was fitted to the model of a harmonic oscillator. Measurements were performed at 20 kPa PNP in order to keep the intrinsic nonlinear microbubble response to a minimum [77]. However, the viscoelastic shell parameters are pressure-dependent[272]. With our iterative method, we accounted for this nonlinear viscoelastic behavior as the shell was characterized for each individual microbubble. Hence, allowing for a possible change in shell elasticity and viscosity with pressure. Nevertheless, our method does not account for variation of shell parameters during microbubble oscillation itself. Instead, effective shell parameters are obtained that approximate these variations without characterizing the different contributions. The goal of our iterative method is to determine the pressure experienced by the microbubbles, and the effective shell parameters allow us to predict their behavior using the current physical models.

The spread of the x_0 data points (Fig. 9.6) indicates variations among microbubbles: two microbubbles of the same size may have very different relative excursions. Variations amongst microbubbles of identical size have previously been observed for microbubbles with equal and different coating compositions [53], [77], [177], [65]. While the mean microbubble shell properties are often used to describe microbubble dynamics [79], [272], [74], [77], we determined f_0 and δ specifically for each individual microbubble. By incorporating the variation of shell properties among microbubbles, we were able to more accurately describe the behavior of each individual microbubble.

In our study, the ultrasound propagation into the OrganoPlate was compared to that of the OptiCell, since the latter is commonly used in ultrasound-mediated drug

delivery studies. Although the OptiCell has been extensively used in microbubble characterization and ultrasound-mediated drug delivery studies, a thorough acoustic characterization has not been published. Often, the OptiCell is assumed to be acoustically transparent [56], [272], [279], [97] despite the attenuation that was observed in our experiments and simulations. The main difference between the OrganoPlate and the OptiCell was found for incidence frequencies between 1 and 2 MHz, where the pressure amplitude in the OrganoPlate was higher. Nevertheless, when comparing the OrganoPlate to the OptiCell from 2 to 4 MHz, the simulations predict a root mean square deviation (RMSD) of only 0.9 dB and the measurements a RMSD of 1.4 dB between both systems. Considering that our experimental data was influenced by at least a 10% error of the tracking algorithm [74] and a 15% uncertainty of the hydrophone for the transducer calibration, the pressure in the OrganoPlate and OptiCell between 2 and 4 MHz was not significantly different. Furthermore, the characteristic frequency response of microbubbles was unchanged since f_0 and κ_s were the same in both the OrganoPlate and the OptiCell.

The focal region in the OrganoPlate was clearly altered (Fig. 9.10) because of the reflections at the polymer walls and air spacing outside of the microchannels. The parallel membranes of the OptiCell, on the other hand, had a minor effect on the shape of the focus. Nevertheless, as long as this altered focal region is taken into account during the design of future experiments, microbubbles in the OrganoPlate can still be insonified in a controlled manner. To achieve reproducible insonifications, standing waves should be avoided [280]. In other words, we want a quick build-up and decay of the intended 8-cycle pulse. By modeling the pressure field in the OrganoPlate, we found no significant remaining oscillations after the intended pulse. On the other hand, the pressure amplitude observed in the OptiCell after the 8-cycle pulse was slightly larger than in the OrganoPlate. Hence, energy was transported better into and out of the OrganoPlate and no standing wave phenomenon was observed.

When comparing the microbubble spectroscopy measurements to the finite element models, the transmitted pressure from 1 to 2 MHz showed the largest deviation. In this frequency range, the RMSD between measurements and simulations was 4.4 dB for the OrganoPlate and 3.0 dB for the OptiCell. Although both approaches clearly showed higher pressures in the OrganoPlate, the experimental data analysis overestimated this effect. A possible explanation is that a single shell elasticity value was determined for every microbubble based on the full range of transmit frequencies. However, at low frequencies the pressure experienced by the microbubble in the OrganoPlate is larger and χ is overestimated, since the effective shell elasticity should decrease with increasing pressure [272]. An overestimation in shell elasticity implies a stiffer shell and would thus lead to smaller relative excursion amplitudes. Therefore, when fitting our measurements to the model of a linear oscillator, the pressure amplitude is overestimated at low transmit frequencies. Nevertheless, when transmitting between

2 and 4 MHz, the RMSD between the simulations and the measurements is only 2.0 dB for the OrganoPlate and 1.4 dB for the OptiCell.

In both the measurements and simulations, the pressure transmitted into the OrganoPlate showed a clear frequency dependent behavior. For insonifications between 1 and 2 MHz, the mean of the measured and simulated pressure amplitude was about 3 dB larger than in the free field. Between 2 and 4 MHz, the pressure in the OrganoPlate decreased to −5 dB. Frequency dependent behavior is expected, since different wavelengths result in different wave interference patterns caused by the dimensions of the OrganoPlate. In future experiments, ultrasound insonification can be corrected for these changes in pressure as a function of frequency. For instance, to obtain 100 kPa inside the OrganoPlate at 1 MHz, 71 kPa needs to be transmitted, while this is 178 kPa at 3 MHz. On the other hand, the pressure propagated into the OptiCell showed no clear frequency dependence from 1 to 4 MHz, with a mean normalized pressure of measurements and simulations of −4 dB.

A limitation of this study is that only the propagation of an 8-cycle pulse was considered. Although some studies employ short pulses to study ultrasound-mediated drug delivery [15], [53], [37], others use much longer bursts to locally induce drug uptake [56], [64], [40], [281]. However, the finite element model showed minimal oscillations persisting after the 8^{th} cycle, suggesting that energy was easily transported out of the OrganoPlate and therefore longer pulses are not expected to affect the pressure amplitude. Another shortcoming of this study is that the pressure field was only studied in the xy-plane just beneath the top glass plate. When targeting microbubbles to a microvessel grown in the OrganoPlate, insonification in a different xy-plane may be required. Since the beamwidth of the incident ultrasound field is large with respect to the small microchannels, the exact focal location in the OrganoPlate is expected to only be of minor influence on the pressure field. If required, the now validated 3D finite element model can be employed to predict the pressure field at any location within the OrganoPlate. Finally, when using the modified OrganoPlate to study ultrasound-mediated drug delivery, biological aspects such as cell culture protocols may need to be reconsidered.

9.5. CONCLUSION

The feasibility of controlled microbubble oscillation in the OrganoPlate was demonstrated by microbubble spectroscopy and finite element modeling of the acoustic pressure propagation. When transmitting from 1 to 2 MHz, the pressure amplitude inside the OrganoPlate was about 3 dB larger than in the free field. On the other hand, when transmitting between 2 and 4 MHz the pressure amplitude was approximately −5 dB with respect to that of the free field, similarly to −4 dB in the OptiCell. When correcting for the known change in pressure, controlled microbubble behavior can be achieved in the OrganoPlate. This demonstrates the potential of the

OrganoPlate to study ultrasound-mediated drug delivery *in vitro* including 3D cell culture, perfusion, and membrane-free soft boundaries.

ACKNOWLEDGEMENT

The authors thank Frits Mastik and Robert Beurskens from the Department of Biomedical Engineering, Erasmus MC, for technical assistance during the experiments. This work was supported in part by the Applied and Engineering Sciences TTW (Veni-project 13669), a part of NWO, and in part by NanoNextNL, a micro- and nanotechnology consortium of the Government of The Netherlands and 130 partners.

SUPPLEMENTARY MATERIAL

Supplementary material to this article can be found online at http://dx.doi.org/10.1109/TUFFC.2018.2803137, containing the software implementation in PZFlex to simulate the pressure wave propagation into the OrganoPlate and OptiCell.

10

Perfusable microvessels-on-a-chip to study microbubble-mediated drug delivery

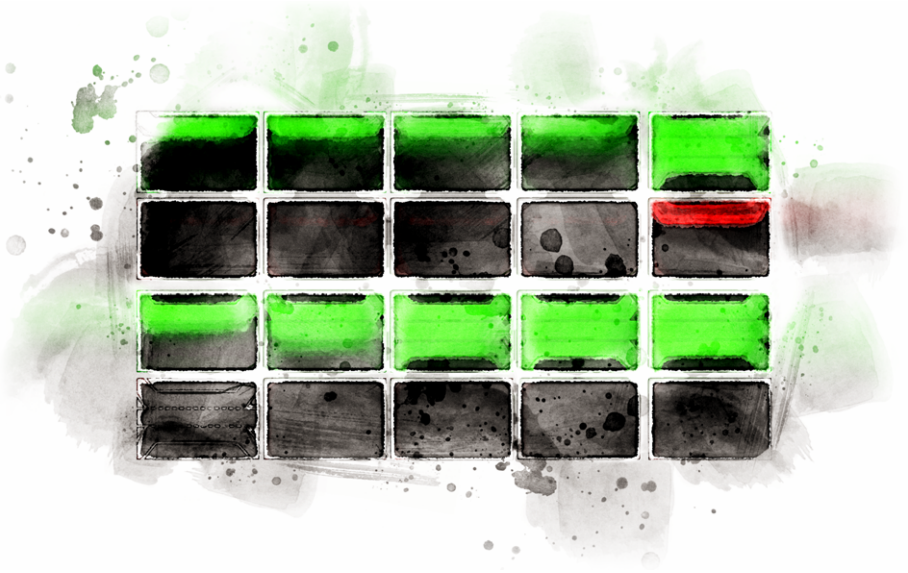

Inés Beekers, Cheryl Mok, Kristina Bishard, Phoei Ying Tang, Merel Vegter, Antonius F. W. van der Steen, Nico de Jong, Sebastiaan J. Trietsch, and Klazina Kooiman

Abstract

Local drug delivery is limited by the presence of natural barriers, such as the vascular endothelium, and consequently higher drug dosages are required to achieve successful treatment. Nevertheless, the vascular permeability can be locally enhanced upon ultrasound insonification of microbubbles to boost drug delivery. Since the underlying mechanisms of microbubble-mediated drug delivery still remain poorly understood, we propose a 3D *in vitro* model to mimic the lumen architecture and physiologically relevant cell behavior. Perfusable microvessels were cultured in the OrganoPlate, a microfluidic organ-on-a-chip platform. The permeability of the barrier formed by human microvascular endothelial cells (HMEC-1) in the OrganoPlate was evaluated. In addition, the potential of this 3D *in vitro* vessel-on-a-chip model to study microbubble-mediated drug delivery was demonstrated by insonifying $\alpha_v\beta_3$-targeted microbubbles and inducing sonoporation.

Index Terms — drug delivery, endothelial, microbubbles, microvessel, vessel-on-a-chip, ultrasound

10.1. INTRODUCTION

To this day, local and efficient drug delivery remains a major clinical challenge. Drugs need to overcome the barriers imposed by the human body to reach their site of action. Therefore, drugs are often given at a higher concentration to still ensure enough extravasation into the region of interest. Since most potent drugs are administered intravenously, the vascular endothelium is one of the main barriers for disease treatment. Due to the inefficient extravasation, a large fraction of the administered dosage will keep circulating in the vasculature, causing systemic toxicity and leading to side effects [9, 18, 282–284]. To locally enhance drug delivery, the vascular permeability can be locally increased with ultrasound insonification of lipid-coated microbubbles. These microbubbles (1 - 10 μm) are ultrasound contrast agents that can be intravenously administered and are widely used as blood-pool markers in clinical ultrasound imaging [1]. Upon ultrasound insonification, the microbubbles will oscillate and can thereby permeabilize the cell membrane (*i.e.* sonoporation), open intercellular junctions, and stimulate endocytosis [3]. However, the underlying mechanisms and relationships between these drug delivery pathways and the microbubble behavior remain poorly understood, hindering maximum therapeutic potential and widespread clinical use.

To elucidate the vascular drug delivery mechanisms, an *in vitro* endothelial cell model ideally achieves physiological relevant cell behavior. Therefore, it should include 3D cell culture, flow, and interaction with extracellular matrix to mimic microcirculation, lumen architecture, and spatial distribution in the absence of

rigid boundaries [261–263]. The *in vivo* physical architecture of a vessel can be reproduced in a vessel-on-a-chip cell culture microfluidic device. We propose using the OrganoPlate®[267] (Mimetas B.V., Leiden, the Netherlands) since it facilitates high throughput cell culture, is optically transparent, provides access to both the apical and basolateral side of the vessel, and it has been characterized for acoustic compatibility [165].

Van Duinen et al. [285] successfully cultured microvessels in the 2-lane OrganoPlate and assessed their permeability. One of their subsequent studies also developed microvascular structures in the 3-lane OrganoPlate to evaluate angiogenesis [286]. These studies demonstrate the potential of the OrganoPlate as a microfluidic platform to develop perfusable microvessels, in a 3D physiological relevant setting. The 3-lane OrganoPlate was also successfully used to develop perfusable intestinal epithelium tubes and evaluate drug-induced barrier integrity loss [270]. To study microbubble-mediated drug delivery, an endothelial microvascular model is required. However, both previous endothelial studies in the OrganoPlate used a human umbilical vein endothelial cell line from Angiocrine Bioscences (HUVEC-VeraVec™, hVera101) which is no longer supplied [285, 286]. Hence, a new endothelial cell culture method needs to be developed to achieve perfusable microvessels in the OrganoPlate. Up to now, microbubble-mediated drug delivery has been studied in 3D engineered microvessels from primary HUVEC grown in a collagen matrix by Juang et al. [191]. They evaluated the occurrence of sonoporation, but did not assess the barrier integrity of their microvascular structures. In a different vessel-on-a-chip platform disruption of angiogenic microvessels was observed 24 h after treatment with ultrasound and microbubbles [287]. However, there was no real-time assessment of treatment and sonoporation was not evaluated.

The aim of this study was to develop a method for 3D endothelial cell culture of microvessels in the OrganoPlate in order to study microbubble-mediated drug delivery in a more physiological relevant setting. We cultured human microvascular endothelial cells (HMEC-1) under perfusion against a scaffold of polymerized collagen-I. The barrier integrity of the cultured microvessels was assessed with a real-time permeability assay by quantifying the diffusion of a fluorescently labeled 150 kDa dextran through the vessel wall. Finally, we evaluated the effect of ultrasound insonification of microbubbles targeted to the microvessel wall, thereby studying microbubble-mediated drug delivery in the OrganoPlate for the first time.

10.2. MATERIALS AND METHODS

The OrganoPlate

The 3-lane OrganoPlate (4003400B, Mimetas B.V.) is a platform developed for 3D cell culture incorporated in a standard 384-wells microtiter plate [267]. The OrganoPlate consists of 40 identical chips, each with 3 parallel microfluidic channels encased between two glass plates (each 175 µm thick) and separated by polymer walls and PhaseGuides [268], as illustrated in Fig. 10.1. The PhaseGuides allow for patterning of an extracellular matrix by the meniscus pinning effect. This prevents overflow of the extracellular matrix to the adjacent channels, resulting in a curved gel boundary that shortens the diffusion distance and makes membrane-free culture possible [267]. In this study we used the 3-lane OrganoPlate, in which the microfluidic channels are each 400×200 µm. The wells of the microtiter plate are connected to the in- and outlets of the microchannels, allowing easy access to the apical side of each channel and acting as medium reservoirs.

Immortalized human dermal microvascular endothelial cells [288] (HMEC-1, CRL-3242, ATCC) were cultured in T75 filter cap flasks (353136, BD Falcon) in MCDB131 medium (10372019, Gibco). This basal medium was supplemented with 10 ng/ml Epidermal Growth Factor (EGF) (E9644, Sigma-Aldrich), 1 µg/ml Hydrocortisone (H0135, Sigma-Aldrich), 10 mM L-Glutamine (G7513, Sigma-Aldrich), 10% fetal bovine serum (FBS, 16140063, Gibco), and 1% Penicillin-Streptomycin (15140122, Gibco). The HMEC-1 were grown in a humidified incubator at 37°C and

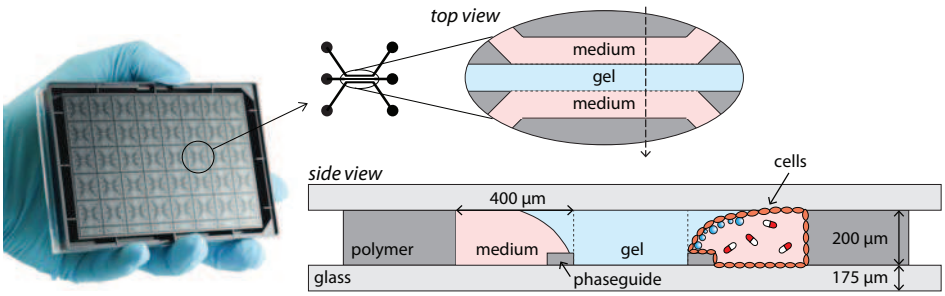

Figure 10.1: Photo of the bottom of the 3-lane OrganoPlate (left), revealing the microfluidic structure incorporated in the standard 384-well microtiter plate. The top view (top right) shows the three adjacent microchannels: two for medium perfusion and one for gel (*i.e.* extracellular matrix). The side view (bottom right) shows the microchannels encased between two glass plates (light gray), bound by polymer walls (dark gray), and separated by polymer PhaseGuides (dark gray, 50×100 µm). The PhaseGuides cause a curved gel meniscus (boundary between blue and pink), acting as a soft cell culture boundary. The side view also illustrates the desired 3D *in vitro* setup with cultured endothelial cells (orange), to which targeted microbubbles (blue spheres) can bind and which can be perfused with therapeutic agent (red/white). Not drawn to scale, adapted from [165].

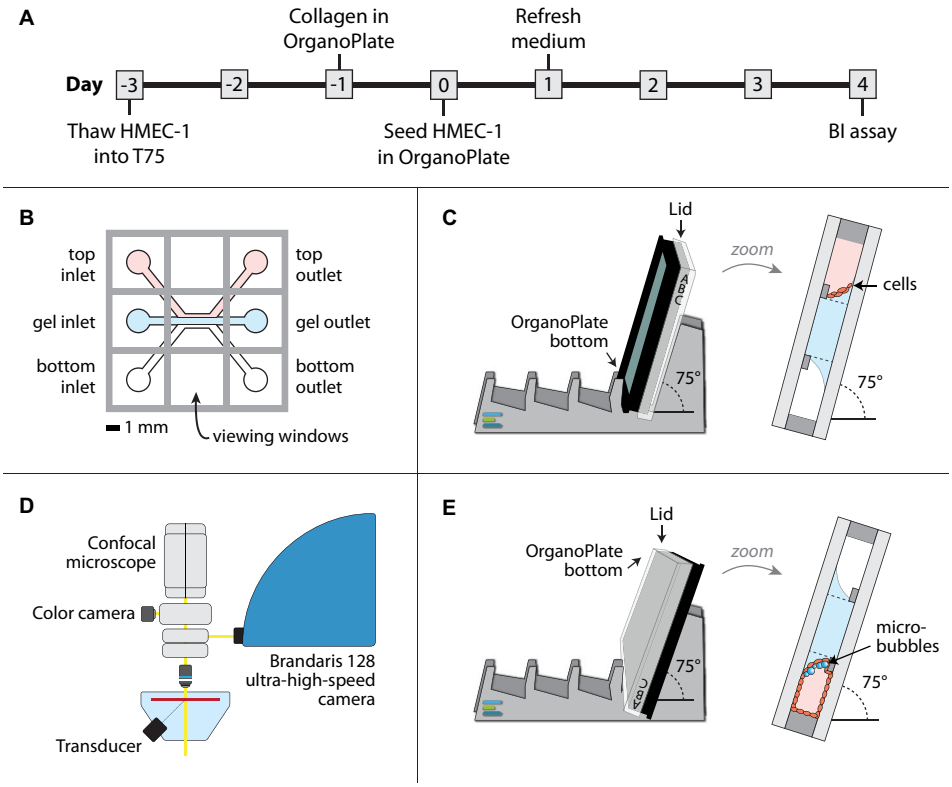

Figure 10.2: Experimental procedure to culture, image, and target microbubbles to microvessels in the OrganoPlate. (**A**) Timeline of OrganoPlate cell culture starting with HMEC-1 thawing, followed by plating of Triton X-100, cell seeding in the OrganoPlate, medium refreshing, and finally the barrier integrity (BI) assay. (**B**) Schematic representation of the wells connected to the different in- and outlets of the top channel, gel channel, and bottom channel. The wells indicated as 'viewing windows' provided optical access, and were also used as humidifying reservoirs. (**C**) Orientation of the OrganoPlate on the Mimetas plate stand for incubation of cells against the meniscus formed by the polymerized collagen. (**D**) Schematic of the experimental set-up for a BI assay imaging with the DS-Fi3 color camera, live cell confocal microscopy with the A1R+ confocal, and ultrasound insonification with a single element focused transducer under a 45°incidence angle from below. (**E**) Orientation of the OrganoPlate on the Mimetas plate stand for incubation of targeted microbubbles for successful binding to the cells on the meniscus formed by the collagen.

5% CO_2. The OrganoPlate cell culture timeline is shown in Fig. 10.2A. For every OrganoPlate, HMEC-1 (passage number 24) were thawed and plated in two T75 flasks at a cell density of $\sim 1.5 \cdot 10^6$ cells/T75 and cultured for three days.

The day before seeding the HMEC-1 from the T75s into the OrganoPlate, extracellular matrix was plated in the middle channel of each chip (Day 1, Fig. 10.2A). To prevent dehydration of the gel, 50 µl phosphate buffered saline (PBS, 14190094, Gibco) was added to the viewing windows (Fig. 10.2B) as humidifying reservoirs. Triton X-100

diluted to 5 mg/ml in 20 mM acetic acid was used as extracellular matrix and two different suppliers were tested, Triton X-100 from Corning (354249, LOT# 8267004) and Cultrex (3447-020-011, LOT# 1532889). A maximum of 30 min before seeding, the collagen was neutralized using HEPES 1 M (15630-056, Gibco) and $NaCO_3$ 37 g/l pH 9.5 (S5761, Sigma-Aldrich) and placed on ice. To pattern the extracellular matrix in the OrganoPlate, 2 µl of collagen was added to all gel inlets (Fig. 10.2B). Next, the OrganoPlate was incubated for 15 minutes on a flat surface in the humidified incubator at 37 °C and 5% CO_2 to promote polymerization of collagen. After incubation, 20 µl of PBS was added to the gel inlets to prevent dehydration of the collagen. The OrganoPlate was placed in the humidified incubator overnight.

The next day (Day 0, Fig. 10.2A), the HMEC-1 in the T75s had roughly reached a cell density of $\sim 5.0 \cdot 10^6$ cells/T75 and were harvested for cell seeding in the OrganoPlate. The HMEC-1 were trypsinized with trypsin/EDTA (30-2101, ATCC) and centrifuged at 250 *g*, 5 min, brake 2. The supernatant was aspirated and the pellet resuspended in MCDB131 at $1.0 \cdot 10^7$ cells/ml. Cell seeding of the OrganoPlate was done by adding 2 µl of cell suspension to each top channel inlet ('cell' chips). In control chip without cells, 2 µl of MCDB131 was added instead ('no cell' chips). Immediately after, an additional 50 µl MCDB131 was added to all top channel inlets to make sure the cells flowed through the channel. The OrganoPlate was incubated for 2 h at 37 °C and 5% CO_2 at an angle of 75° using the Mimetas plate stand (Fig. 10.2C) to promote HMEC-1 adherence to the gel. After incubation, 50 µl MCDB131 was added to the top channel outlets and the bottom channels were kept without medium during cell culture. The OrganoPlate was placed back in the humidified incubator on a Perfusion Rocker (Mimetas B.V.). The rocker was set at a 7° inclination angle and at an 8 min cycle time to create height differences between the wells, which results in a gravity driven, continuous, and bi-directional flow [285]. The medium was refreshed the day after cell seeding (Day 1, Fig. 10.2A).

In this study seven different OrganoPlates were seeded and at least three no-cell chips were included as controls in each. To monitor the development of the microvessel during cell culture, imaging was performed with a brightfield microscope (Zeiss Axiovert 40C Inverted Phase Contrast Microscope, Carl Zeiss) using a 5× objective. The OrganoPlates were used for immunohistochemistry, live cell confocal microscopy imaging, and barrier integrity assays, with or without treatment with microbubbles and ultrasound. The distinct experimental protocols are described below.

Immunohistochemistry in the OrganoPlate

To evaluate the expression of $\alpha_v\beta_3$ (also known as CD51/61) and the presence of intercellular junctions (ZO-1 and VE-cadherin), an immunohistochemistry assay was performed on the HMEC-1 in the OrganoPlate. Unless indicated otherwise, during this protocol all solutions were added with the following volumes: 100 µl / 50 µl to top channel inlet / outlet, 50 µl / 50 µl to the gel inlet / outlet, and 50 µl / 50 µl to the bottom channel inlet / outlet. To enhance perfusion during all incubation steps, when not on the rocker, the OrganoPlate was placed under a slight angle (~7 °), such that the inlets were higher than the outlets.

The HMEC-1 were fixated by incubating for 15 min at room temperature with 4% formaldehyde. After washing twice for 5 min using PBS, the fixated HMEC-1 were stored overnight at 4 °C with PBS in all channels. The following day, all chips were washed again for 5 min with PBS. The chips to be stained for ZO-1 or VE-cadherin were permeabilized by incubating with 0.1% Triton X-100 for 10 min (T8787, Sigma-Aldrich). After washing three times with PBS, all cells were blocked with 5% goat serum (G6767, Sigma Aldrich) by incubating for 30 min. Next, they were incubated overnight at 4°C with the primary antibodies ZO-1 (1:20, 617300, Thermo Fisher), VE-cadherin (1:30, ALX-210-232-C100, Enzo), $\alpha_v\beta_3$ (1:50, 304412, Biolegend), or mouse IgG1 isotype control (1:50, 2600520, Sony Biotechnology). The primary antibodies were added using the following volumes: 25 µl / 25 µl in the top channel inlet / outlet, 0 µl in the gel channel, and 15 µl / 15 µl in the bottom channel inlet / outlet. After overnight incubation the cells were washed once with 0.5% Tween-20 and blocked with 5% goat serum for 30 min. The secondary antibodies anti-mouse (against $\alpha_v\beta_3$, 1:100, A-11029, Thermo Fisher) or anti-rabbit (against ZO-1 and VE-cadherin, 1:100, A 11008, Thermo Fisher) were added using the volumes 25 µl / 25 µl in the top channel inlet / outlet, 0 µl in the gel channel, and 15 µl / 15 µl in the bottom channel inlet / outlet. After incubation in the dark for 60 min at room temperature, the cells were washed three times for 5 min with 0.5% Tween-20. The cytoskeleton of the permeabilized cells was stained with Rhodamine-Phalloidin (1:150, R415, Thermo Fisher) diluted in 0.1% BSA + PBS, by incubating for 40 min in the dark at room temperature followed by washing three times with 0.5% Tween-20 for 5 min. The nuclei of all cells were stained using DRAQ5 (1:500, 62251, Life Technologies) by incubating for 20 min. Finally, all chips were washed once for 5 min with PBS and mounted by incubating for 15 min with 8 µl of Vectashield (H-1400-10, Vector Laboratories Inc.) added to all channel inlets. The cells were imaged with a 63× oil immersion objective using an inverted Meta311 confocal microscope (LSM510META, Carl Zeiss).

Microbubble preparation

Lipid-coated microbubbles with a C_4F_{10} gas core and a 1,2-distearoyl-*sn*-glycero-3-phosphocholine (DSPC)-based coating were produced in-house by probe sonication for 1 min, as previously described [77, 88, 93]. The microbubble coating was fluorescently labeled by adding the lipid dye DiD (1,1'-dioctadecyl-3,3,3',3'-tetramethylindodicarbocyanine perchlorate; D307, Thermo Fisher Scientific) before sonication. The microbubbles were targeted to the $\alpha_v\beta_3$ integrin using biotin-streptavidin bridging, as previously described by others [15, 16, 135, 206–208], with the exception of the type of ligand. Briefly, after washing three times by centrifugation (brake 2, 400 *g*, 1 min) using PBS saturated with C_4F_{10}, the microbubble concentration was determined with a Coulter Counter Multisizer 3 (n=3) (20 µm aperture tube, Beckman Coulter). Next, $6 \cdot 10^8$ microbubbles were incubated on ice for 30 min with 60 µg of streptavidin (S4762, Sigma-Aldrich) and washed. These streptavidin-conjugated microbubbles were incubated on ice for 30 min with 6 µg of biotinylated anti-human $\alpha_v\beta_3$ antibody (304412, BioLegend), followed by a final washing step.

Microbubble-mediated drug delivery in 2D

Before studying microbubble-mediated drug delivery in 3D microvessels in the OrganoPlate, the susceptibility of HMEC-1 to treatment with ultrasound and microbubbles was evaluated in a conventional 2D cell culture setup. Hereby we aimed to determine the ultrasound settings at which sonoporation and opening of cell-cell contacts can be induced in a monolayer of HMEC-1. To both resolve the microbubble oscillation behavior and the resulting cellular response, an optical imaging system was used consisting of the Brandaris 128 ultra-high-speed camera coupled to a custom-built confocal microscope [167]. For this experiment, the HMEC-1 were seeded on the bottom membrane of an OptiCell™ (Thermo Scientific, NUNC GmbH & Co) at a cell density of $3.0 \cdot 10^6$ cells/OptiCell in supplemented MCDB131 medium. The cells were cultured for two days in a humidified incubator at 37 °C and 5% CO_2, without refreshing the medium. The HMEC-1 were stained with fluorescent dyes for live confocal microscopy imaging. They were incubated with CellMask™ Green Plasma Membrane Stain (5 µg/ml final concentration, C37608, Thermo Fisher Scientific), at 37 °C for 10 min. Subsequently, Hoechst (12 µg/ml final concentration, H-3570, Molecular Probes), PI (30 µg/ml final concentration), and $3.0 \cdot 10^6$ microbubbles/ml (final concentration) were added. The OptiCell was then incubated for 5 min, while turned upside down such that the microbubbles would float towards the cells to allow targeted binding. The OptiCell was flipped back just before inserting it in the water bath for simultaneous insonification and imaging (Fig. 10.2D), such that the cells would be at the bottom and the non-bound microbubbles would float away from the cells. Using a 100× water dipping objective (CFI Plan 100XC W, Nikon Instruments)

the cells were imaged with a custom-built upright confocal microscope (A1R+, Nikon Instruments) [167].

For treatment with ultrasound, a single element focused transducer (2.25 MHz center frequency, 76.2 mm focal length, V305, Panametrics-NDT, Olympus) was used to insonify at a 45° incidence angle, while submersed in water (Fig. 10.2D). The transducer output was calibrated in a separate experiment using a needle hydrophone (1-mm diameter, PA2293, Precision Acoustics). The ultrasound and optical foci were aligned such that the cells on the bottom membrane could be simultaneously imaged and insonified, using a single 10-cycle 2 MHz pulse at 400 kPa peak negative pressure (PNP). The pulse was generated with an arbitrary waveform generator (33220A, Agilent) and amplified with a broadband amplifier (ENI A-500, Electronics & Innovation). Upon ultrasound insonification, the microbubble oscillation was recorded with the Brandaris 128 ultra-high-speed camera, as described by Beekers et al. [167]. The microbubble oscillation amplitude, defined as the difference between maximum and resting radius, was determined from the Brandaris 128 ultra-high-speed recordings using custom-designed image analysis software [74].

Barrier integrity assay

The permeability of the microvessel was evaluated with a barrier integrity (BI) assay, by determining the real-time diffusion of a fluorescently labeled 150 kDa dextran through the endothelial layer [285]. This is representative of an *in vivo* microvessel, since molecules with a molecular weight above that of albumin (> 70 kDa) are retained in the vascular lumen [289]. All solutions added to the OrganoPlate during this assay were at 37 °C. Prior to the BI assay, we performed a washing step by aspirating and adding 25 µl of MCDB131 to all in- and outlets. This washing step was incubated for 5 min in the humidified incubator at a 7° inclination angle.

For the BI assay itself, a fluorescent solution was prepared containing 0.5 mg/ml 150 kDa FITC-dextran (fluorescein isothiocyanate–dextran; 46946, Sigma-Aldrich) and 25 µg/ml PI (propidium iodide; P4864, Sigma-Aldrich), diluted in MCDB131 medium at 37 °C. The FITC-dextran was used to assess the permeability of the vessel wall and the PI to assess cell viability and membrane compromise upon sonoporation. All in- and outlets were aspirated and 20 µl / 20 µl MCDB131 was added to the inlets / outlets of the gel and bottom channels. Subsequently, 40 µl of fluorescent solution was added to the inlets of the top channels in which the microvessel was cultured. Next, 30 µl of fluorescent solution was added to the outlets of the top channels.

The BI assay in the OrganoPlate was imaged with the custom-built upright microscope (A1R+, Nikon Instruments) using a 4× air objective and the DS-Fi3 color camera (Nikon Instruments), while the OrganoPlate was placed in a water bath at 37 °C (Fig. 10.2D). The OrganoPlate was imaged following *snake* patterns, meaning that the chips were split up in groups of maximum eight chips and these chips were then imaged one by

one in a cyclical order. On average, each chip was imaged every 8.7 min. The washing step prior to the BI assay was performed on all chips at once and the BI assay was initiated per individual *snake* pattern by adding the fluorescent solution each time. The *snake* patterns were adjusted depending on the experiment and number of seeded chips.

The BI assay ended with a positive control in each chip, which consisted of disrupting the endothelial membrane using 0.1% Triton X-100 [281]. In order to add Triton X-100 but maintain the same perfusion volume in each chip, 10 µl of fluorescent solution was first taken from all top channel inlets. Next, 0.1% Triton X-100 was diluted 1:1 in this fluorescent solution taken from the chips. Of this diluted solution, 10 µl was added back into each top channel inlet. Hereby we inserted a total of 5 µl of 0.1% Triton X-100 in each chip. On average, imaging continued for 18 min after addition of Triton X-100.

Microbubble-mediated drug delivery in 3D

In case microbubbles were added to the microvessels in the OrganoPlate, they were introduced after the washing step of the BI assay and before adding the fluorescent solution containing FITC-dextran and PI. The microbubbles were diluted to $3.0 \cdot 10^6$ microbubbles/ml in MCDB131. The in- and outlets of the top channels were aspirated and 40 µl / 30 µl of microbubble dilution was added to in the inlet / outlets of the top channel. The same volumes of plain MCDB131 were added to control chips and for sham treatment without microbubbles. The OrganoPlate was then placed on the Mimetas plate stand, oriented such that the microbubbles would float upwards towards the endothelial cells on the meniscus of the collagen (Fig. 10.2E). By incubating the OrganoPlate in this orientation for 5 min in the humidified incubator at 37 °C and 5% CO_2, we allowed the targeted microbubbles to bind to the endothelial cells.

To confirm successful binding of the $\alpha_v\beta_3$-targeted microbubbles to the HMEC-1 on the collagen side of the microvessel, a live cell confocal microscopy assay was performed. The cells were stained with 20 µg/ml of Hoechst 33342 (H3570, Thermo Fisher Scientific), 12 µg/ml of CellMask™ Green Plasma Membrane Stain, and 25 µg/ml of PI. Of this dye solution, 40 µl / 30 µl was added to the inlet / outlet of the top channels and incubated for 10 min at 37 °C and 5% CO_2. Next, the wells were aspirated and 40 µl / 30 µl of $1.5 \cdot 10^7$ microbubbles/ml was added to the top channel inlet / outlet. The OrganoPlate was placed on the Mimetas plate stand during 5 min as described above, to allow the microbubbles to target to the endothelial cells on the collagen (Fig. 10.2E). The OrganoPlate was then imaged using the custom-built A1R+ confocal microscope (Nikon Instruments) using a 20× water immersion objective. The plate had to be flipped upside down because it is an upright microscope and the working

distance of the 20× objective is not long enough to image through the microtiter wells on top of the OrganoPlate.

For treatment with ultrasound in the OrganoPlate, the same ultrasound setup was used as described in '*Microbubble-mediated drug delivery in 2D*' (schematic in Fig. 10.2). Insonification occurred at 2 MHz and 400 kPa PNP with a burst of either 5× or 10× 10 cycles, using a repetition frequency of approximately 1 Hz. When chips were treated with ultrasound and microbubbles, control experiments were always included in the same OrganoPlate. These control experiments without ultrasound were performed to control for the imaging procedure and the microvessel permeability as a function of time, with and without microbubbles.

Barrier integrity data analysis

Barrier integrity (BI) assays were performed in four OrganoPlates. The amount of 150 kDa FITC-dextran that diffuses through the endothelial layer into the adjacent gel channel is a measure for the barrier integrity. Therefore, we determined the mean FITC fluorescent intensity within a region of interest (ROI) in the top channel and within a ROI in the gel channel as a function of time. The leakage score was defined as the ratio between the FITC intensity in the gel channel and that in the top channel. For all experiments, time point t = 0 min was defined as the moment when 30 µl of fluorescent solution containing FITC dextran and PI was added to the outlet of the top channel.

First of all, the initial leakage score of the cultured microvessels was quantified. The initial state encompasses the time interval from t = 10 min up to t = 27 min. The first 10 min are disregarded to allow for the fluorescent solution to perfuse through the microvessel and for the volume differences among the in- and outlet wells to equilibrate. We evaluated the inter-plate variability by comparing the mean leakage score in the initial state for each OrganoPlate, separating the data in chips with HMEC-1 culture (*i.e.* 'cell') and control chips without cell culture (*i.e.* 'no-cell'). Due to biological variation, there can be some poorly formed microvessels that have less barrier integrity than others [285]. In order to adequately evaluate the effect of treatment, we excluded the cell chips that showed a leakage score > 50% in their initial state from further treatment and analysis. This ensures that a possible increase in microvessel permeability due to treatment will be distinguished.

The effect of ultrasound and microbubbles was quantified as the change in leakage score upon treatment. Since all chips were insonified individually, the time points of insonification varied between t = 27 min and t = 66 min. To fairly compare enhancement of permeability for all chips, we determined the leakage score 39 min after treatment relative to that just before treatment. For example, when the chip was insonified at t = 30 min (*i.e.* 30 min after addition of the fluorescent BI assay solution) then the relative increase in leakage score was determined as the ratio between the

leakage score at t = 30+39 = 69 min (after treatment) and that at t = 30 min (before treatment).

Lastly, the microvessel permeability was evaluated after the addition of Triton X-100. This provided us with a positive control in each chip, since it disrupts the permeability of the endothelial barrier and therefore yields the maximum leakage score.

Statistical testing to compare the initial state of 'cell' and 'no-cell' chips in each OrganoPlate was performed with the Wilcoxon rank sum test, since the data was non-parametric. The Kruskal Wallis test was performed to distinguish statistical differences in leakage score among chips with or without microbubbles, among different *snake* patterns, among different OrganoPlates, and among the initial state and addition of Triton X-100. Additionally, the Kruskal Wallis test was also performed to distinguish statistical differences between the relative increase in leakage score of controls without ultrasound, treatment with ultrasound and microbubbles, and addition of Triton X-100. Statistically significant differences are indicated with *p<0.05, **p<0.01, ***p<0.001.

10.3. RESULTS

Immunohistochemistry of HMEC-1

The immunohistochemistry revealed the expression of $\alpha_v\beta_3$ on the surface of the HMEC-1 cultured in the OrganoPlate (Fig. 10.3A). When the antibody was substituted for its isotype control, the green fluorescent signal was not observed (Fig. 10.3B). Therefore, the HMEC-1 expressed the angiogenesis receptor that was used to target the microbubbles at least up to six days of culture in the OrganoPlate. The HMEC-1 also developed intercellular junctions since there was a green fluorescent signal present when staining for ZO-1 (Fig. 10.3C) and VE cadherin (Fig. 10.3E) where VE-cadherin distribution was clearly observed at intercellular junctions, which was not visible in the respective anti-rabbit isotype controls (Fig. 10.3D and F).

Barrier integrity of perfusable microvessels

When collagen-I from Corning was seeded as extracellular matrix, the resulting microvessels had protrusions of HMEC-1 growing over the PhaseGuide and into the gel channel (Fig. 10.4A). Variation in gel polymerization can change the density and structure of the patterned extracellular matrix, causing the unwanted growth of cells into the gel. Instead, when collagen-I from Cultrex was used, the HMEC-1 formed a microvessel without growing into the adjacent gel channel (Fig. 10.4).

The development of HMEC-1 into a microvessel was evaluated up to six days after culture. The HMEC-1 adhered to the Cultrex collagen-I meniscus (Fig. 10.5A-B). The droplets in the top and bottom channel are due to condensation and indicative of a proper humidity in the OrganoPlate. Within one day of culture, the HMEC-1

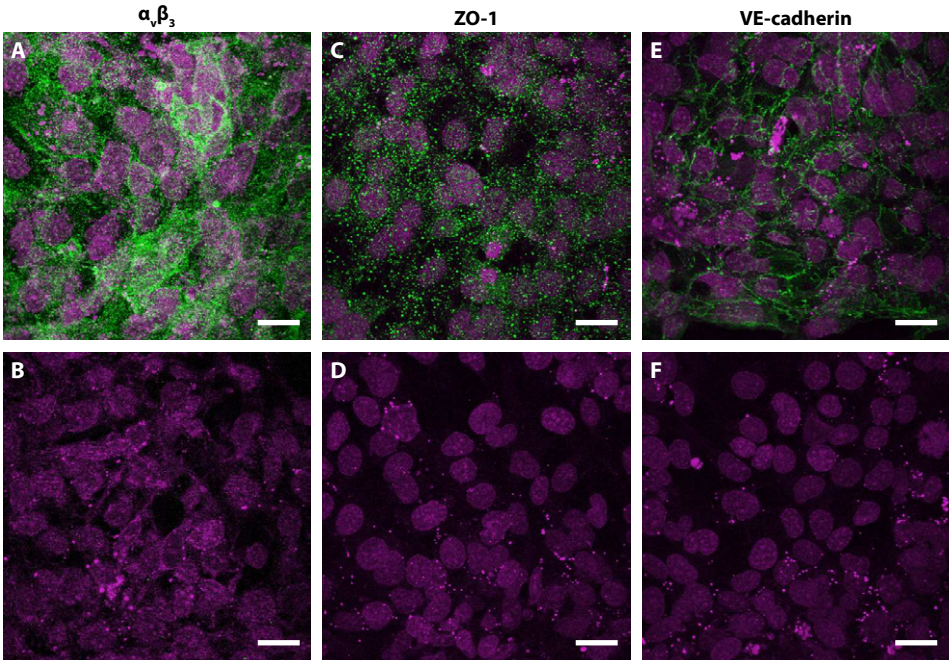

Figure 10.3: Confocal microscopy images of immunohistochemistry of HMEC-1 in the OrganoPlate. The expression of (**A**) $\alpha_v\beta_3$ and its (**B**) isotype control antibody was evaluated. The development of intercellular junctions was assessed by the presence of (**C**) ZO 1 and its (**D**) anti-rabbit control as well as (**E**) VE-cadherin and the corresponding (**F**) anti-rabbit control. The maximum intensity projections are shown of the secondary antibodies in green and the cell nuclei in pink. Corning Triton X-100 was used and the OrganoPlate was cultured for six days. Scale bars are 20 µm.

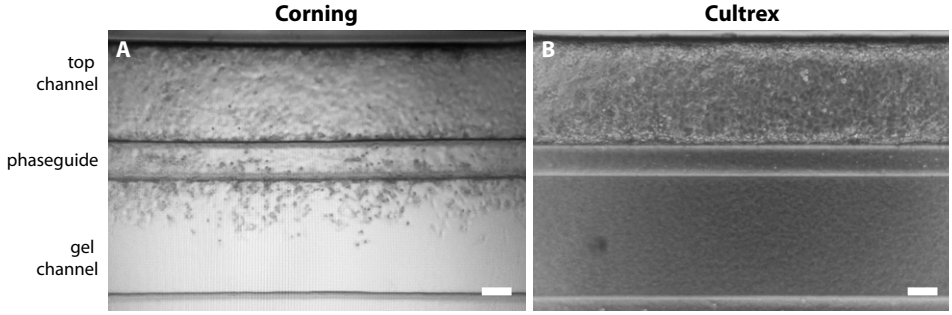

Figure 10.4: Microscopy images of HMEC-1 after four days of culture in the OrganoPlate, in which the seeded collagen-I was either supplied by (**A**) Corning or (**B**) Cultrex. Scale bars are 100 µm.

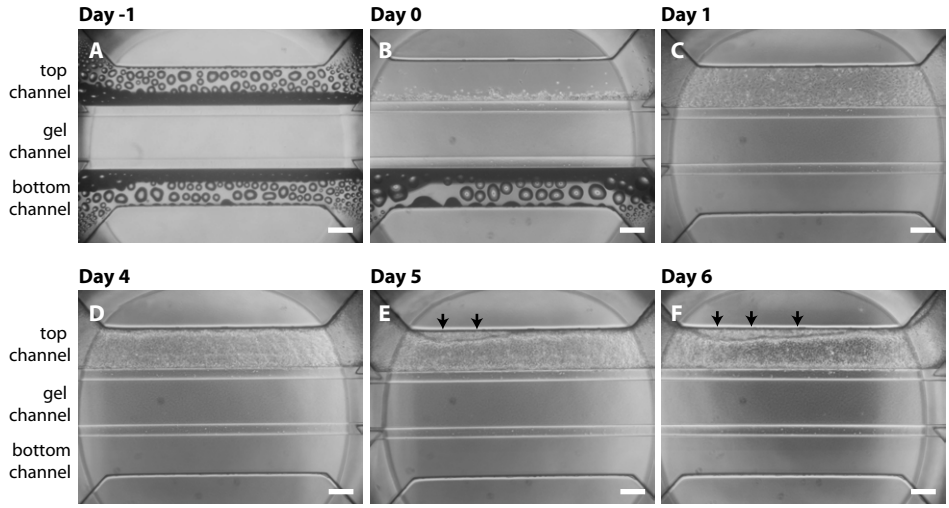

Figure 10.5: Microscopy images showing the cell culture timeline of one chip in the OrganoPlate. (**A**) Collagen-I from Cultrex was seeded, forming a meniscus (shadow in top and bottom channel) by the PhaseGuides. (**B**) HMEC-1 were seeded in the top channel at day 0. They all adhered to the gel side after incubation on the Mimetas plate stand. (**C**) At day 1 the HMEC-1 covered the top channel at low confluency. (**D**) After four days of culture the HMEC-1 developed into a confluent tube. (**E**) At day 5 the tube detached from the walls (black arrows). (**F**) At day 6 detachment of the tube aggravated (black arrows). Scale bars are 200 μm.

proliferated and reached confluence in the top channel, but still at low density (Fig. 10.5C). After four days of cell culture, the cell density in the top channel increased showing a tighter cobblestone morphology, without cells protruding into the gel channel. The change in contrast along the wall of the channel suggests they developed into a full tube (Fig. 10.5D). At day five and six a progressive detachment of the tube from the walls was observed (Fig. 10.5E-F). Based on these results, the BI assays were performed four days after cell seeding.

The permeability of HMEC-1 microvessels after four days of culture was evaluated in four OrganoPlates, resulting into a total of 45 cell chips and 23 no-cell chips. Typical examples of fluorescent images acquired during a BI assay are shown in Fig. 10.6. The cells inhibited the diffusion of the 150 kDa FITC-dextran from the microvessel into the gel channel, since the green fluorescent intensity was much higher in the top channel than in the gel or bottom channel. There was minimal PI signal, indicating high cell viability. However, upon addition of Triton X-100 the permeability of the microvessel was vastly enhanced (green fluorescent signal in all three channels) and cell death was induced (observed by PI uptake in red), causing a clear loss of barrier integrity. In the no-cell control chip, the 150 kDa FITC-dextran needed ~10 min to diffuse through the gel, after which the green fluorescent signal was present in all three channels. Hence,

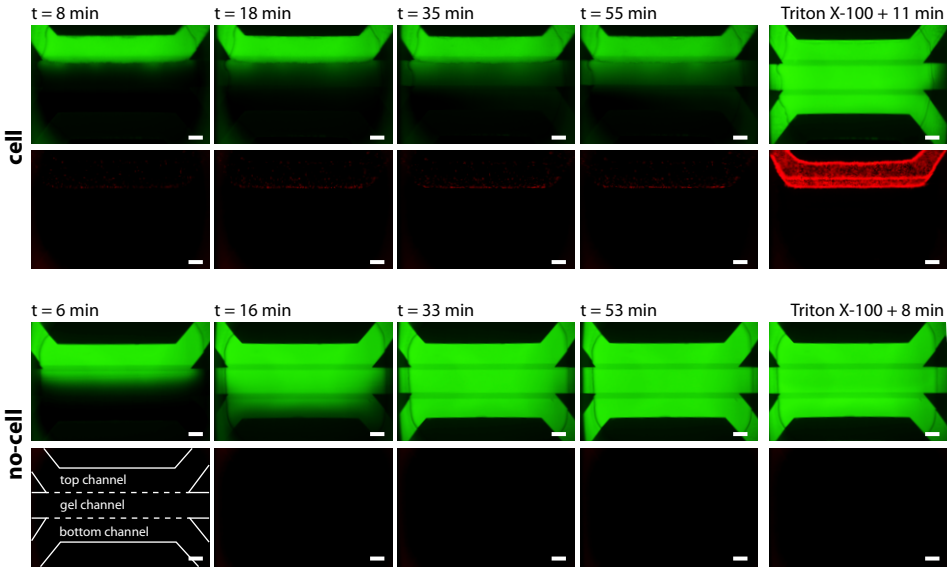

Figure 10.6: Fluorescent microscopy images of a BI assay in a HMEC-1 cell chip (top) and a no-cell control chip (bottom). The microvessel permeability was evaluated with 150 kDa FITC-dextran (green) and cell death with PI (red). The moment the dye solution was added was defined as t = 0 min and 0.1% Triton X-100 was added at t = 61 min to both chips. In these examples there was no treatment with ultrasound and/or microbubbles. The channel structure is delineated in the bottom left panel. Scale bars are 200 µm.

there was no barrier and thus free diffusion among the adjacent channels. Upon addition of Triton X-100 to the no-cell chip there was no change observed, since there was no barrier to disrupt.

By quantifying the fluorescent intensity of 150 kDa FITC-dextran as a function of time, the obtained leakage score showed two distinct time profiles (Fig. 10.7). For a cell chip, we observed a gradual increase in leakage score during the BI assay, since diffusion was inhibited by the endothelial barrier. The leakage score rapidly increased to ~100% when Triton X-100 was added. For a no-cell chip, the leakage score rapidly increased to > 90% within approximately 10 min. The mean leakage score of each chip during the initial state (10 min < t < 27 min) is shown in Fig. 10.8. The spread of scatter points in cell chips shows that there is inter-chip variability among microvessels, even within a single OrganoPlate. However, the initial leakage score of cell chips was always significantly lower than that of the no-cell chips. In some OrganoPlates multiple *snake* patterns were imaged. Although a second or third *snake* pattern was acquired after the previous *snake* was completed (up to 130 min later), we observed no significant differences in leakage score between *snakes*. In other words, the barrier by HMEC-1 was maintained while the OrganoPlate was imaged and placed in the 37 °C water bath. Also, no statistically significant differences were found between the initial leakage score of microvessels with or without microbubbles. When comparing the cell chips

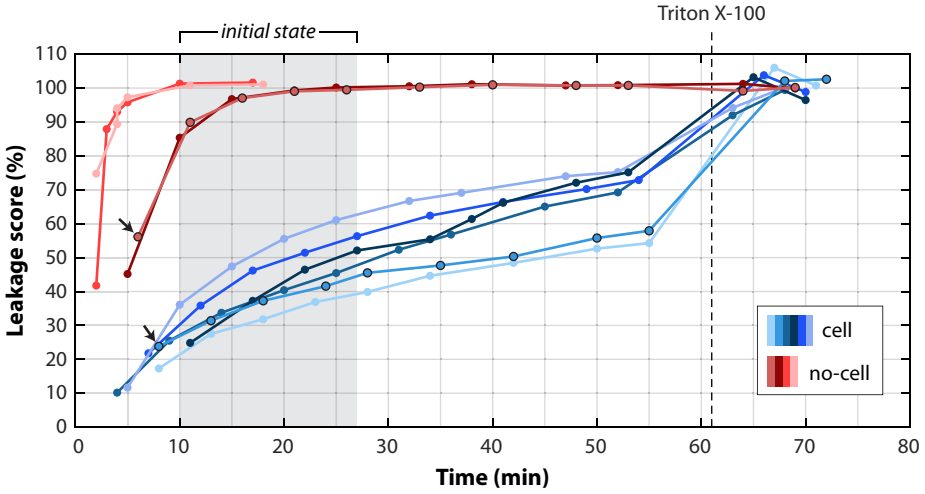

Figure 10.7: The leakage score as a function of time for a BI assay in an OrganoPlate with six cell chips (blue shades) and four no cell chips (red shades). The black arrows indicate the leakage score curves that correspond to the examples shown in Fig. 10.6. The initial state was defined as the mean fluorescence from 10 min to 27 min after the start of the BI assay.

among the four OrganoPlates, there was no statistically significant difference in initial leakage score. Also, the no-cell chips showed the same high leakage score in all OrganoPlates. Therefore, there was no significant inter-plate variability.

In the current study, 34 out of 45 cell chips were included to adequately evaluate the effect of treatment, based on these chips showing an initial state leakage score < 50%. Additionally, all 23 no-cell chips were included. As a positive control, the leakage score of these chips upon addition of Triton X-100 was evaluated. As shown in Fig. 10.9, the initial leakage score of the cell chips [37 (32-41) %, median with interquartile range between parenthesis] was significantly lower than that after addition of Triton X-100 to the cells [102 (100-103) %]. It was also significantly lower than the initial leakage score of the no-cell chips [101 (95-101) %] and than that after addition of Triton X-100 to the no-cell chips [101 (100-102) %]. Addition of Triton X-100 fully disrupted the barrier integrity, since there was no significant difference in leakage score between cell and no-cell chips with Triton X-100. In a few chips it was not possible to evaluate the positive control because of an accidental introduction of an air bubble in the channel when Triton X-100 was added (three of the cell chips and six of the no-cell chips).

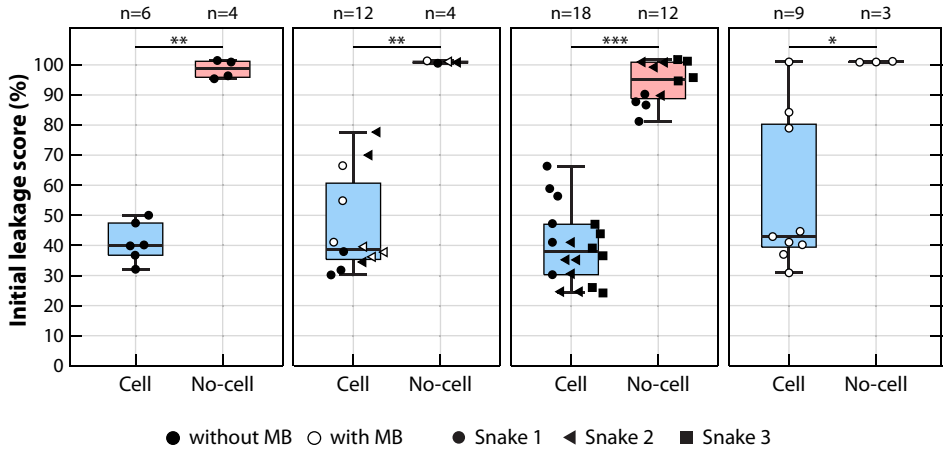

Figure 10.8: The initial leakage score (10 min < t < 27 min) of cell chips (blue) and no cell chips (pink). Each panel shows the leakage score for a different OrganoPlate (the left panel corresponds to Fig. 10.7). The box plots show the median and interquartile range and the whiskers extend from the minimum to maximum value. The scatter plots overlaid on the boxplots show the leakage score for each chip. When microbubbles (MB) were introduced in the microchannel the scatter icons are white, without microbubbles they are black. When the chips in an OrganoPlate were split up into different *snake* patterns during the BI assay, these are indicated by differently shaped icons. Statistically significant differences are indicated with *p<0.05, **p<0.01, ***p<0.001.

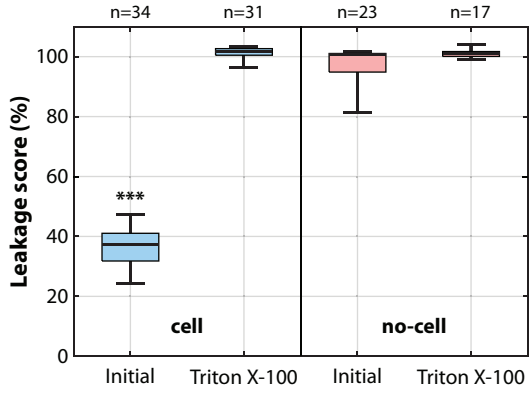

Figure 10.9: Mean leakage score of chips with and without cells in their initial state (10 < t < 27 min) and after treatment with Triton X-100. The initial leakage score of cell chips was significantly lower ($p < 0.001$) than that of the other conditions. The box plots show the median and interquartile range and the whiskers extend from the minimum to maximum.

Microbubble-mediated drug delivery

The HMEC-1 in a conventional 2D monolayer were susceptible to microbubble-mediated drug delivery. Upon insonification with a single 10-cycle burst at 2 MHz and 400 kPa PNP we observed influx of PI locally at the microbubble location and formation of gaps between neighboring cells (Fig. 10.10, arrowheads indicate gap formation). Hence, the oscillating microbubble caused both sonoporation and opening of cell-cell contacts. The microbubble had an oscillation amplitude of

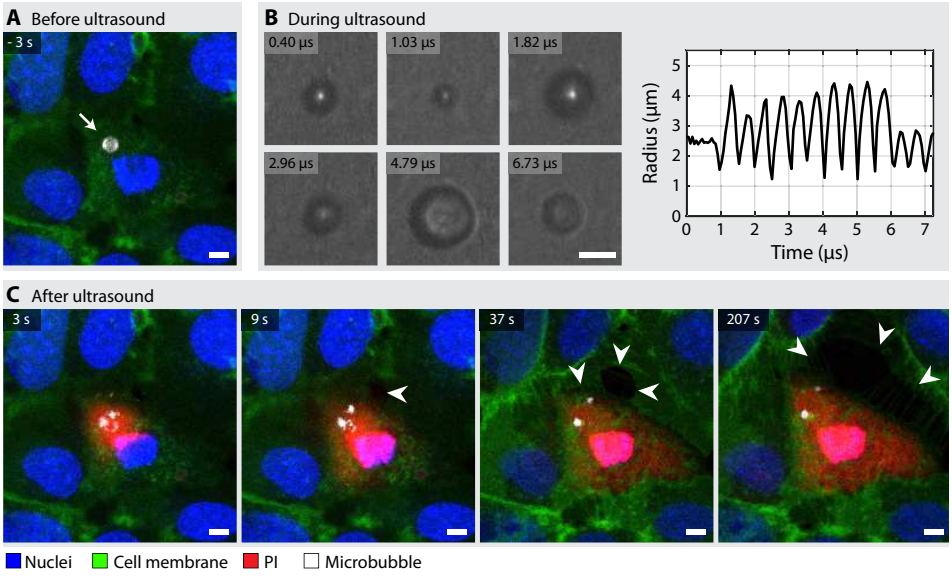

Figure 10.10: Microbubble-mediated drug delivery in a 2D monolayer of HMEC-1 in the OptiCell. (**A**) Selected frame of confocal microscopy time-lapse imaging before ultrasound, showing a single microbubble (arrow) bound to the HMEC-1. (**B**) Selected frames of Brandaris 128 ultra-high-speed imaging during ultrasound insonification, single 10-cycle burst at 2 MHz and 400 kPa PNP, and the microbubble radius as a function of time. (**C**) Selected frames of confocal microscopy time-lapse imaging after ultrasound. The cell nuclei are shown in blue, cell membrane in green, propidium iodide in red, and the microbubble in white. Scale bars are 5 µm.

1.95 µm. Additionally, this conventional OptiCell experiment confirmed successful binding of the $\alpha_v\beta_3$-targeted microbubbles, since a non-bound microbubble would have floated away from the cells. In the OrganoPlate, we were able to bind the $\alpha_v\beta_3$-targeted microbubbles specifically to the HMEC-1 that grew against the soft boundary formed by the gel meniscus by using the Mimetas plate stand during incubation (Fig. 10.11). The image contrast along the vertical sides of the microvessels is poorer, since the confocal microscopy's axial resolution is lower than the in-plane resolution.

10

Once the initial state confirmed proper barrier integrity of the HMEC-1 microvessels (leakage score < 50%), preliminary data was acquired to evaluated the effect of ultrasound and microbubbles on the endothelial permeability. Typical images taken before and after ultrasound insonification with a 2 MHz, 400 kPa, 5× 10-cycle burst are shown in Fig. 10.12. Successful insonification of the microbubbles was achieved since the spatial distribution of the microbubbles among the microvessel changed upon treatment; both microbubble dissolution and clustering were observed (Fig. 10.12A-B). No discernible change in the diffusion of 150 kDa FITC-dextran was

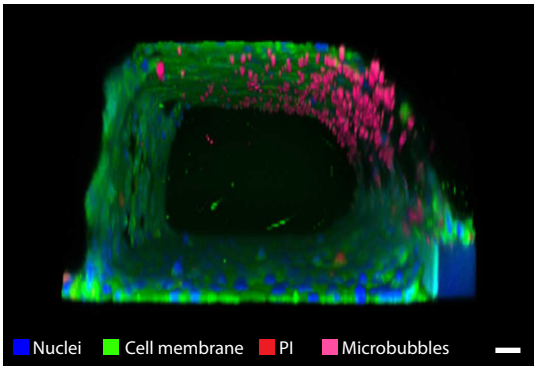

Figure 10.11: Confocal microscopy 3D reconstruction of a microvessel, showing the $\alpha_v\beta_3$-targeted microbubbles (pink) bound to the X at the side of the collagen meniscus. Live cell staining shows the cell nuclei (blue), cell membranes (green), and cells with propidium iodide uptake (PI, red). The OrganoPlate was turned upside down during imaging. Scale bar is 20 µm.

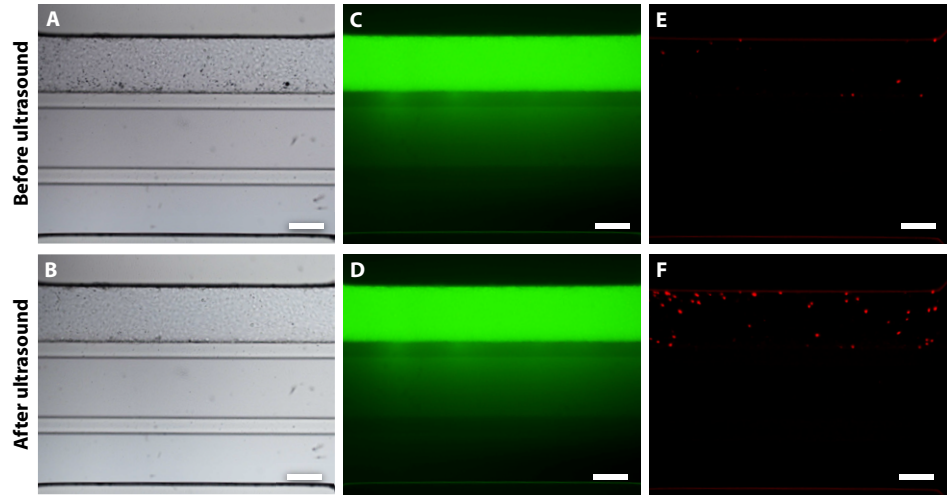

Figure 10.12: Microbubble-mediated drug delivery in 3D microvessels cultured in the OrganoPlate upon insonification with a 2 MHz, 400 kPa, 5× 10-cycle burst. The brightfield images show the channel structure and microbubbles (small black dots) that are present (**A**) before and (**B**) after ultrasound. The fluorescent 150 kDa FITC-dextran images show diffusion from the top channel into the gel channel (**C**) before and (**D**) after ultrasound. The fluorescent PI images show the uptake of model drug in membrane disrupted cells (**E**) before and (**F**) after ultrasound. Scale bars are 200 µm.

seen upon treatment (Fig. 10.12C-D). A local increase in PI was detected in several cells, indicating that uptake of this model drug occurred due to sonoporation (Fig. 10.12E-F). After sham treatment, we observed no change in microbubble distribution or PI uptake.

The change in leakage score 39 min after treatment relative to that just before treatment was evaluated (Fig. 10.13). As a control for the imaging procedure, the treatment without ultrasound (with and without microbubbles) showed an increase in leakage score of 1.3 (1.2 - 1.5) (median with interquartile range in parenthesis).

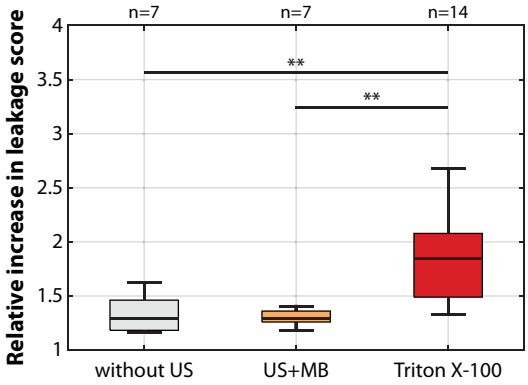

Figure 10.13: Relative increase in leakage score upon control treatment without ultrasound (US), treatment with US and microbubbles (MB), and upon addition of Triton X-100. Data was quantified as the leakage score 39 min after treatment (without US and US+MB) and >10 min after Triton X-100 addition (Triton X-100), relative to the leakage score before treatment. Insonification occurred with a 2 MHz, 400 kPa, and a 5× or 10× 10-cycle burst.

When microbubbles were present in the OrganoPlate, treatment with ultrasound (2 MHz, 400 kPa, 5× or 10× 10-cycle burst) did not result in a significant increase in permeability, since the leakage score after ultrasound and microbubbles was only 1.3 (1.3 - 1.4) times higher than before treatment. As a positive control, Triton X-100 was added to each of these chips after the treatment (or control treatment). This resulted in a significant increase in permeability, since it increased the leakage score by a factor of 1.8 (1.5 - 2.1).

10.4. DISCUSSION

A 3D cell culture method for HMEC-1 in the OrganoPlate was established and perfusable microvessels were successfully cultured to study microbubble-mediated drug delivery. The diffusion of 150 kDa FITC dextran was significantly lower in chips with cells than in those without cells, hence the endothelial wall of the microvessels formed a barrier that inhibited extravasation. Upon addition of an agent for cell permeabilization (Triton X-100), the diffusion of 150 kDa FITC dextran was significantly enhanced. This demonstrates the potential of the OrganoPlate as a 3D *in vitro* model to study enhanced vascular permeability upon treatment.

There was variability in leakage score among chips, even within the same OrganoPlate. Here we discuss various parameters that influence the microvessel quality and could therefore have been responsible for the observed inter-chip variability. As demonstrated by the distinct outcome of different collagen-I suppliers (Fig. 10.4), the gel consistency can hugely affect the structural development of the microvessel. Since the properties of the collagen-I after neutralization are very sensitive to temperature and time, inconsistencies in gel seeding or polymerization among the different chips could easily have taken place. It is also likely that variability in cell seeding density occurred, because of the small volumes that are handled during cell seeding (2 µl). A different initial cell density can influence the structural stability of the microvessel

later on. If the cell density is higher than intended, the cells will sooner reach an over-confluent state, leading to tubular detachment (Fig. 10.5). On the other hand, if the cell density is lower than intended, it might not have developed into a fully confluent microvessel by the time the BI assay was performed (at day 4). Finally, there is also intrinsic variation between chips that can affect the capillary flow during cell loading, leading to variation in cell density and distribution. Despite this inter-chip variability, the leakage score was independent of the presence of microbubbles and of the *snake* pattern in which they were imaged. Most importantly, we found no significant variability among different OrganoPlates. The leakage score in the initial state (10 min < t < 27 min) was used to quantitatively differentiate the chips properly seeded from those that were not. Based on this, 24% of the seeded chips were excluded in the current study due to improper barrier formation. User experience and a standardized timeline during seeding may improve robustness of the protocols.

Achieving proper barrier integrity in the microvessels was essential before proceeding to study microbubble-mediated drug delivery in the OrganoPlate. The susceptibility of HMEC-1 to treatment was demonstrated in a conventional 2D monolayer cell culture system. The microbubble oscillation amplitude that resulted in sonoporation and opening of cell-cell contacts of HMEC-1 was in agreement with those previously reported by others for sonoporation in a monolayer of HUVEC [15, 53, 178, 201]. Additionally, we confirmed that the $\alpha_v\beta_3$-targeted microbubbles bound to the HMEC-1. Using a specific orientation of the OrganoPlate on the Mimetas plate stand during incubation with microbubbles, we were able to control the side of the microvessel to which the microbubbles targeted. In this study we chose to bind them along the meniscus of the gel, since we expect that increasing permeability of those cells will most effectively enhance the diffusion from the microvascular channel into the gel channel.

In the current preliminary study, the microbubbles induced only minimal sonoporation and no significant increase in leakage score upon treatment with ultrasound. We hypothesize that more cells need to be affected for a distinguishable increase in endothelial permeability to be detected by the BI assay. Hence, the microbubble-mediated drug delivery efficiency needs to be improved. More microbubbles could be used, however at too high concentrations acoustic shielding can reduce the oscillation amplitude and thereby end up reducing drug delivery efficiency instead. Possibly a larger microbubble oscillation amplitude might be required to enhance the vascular permeability. Although a single 10-cycle burst at 400 kPa PNP was sufficient to sonoporate and open cell-cell contacts in the monolayer of HMEC-1, the cell culture in the OrganoPlate occurred under continuous perfusion. The flow and 3D physiological relevant structure could influence the robustness of the HMEC-1, making them less susceptible to treatment. Price et al. [290] have investigated the effect of flow on engineered vessels in collagen gels and found that

increased flow resulted in a greater vessel stability and barrier integrity. Additionally, the acoustic transmission into the OrganoPlate is less straightforward than in the OptiCell. It was characterized in an OrganoPlate without the standard microtiter wells on top of the glass microfluidic plates [165]. Hence, this structural modification could potentially reduce the transmission efficiency and higher acoustic pressures might be required to achieve the same microbubble oscillation amplitude in the microchannels. Finally, the fact that the cells are grown against a soft collagen gel, as opposed to on a hard surface, may mean that the cells are more able to move with the microbubble oscillation experiencing less mechanical shear. Although potentially more physiologically relevant, this could hamper easy comparison to literature data. All in all, further testing is needed to find the ultrasound parameters and microbubble concentration required to enhance the microvascular permeability in the OrganoPlate.

The effect of ultrasound only (without microbubbles) on the structural and barrier integrity of the microvessel remains to be investigated. We expect no effect of ultrasound in the range of acoustic pressures used in this study (400 kPa), since in 2D cell culture studies ultrasound insonification without microbubbles did not induce cell detachment or sonoporation [201].

In the perfusable 3D microvascular networks of Juang et al., sonoporation of HUVECs was achieved at 1400 kPa, 500 cycles, 5% duty cycle [191]. They observed less efficient sonoporation at 400 kPa, 1000 cycles, 20% duty cycle. However, the barrier integrity of these microvessels was not evaluated. It remains unknown if the sonoporation they observed would have caused a significant enhancement of microvascular permeability. In general, there is a lack of consensus in current *in vitro* and *in vivo* studies on the necessary acoustic pressure amplitudes to achieve efficient drug delivery, since they range from 80 kPa to 1900 kPa [3]. When studies solely focus on sonoporation by studying the uptake of model drug (such as PI), they only quantify the achieved cell membrane disruption, *i.e.* pore formation. However, drug delivery to the region of interest/target region outside of the vascular system is limited by the presence of intercellular junctions. Hence, sonoporation alone is not sufficient to enhance delivery to the extracellular space. Most studies lack information on the enhanced permeability that can be achieved with microbubble-mediated drug delivery. If the OrganoPlate can be used to evaluate both sonoporation and vascular permeability, it will provide valuable insights into the mechanism of enhanced drug delivery to the extravascular space. Understanding and controlling this mechanism is the first step towards safe and efficient clinical implementation of the therapeutic potential of microbubble-mediated drug delivery.

10.5. CONCLUSION

Development of a HMEC-1 microvessel in the OrganoPlate with barrier integrity for a 150 kDa dextran was successfully demonstrated. Insonification of $\alpha_v\beta_3$-targeted microbubbles induced sonoporation and opening of cell-cell contacts in monolayers of HMEC-1. However, the enhancement of the drug delivery pathways achieved in this preliminary study was still insufficient to detect a significant increase in endothelial permeability in the OrganoPlate. This study is the first step towards elucidating the underlying physical and biological mechanisms of microbubble-mediated drug delivery in a physiological relevant 3D vascular model.

ACKNOWLEDGEMENT

The authors would like to thank Angelique van den Heuvel, Dorota Kurek, Henriëtte Lanz, Manon Haarmans, and Xandor Spijkers, all from Mimetas B.V. the Organ-on-a-Chip company, the Netherlands, for support during cell culture optimization. They would also like to thank R. Beurskens and F. Mastik from the Department of Biomedical Engineering, and M. Manten and G. Springeling from the Department of Experimental Medical Instrumentation, for technical assistance, all from the Erasmus MC University Medical Center Rotterdam, the Netherlands. This work was supported in part by the Applied and Engineering Sciences TTW (Veni-project 13669), part of NWO, and in part by NanoNextNL, a micro- and nanotechnology consortium of the Government of the Netherlands and 130 partners.

11

Discussion

Image by ©Milo, www.milo.nu, *De Groene Amsterdammer*, vol. 142, nr. 1-2, 2018.

Microbubbles are excellent theragnostic agents that can enhance contrast of diagnostic ultrasound imaging and permeabile biological barriers for improved drug delivery. However, to control and maximize the theragnostic potential the underlying physical and biological mechanisms need to be unraveled. In this thesis, we investigated microbubbles targeted to specific biomarkers for molecular imaging and drug delivery, we introduced methodological developments that advance *in vitro* studies, and we elucidated the interplay of microbubble dynamics and the resulting cellular response. In this final chapter we discuss the novel insights gained in this thesis and the future and clinical perspectives of safe and efficient microbubble-mediated drug delivery.

11.1. THE THERAPEUTIC MICROBUBBLE

The ideal therapeutic microbubble should induce predictable bioeffects tunable to the requirements of each therapeutic application. These bioeffects should be delivered locally to only treat the required area of target. This will provide us with the optimal therapeutic tool to enhance drug delivery in a safe and controlled manner for excellent clinical translation and widespread clinical use.

Bound vs. non-bound microbubbles

For molecular imaging, it would be desirable to discriminate microbubbles that are bound to a specific biomarker from those freely floating through the bloodstream. In **Chapter 2** we found that bound microbubbles had a higher resonance frequency and larger relative radial excursion than non-bound microbubbles, upon insonification at low pressures (50 kPa). We could not identify acoustic parameters that distinguished bound from non-bound microbubbles at a more clinically relevant pressure (150 kPa). This does not impede molecular imaging, since bound microbubbles are still distinguishable because they will remain targeted while non-bound microbubbles will flow away through the bloodstream and be cleared within ~10 min, but relies on long acquisition times [291, 292]. Nevertheless, if more in depth and possibly *in vivo* research could identify acoustic parameters at clinical relevant pressures to distinguish bound microbubbles the specificity and acquisition time of molecular imaging could be improved.

Additionally, targeting microbubbles to specific biomarkers increases the specificity of microbubble-mediated drug delivery. By binding microbubbles to diseased cells, local and targeted treatment can be achieved. This boosts the controllability and thereby safety of the therapeutic potential for clinical use. In **Chapter 3** we compared the drug delivery potential of bound and non-bound microbubbles, assessing the microbubble displacement and reversibility of sonoporation. Non-displacing microbubbles induced irreversible sonoporation and therefore appeared to be the main contributor to cell death. The prolonged microbubble oscillation at the

same location on the cell membrane presumably causes a large non-resealing cell membrane pore. Since bound microbubbles are attached at a fixed location on the cell membrane, they are efficient for lethal cell damage when exposed to long acoustic pulses. On the contrary, displacing microbubbles better preserved cell viability. Especially, when a bound microbubble displaced (i.e. it detached during insonification), it became the most efficient at reversible sonoporation. In the setup of this study, detachment of the bound microbubble allowed it to float away and thereby reduced the exposure of the cell to microbubble oscillation. Non-bound microbubbles showed so much more displacement than bound microbubbles, that sometimes multiple microbubbles affected a cell. As a result, non-bound microbubbles caused both reversible and irreversible sonoporation, resulting in a more unpredictable therapeutic outcome.

The studies in **Chapter 2** and **3** were both performed *in vitro*, providing only limited physiological relevance. In the *in vivo* situation the non-bound microbubbles are further from the vascular wall. This will alter their acoustic response and maybe provide parameters to distinguish them from bound microbubbles, which would be closer to the vessel wall [8, 293, 294]. Additionally, non-bound microbubbles were very efficient at sonoporation, maybe just because they could not float away from the cells due to the setup orientation. However, non-bound microbubbles flowing through the vasculature would have very little contact with the endothelial cell. Drug delivery or transfection *in vivo* has indeed shown to be more efficient for bound than for non-bound microbubbles [123–126, 295–297]. Additionally, treatment specificity can be achieved if microbubbles are targeted to the diseased cells, thereby favoring bound microbubbles for therapeutic applications.

Predictable microbubbles

The microbubble excursion amplitude upon insonification was determined from Brandaris 128 ultra-high-speed camera recordings in **Chapter 2**, **4** – **7**, and **9**. All these studies showed large variability in acoustic response among microbubbles, even for microbubbles of the same size and under the same ultrasound insonification parameters [65]. In **Chapter 6** we showed that there is a very narrow range of excursion amplitudes that induce sonoporation without irreversible cell damage. Hence, if we want to make sure we induce viable sonoporation we need to be able to precisely predict the microbubble acoustic response. This highlights the importance of predictable microbubbles, to favor the controllability of microbubble-mediated drug delivery. Additionally, the variability in acoustic response might be obscuring otherwise identifiable differences between bound and non-bound microbubbles, limiting specificity of molecular imaging.

The acoustic properties of microbubbles are believed to be influenced by microstructures in the phospholipid coating [99]. Therefore, in **Chapter 8** the lipid

phase behavior in the microbubble coating was investigated. Lipid handling before microbubble insonification affected the amount of liquid condensed phase, but the heterogeneity in domain morphology of the microstructure remained. Using the indirect lipid handling method, a homogeneous ligand distribution was achieved in DSPC-based microbubbles, expected to improve targeting specificity. By further development of the microbubble composition or adjusting the production methods, we hope to additionally obtain lipid microstructure homogeneity, to achieve a controlled acoustic response on demand. Both homogeneous lipid and ligand distribution will aid the development of tailored microbubble formulations for specific clinical applications.

Using microbubbles with a monodisperse size distribution would reduce the variability in response of a microbubble population [109, 111], and therefore already improve precision in controlling drug delivery. Based on the studies of both **Chapter 6** and **7**, the threshold for sonoporation was independent of microbubble size. Therefore, choosing the adequate size of a monodisperse therapeutic microbubble will only depend on the intended ultrasound frequency, such that microbubbles are insonified at resonance to achieve high excursion amplitudes with relatively low acoustic pressures.

11.2. METHODOLOGICAL DEVELOPMENTS

In this thesis several methodological developments were presented that advanced *in vitro* studies, by improving the imaging capabilities to better resolve the microbubble–cell interaction and by introducing novel acoustically and optically compatible cell culture platforms.

Imaging system

Elucidating the microbubble–cell interaction is an intricate challenge, because the time scales involved range from nanoseconds to hours and the bioeffects occur at nanometer spatial resolution. To overcome the technological gap and achieve imaging at both nanosecond and nanometer resolution, in **Chapter 5** we presented a novel optical imaging system to study the microbubble–cell interaction. To emphasize the added value of high-resolution confocal microscopy to resolve the cellular response, in Fig. 11.1 we present two images of a sonoporated endothelial cell either acquired with widefield microscopy or confocal microscopy. Using this system in **Chapter 6** and **7**, we could for the first time unravel which specific microbubble oscillation behavior leads to which cellular response.

The versatile custom-built confocal microscope allowed us to tune the imaging configuration to the requirements of each experiment. The Resonant scanner was used for fast imaging to resolve Ca_i^{2+} fluctuations and calcium waves (**Chapter 6**). The Galvano scanner was used for higher resolution imaging to resolve the opening of

intercellular junctions (**Chapter 7**). It remains on the wish list to exploit the available motorized z-axis for 3D imaging and study how deep a microbubble is embedded into a cell membrane and the alterations in the 3D cell structure. The cellular response was studied up to 4 min after ultrasound insonification in **Chapter 6** and **7**. To monitor the cell response up to hours and unravel the downstream pathways, we need to further improve the experimental set-up with a controllable atmosphere for stable imaging at 37°C and 5% CO_2.

Cell culture systems

A wide range of *in vitro* experimental techniques exist to study microbubble-mediated drug delivery in a controlled environment. Some platforms are more suitable to understand the fundamental processes, while others are more complex biological platforms that better resemble the *in vivo* situation to advance pre-clinical studies [161]. The *in vitro* systems used for ultrasound studies do not only need to be optically transparent, but also the acoustic transmission into the cell culture chambers needs to be quantified to ensure predictable microbubble oscillation behavior. In this thesis, we demonstrated acoustic and optical compatibility of the CLINIcell (Mabio) for 2D cell culture (**Chapter 4**) and of the OrganoPlate (Mimetas B.V.) for 3D cell culture (**Chapter 9**). The CLINIcell is an easy to use platform for simple biological cell culture, that gives excellent optical and acoustical access to study the microbubble–cell interaction at high resolution and single cell level (**Chapter 6** and **7**). The OrganoPlate is a more complex biological platform that mimics the vascular architecture and is suitable for cell culture against soft boundaries under perfusion. However, the OrganoPlate is a lot more challenging to use (**Chapter 10**). We embrace this complexity, since the OrganoPlate has great potential to investigate extravascular drug delivery, penetration depth, and recovery of the intercellular junction integrity.

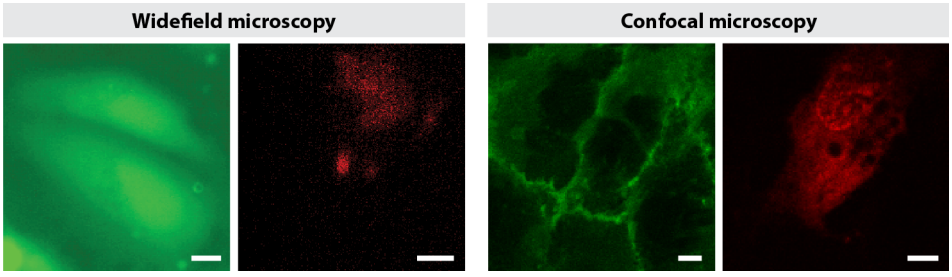

Figure 11.1: Typical images of HUVEC either acquired with the Olympus widefield microscope originally coupled to the Brandaris 128 ultra-high-speed camera [6] or acquired with the new custom-built Nikon confocal microscope [167]. The green channels show the cell image used for cell delineation (Calcein-AM for widefield microscopy and CellMask for confocal microscopy). The red channels show the propidium uptake 15 s after ultrasound insonification of a single targeted microbubble. Scale bars are 5 µm.

Ideally acoustic and optical compatible *in vitro* platforms should be tested or developed that also include flow during treatment. This would better represent the *in vivo* situation to, among others, investigate the differences among bound and non-bound microbubbles. Additionally, co-culture of endothelial cells with pericytes will better simulate the robustness of a microvessel and co-culture with brain or cancer cells will provide better insight into the penetration depth and efficacy of extravascular delivery.

11.3. UNRAVELING THE UNDERLYING MECHANISMS

Microbubble-mediated treatment by co-administration was studied in **Chapter 3**, **6**, **7**, and **10**, providing novel insights into the bioeffects caused by oscillating microbubbles. There are three main drug delivery pathways that can be stimulated: sonoporation, opening of intercellular junctions, and endocytosis [3]. These pathways are often considered as independent delivery routes, suggesting that certain microbubble behavior could favor one route over another. However, an important conclusion from this thesis is that drug delivery pathways are strongly interconnected. Microbubble oscillation will not enhance just a single delivery route, but instead triggers a complex and dynamic chain of biological mechanisms, from which we have only seen the tip of the iceberg. In Fig. 11.2 we present a schematic overview of the chain of bioeffects, based on the insights gained in this thesis.

Sonoporation

Pore formation upon microbubble oscillation is the most extensively studied drug delivery pathway in literature and in this thesis. In **Chapter 3** the occurrence of sonoporation increased significantly when applying higher acoustic pressures and more cycles. Although in that study the microbubble oscillation amplitude was not determined, this did suggest that higher excursion amplitudes increased the chance of sonoporation. In **Chapter 6** and **7** the microbubble oscillation was resolved with the Brandaris 128 ultra-high-speed camera and both studies found that the absolute radial excursion threshold for sonoporation was > 0.7 μm(for a total of 260 single cell responses). It is not the first time that the excursion threshold for sonoporation was determined, since both Kooiman et al. [15] and Helfield et al. [53] found similar thresholds, using a slightly different acoustic frequency and pulse length. Widefield microscopy was used in both these studies to determine the cellular response. However, the confocal microscope's high sensitivity and fast imaging allowed us to detect even lower cytoplasmic uptake and quantify the time profiles of PI uptake. Based on the PI uptake time profiles the reversibility of sonoporation was evaluated, as will be further discussed below. Additionally, the role of asymmetric and nonlinear microbubble oscillation was evaluated in drug delivery for the first time. Despite what has been hypothesized in literature [58], the susceptibly to treatment

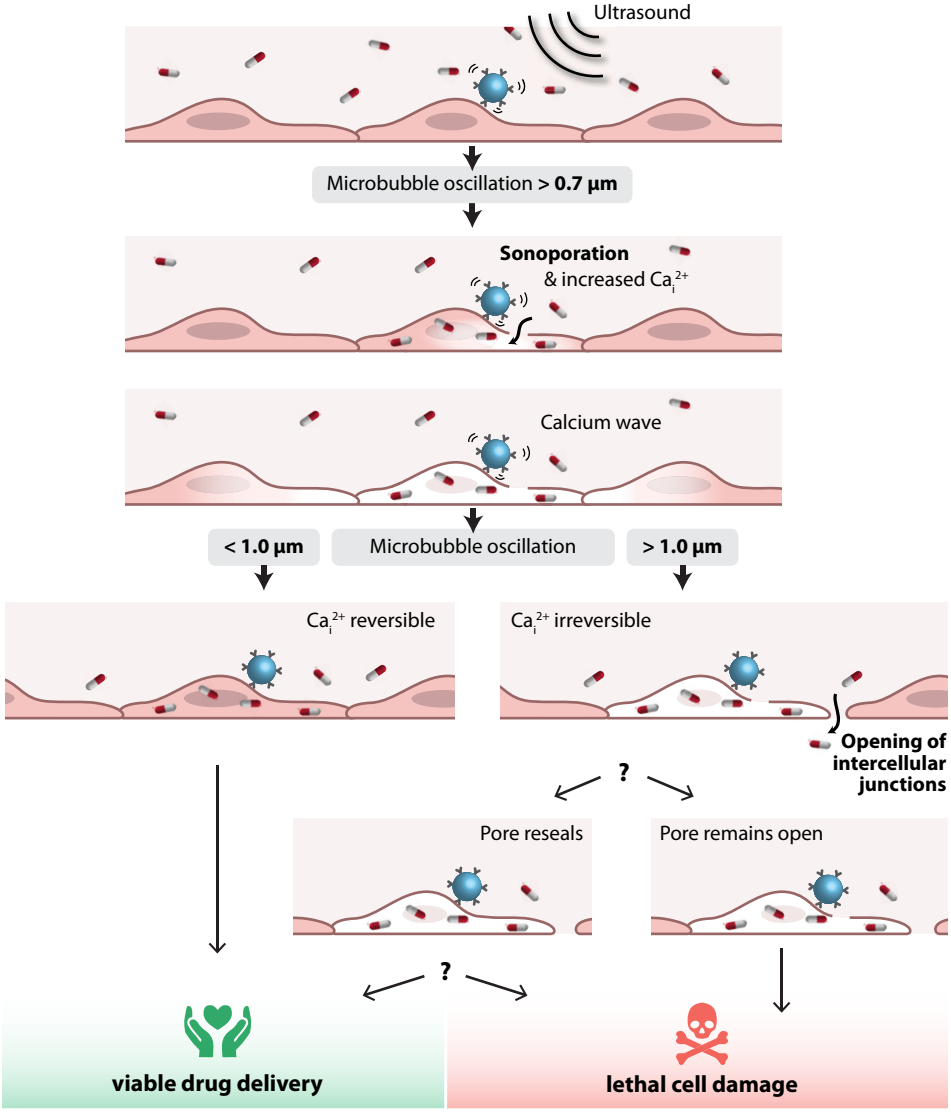

Figure 11.2: The complex chain of drug delivery pathways triggered upon microbubble oscillation unraveled in this thesis. Drug delivery is schematically represented by the pill entering the cell (sonoporation) or extravasating through the cell monolayer (opening of intercellular junctions). Elevated intracellular calcium (Ca_i^{2+}) levels are indicated by white shading in the cell.

did not change upon compression-only behavior or increased harmonic amplitudes (**Chapter 7**).

In the preliminary study of **Chapter 10**, minimal sonoporation of endothelial cells (HMEC-1) was achieved when grown into 3D microvessels in the OrganoPlate. We confirmed that when HMEC-1 were cultured in 2D monolayers, they were sonoporated as easily as HUVEC using the same acoustical settings. This suggests that it is not the cell type, but the 3D morphology and physiological cell behavior that is making sonoporation more challenging. However, the low magnification used in that study makes it very difficult to evaluate the single cell response because it is hard to distinguish the microbubbles and there is lower sensitivity for PI uptake. An in-depth study on microbubble-mediated drug delivery in 3D microvessels will provide a better answer to these remaining questions.

Intracellular calcium

Sonoporation always resulted in a Ca_i^{2+} fluctuation (**Chapter 6**, Fig. 11.2). This is predictable response upon membrane pore formation, since the extracellular concentration of calcium ions is about 10,000 times higher than in the cytosol [298]. Presumably Ca_i^{2+} could also increase by mechanotransduction, triggered upon shear stress or microstreaming by prolonged insonification of the microbubble [188]. The acoustic settings in our study did not show Ca_i^{2+} increase without sonoporation, but maybe longer acoustic pulses at low pressures would stimulate the mechanosensory receptors and enhance Ca_i^{2+} without requiring cell membrane disruption. If so, the Ca_i^{2+} increase could trigger endocytosis [33] to achieve macromolecular uptake without sonoporation, and thereby possibly cause less cell damage on the long-term. This could be the underlying pathway to enhanced macromolecular uptake reported at 40 kPa and 10,000 cycles [299].

Changes in the Ca_i^{2+} concentration are involved in many biological processes and therefore Ca_i^{2+} is often labeled as a *'universal intracellular messenger'* [193]. Differences in speed, amplitude, and spatio-temporal profile of a Ca_i^{2+} fluctuation will result in a different cellular response. Among many others, Ca_i^{2+} is a regulator of endocytosis, exocytosis, membrane resealing, intercellular junction integrity, gene transcription, apoptosis, cell proliferation, cell differentiation, angiogenesis, and motility [47, 59, 193, 196, 300]. In **Chapter 6** we evaluated the changes in Ca_i^{2+} up to 4 min after insonification, hence resolving only the beginning of a complex signaling pathway. It remains to be explored which specific microbubble-induced spatio-temporal Ca_i^{2+} fluctuations correlate with the regulation of which downstream processes.

Upon microbubble oscillation, the Ca_i^{2+} fluctuation in the sonoporated cell propagated to adjacent cells through a calcium wave (**Chapter 6**). In the adjacent non-sonoporated cells, Ca_i^{2+} increased due to triggered release from their internal stores [193]. In these cells, the Ca_i^{2+} fluctuations were always reversible since their Ca_i^{2+} concentration

returned to equilibrium within 180 s. Although the drug delivery potential of the calcium wave was not further evaluated in this thesis, the rise in Ca_i^{2+} could be triggering other biological pathways. For instance, if it could enhance endocytosis in the adjacent cell it would greatly enhance the drug delivery potential of a single microbubble: from enhancing drug delivery in a single cell to delivering in ~9 cells at once, while only sonoporating one of them.

Finally, the role of Ca_i^{2+} in cell fate post-treatment is two-sided. On the one hand, Ca_i^{2+} is required for membrane resealing to take place and therefore essential for cell viability. Deng et al. [49] showed that sonoporation was indeed irreversible if a Ca_i^{2+}-free buffer was used. On the other hand, an overload of Ca_i^{2+} will trigger apoptotic pathways and thus result in cell death [195, 196]. The fine line between these two outcomes is where efficient but viable drug delivery can take place (Fig. 11.2).

Viability post-treatment

For optimal drug delivery we desire maximum intracellular uptake and/or drug extravasation, while causing minimal cell death. In live cell microscopy studies, the cell viability after microbubble-mediated drug delivery is assessed from fluorescent probe leakage (such as Calciein AM) or inferred from pore resealing characteristics [40, 129]. However, cell viability is often assessed in a different sample/field of view/experiment than the drug delivery pathway. Therefore, the direct link between microbubble oscillation – drug delivery – cell death remains to be fully unraveled.

In **Chapter 3**, **6**, and **7** the mathematical diffusion model by Fan et al. [38] was used to correlate the time profiles of PI uptake to the pore size and pore resealing characteristics upon sonoporation. This provided insight into viability post-treatment, since resealing of a pore after sonoporation is essential for a cell to remain viable (Fig. 11.2). In **Chapter 3** we correlated these patterns to a separate cell viability assay, concluding that when pores remained open for more than 120 s the cell was irreversibly sonoporated. In **Chapter 6** we found that irreversible Ca_i^{2+} fluctuations correlated with high amounts of PI uptake and pores that did not reseal within 120 s. Since these cells were not able to recover the homeostatic Ca_i^{2+} concentration, it confirms that cell death will occur when pores remain open > 120 s. However, it remains conjecture and future research should confirm exactly which PI uptake profiles and Ca_i^{2+} fluctuations will indeed induce apoptosis. To study the direct link, ideally a live cell dye that can indicate the onset of cell death should be used, instead of a separate cell death assay. Since mitochondrial depolarization indicates the onset of apoptosis, using a fluorescent probe such as JC-1 (Thermo Fisher Scientific) could help us further unravel when an oscillating microbubble causes a fatal outcome on a single microbubble–cell level.

To distinguish high from low PI uptake, in **Chapter 3** and **6** we used principal component analysis (PCA). Additional thresholding was performed to differentiate the

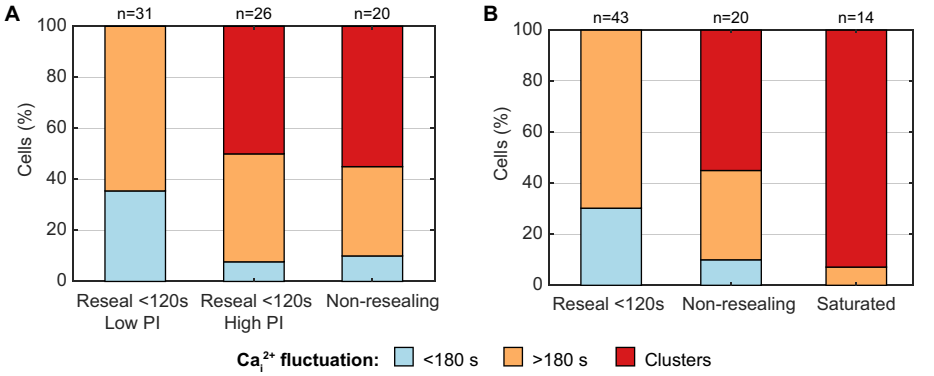

Figure 11.3: Two distinct methods to classify sonoporation were applied on the dataset from Chapter 6 and correlated to the occurrence of different intracellular calcium (Ca_i^{2+}) fluctuations. Sonoporation was quantified based on the pore size and resealing coefficients obtained by Fan et al. [38]. (**A**) Sonoporation was classified based on PCA and pore resealing (see Chapter 6) into *Reseal <120s with Low PI*, *Reseal <120s with High PI*, and *Non-resealing* (corresponding to Fig. 6.5). (**B**) Sonoporation was classified based on pore resealing and PI signal saturation (see Chapter 7) into *Reseal <120s*, *Non-resealing*, and *Saturated*.

cells with resealing pores, based on if PI uptake plateaued within 120 s. However, In **Chapter 7** we re-evaluated the classification of the pore size and pore resealing coefficients. We observed that PI uptake can also appear to stabilize when the detected PI fluorescent intensity becomes saturated. However, the reversibility of sonoporation cannot be assessed upon saturation since the pore might remain open while the corresponding PI increase can no longer be detected. Hence, many pores that were previously classified as resealing < 120 s with high PI uptake, actually showed signal saturation. Consequently, determining pore resealing within 120 s based on the stabilization of PI without taking signal saturation into consideration probably underestimates cell death in **Chapter 3** and **6**. For instance, when we apply both classification methods to the data in **Chapter 6** (Fig. 11.3), pores that seemed to reseal due to PI uptake stabilization caused signal saturation actually all showed irreversible Ca_i^{2+} fluctuations. Hence, taking into account signal saturation is a better measure for cell fate post-treatment.

The pore size and resealing coefficients obtained from the three different studies (**Chapter 3**, **6**, and **7**) cannot be directly compared, because the imaging dependent calibration coefficient α was not quantified (in Equations 3.1, 6.1, and 7.1). Hence, the obtained values are *coefficients* that provide us with relative sizes and resealing as long as imaging is performed under the same fluorescent imaging conditions, i.e. with the same α and using the same extracellular PI concentration (C_0). However, we used a widefield microscopy system in **Chapter 3**, a confocal microscopy Resonant scanner in **Chapter 6**, and a confocal microscopy Galvano scanner in **Chapter 7**. It

would be ideal to directly image the pore created upon sonoporation and its resealing, just like Hu et al. [37]. To do so, an experiment could be devised in which the cells are on the top membrane of the CLINIcell (or similar cell culture platform) and the microbubble below, thereby avoiding that the gas core of the microbubble obscures pore formation.

Cell-cell contacts opening

To enhance drug extravasation, the oscillating microbubble should open the intercellular junctions between the endothelial cells lining the vasculature. Despite the imperative clinical impact of this drug delivery pathway, it has only been investigated in a few fundamental microbubble–cell studies. Up to now, only a single example of live-cell microscopy imaging had been reported showing the transient opening of cell-cell contacts upon sonoporation by an oscillating microbubble [53].

In **Chapter 6** and **7**, the opening of endothelial cell-cell contacts was investigated with high resolution confocal live-cell microscopy. In both studies, there was no distinct microbubble oscillation amplitude associated with the opening of cell-cell contacts. In **Chapter 6** we found that when the Ca_i^{2+} fluctuation upon sonoporation was most severe, showing clustered uptake in the internal Ca_i^{2+} stores, opening of cell-cell contacts was observed most often. This was a first sign suggesting that opening of intercellular junctions might actually be a mechanism triggered by the Ca_i^{2+} messenger upon sonoporation. It could be directly triggered by the rise in Ca_i^{2+} or indirectly through for instance cytoskeletal re-arrangement. The more in depth study in **Chapter 7** demonstrated that opening of cell-cell contact was only enhanced upon sonoporation. Additionally, the microbubble did not have to be near the cell edge to open the intercellular contacts, although that is often hypothesized [3, 33]. Hence, it is not a drug delivery pathway that can be induced separately from sonoporation due to mechanical forces on existing junctions. Opening of cell-cell contacts appeared to be a biological response mechanism due to sonoporation (Fig. 11.2). It is important to realize that this conclusion is based on results for the acoustic parameters evaluated in these studies (short 10-cycle pulses, ranging from 100 to 400 PNP), but it remains to be investigated if the same holds for longer acoustic pulses at lower pressures.

In **Chapter 10**, we evaluated the permeability of a 3D microvessel upon treatment with ultrasound and microbubbles. We expect that this microvessel-on-a-chip in the OrganoPlate is a great model to evaluate drug extravasation achieved by oscillating microbubbles. In the current preliminary study, no significant enhancement of permeability was detected. This suggests that it is more challenging to achieve opening of cell-cell contacts in a physiological cell environment than in 2D monolayers, emphasizing the need of a 3D cell culture model to study microbubble-mediated drug delivery in a set-up representative of the *in vivo* situation.

Initial cell state is crucial

When studying the opening of cell-cell contacts due to oscillating microbubbles in **Chapter 7**, the integrity of the junctions prior to treatment was evaluated. There was a striking difference in cellular response depending on the initial state of the cells. Namely, when the cells were only partially attached to their adjacent cells (partial junctions) it was a lot easier to open those junctions with an oscillating microbubble, than when the cells were fully attached to their neighboring cells (full junctions). In other words, the susceptibility to treatment strongly depended on the initial state of the cells. This emphasizes again the importance of an *in vivo* like model to study microbubble-mediated drug delivery. In future studies, the cell integrity prior to treatment should be assessed and the cell culture should match the appropriate clinical model. For instance, when mimicking tumor vasculature, we should take into account that partial junctions are more predominant, and therefore those vessels may show a larger susceptibility to treatment.

In **Chapter 7**, cells grown in 2D monolayers did not show a different susceptibility to sonoporation depending on the initial integrity of their junctions. However, in **Chapter 10** the endothelial cells cultured in 3D microvessels did appear to be less susceptible to sonoporation, indicating that the perfusion, 3D morphology, or collagen substrate can also influence the cellular response to an oscillating microbubble.

11.4. FUTURE PERSPECTIVES

Clinical translation and safety

Microbubble-mediated drug delivery is transitioning into the clinic, starting with human trials to demonstrate safety and preliminary efficacy. Up to now, the clinical studies focus on treatment of pancreatic cancer [19, 301], liver metastases from gastrointestinal tumors [301], malignant brain tumors [25, 302], Alzheimer's disease [23], and amyotrophic lateral sclerosis [24]. All clinical data showed that microbubble-mediated drug delivery did not induce any serious adverse effects. Additionally, improved therapeutic efficacy compared to a patient control group was demonstrated for pancreatic cancer [19], resulting in an increased median survival. For all brain studies, disruption of the blood-brain barrier was shown to occur upon treatment [23–25, 302]. However, these clinical studies did not evaluate if the available drug concentration was actually higher *in vivo* in the tissue regions treated with ultrasound and microbubbles. Also, no assessments were performed to evaluated if the drug penetration depth was enhanced. Only in one study, the concentration of chemotherapeutic was shown to be higher in sonicated versus unsonicated tissue upon biochemical analysis after tumor resection [25].

The *in vivo* response and risks need to be well evaluated for different applications, since ultrasound transmission is different for each tissue, resulting in different

microbubble oscillation behavior, and thereby causing different cellular responses. Therefore, treatment monitoring is essential to demonstrate the potential of microbubble-mediated drug delivery. If we can monitor how much the therapeutic delivery is actually enhanced, we can design application-specific treatment protocols and tune them per patient, to achieve personalized treatment. To ease clinical translation, there is a need for improved and real-time methods of detection [10]. Treatment can be monitored with MRI-guided techniques [23–25]. However, an ultrasound-based alternative, such as passive acoustic mapping [303], allows to monitor the actual microbubble cavitation activity. Based on the microbubble cavitation, we should ideally be able to predict the cellular responses to control the balance between maximal drug delivery and minimal tissue damage (*i.e.* safety). For instance, a blood-brain opening insonification protocol was implemented by Lipsman et al. [23] and Mainprize et al. [25] that determines the acoustic pressure needed for cavitation, based on sub-harmonic emission, and then uses 50% of this acoustic pressure for treatment. This insonification protocol was developed through an animal study that aimed for successful blood-brain barrier opening while avoiding edema [304, 305]. If we can more specifically predict the cellular response and biological damage based on the microbubble oscillation behavior, we can more effectively monitor treatment through acoustic emission. Hence, it is of crucial importance to unravel the microbubble–cell interaction.

Outlook for the future

Fundamental studies on the microbubble–cell interaction will aid our understanding of microbubble-mediated drug delivery. Predicting the cellular bioeffects in a controlled *in vitro* situation is the first step to achieve control over the drug delivery pathways and complex downstream biological processes enhanced *in vivo*. If we know which microbubble oscillation behavior is responsible for which *in vivo* bioeffects, the microbubble characteristics and/or acoustic parameters can be tuned to the requirements of a specific application. For instance, by designing an insonification scheme for chemotherapeutic treatment that maximizes extravasation towards the tumor but minimizes endothelial cell death. Also, the specificity and/or efficacy of therapeutic treatment could be further enhanced by incorporating drugs in the microbubble core or coating [3]. A better understanding of the underlying bioeffects by studying simpler co-administration will help aid the design of the ideal delivery method. The better we can control the bioeffects of the oscillating microbubble, the safer and more efficient the therapy will be.

In this thesis, we showed that opening of intercellular junctions occurred due to sonoporation, and the more severe the sonoporation, the more often the intercellular junctions were opened. However, upon severe sonoporation the pore formation becomes irreversible and we actually also induce cell death. This suggests that

maximum drug extravasation comes hand in hand with cell death of the vascular endothelium. Although this was the case for our *in vitro* monolayer cell culture, we should point out that *in vivo* the body has response mechanisms that can cure the vascularization upon cell death. For instance, an inflammatory response following increased blood-brain barrier permeability has been reported *in vivo* [306]. It has been shown *in vivo* that blood-brain barrier disruption is reversible and that vascular integrity is restored within 24 h [23–25]. Although recovery of the intercellular junction integrity was not evaluated in this thesis, it is essential to direct future studies towards unraveling the long-term effects of an oscillating microbubble and understanding the recovery mechanisms.

Clinical trials currently use non-targeted microbubbles that have been developed for diagnostic ultrasound contrast enhanced imaging, because these are already clinically approved and commercially available [10]. Although this might speed up clinical translation, these microbubbles were never developed to maximize therapeutic outcome. Additionally, it might well be that the required controllability for safe and maximal drug delivery efficiency can only be achieved with targeted microbubbles. The first clinical trials have demonstrated the safety and molecular imaging potential of BR55 (Bracco Diagnostics), a VEGFR-2-targeted microbubble [221, 307]. All in all, there is a great opportunity for future research to design the ideal and application-specific therapeutic microbubble and slowly advance towards clinical translation of targeted microbubble-mediated drug delivery.

The targeted microbubble has the potential to become a wonderful theragnostic tool. Targeted microbubbles can bind to disease specific biomarkers for molecular imaging using real-time contrast enhanced ultrasound imaging. Next, the same microbubbles can be used to locally enhance drug delivery and treat the diseased tissue, reducing side-effects of systematically administered drugs. All in all, with ultrasound and microbubbles we can diagnose and treat at low cost, high sensitivity, and with portable equipment.

In conclusion, microbubble-mediated drug is climbing its way up into widespread clinical use. Although there are still mysteries to unravel and challenges to overcome, the oscillating microbubble has certainly demonstrated its powerful therapeutic capabilities.

References

[1] D. Cosgrove, "Ultrasound contrast agents: An overview", *European Journal of Radiology*, vol. 60, no. 3, pp. 324–330, 2006. DOI: 10.1016/j.ejrad.2006.06.022.

[2] S. B. Feinstein, B. Coll, D. Staub, D. Adam, A. F. L. Schinkel, F. J. ten Cate, and K. Thomenius, "Contrast enhanced ultrasound imaging", *Journal of Nuclear Cardiology*, vol. 17, no. 1, pp. 106–115, 2010. DOI: 10.1007/s12350-009-9165-y.

[3] K. Kooiman, H. J. Vos, M. Versluis, and N. de Jong, "Acoustic behavior of microbubbles and implications for drug delivery", *Advanced Drug Delivery Reviews*, vol. 72, pp. 28–48, 2014. DOI: 10.1016/j.addr.2014.03.003.

[4] E. P. Stride and C. C. Coussios, "Cavitation and contrast: The use of bubbles in ultrasound imaging and therapy", *Proceedings of the Institution of Mechanical Engineers, Part H: Journal of Engineering in Medicine*, vol. 224, no. 2, pp. 171–191, 2010. DOI: 10.1243/09544119JEIM622.

[5] N. de Jong, F. Ten Cate, C. Lancée, J. Roelandt, and N. Bom, "Principles and recent developments in ultrasound contrast agents", *Ultrasonics*, vol. 29, no. 4, pp. 324–330, 1991. DOI: 10.1016/0041-624X(91)90030-C.

[6] C. T. Chin, C. Lancée, J. Borsboom, F. Mastik, M. E. Frijlink, N. de Jong, M. Versluis, and D. Lohse, "Brandaris 128: A digital 25 million frames per second camera with 128 highly sensitive frames", *Review of Scientific Instruments*, vol. 74, no. 12, pp. 5026–5034, 2003. DOI: 10.1063/1.1626013.

[7] X. Chen, J. Wang, M. Versluis, N. de Jong, and F. S. Villanueva, "Ultra-fast bright field and fluorescence imaging of the dynamics of micrometer-sized objects", *Review of Scientific Instruments*, vol. 84, no. 6, p. 063 701, 2013. DOI: 10.1063/1.4809168.

[8] H. J. Vos, B. Dollet, M. Versluis, and N. de Jong, "Nonspherical Shape Oscillations of Coated Microbubbles in Contact With a Wall", *Ultrasound in Medicine & Biology*, vol. 37, no. 6, pp. 935–948, 2011. DOI: 10.1016/j.ultrasmedbio.2011.02.013.

[9] E. Neuwelt, N. J. Abbott, L. Abrey, W. A. Banks, B. Blakley, T. Davis, B. Engelhardt, P. Grammas, M. Nedergaard, J. Nutt, W. Pardridge, G. A. Rosenberg, Q. Smith, and L. R. Drewes, "Strategies to advance translational research into brain barriers", *The Lancet Neurology*, vol. 7, no. 1, pp. 84–96, 2008. DOI: 10.1016/S1474-4422(07)70326-5.

[10] E. Stride and C. Coussios, "Nucleation, mapping and control of cavitation for drug delivery", *Nature Reviews Physics*, vol. 1, no. 8, pp. 495–509, 2019. DOI: 10.1038/s42254-019-0074-y.

[11] S. Hernot and A. L. Klibanov, "Microbubbles in ultrasound-triggered drug and gene delivery", *Advanced Drug Delivery Reviews*, vol. 60, no. 10, pp. 1153–1166, 2008. DOI: 10.1016/j.addr.2008.03.005.

[12] I. Lentacker, B. Geers, J. Demeester, S. C. De Smedt, and N. N. Sanders, "Design and Evaluation of Doxorubicin-containing Microbubbles for Ultrasound-triggered Doxorubicin Delivery: Cytotoxicity and Mechanisms Involved", *Molecular Therapy*, vol. 18, no. 1, pp. 101–108, 2010. DOI: 10.1038/mt.2009.160.

[13] J. R. Lindner, "Molecular imaging of cardiovascular disease with contrast-enhanced ultrasonography", eng, *Nature Reviews Cardiology*, vol. 6, no. 7, pp. 475–481, 2009. DOI: 10.1038/nrcardio.2009.77.

[14] F. Tranquart, M. Arditi, T. Bettinger, P. Frinking, J. M. Hyvelin, A. Nunn, S. Pochon, and I. Tardy, "Ultrasound contrast agents for ultrasound molecular imaging.", eng, *Zeitschrift fur Gastroenterologie*, vol. 52, no. 11, pp. 1268–1276, 2014. DOI: 10.1055/s-0034-1384999.

[15] K. Kooiman, M. Foppen-Harteveld, A. F. van der Steen, and N. de Jong, "Sonoporation of endothelial cells by vibrating targeted microbubbles", *Journal of Controlled Release*, vol. 154, no. 1, pp. 35–41, 2011. DOI: 10.1016/j.jconrel.2011.04.008.

[16] I. Skachkov, Y. Luan, A. F. W. van der Steen, N. de Jong, and K. Kooiman, "Targeted microbubble mediated sonoporation of endothelial cells in vivo", *IEEE Transactions on Ultrasonics, Ferroelectrics, and Frequency Control*, vol. 61, no. 10, pp. 1661–1667, 2014. DOI: 10.1109/TUFFC.2014.006440.

[17] R. Carlisle and C.-C. Coussios, *Mechanical approaches to oncological drug delivery*. eng, 2013. DOI: 10.4155/tde.13.94.

[18] S. Mullick Chowdhury, T. Lee, and J. K. Willmann, "Ultrasound-guided drug delivery in cancer", eng, *Ultrasonography*, vol. 36, no. 3, pp. 171–184, 2017. DOI: 10.14366/usg.17021.

[19] G. Dimcevski, S. Kotopoulis, T. Bjånes, D. Hoem, J. Schjøtt, B. T. Gjertsen, M. Biermann, A. Molven, H. Sorbye, E. McCormack, M. Postema, and O. H. Gilja, "A human clinical trial using ultrasound and microbubbles to enhance gemcitabine treatment of inoperable pancreatic cancer", *Journal of Controlled Release*, vol. 243, pp. 172–181, 2016. DOI: 10.1016/j.jconrel.2016.10.007.

[20] K. Hynynen, "Ultrasound for drug and gene delivery to the brain", *Advanced Drug Delivery Reviews*, vol. 60, no. 10, pp. 1209–1217, 2008. DOI: 10.1016/j.addr.2008.03.010.

[21] W. M. Pardridge, "Drug and Gene Delivery to the Brain", *Neuron*, vol. 36, no. 4, pp. 555–558, 2002. DOI: 10.1016/S0896-6273(02)01054-1.

[22] K. Hynynen, N. McDannold, N. Vykhodtseva, and F. A. Jolesz, "Noninvasive MR Imaging–guided Focal Opening of the Blood-Brain Barrier in Rabbits", *Radiology*, vol. 220, no. 3, pp. 640–646, 2001. DOI: 10.1148/radiol.2202001804.

[23] N. Lipsman, Y. Meng, A. J. Bethune, Y. Huang, B. Lam, M. Masellis, N. Herrmann, C. Heyn, I. Aubert, A. Boutet, G. S. Smith, K. Hynynen, and S. E. Black, "Blood–brain barrier opening in Alzheimer's disease using MR-guided focused ultrasound", *Nature Communications*, vol. 9, no. 1, p. 2336, 2018. DOI: 10.1038/s41467-018-04529-6.

[24] A. Abrahao, Y. Meng, M. Llinas, Y. Huang, C. Hamani, T. Mainprize, I. Aubert, C. Heyn, S. E. Black, K. Hynynen, N. Lipsman, and L. Zinman, "First-in-human trial of blood–brain barrier opening in amyotrophic lateral sclerosis using MR-guided focused ultrasound", *Nature Communications*, vol. 10, no. 1, p. 4373, 2019. DOI: 10.1038/s41467-019-12426-9.

[25] T. Mainprize, N. Lipsman, Y. Huang, Y. Meng, A. Bethune, S. Ironside, C. Heyn, R. Alkins, M. Trudeau, A. Sahgal, J. Perry, and K. Hynynen, "Blood-Brain Barrier Opening in Primary Brain Tumors with Non-invasive MR-Guided Focused Ultrasound: A Clinical Safety and Feasibility Study", *Scientific Reports*, vol. 9, no. 1, p. 321, 2019. DOI: 10.1038/s41598-018-36340-0.

[26] J. T. Sutton, K. J. Haworth, G. Pyne-Geithman, and C. K. Holland, "Ultrasound-mediated drug delivery for cardiovascular disease", *Expert Opinion on Drug Delivery*, vol. 10, no. 5, pp. 573–592, 2013. DOI: 10.1517/17425247.2013.772578.

[27] E. Unger, T. Porter, J. Lindner, and P. Grayburn, "Cardiovascular drug delivery with ultrasound and microbubbles", *Advanced Drug Delivery Reviews*, vol. 72, pp. 110–126, 2014. DOI: 10.1016/j.addr.2014.01.012.

[28] C. A. Molina, M. Ribo, M. Rubiera, J. Montaner, E. Santamarina, R. Delgado-Mederos, J. F. Arenillas, R. Huertas, F. Purroy, P. Delgado, and J. Alvarez-Sabín, "Microbubble Administration Accelerates Clot Lysis During Continuous 2-MHz Ultrasound Monitoring in Stroke Patients Treated With Intravenous Tissue Plasminogen Activator", *Stroke*, vol. 37, no. 2, pp. 425–429, 2006. DOI: 10.1161/01.STR.0000199064.94588.39.

[29] W. Mathias, J. M. Tsutsui, B. G. Tavares, A. M. Fava, M. O. Aguiar, B. C. Borges, M. T. Oliveira, A. Soeiro, J. C. Nicolau, H. B. Ribeiro, H. P. Chiang, J. C. Sbano, A. Morad, A. Goldsweig, C. E. Rochitte, B. B. Lopes, J. A. Ramirez, R. Kalil Filho, and T. R. Porter, "Sonothrombolysis in ST-Segment Elevation Myocardial Infarction Treated With Primary Percutaneous Coronary Intervention", *Journal of the American College of Cardiology*, vol. 73, no. 22, pp. 2832–2842, 2019. DOI: 10.1016/j.jacc.2019.03.006.

[30] J. T. Belcik, B. P. Davidson, A. Xie, M. D. Wu, M. Yadava, Y. Qi, S. Liang, C. R. Chon, A. Y. Ammi, J. Field, L. Harmann, W. M. Chilian, J. Linden, and J. R. Lindner, "Augmentation of Muscle Blood Flow by Ultrasound Cavitation Is Mediated by ATP and Purinergic Signaling", *Circulation*, vol. 135, no. 13, pp. 1240–1252, 2017. DOI: 10.1161/CIRCULATIONAHA.116.024826.

[31] K. R. Lattwein, H. Shekhar, J. J. Kouijzer, W. J. van Wamel, C. K. Holland, and K. Kooiman, "Sonobactericide: An Emerging Treatment Strategy for Bacterial Infections", *Ultrasound in Medicine & Biology*, vol. 46, no. 2, pp. 193–215, 2020. DOI: 10.1016/j.ultrasmedbio.2019.09.011.

[32] I. Lentacker, I. De Cock, R. Deckers, S. C. De Smedt, and C. T. Moonen, "Understanding ultrasound induced sonoporation: Definitions and underlying mechanisms", *Advanced Drug Delivery Reviews*, vol. 72, pp. 49–64, 2014. DOI: 10.1016/j.addr.2013.11.008.

[33] P. Qin, T. Han, A. C. Yu, and L. Xu, "Mechanistic understanding the bioeffects of ultrasound-driven microbubbles to enhance macromolecule delivery", *Journal of Controlled Release*, vol. 272, pp. 169–181, 2018. DOI: 10.1016/j.jconrel.2018.01.001.

[34] S. Roovers, T. Segers, G. Lajoinie, J. Deprez, M. Versluis, S. C. De Smedt, and I. Lentacker, "The Role of Ultrasound-Driven Microbubble Dynamics in Drug Delivery: From Microbubble Fundamentals to Clinical Translation", *Langmuir*, vol. 35, no. 31, pp. 10 173–10 191, 2019. DOI: 10.1021/acs.langmuir.8b03779.

[35] M. Edidin, "A rapid, quantitative fluorescence assay for cell damage by cytotoxic antibodies.", *Journal of Immunology*, vol. 104, no. 5, pp. 1303–1306, 1970.

[36] F. Yang, N. Gu, D. Chen, X. Xi, D. Zhang, Y. Li, and J. Wu, "Experimental study on cell self-sealing during sonoporation", *Journal of Controlled Release*, vol. 131, no. 3, pp. 205–210, 2008. DOI: 10.1016/j.jconrel.2008.07.038.

[37] Y. Hu, J. M. Wan, and A. C. Yu, "Membrane Perforation and Recovery Dynamics in Microbubble-Mediated Sonoporation", *Ultrasound in Medicine & Biology*, vol. 39, no. 12, pp. 2393–2405, 2013. DOI: 10.1016/j.ultrasmedbio.2013.08.003.

[38] Z. Fan, H. Liu, M. Mayer, and C. X. Deng, "Spatiotemporally controlled single cell sonoporation", *Proceedings of the National Academy of Sciences*, vol. 109, no. 41, pp. 16 486–16 491, 2012. DOI: 10.1073/pnas.1208198109.

[39] Y. Zhou, R. E. Kumon, J. Cui, and C. X. Deng, "The Size of Sonoporation Pores on the Cell Membrane", *Ultrasound in Medicine & Biology*, vol. 35, no. 10, pp. 1756–1760, 2009. DOI: 10.1016/j.ultrasmedbio.2009.05.012.

[40] T. van Rooij, I. Skachkov, I. Beekers, K. R. Lattwein, J. D. Voorneveld, T. J. Kokhuis, D. Bera, Y. Luan, A. F. van der Steen, N. de Jong, and K. Kooiman, "Viability of endothelial cells after ultrasound-mediated sonoporation: Influence of targeting, oscillation, and displacement of microbubbles", *Journal of Controlled Release*, vol. 238, pp. 197–211, 2016. DOI: 10.1016/j.jconrel.2016.07.037.

[41] X. Chen, J. M. Wan, and A. C. Yu, "Sonoporation as a Cellular Stress: Induction of Morphological Repression and Developmental Delays", *Ultrasound in Medicine & Biology*, vol. 39, no. 6, pp. 1075–1086, 2013. DOI: 10.1016/j.ultrasmedbio.2013.01.008.

[42] R. S. Leow, J. M. F. Wan, and A. C. H. Yu, "Membrane blebbing as a recovery manoeuvre in site-specific sonoporation mediated by targeted microbubbles", eng, *Journal of the Royal Society, Interface*, vol. 12, no. 105, p. 20 150 029, 2015. DOI: 10.1098/rsif.2015.0029.

[43] M. Wang, Y. Zhang, C. Cai, J. Tu, X. Guo, and D. Zhang, "Sonoporation-induced cell membrane permeabilization and cytoskeleton disassembly at varied acoustic and microbubble-cell parameters", *Scientific Reports*, vol. 8, no. 1, p. 3885, 2018. DOI: 10.1038/s41598-018-22056-8.

[44] W. Zhong, W. H. Sit, J. M. Wan, and A. C. Yu, "Sonoporation Induces Apoptosis and Cell Cycle Arrest in Human Promyelocytic Leukemia Cells", *Ultrasound in Medicine & Biology*, vol. 37, no. 12, pp. 2149–2159, 2011. DOI: 10.1016/j.ultrasmedbio.2011.09.012.

[45] C. Jia, L. Xu, T. Han, P. Cai, A. C. Yu, and P. Qin, "Generation of Reactive Oxygen Species in Heterogeneously Sonoporated Cells by Microbubbles with Single-Pulse Ultrasound", *Ultrasound in Medicine & Biology*, vol. 44, no. 5, pp. 1074–1085, 2018. DOI: 10.1016/j.ultrasmedbio.2018.01.006.

[46] P. Qin, L. Xu, Y. Hu, W. Zhong, P. Cai, L. Du, L. Jin, and A. C. Yu, "Sonoporation-Induced Depolarization of Plasma Membrane Potential: Analysis of Heterogeneous Impact", *Ultrasound in Medicine & Biology*, vol. 40, no. 5, pp. 979–989, 2014. DOI: 10.1016/j.ultrasmedbio.2013.11.024.

[47] E. Carafoli and J. Krebs, "Why calcium? How calcium became the best communicator", *Journal of Biological Chemistry*, vol. 291, no. 40, pp. 20 849–20 857, 2016. DOI: 10.1074/jbc.R116.735894.

[48] B. Nilius, G. Droogmans, and R. Wondergem, "Transient Receptor Potential Channels in Endothelium: Solving the Calcium Entry Puzzle?", *Endothelium*, vol. 10, no. 1, pp. 5–15, 2003. DOI: 10.1080/10623320303356.

[49] C. X. Deng, F. Sieling, H. Pan, and J. Cui, "Ultrasound-induced cell membrane porosity", *Ultrasound in Medicine & Biology*, vol. 30, no. 4, pp. 519–526, 2004. DOI: 10.1016/j.ultrasmedbio.2004.01.005.

[50] C. F. Caskey, S. M. Stieger, S. Qin, P. A. Dayton, and K. W. Ferrara, "Direct observations of ultrasound microbubble contrast agent interaction with the microvessel wall", *The Journal of the Acoustical Society of America*, vol. 122, no. 2, pp. 1191–1200, 2007. DOI: 10.1121/1.2747204.

[51] X. Chen, R. S. Leow, Y. Hu, J. M. F. Wan, and A. C. H. Yu, "Single-site sonoporation disrupts actin cytoskeleton organization", *Journal of The Royal Society Interface*, vol. 11, no. 95, p. 20 140 071, 2014. DOI: 10.1098/rsif.2014.0071.

[52] R. C. Brown and T. P. Davis, "Calcium modulation of adherens and tight junction function: A potential mechanism for blood-brain barrier disruption after stroke", *Stroke*, vol. 33, no. 6, pp. 1706–1711, 2002. DOI: 10.1161/01.STR.0000016405.06729.83.

[53] B. L. Helfield, X. Chen, S. C. Watkins, and F. S. Villanueva, "Biophysical insight into mechanisms of sonoporation.", *Proceedings of the National Academy of Sciences*, vol. 113, no. 36, pp. 9983–8, 2016. DOI: 10.1073/pnas.1606915113.

[54] N. Sheikov, N. McDannold, S. Sharma, and K. Hynynen, "Effect of Focused Ultrasound Applied With an Ultrasound Contrast Agent on the Tight Junctional Integrity of the Brain Microvascular Endothelium", *Ultrasound in Medicine & Biology*, vol. 34, no. 7, pp. 1093–1104, 2008. DOI: 10.1016/j.ultrasmedbio.2007.12.015.

[55] Y. Liu, S. Yi, J. Zhang, Z. Fang, F. Zhou, W. Jia, Z. Liu, and G. Ye, "Effect of microbubble-enhanced ultrasound on prostate permeability: A potential therapeutic method for prostate disease", *Urology*, vol. 81, no. 4, 921.e1–921.e7, 2013. DOI: 10.1016/j.urology.2012.12.022.

[56] B. D. M. Meijering, L. J. M. Juffermans, A. van Wamel, R. H. Henning, I. S. Zuhorn, M. Emmer, A. M. G. Versteilen, W. J. Paulus, W. H. van Gilst, K. Kooiman, N. de Jong, R. J. Musters, L. E. Deelman, and O. Kamp, "Ultrasound and microbubble-targeted delivery of macromolecules is regulated by induction of endocytosis and pore formation", *Circulation Research*, vol. 104, no. 5, pp. 679–687, 2009. DOI: 10.1161/CIRCRESAHA.108.183806.

[57] L.-F. Jin, F. Li, H.-P. Wang, F. Wei, P. Qin, and L.-F. Du, "Ultrasound Targeted Microbubble Destruction Stimulates Cellular Endocytosis in Facilitation of Adeno-Associated Virus Delivery", eng, *International Journal of Molecular Sciences*, vol. 14, no. 5, pp. 9737–9750, 2013. DOI: 10.3390/ijms14059737.

[58] A. van Wamel, K. Kooiman, M. Harteveld, M. Emmer, F. J. ten Cate, M. Versluis, and N. de Jong, "Vibrating microbubbles poking individual cells: drug transfer into cells via sonoporation.", *Journal of controlled release : official journal of the Controlled Release Society*, vol. 112, no. 2, pp. 149–55, 2006. DOI: 10.1016/j.jconrel.2006.02.007.

[59] M. A. Hassan, P. Campbell, and T. Kondo, "The role of Ca2+ in ultrasound-elicited bioeffects: progress, perspectives and prospects", *Drug Discovery Today*, vol. 15, no. 21-22, pp. 892–906, 2010. DOI: 10.1016/j.drudis.2010.08.005.

[60] A. Sternberg, M. Amar, R. Alfici, and G. Groisman, "Conclusions from a study of venous invasion in stage IV colorectal adenocarcinoma", eng, *Journal of clinical pathology*, vol. 55, no. 1, pp. 17–21, 2002. DOI: 10.1136/jcp.55.1.17.

[61] S. Eguchi, M. Takatsuki, M. Hidaka, A. Soyama, T. Tomonaga, I. Muraoka, and T. Kanematsu, "Predictor for Histological Microvascular Invasion of Hepatocellular Carcinoma: A Lesson from 229 Consecutive Cases of Curative Liver Resection", *World Journal of Surgery*, vol. 34, no. 5, pp. 1034–1038, 2010. DOI: 10.1007/s00268-010-0424-5.

[62] B. L. Helfield, X. Chen, B. Qin, S. C. Watkins, and F. S. Villanueva, "Mechanistic Insight into Sonoporation with Ultrasound-Stimulated Polymer Microbubbles", *Ultrasound in Medicine & Biology*, vol. 43, no. 11, pp. 2678–2689, 2017. DOI: 10.1016/j.ultrasmedbio.2017.07.017.

[63] Z. Fan, D. Chen, and C. Deng, "Improving ultrasound gene transfection efficiency by controlling ultrasound excitation of microbubbles", *Journal of Controlled Release*, vol. 170, no. 3, pp. 401–413, 2013. DOI: 10.1016/j.jconrel.2013.05.039.

[64] I. De Cock, E. Zagato, K. Braeckmans, Y. Luan, N. de Jong, S. C. De Smedt, and I. Lentacker, "Ultrasound and microbubble mediated drug delivery: Acoustic pressure as determinant for uptake via membrane pores or endocytosis", *Journal of Controlled Release*, vol. 197, pp. 20–28, 2015. DOI: 10.1016/j.jconrel.2014.10.031.

[65] M. Emmer, H. J. Vos, M. Versluis, and N. de Jong, "Radial modulation of single microbubbles", *IEEE Transactions on Ultrasonics, Ferroelectrics, and Frequency Control*, vol. 56, no. 11, pp. 2370–2379, 2009. DOI: 10.1109/TUFFC.2009.1325.

[66] D. Maresca, M. Emmer, P. L. van Neer, H. J. Vos, M. Versluis, M. Muller, N. de Jong, and A. F. van der Steen, "Acoustic Sizing of an Ultrasound Contrast Agent", *Ultrasound in Medicine & Biology*, vol. 36, no. 10, pp. 1713–1721, 2010. DOI: 10.1016/j.ultrasmedbio.2010.06.014.

[67] J. Park, Z. Fan, and C. X. Deng, "Effects of shear stress cultivation on cell membrane disruption and intracellular calcium concentration in sonoporation of endothelial cells", *Journal of Biomechanics*, vol. 44, no. 1, pp. 164–169, 2011. DOI: 10.1016/j.jbiomech.2010.09.003.

[68] T. van Rooij, I. Beekers, K. R. Lattwein, A. F. W. van der Steen, N. de Jong, and K. Kooiman, "Vibrational Responses of Bound and Nonbound Targeted Lipid-Coated Single Microbubbles", *IEEE Transactions on Ultrasonics, Ferroelectrics, and Frequency Control*, vol. 64, no. 5, pp. 785–797, 2017. DOI: 10.1109/TUFFC.2017.2679160.

[69] A. Alzaraa, G. Gravante, W. Y. Chung, D. Al-Leswas, M. Bruno, A. R. Dennison, and D. M. Lloyd, "Targeted microbubbles in the experimental and clinical setting", *American Journal of Surgery*, vol. 204, no. 3, pp. 355–366, 2012. DOI: 10.1016/j.amjsurg.2011.10.024.

[70] J. S.-M. Yeh, C. A. Sennoga, E. McConnell, R. Eckersley, M.-X. Tang, S. Nourshargh, J. M. Seddon, D. O. Haskard, and P. Nihoyannopoulos, "Quantitative Ultrasound Molecular Imaging", *Ultrasound in Medicine & Biology*, vol. 41, no. 9, pp. 2478–2496, 2015. DOI: 10.1016/j.ultrasmedbio.2015.04.011.

[71] L. Abou-Elkacem, S. V. Bachawal, and J. K. Willmann, "Ultrasound molecular imaging: Moving toward clinical translation", *European Journal of Radiology*, vol. 84, no. 9, pp. 1685–1693, 2015. DOI: 10.1016/j.ejrad.2015.03.016.

[72] F. Kiessling, S. Fokong, J. Bzyl, W. Lederle, M. Palmowski, and T. Lammers, "Recent advances in molecular, multimodal and theranostic ultrasound imaging", *Advanced Drug Delivery Reviews*, vol. 72, pp. 15–27, 2014. DOI: 10.1016/j.addr.2013.11.013.

[73] A. L. Klibanov, "Ultrasound contrast materials in cardiovascular medicine: From perfusion assessment to molecular imaging", *Journal of Cardiovascular Translational Research*, vol. 6, no. 5, pp. 729–739, 2013. DOI: 10.1007/s12265-013-9501-0.

[74] S. M. van der Meer, B. Dollet, M. M. Voormolen, C. T. Chin, A. Bouakaz, N. de Jong, M. Versluis, and D. Lohse, "Microbubble spectroscopy of ultrasound contrast agents", *The Journal of the Acoustical Society of America*, vol. 121, no. 1, pp. 648–656, 2007. DOI: 10.1121/1.2390673.

[75] Y. Luan, T. Faez, E. Gelderblom, I. Skachkov, B. Geers, I. Lentacker, T. van der Steen, M. Versluis, and N. de Jong, "Acoustical Properties of Individual Liposome-Loaded Microbubbles", *Ultrasound in Medicine & Biology*, vol. 38, no. 12, pp. 2174–2185, 2012. DOI: 10.1016/j.ultrasmedbio.2012.07.023.

[76] T. Faez, M. Emmer, M. Docter, J. Sijl, M. Versluis, and N. de Jong, "Characterizing the Subharmonic Response of Phospholipid-Coated Microbubbles for Carotid Imaging", *Ultrasound in Medicine & Biology*, vol. 37, no. 6, pp. 958–970, 2011. DOI: 10.1016/j.ultrasmedbio.2011.02.017.

[77] T. van Rooij, Y. Luan, G. Renaud, A. F. van der Steen, M. Versluis, N. de Jong, and K. Kooiman, "Non-linear Response and Viscoelastic Properties of Lipid-Coated Microbubbles: DSPC versus DPPC", *Ultrasound in Medicine & Biology*, vol. 41, no. 5, pp. 1432–1445, 2015. DOI: 10.1016/j.ultrasmedbio.2015.01.004.

[78] S. Zhao, D. E. Kruse, K. W. Ferrara, and P. A. Dayton, "Acoustic response from adherent targeted contrast agents", *The Journal of the Acoustical Society of America*, vol. 120, no. 6, EL63–EL69, 2006. DOI: 10.1121/1.2364303.

[79] M. Overvelde, V. Garbin, B. Dollet, N. de Jong, D. Lohse, and M. Versluis, "Dynamics of Coated Microbubbles Adherent to a Wall", *Ultrasound in Medicine & Biology*, vol. 37, no. 9, pp. 1500–1508, 2011. DOI: 10.1016/j.ultrasmedbio.2011.05.025.

[80] B. L. Helfield, E. Cherin, F. S. Foster, and D. E. Goertz, "The Effect of Binding on the Subharmonic Emissions from Individual Lipid-Encapsulated Microbubbles at Transmit Frequencies of 11 and 25 MHz", *Ultrasound in Medicine & Biology*, vol. 39, no. 2, pp. 345–359, 2013. DOI: 10.1016/j.ultrasmedbio.2012.09.011.

[81] S. Zhao, K. W. Ferrara, and P. A. Dayton, "Asymmetric oscillation of adherent targeted ultrasound contrast agents", *Applied Physics Letters*, vol. 87, no. 13, pp. 1–3, 2005. DOI: 10.1063/1.2061872.

[82] J. Casey, C. Sennoga, H. Mulvana, J. V. Hajnal, M.-X. Tang, and R. J. Eckersley, "Single Bubble Acoustic Characterization and Stability Measurement of Adherent Microbubbles", *Ultrasound in Medicine & Biology*, vol. 39, no. 5, pp. 903–914, 2013. DOI: 10.1016/j.ultrasmedbio.2012.12.007.

[83] D. Kim and A. E. Herr, "Protein immobilization techniques for microfluidic assays", *Biomicrofluidics*, vol. 7, no. 4, p. 41501, 2013. DOI: 10.1063/1.4816934.

[84] K. Kooiman, T. J. A. Kokhuis, I. Skachkov, J. G. Bosch, A. F. W. van der Steen, W. A. van Cappellen, and N. de Jong, "Surface contact of bound targeted microbubbles", *IEEE International Ultrasonics Symposium, IUS*, pp. 2161–2163, 2012. DOI: 10.1109/ULTSYM.2012.0539.

[85] R. H. Abou-Saleh, S. A. Peyman, K. Critchley, S. D. Evans, and N. H. Thomson, "Nanomechanics of lipid encapsulated microbubbles with functional coatings", *Langmuir*, vol. 29, no. 12, pp. 4096–4103, 2013. DOI: 10.1021/la304093t.

[86] J. E. McKendry, C. A. Grant, B. R. Johnson, P. L. Coletta, J. A. Evans, and S. D. Evans, "Force spectroscopy of streptavidin conjugated lipid coated microbubbles", *Bubble Science, Engineering and Technology*, vol. 2, no. 2, pp. 48–54, 2010. DOI: 10.1179/175889610X12865266108541.

[87] T. van Rooij, V. Daeichin, I. Skachkov, N. de Jong, and K. Kooiman, "Targeted ultrasound contrast agents for ultrasound molecular imaging and therapy", *International Journal of Hyperthermia*, vol. 31, no. 2, pp. 90–106, 2015. DOI: 10.3109/02656736.2014.997809.

[88] K. Kooiman, T. J. A. Kokhuis, T. van Rooij, I. Skachkov, A. Nigg, J. G. Bosch, A. F. W. van der Steen, W. A. van Cappellen, and N. de Jong, "DSPC or DPPC as main shell component influences ligand distribution and binding area of lipid-coated targeted microbubbles", *European Journal of Lipid Science and Technology*, vol. 116, no. 9, pp. 1217–1227, 2014. DOI: 10.1002/ejlt.201300434.

[89] Lantheus Medical Imaging, "Definity Safety Label", FDA/Center Drug Eval. Res., Silver Spring, USA, Tech. Rep. 3910678, 2011.

[90] M. Schneider, M. Arditi, M. B. Barrau, J. Brochot, A. Broillet, R. Ventrone, and F. Yan, "BR1: A new ultrasonographic contrast agent based on sulfur hexafluoride-filled microbubbles", *Investigative Radiology*, vol. 30, no. 8, pp. 451–457, 1995. DOI: 10.1097/00004424-199508000-00001.

[91] M. Schneider, A. Broillet, P. Bussat, N. Giessinger, J. Puginier, R. Ventrone, and F. Yan, "Gray-scale liver enhancement in VX2 tumor-bearing rabbits using BR14, a new ultrasonographic contrast agent", *Investigative Radiology*, vol. 32, no. 7, pp. 410–417, 1997. DOI: 10.1097/00004424-199707000-00007.

[92] Bracco Diagnostics Inc, "Lumason Safety Label", FDA/Center Drug Eval. Res., Silver Spring, USA, Tech. Rep. 3033313, 2016.

[93] A. L. Klibanov, P. T. Rasche, M. S. Hughes, J. K. Wojdyla, K. P. Galen, J. H. Wible, and G. H. Brandenburger, "Detection of Individual Microbubbles of Ultrasound Contrast Agents: Imaging of Free-Floating and Targeted Bubbles", *Investigative Radiology*, vol. 39, no. 3, pp. 187–195, 2004. DOI: 10.1097/01.rli.0000115926.96796.75.

[94] E. C. Gelderblom, H. J. Vos, F. Mastik, T. Faez, Y. Luan, T. J. A. Kokhuis, A. F. W. van der Steen, D. Lohse, N. de Jong, and M. Versluis, "Brandaris 128 ultra-high-speed imaging facility: 10 years of operation, updates, and enhanced features", in *Review of Scientific Instruments*, vol. 83, American Institute of Physics, 2012, p. 103 706. DOI: 10.1063/1.4758783.

[95] N. de Jong, M. Emmer, C. T. Chin, A. Bouakaz, F. Mastik, D. Lohse, and M. Versluis, ""COMPRESSION-ONLY" BEHAVIOR OF PHOSPHOLIPID-COATED CONTRAST BUBBLES", *Ultrasound in Medicine & Biology*, vol. 33, no. 4, pp. 653–656, 2007. DOI: 10.1016/j.ultrasmedbio.2006.09.016.

[96] J. Chomas, P. Dayton, D. May, and K. Ferrara, "Nondestructive subharmonic imaging", *IEEE Transactions on Ultrasonics, Ferroelectrics and Frequency Control*, vol. 49, no. 7, pp. 883–892, 2002. DOI: 10.1109/TUFFC.2002.1020158.

[97] J. Sijl, B. Dollet, M. Overvelde, V. Garbin, T. Rozendal, N. de Jong, D. Lohse, and M. Versluis, "Subharmonic behavior of phospholipid-coated ultrasound contrast agent microbubbles", *The Journal of the Acoustical Society of America*, vol. 128, no. 5, pp. 3239–3252, 2010. DOI: 10.1121/1.3493443.

[98] P. L. van Neer, G. Matte, M. G. Danilouchkine, N. de Jong, C. Prins, and F. van den Adel, "Super-Harmonic Imaging: Development of an Interleaved Phased-Array Transducer", *IEEE Transactions on Ultrasonics, Ferroelectrics, and Frequency Control*, vol. 57, no. 2, pp. 455–468, 2010. DOI: 10.1109/TUFFC.2010.1426.

[99] D. H. Kim, M. J. Costello, P. B. Duncan, and D. Needham, "Mechanical properties and microstructure of polycrystalline phospholipid monolayer shells: Novel solid microparticles", *Langmuir*, vol. 19, no. 20, pp. 8455–8466, 2003. DOI: 10.1021/la034779c.

[100] P. Marmottant, S. van der Meer, M. Emmer, M. Versluis, N. de Jong, S. Hilgenfeldt, and D. Lohse, "A model for large amplitude oscillations of coated bubbles accounting for buckling and rupture", *The Journal of the Acoustical Society of America*, vol. 118, no. 6, pp. 3499–3505, 2005. DOI: 10.1121/1.2109427.

[101] M. Minnaert, "XVI. On musical air-bubbles and the sounds of running water", *The London, Edinburgh, and Dublin Philosophical Magazine and Journal of Science*, vol. 16, no. 104, pp. 235–248, 1933. DOI: 10.1080/14786443309462277.

[102] A. Needles, M. Arditi, N. Rognin, J. Mehi, T. Coulthard, C. Bilan-Tracey, E. Gaud, P. Frinking, D. Hirson, and F. Foster, "Nonlinear Contrast Imaging with an Array-Based Micro-Ultrasound System", *Ultrasound in Medicine & Biology*, vol. 36, no. 12, pp. 2097–2106, 2010. DOI: 10.1016/j.ultrasmedbio.2010.08.012.

[103] S. Zhao, M. Borden, S. H. Bloch, D. Kruse, K. W. Ferrara, and P. A. Dayton, "Radiation-force assisted targeting facilitates ultrasonic molecular imaging", in *Molecular Imaging*, vol. 3, 2004, pp. 135–148. DOI: 10.1162/1535350042380317.

[104] P. A. Dayton, K. E. Morgan, A. L. Klibanov, G. H. Brandenburger, and K. W. Ferrara, "Optical and acoustical observations of the effects of ultrasound on contrast agents", *IEEE Transactions on Ultrasonics, Ferroelectrics, and Frequency Control*, vol. 46, no. 1, pp. 220–232, 1999. DOI: 10.1109/58.741536.

[105] T. van Rooij, A. F. W. van der Steen, N. de Jong, and K. Kooiman, "Influence of binding on the vibrational responses of targeted lipid-coated microbubbles", in *2014 IEEE International Ultrasonics Symposium*, 2014, pp. 413–416. DOI: 10.1109/ULTSYM.2014.0102.

[106] P. M. Shankar, P. D. Krishna, and V. L. Newhouse, "Subharmonic backscattering from ultrasound contrast agents", *The Journal of the Acoustical Society of America*, vol. 106, no. 4, pp. 2104–2110, 1999. DOI: 10.1121/1.428142.

[107] P. Shankar, P. Krishna, and V. Newhouse, "Advantages of Subharmonic Over Second Harmonic Backscatter for Contrast-To-Tissue Echo Enhancement", *Ultrasound in Medicine & Biology*, vol. 24, no. 3, pp. 395–399, 1998. DOI: 10.1016/S0301-5629(97)00262-7.

[108] K. Hettiarachchi, E. Talu, M. L. Longo, P. A. Dayton, and A. P. Lee, "On-chip generation of microbubbles as a practical technology for manufacturing contrast agents for ultrasonic imaging", *Lab on a Chip*, vol. 7, no. 4, pp. 463–468, 2007. DOI: 10.1039/b701481n.

[109] M. Kaya, S. Feingold, K. Hettiarachchi, A. P. Lee, and P. A. Dayton, *Acoustic responses of monodisperse lipid encapsulated microbubble contrast agents produced by flow focusing*, 2010. DOI: 10.1179/175889610X12779105661532.

[110] E. Talu, K. Hettiarachchi, R. L. Powell, A. P. Lee, P. A. Dayton, and M. L. Longo, "Maintaining monodispersity in a microbubble population formed by flow-focusing", *Langmuir*, vol. 24, no. 5, pp. 1745–1749, 2008. DOI: 10.1021/la703065v.

[111] E. Talu, K. Hettiarachchi, S. Zhao, R. L. Powell, A. P. Lee, M. L. Longo, and P. A. Dayton, "Tailoring the size distribution of ultrasound contrast agents: Possible method for improving sensitivity in molecular imaging", *Molecular Imaging*, vol. 6, no. 6, pp. 384–392, 2007. DOI: 10.2310/7290.2007.00034.

[112] T. Segers and M. Versluis, "Acoustic bubble sorting for ultrasound contrast agent enrichment", *Lab on a Chip*, vol. 14, no. 10, pp. 1705–1714, 2014. DOI: 10.1039/c3lc51296g.

[113] T. Faez, I. Skachkov, M. Versluis, K. Kooiman, and N. de Jong, "In Vivo Characterization of Ultrasound Contrast Agents: Microbubble Spectroscopy in a Chicken Embryo", *Ultrasound in Medicine & Biology*, vol. 38, no. 9, pp. 1608–1617, 2012. DOI: 10.1016/j.ultrasmedbio.2012.05.014.

[114] T. J. Kokhuis, V. Garbin, K. Kooiman, B. A. Naaijkens, L. J. Juffermans, O. Kamp, A. F. van der Steen, M. Versluis, and N. de Jong, "Secondary Bjerknes Forces Deform Targeted Microbubbles", *Ultrasound in Medicine & Biology*, vol. 39, no. 3, pp. 490–506, 2013. DOI: 10.1016/j.ultrasmedbio.2012.09.025.

[115] V. Garbin, D. Cojoc, E. Ferrari, E. di Fabrizio, M. L. J. Overvelde, S. M. van der Meer, N. de Jong, D. Lohse, and M. Versluis, "Changes in microbubble dynamics near a boundary revealed by combined optical micromanipulation and high-speed imaging", *Applied Physics Letters*, vol. 90, no. 11, p. 114 103, 2007. DOI: 10.1063/1.2713164.

[116] D. Cosgrove and C. Harvey, "Clinical uses of microbubbles in diagnosis and treatment", *Medical & Biological Engineering & Computing*, vol. 47, no. 8, pp. 813–826, 2009. DOI: 10.1007/s11517-009-0434-3.

[117] E. C. Pua and P. Zhong, "Ultrasound-Mediated Drug Delivery: Range of Ultrasonic Interactions and Applications in Biological Systems", *IEEE Engineering in Medicine and Biology*, vol. 28, no. 1, pp. 64–75, 2009. DOI: 10.1109/MEMB.2008.931017.

[118] F. Yan, X. Li, Q. Jin, C. Jiang, Z. Zhang, T. Ling, B. Qiu, and H. Zheng, "Therapeutic Ultrasonic Microbubbles Carrying Paclitaxel and LyP-1 Peptide: Preparation, Characterization and Application to Ultrasound-Assisted Chemotherapy in Breast Cancer Cells", *Ultrasound in Medicine & Biology*, vol. 37, no. 5, pp. 768–779, 2011. DOI: 10.1016/j.ultrasmedbio.2011.02.006.

[119] L. C. Phillips, A. L. Klibanov, B. R. Wamhoff, and J. A. Hossack, "Intravascular ultrasound detection and delivery of molecularly targeted microbubbles for gene delivery", *IEEE Transactions on Ultrasonics, Ferroelectrics, and Frequency Control*, vol. 59, no. 7, pp. 1596–1601, 2012. DOI: 10.1109/TUFFC.2012.2359.

[120] S. Chang, J. Guo, J. Sun, S. Zhu, Y. Yan, Y. Zhu, M. Li, Z. Wang, and R. X. Xu, "Targeted microbubbles for ultrasound mediated gene transfection and apoptosis induction in ovarian cancer cells", *Ultrasonics Sonochemistry*, vol. 20, no. 1, pp. 171–179, 2013. DOI: 10.1016/j.ultsonch.2012.06.015.

[121] J. McLaughlan, N. Ingram, P. R. Smith, S. Harput, P. L. Coletta, S. Evans, and S. Freear, "Increasing the sonoporation efficiency of targeted polydisperse microbubble populations using chirp excitation", *IEEE Transactions on Ultrasonics, Ferroelectrics, and Frequency Control*, vol. 60, no. 12, pp. 2511–2520, 2013. DOI: 10.1109/TUFFC.2013.2850.

[122] H. Liu, S. Chang, J. Sun, S. Zhu, C. Pu, Y. Zhu, Z. Wang, and R. X. Xu, "Ultrasound-mediated destruction of LHRHa-targeted and paclitaxel-loaded lipid microbubbles induces proliferation inhibition and apoptosis in ovarian cancer cells", *Molecular Pharmaceutics*, vol. 11, no. 1, pp. 40–48, 2014. DOI: 10.1021/mp4005244.

[123] A. Xie, T. Belcik, Y. Qi, T. K. Morgan, S. A. Champaneri, S. Taylor, B. P. Davidson, Y. Zhao, A. L. Klibanov, M. A. Kuliszewski, H. Leong-Poi, A. Ammi, and J. R. Lindner, "Ultrasound-Mediated Vascular Gene Transfection by Cavitation of Endothelial-Targeted Cationic Microbubbles", *JACC: Cardiovascular Imaging*, vol. 5, no. 12, pp. 1253–1262, 2012. DOI: 10.1016/j.jcmg.2012.05.017.

[124] J. L. Tlaxca, J. J. Rychak, P. B. Ernst, P. R. Konkalmatt, T. I. Shevchenko, T. T. Pizzaro, J. Rivera-Nieves, A. L. Klibanov, and M. B. Lawrence, "Ultrasound-based molecular imaging and specific gene delivery to mesenteric vasculature by endothelial adhesion molecule targeted microbubbles in a mouse model of Crohn's disease", *Journal of Controlled Release*, vol. 165, no. 3, pp. 216–225, 2013. DOI: 10.1016/j.jconrel.2012.10.021.

[125] C. Pu, S. Chang, J. Sun, S. Zhu, H. Liu, Y. Zhu, Z. Wang, and R. X. Xu, "Ultrasound-mediated destruction of LHRHa-targeted and paclitaxel-loaded lipid microbubbles for the treatment of intraperitoneal ovarian cancer xenografts", *Molecular Pharmaceutics*, vol. 11, no. 1, pp. 49–58, 2014. DOI: 10.1021/mp400523h.

[126] C. H. Fan, C. Y. Ting, H. L. Liu, C. Y. Huang, H. Y. Hsieh, T. C. Yen, K. C. Wei, and C. K. Yeh, "Antiangiogenic-targeting drug-loaded microbubbles combined with focused ultrasound for glioma treatment", *Biomaterials*, vol. 34, no. 8, pp. 2142–2155, 2013. DOI: 10.1016/j.biomaterials.2012.11.048.

[127] F. E. Shamout, A. N. Pouliopoulos, P. Lee, S. Bonaccorsi, L. Towhidi, R. Krams, and J. J. Choi, "Enhancement of Non-Invasive Trans-Membrane Drug Delivery Using Ultrasound and Microbubbles During Physiologically Relevant Flow", *Ultrasound in Medicine & Biology*, vol. 41, no. 9, pp. 2435–2448, 2015. DOI: 10.1016/j.ultrasmedbio.2015.05.003.

[128] C. E. Shannon, "Communication In The Presence Of Noise", *Proceedings of the IEEE*, vol. 86, no. 2, pp. 447–457, 1998. DOI: 10.1109/JPROC.1998.659497.

[129] Z. Fan, D. Chen, and C. X. Deng, "Characterization of the Dynamic Activities of a Population of Microbubbles Driven by Pulsed Ultrasound Exposure in Sonoporation", *Ultrasound in Medicine & Biology*, vol. 40, no. 6, pp. 1260–1272, 2014. DOI: 10.1016/j.ultrasmedbio.2013.12.002.

[130] T. J. A. Kokhuis, I. Skachkov, B. A. Naaijkens, L. J. M. Juffermans, O. Kamp, K. Kooiman, A. F. W. van der Steen, M. Versluis, and N. de Jong, "Intravital microscopy of localized stem cell delivery using microbubbles and acoustic radiation force", *Biotechnology and Bioengineering*, vol. 112, no. 1, pp. 220–227, 2015. DOI: 10.1002/bit.25337.

[131] J. R. Doherty, G. E. Trahey, K. R. Nightingale, and M. L. Palmeri, "Acoustic radiation force elasticity imaging in diagnostic ultrasound", *IEEE Transactions on Ultrasonics, Ferroelectrics, and Frequency Control*, vol. 60, no. 4, pp. 685–701, 2013. DOI: 10.1109/TUFFC.2013.2617.

[132] D. L. Miller and J. Song, "Tumor growth reduction and DNA transfer by cavitation-enhanced high-intensity focused ultrasound in vivo", *Ultrasound in Medicine & Biology*, vol. 29, no. 6, pp. 887–893, 2003. DOI: 10.1016/S0301-5629(03)00031-0.

[133] A. Ghanem, C. Steingen, F. Brenig, F. Funcke, Z. Y. Bai, C. Hall, C. T. Chin, G. Nickenig, W. Bloch, and K. Tiemann, "Focused ultrasound-induced stimulation of microbubbles augments site-targeted engraftment of mesenchymal stem cells after acute myocardial infarction", *Journal of Molecular and Cellular Cardiology*, vol. 47, no. 3, pp. 411–418, 2009. DOI: 10.1016/j.yjmcc.2009.06.008.

[134] B. D. M. Meijering, R. H. Henning, W. H. Van Gilst, I. Gavrilovic, A. Van Wamel, and L. E. Deelman, "Optimization of ultrasound and microbubbles targeted gene delivery to cultured primary endothelial cells", *Journal of Drug Targeting*, vol. 15, no. 10, pp. 664–671, 2007. DOI: 10.1080/10611860701605088.

[135] J. R. Lindner, J. Song, J. Christiansen, A. L. Klibanov, F. Xu, and K. Ley, "Ultrasound assessment of inflammation and renal tissue injury with microbubbles targeted to P-selectin", *Circulation*, vol. 104, no. 17, pp. 2107–2112, 2001. DOI: 10.1161/hc4201.097061.

[136] D. Bratosin, L. Mitrofan, C. Palii, J. Estaquier, and J. Montreuil, "Novel fluorescence assay using calcein-AM for the determination of human erythrocyte viability and aging", *Cytometry Part A*, vol. 66A, no. 1, pp. 78–84, 2005. DOI: 10.1002/cyto.a.20152.

[137] K. Smith, S. Hill, A. Begg, and J. Denekamp, "Validation of the fluorescent dye Hoechst 33342 as a vascular space marker in tumours", *British Journal of Cancer*, vol. 57, no. 3, pp. 247–253, 1988. DOI: 10.1038/bjc.1988.54.

[138] M. Sriram, G. van der Marel, H. Roelen, J. van Boom, and A. Wang, "Conformation of B-DNA containing O6-ethyl-G-C base pairs stabilized by minor groove binding drugs: molecular structure of d(CGC[e6G]AATTCGCG complexed with Hoechst 33258 or Hoechst 33342.", *The EMBO Journal*, vol. 11, no. 1, pp. 225–232, 1992. DOI: 10.1002/j.1460-2075.1992.tb05045.x.

[139] W. D. Wilson, C. R. Krishnamoorthy, Y.-H. Wang, and J. C. Smith, "Mechanism of intercalation: Ion effects on the equilibrium and kinetic constants for the interaction of propidium and ethidium with DNA", *Biopolymers*, vol. 24, no. 10, pp. 1941–1961, 1985. DOI: 10.1002/bip.360241008.

[140] W. S. Rasband, *ImageJ (1997-2016)*, Bethesda, Maryland, USA.

[141] N. Otsu, "A Threshold Selection Method from Gray-Level Histograms", *IEEE Transactions on Systems, Man, and Cybernetics*, vol. 9, no. 1, pp. 62–66, 1979. DOI: 10.1109/TSMC.1979.4310076.

[142] T. R. Jones, A. Carpenter, and P. Golland, "Voronoi-Based Segmentation of Cells on Image Manifolds", in *Lecture Notes in Computer Science (including subseries Lecture Notes in Artificial Intelligence and Lecture Notes in Bioinformatics)*, vol. 3765 LNCS, 2005, pp. 535–543. DOI: 10.1007/11569541_54.

[143] S. Wold, K. Esbensen, and P. Geladi, "Principal component analysis", *Chemometrics and Intelligent Laboratory Systems*, vol. 2, no. 1-3, pp. 37–52, 1987. DOI: 10.1016/0169-7439(87)80084-9.

[144] R. L. Tatusov, "The COG database: new developments in phylogenetic classification of proteins from complete genomes", *Nucleic Acids Research*, vol. 29, no. 1, pp. 22–28, 2001. DOI: 10.1093/nar/29.1.22.

[145] Z. Zivkovic and F. van der Heijden, "Efficient adaptive density estimation per image pixel for the task of background subtraction", *Pattern Recognition Letters*, vol. 27, no. 7, pp. 773–780, 2006. DOI: 10.1016/j.patrec.2005.11.005.

[146] D. Allan, N. Keim, T. Caswell, and C. van der Wel. (2015). Trackpy v0.3.0, [Online]. Available: http://zenodo.org/record/34028%202015.

[147] S. van der Walt, J. L. Schonberger, J. Nunez-Iglesias, F. Boulogne, J. D. Warner, N. Yager, E. Gouillart, and T. Yu, "scikit-image: image processing in Python", 2014. DOI: 10.7717/peerj.453.

[148] Y. Zhou, K. Yang, J. Cui, J. Ye, and C. Deng, "Controlled permeation of cell membrane by single bubble acoustic cavitation", *Journal of Controlled Release*, vol. 157, no. 1, pp. 103–111, 2012. DOI: 10.1016/j.jconrel.2011.09.068.

[149] B. Lammertink, R. Deckers, G. Storm, C. Moonen, and C. Bos, "Duration of ultrasound-mediated enhanced plasma membrane permeability", *International Journal of Pharmaceutics*, vol. 482, no. 1-2, pp. 92–98, 2015. DOI: 10.1016/j.ijpharm.2014.12.013.

[150] A. Yudina, M. Lepetit-Coiffé, and C. T. W. Moonen, "Evaluation of the temporal window for drug delivery following ultrasound-mediated membrane permeability enhancement", *Molecular Imaging and Biology*, vol. 13, no. 2, pp. 239–249, 2011. DOI: 10.1007/s11307-010-0346-5.

[151] P. G. Wu and L. Brand, "Resonance energy transfer: Methods and applications", *Analytical Biochemistry*, vol. 218, no. 1, pp. 1–13, 1994. DOI: 10.1006/abio.1994.1134.

[152] T. Frey, "Detection of bromodeoxyuridine incorporation by alteration of the fluorescence emission from nucleic acid binding dyes using only an argon ion laser", *Cytometry*, vol. 17, no. 4, pp. 310–318, 1994. DOI: 10.1002/cyto.990170406.

[153] C. Mannaris and M. A. Averkiou, "Investigation of Microbubble Response to Long Pulses Used in Ultrasound-Enhanced Drug Delivery", *Ultrasound in Medicine & Biology*, vol. 38, no. 4, pp. 681–691, 2012. DOI: 10.1016/j.ultrasmedbio.2011.12.018.

[154] X. Chen, J. Wang, J. J. Pacella, and F. S. Villanueva, "Dynamic Behavior of Microbubbles during Long Ultrasound Tone-Burst Excitation: Mechanistic Insights into Ultrasound-Microbubble Mediated Therapeutics Using High-Speed Imaging and Cavitation Detection", *Ultrasound in Medicine & Biology*, vol. 42, no. 2, pp. 528–538, 2016. DOI: 10.1016/j.ultrasmedbio.2015.09.017.

[155] B. L. Helfield, E. Cherin, F. S. Foster, and D. E. Goertz, "Investigating the Subharmonic Response of Individual Phospholipid Encapsulated Microbubbles at High Frequencies: A Comparative Study of Five Agents", *Ultrasound in Medicine & Biology*, vol. 38, no. 5, pp. 846–863, 2012. DOI: 10.1016/j.ultrasmedbio.2012.01.011.

[156] H. M. DeLisser, P. J. Newman, and S. M. Albelda, "Molecular and functional aspects of PECAM-1/CD31", *Immunology Today*, vol. 15, no. 10, pp. 490–495, 1994. DOI: 10.1016/0167-5699(94)90195-3.

[157] L. M. Kornmann, K. D. Reesink, R. S. Reneman, and A. P. Hoeks, "Critical Appraisal of Targeted Ultrasound Contrast Agents for Molecular Imaging in Large Arteries", *Ultrasound in Medicine & Biology*, vol. 36, no. 2, pp. 181–191, 2010. DOI: 10.1016/j.ultrasmedbio.2009.09.009.

[158] M. de Saint Victor, C. Crake, C.-C. Coussios, and E. Stride, "Properties, characteristics and applications of microbubbles for sonothrombolysis", *Expert Opinion on Drug Delivery*, vol. 11, no. 2, pp. 187–209, 2014. DOI: 10.1517/17425247.2014.868434.

[159] Z. Fan, R. E. Kumon, J. Park, and C. X. Deng, "Intracellular delivery and calcium transients generated in sonoporation facilitated by microbubbles", *Journal of Controlled Release*, vol. 142, no. 1, pp. 31–39, 2010. DOI: 10.1016/j.jconrel.2009.09.031.

[160] I. Beekers, T. van Rooij, A. F. W. van der Steen, N. de Jong, M. D. Verweij, and K. Kooiman, "Acoustic Characterization of the CLINIcell for Ultrasound Contrast Agent Studies", *IEEE Transactions on Ultrasonics, Ferroelectrics, and Frequency Control*, vol. 66, no. 1, pp. 244–246, 2019. DOI: 10.1109/TUFFC.2018.2881724.

[161] G. Lajoinie, I. De Cock, C. C. Coussios, I. Lentacker, S. Le Gac, E. Stride, and M. Versluis, "In vitro methods to study bubble-cell interactions: Fundamentals and therapeutic applications", *Biomicrofluidics*, vol. 10, no. 1, 2016. DOI: 10.1063/1.4940429.

[162] H. Shekhar, N. J. Smith, J. L. Raymond, and C. K. Holland, "Effect of Temperature on the Size Distribution, Shell Properties, and Stability of Definity®", *Ultrasound in Medicine & Biology*, vol. 44, no. 2, pp. 434–446, 2018. DOI: 10.1016/j.ultrasmedbio.2017.09.021.

[163] A. Nio, A. Faraci, K. Christensen-Jeffries, R. Eckersley, M. Monaghan, J. Raymond, F. Forsberg, and P. Lamata, "The subharmonic amplitude of SonoVue increases with hydrostatic pressure at low incident acoustic pressures", in *2017 IEEE International Ultrasonics Symposium (IUS)*, IEEE, 2017, pp. 1–1. DOI: 10.1109/ULTSYM.2017.8091873.

[164] B. H. Lammertink, R. Deckers, M. Derieppe, I. De Cock, I. Lentacker, G. Storm, C. T. Moonen, and C. Bos, "Dynamic Fluorescence Microscopy of Cellular Uptake of Intercalating Model Drugs by Ultrasound-Activated Microbubbles", *Molecular Imaging and Biology*, vol. 19, no. 5, pp. 683–693, 2017. DOI: 10.1007/s11307-016-1042-x.

[165] I. Beekers, T. van Rooij, M. D. Verweij, M. Versluis, N. de Jong, S. J. Trietsch, and K. Kooiman, "Acoustic Characterization of a Vessel-on-a-Chip Microfluidic System for Ultrasound-Mediated Drug Delivery", *IEEE Transactions on Ultrasonics, Ferroelectrics, and Frequency Control*, vol. 65, no. 4, pp. 570–581, 2018. DOI: 10.1109/TUFFC.2018.2803137.

[166] J. Sijl, M. Overvelde, B. Dollet, V. Garbin, N. de Jong, D. Lohse, and M. Versluis, "'Compression-only' behavior: A second-order nonlinear response of ultrasound contrast agent microbubbles", *The Journal of the Acoustical Society of America*, vol. 129, no. 4, pp. 1729–1739, 2011. DOI: 10.1121/1.3505116.

[167] I. Beekers, K. R. Lattwein, J. J. Kouijzer, S. A. Langeveld, M. Vegter, R. Beurskens, F. Mastik, R. Verduyn Lunel, E. Verver, A. F. van der Steen, N. de Jong, and K. Kooiman, "Combined Confocal Microscope and Brandaris 128 Ultra-High-Speed Camera", *Ultrasound in Medicine & Biology*, vol. 45, no. 9, pp. 2575–2582, 2019. DOI: 10.1016/j.ultrasmedbio.2019.06.004.

[168] Z. M. Binsalamah, A. Paul, S. Prakash, and D. Shum-Tim, "Nanomedicine in cardiovascular therapy: Recent advancements", *Expert Review of Cardiovascular Therapy*, vol. 10, no. 6, pp. 805–815, 2012. DOI: 10.1586/erc.12.41.

[169] E. Westein, U. Flierl, C. E. Hagemeyer, and K. Peter, "Destination Known: Targeted Drug Delivery in Atherosclerosis and Thrombosis", *Drug Development Research*, vol. 74, no. 7, pp. 460–471, 2013. DOI: 10.1002/ddr.21103.

[170] B. H. T. Goh, M. Conneely, H. Kneuper, T. Palmer, E. Klaseboer, B. C. Khoo, and P. Campbell, "High-speed imaging of ultrasound-mediated bacterial Biofilm Disruption", *IFMBE Proceedings*, vol. 45, pp. 533–536, 2015. DOI: 10.1007/978-3-319-11128-5_133.

[171] I. Lentacker, N. Wang, R. E. Vandenbroucke, J. Demeester, S. C. De Smedt, and N. N. Sanders, "Ultrasound Exposure of Lipoplex Loaded Microbubbles Facilitates Direct Cytoplasmic Entry of the Lipoplexes", *Molecular Pharmaceutics*, vol. 6, no. 2, pp. 457–467, 2009. DOI: 10.1021/mp800154s.

[172] J. Hu, N. Zhang, L. Li, Y. Ma, C. Zhao, Q. Wu, Y. Li, N. He, and X. Wang, "The synergistic bactericidal effect of vancomycin on UTMD treated biofilm involves damage to bacterial cells and enhancement of metabolic activities", eng, *Scientific Reports*, vol. 8, no. 1, p. 192, 2018. DOI: 10.1038/s41598-017-18496-3.

[173] I. De Cock, G. Lajoinie, M. Versluis, S. C. De Smedt, and I. Lentacker, "Sonoprinting and the importance of microbubble loading for the ultrasound mediated cellular delivery of nanoparticles", *Biomaterials*, vol. 83, pp. 294–307, 2016. DOI: 10.1016/j.biomaterials.2016.01.022.

[174] J. J. Kwan and M. A. Borden, "Lipid monolayer collapse and microbubble stability", *Advances in Colloid and Interface Science*, vol. 183-184, pp. 82–99, 2012. DOI: 10.1016/j.cis.2012.08.005.

[175] T. Baumgart, G. Hunt, E. R. Farkas, W. W. Webb, and G. W. Feigenson, "Fluorescence probe partitioning between Lo/Ld phases in lipid membranes", *Biochimica et Biophysica Acta (BBA) - Biomembranes*, vol. 1768, no. 9, pp. 2182–2194, 2007. DOI: 10.1016/j.bbamem.2007.05.012.

[176] Y. Luan, G. Lajoinie, E. Gelderblom, I. Skachkov, A. F. van der Steen, H. J. Vos, M. Versluis, and N. De Jong, "Lipid Shedding from Single Oscillating Microbubbles", *Ultrasound in Medicine & Biology*, vol. 40, no. 8, pp. 1834–1846, 2014. DOI: 10.1016/j.ultrasmedbio.2014.02.031.

[177] K. Kooiman, T. van Rooij, B. Qin, F. Mastik, H. J. Vos, M. Versluis, A. L. Klibanov, N. de Jong, F. S. Villanueva, and X. Chen, "Focal areas of increased lipid concentration on the coating of microbubbles during short tone-burst ultrasound insonification", *PLoS ONE*, vol. 12, no. 7, e0180747, 2017. DOI: 10.1371/journal.pone.0180747.

[178] I. Beekers, F. Mastik, R. Beurskens, P. Y. Tang, M. Vegter, A. F. W. van der Steen, N. de Jong, M. D. Verweij, and K. Kooiman, "High-resolution imaging of intracellular calcium fluctuations caused by oscillating microbubbles", *Ultrasound in Medicine & Biology*, 2020. DOI: 10.1016/j.ultrasmedbio.2020.03.029.

[179] C. Yang, Y. Li, M. Du, and Z. Chen, "Recent advances in ultrasound-triggered therapy", *Journal of Drug Targeting*, vol. 27, no. 1, pp. 33–50, 2019. DOI: 10.1080/1061186X.2018.1464012.

[180] S. Bao, B. D. Thrall, and D. L. Miller, "Transfection of a reporter plasmid into cultured cells by sonoporation in vitro", *Ultrasound in Medicine & Biology*, vol. 23, no. 6, pp. 953–959, 1997. DOI: 10.1016/S0301-5629(97)00025-2.

[181] D. L. Miller, S. Bao, and J. E. Morris, "Sonoporation of cultured cells in the rotating tube exposure system", *Ultrasound in Medicine & Biology*, vol. 25, no. 1, pp. 143–149, 1999. DOI: 10.1016/S0301-5629(98)00137-9.

[182] J. Wu and W. L. Nyborg, "Ultrasound, cavitation bubbles and their interaction with cells", *Advanced Drug Delivery Reviews*, vol. 60, no. 10, pp. 1103–1116, 2008. DOI: 10.1016/j.addr.2008.03.009.

[183] R. E. Kumon, M. Aehle, D. Sabens, P. Parikh, D. Kourennyi, and C. X. Deng, "Ultrasound-induced calcium oscillations and waves in Chinese hamster ovary cells in the presence of microbubbles", *Biophysical Journal*, 2007. DOI: 10.1529/biophysj.107.113365.

[184] R. Kumon, M. Aehle, D. Sabens, P. Parikh, Y. Han, D. Kourennyi, and C. Deng, "Spatiotemporal Effects of Sonoporation Measured by Real-Time Calcium Imaging", *Ultrasound in Medicine & Biology*, vol. 35, no. 3, pp. 494–506, 2009. DOI: 10.1016/j.ultrasmedbio.2008.09.003.

[185] L. J. Juffermans, A. van Dijk, C. A. Jongenelen, B. Drukarch, A. Reijerkerk, H. E. de Vries, O. Kamp, and R. J. Musters, "Ultrasound and Microbubble-Induced Intra- and Intercellular Bioeffects in Primary Endothelial Cells", *Ultrasound in Medicine & Biology*, vol. 35, no. 11, pp. 1917–1927, 2009. DOI: 10.1016/j.ultrasmedbio.2009.06.1091.

[186] L. J. Juffermans, P. A. Dijkmans, R. J. Musters, C. A. Visser, and O. Kamp, "Transient permeabilization of cell membranes by ultrasound-exposed microbubbles is related to formation of hydrogen peroxide", *American Journal of Physiology - Heart and Circulatory Physiology*, vol. 291, no. 4, H1595–H1601, 2006. DOI: 10.1152/ajpheart.01120.2005.

[187] H. Honda, T. Kondo, Q.-L. Zhao, L. B. Feril, and H. Kitagawa, "Role of intracellular calcium ions and reactive oxygen species in apoptosis induced by ultrasound", *Ultrasound in Medicine & Biology*, vol. 30, no. 5, pp. 683–692, 2004. DOI: 10.1016/j.ultrasmedbio.2004.02.008.

[188] L. Leybaert and M. J. Sanderson, "Intercellular Ca2+ Waves: Mechanisms and Function", *Physiological Reviews*, vol. 92, no. 3, pp. 1359–1392, 2012. DOI: 10.1152/physrev.00029.2011.

[189] D. Mehta and A. B. Malik, "Signaling Mechanisms Regulating Endothelial Permeability", *Physiological Reviews*, vol. 86, no. 1, pp. 279–367, 2006. DOI: 10.1152/physrev.00012.2005.

[190] D. Qin, L. Zhang, N. Chang, P. Ni, Y. Zong, A. Bouakaz, M. Wan, and Y. Feng, "In situ observation of single cell response to acoustic droplet vaporization: Membrane deformation, permeabilization, and blebbing", *Ultrasonics Sonochemistry*, vol. 47, pp. 141–150, 2018. DOI: 10.1016/j.ultsonch.2018.02.004.

[191] E. K. Juang, I. De Cock, C. Keravnou, M. K. Gallagher, S. B. Keller, Y. Zheng, and M. Averkiou, "Engineered 3D Microvascular Networks for the Study of Ultrasound-Microbubble-Mediated Drug Delivery", *Langmuir*, vol. 35, no. 31, pp. 10 128–10 138, 2019. DOI: 10.1021/acs.langmuir.8b03288.

[192] T. G. Leighton, *The Acoustic Bubble*. London: Academic Press, 1994.

[193] M. J. Berridge, P. Lipp, and M. D. Bootman, "The versatility and universality of calcium signalling", eng, *Nature Reviews Molecular Cell Biology*, vol. 1, no. 1, pp. 11–21, 2000. DOI: 10.1038/35036035.

[194] D. Thomas, S. C. Tovey, T. J. Collins, M. D. Bootman, M. J. Berridge, and P. Lipp, "A comparison of fluorescent Ca2+ indicator properties and their use in measuring elementary and global Ca2+ signals", *Cell Calcium*, vol. 28, no. 4, pp. 213–223, 2000. DOI: 10.1054/ceca.2000.0152.

[195] S. Orrenius, B. Zhivotovsky, and P. Nicotera, "Regulation of cell death: The calcium-apoptosis link", *Nature Reviews Molecular Cell Biology*, vol. 4, no. 7, pp. 552–565, 2003. DOI: 10.1038/nrm1150.

[196] P. Nicotera and S. Orrenius, "The role of calcium in apoptosis", *Cell Calcium*, vol. 23, no. 2-3, pp. 173–180, 1998. DOI: 10.1016/S0143-4160(98)90116-6.

[197] M. D. Bootman, K. Rietdorf, T. Collins, S. Walker, and M. Sanderson, "Ca2+-sensitive fluorescent dyes and intracellular Ca2+imaging", *Cold Spring Harbor Protocols*, vol. 8, no. 2, pp. 83–99, 2013. DOI: 10.1101/pdb.top066050.

[198] J. Long, M. Junkin, P. K. Wong, J. Hoying, and P. Deymier, "Calcium Wave Propagation in Networks of Endothelial Cells: Model-based Theoretical and Experimental Study", *PLoS Computational Biology*, vol. 8, no. 12, D. Ho, Ed., e1002847, 2012. DOI: 10.1371/journal.pcbi.1002847.

[199] E. E. Konofagou, "Optimization of the ultrasound-induced blood-brain barrier opening", eng, *Theranostics*, vol. 2, no. 12, pp. 1223–1237, 2012. DOI: 10.7150/thno.5576.

[200] F. Li, C. Yang, F. Yuan, D. Liao, T. Li, F. Guilak, and P. Zhong, "Dynamics and mechanisms of intracellular calcium waves elicited by tandem bubble-induced jetting flow", *Proceedings of the National Academy of Sciences*, vol. 115, no. 3, E353–E362, 2018. DOI: 10.1073/pnas.1713905115.

[201] I. Beekers, M. Vegter, K. R. Lattwein, F. Mastik, R. Beurskens, A. F. van der Steen, N. de Jong, M. D. Verweij, and K. Kooiman, "Opening of endothelial cell–cell contacts due to sonoporation", *Journal of Controlled Release*, vol. 322, pp. 426–438, 2020. DOI: 10.1016/j.jconrel.2020.03.038.

[202] S. Roovers, G. Lajoinie, I. De Cock, T. Brans, H. Dewitte, K. Braeckmans, M. Versuis, S. C. De Smedt, and I. Lentacker, "Sonoprinting of nanoparticle-loaded microbubbles: Unraveling the multi-timescale mechanism", *Biomaterials*, vol. 217, p. 119 250, 2019. DOI: 10.1016/j.biomaterials.2019.119250.

[203] N. Kudo, K. Okada, and K. Yamamoto, "Sonoporation by single-shot pulsed ultrasound with microbubbles adjacent to cells", *Biophysical Journal*, vol. 96, no. 12, pp. 4866–4876, 2009. DOI: 10.1016/j.bpj.2009.02.072.

[204] P. C. Brooks, R. A. Clark, and D. A. Cheresh, "Requirement of vascular integrin alpha v beta 3 for angiogenesis", *Science*, vol. 264, no. 5158, 569 LP –571, 1994. DOI: 10.1126/science.7512751.

[205] F. W. Kremkau, "General Principles of Echocardiography", in *ASE's Comprehensive Echocardiography*, 2015, pp. 11–24. DOI: 10.1016/B978-0-323-26011-4.09971-X.

[206] P. A. Dayton, D. Pearson, J. Clark, S. Simon, P. A. Schumann, R. Zutshi, T. O. Matsunaga, and K. W. Ferrara, "Ultrasonic Analysis of Peptide- and Antibody-Targeted Microbubble Contrast Agents for Molecular Imaging of $\alpha v\beta 3$-Expressing Cells", *Molecular Imaging*, vol. 3, no. 2, pp. 125–134, 2004. DOI: 10.1162/1535350041464883.

[207] V. Daeichin, K. Kooiman, I. Skachkov, J. G. Bosch, T. L. Theelen, K. Steiger, A. Needles, B. J. Janssen, M. J. Daemen, A. F. van der Steen, N. de Jong, and J. C. Sluimer, "Quantification of Endothelial $\alpha v\beta 3$ Expression with High-Frequency Ultrasound and Targeted Microbubbles: In Vitro and In Vivo Studies", *Ultrasound in Medicine & Biology*, vol. 42, no. 9, pp. 2283–2293, 2016. DOI: 10.1016/j.ultrasmedbio.2016.05.005.

[208] D. B. Ellegala, H. Leong-Poi, J. E. Carpenter, A. L. Klibanov, S. Kaul, M. E. Shaffrey, J. Sklenar, and J. R. Lindner, "Imaging tumor angiogenesis with contrast ultrasound and microbubbles targeted to $\alpha v\beta 3$", *Circulation*, vol. 108, no. 3, pp. 336–341, 2003. DOI: 10.1161/01.CIR.0000080326.15367.0C.

[209] L. Schermelleh, R. Heintzmann, and H. Leonhardt, "A guide to super-resolution fluorescence microscopy", *Journal of Cell Biology*, vol. 190, no. 2, pp. 165–175, 2010. DOI: 10.1083/jcb.201002018.

[210] M. Emmer, A. van Wamel, D. E. Goertz, and N. de Jong, "The Onset of Microbubble Vibration", *Ultrasound in Medicine & Biology*, vol. 33, no. 6, pp. 941–949, 2007. DOI: 10.1016/j.ultrasmedbio.2006.11.004.

[211] D. Tsvirkun, A. Grichine, A. Duperray, C. Misbah, and L. Bureau, "Microvasculature on a chip: Study of the Endothelial Surface Layer and the flow structure of Red Blood Cells", *Scientific Reports*, vol. 7, no. February, pp. 1–11, 2017. DOI: 10.1038/srep45036.

[212] N. de Jong, M. Emmer, A. van Wamel, and M. Versluis, "Ultrasonic characterization of ultrasound contrast agents", *Medical and Biological Engineering and Computing*, vol. 47, no. 8, pp. 861–873, 2009. DOI: 10.1007/s11517-009-0497-1.

[213] H. Hashizume, P. Baluk, S. Morikawa, J. W. McLean, G. Thurston, S. Roberge, R. K. Jain, and D. M. McDonald, "Openings between Defective Endothelial Cells Explain Tumor Vessel Leakiness", *The American Journal of Pathology*, vol. 156, no. 4, pp. 1363–1380, 2000. DOI: 10.1016/S0002-9440(10)65006-7.

[214] H. Maeda, "Macromolecular therapeutics in cancer treatment: The EPR effect and beyond", *Journal of Controlled Release*, vol. 164, no. 2, pp. 138–144, 2012. DOI: 10.1016/j.jconrel.2012.04.038.

[215] D. M. McDonald, G. Thurston, and P. Baluk, "Endothelial Gaps as Sites for Plasma Leakage in Inflammation", *Microcirculation*, vol. 6, no. 1, pp. 7–22, 1999. DOI: 10.1111/j.1549-8719.1999.tb00084.x.

[216] G. P. van Nieuw Amerongen and V. W. van Hinsbergh, "Targets for pharmacological intervention of endothelial hyperpermeability and barrier function", *Vascular Pharmacology*, vol. 39, no. 4-5, pp. 257–272, 2002. DOI: 10.1016/S1537-1891(03)00014-4.

[217] S. A. G. Langeveld, C. Schwieger, I. Beekers, J. Blaffert, T. van Rooij, A. Blume, and K. Kooiman, "Ligand Distribution and Lipid Phase Behavior in Phospholipid-Coated Microbubbles and Monolayers", *Langmuir*, vol. 36, no. 12, pp. 3221–3233, 2020. DOI: 10.1021/acs.langmuir.9b03912.

[218] S. B. Feinstein, J. Cheirif, F. J. Ten Cate, P. R. Silverman, P. A. Heidenreich, C. Dick, R. M. Desir, W. F. Armstrong, M. A. Quinones, and P. M. Shah, "Safety and efficacy of a new transpulmonary ultrasound contrast agent: Initial multicenter clinical results", *Journal of the American College of Cardiology*, vol. 16, no. 2, pp. 316–324, 1990. DOI: 10.1016/0735-1097(90)90580-I.

[219] J.-M. Correas, L. Bridal, A. Lesavre, A. Méjean, M. Claudon, and O. Hélénon, "Ultrasound contrast agents: properties, principles of action, tolerance, and artifacts", *European Radiology*, vol. 11, no. 8, pp. 1316–1328, 2001. DOI: 10.1007/s003300100940.

[220] M. Smeenge, F. Tranquart, C. K. Mannaerts, T. M. de Reijke, M. J. van de Vijver, M. P. Laguna, S. Pochon, J. J. de la Rosette, and H. Wijkstra, "First-in-Human Ultrasound Molecular Imaging With a VEGFR2-Specific Ultrasound Molecular Contrast Agent (BR55) in Prostate Cancer", *Investigative Radiology*, vol. 52, no. 7, pp. 419–427, 2017. DOI: 10.1097/RLI.0000000000000362.

[221] J. K. Willmann, L. Bonomo, A. C. Testa, P. Rinaldi, G. Rindi, K. S. Valluru, G. Petrone, M. Martini, A. M. Lutz, and S. S. Gambhir, "Ultrasound Molecular Imaging With BR55 in Patients With Breast and Ovarian Lesions: First-in-Human Results", eng, *Journal of Clinical Oncology*, vol. 35, no. 19, pp. 2133–2140, 2017. DOI: 10.1200/JCO.2016.70.8594.

[222] M. A. Borden, G. Pu, G. J. Runner, and M. L. Longo, "Surface phase behavior and microstructure of lipid/PEG-emulsifier monolayer-coated microbubbles", *Colloids and Surfaces B: Biointerfaces*, vol. 35, no. 3-4, pp. 209–223, 2004. DOI: 10.1016/j.colsurfb.2004.03.007.

[223] M. A. Borden, G. V. Martinez, J. Ricker, N. Tsvetkova, M. Longo, R. J. Gillies, P. A. Dayton, and K. W. Ferrara, "Lateral Phase Separation in Lipid-Coated Microbubbles", *Langmuir*, vol. 22, no. 9, pp. 4291–4297, 2006. DOI: 10.1021/la052841v.

[224] M. M. Lozano and M. L. Longo, "Microbubbles Coated with Disaturated Lipids and DSPE-PEG2000: Phase Behavior, Collapse Transitions, and Permeability", *Langmuir*, vol. 25, no. 6, pp. 3705–3712, 2009. DOI: 10.1021/la803774q.

[225] O. Albrecht, H. Gruler, and E. Sackmann, "Polymorphism of phospholipid monolayers", *Journal de Physique*, vol. 39, no. 3, pp. 301–313, 1978. DOI: 10.1051/jphys:01978003903030100.

[226] D. Marsh, R. Bartucci, and L. Sportelli, "Lipid membranes with grafted polymers: physicochemical aspects", *Biochimica et Biophysica Acta (BBA) - Biomembranes*, vol. 1615, no. 1-2, pp. 33–59, 2003. DOI: 10.1016/S0005-2736(03)00197-4.

[227] C. W. McConlogue and T. K. Vanderlick, "A Close Look at Domain Formation in DPPC Monolayers", *Langmuir*, vol. 13, no. 26, pp. 7158–7164, 1997. DOI: 10.1021/la970898e.

[228] S. Kilic and E. S. Bolukcu, "Phase behavior of DSPC/PEG40St mixtures at higher emulsifier contents", *Colloids and Surfaces B: Biointerfaces*, vol. 171, pp. 368–376, 2018. DOI: 10.1016/j.colsurfb.2018.07.046.

[229] M. M. Lozano and M. L. Longo, "Complex formation and other phase transformations mapped in saturated phosphatidylcholine/DSPE-PEG2000 monolayers", *Soft Matter*, vol. 5, no. 9, p. 1822, 2009. DOI: 10.1039/b820070j.

[230] J. Owen, S. Kamila, S. Shrivastava, D. Carugo, J. Bernardino de la Serna, C. Mannaris, V. Pereno, R. Browning, E. Beguin, A. P. McHale, J. F. Callan, and E. Stride, "The Role of PEG-40-stearate in the Production, Morphology, and Stability of Microbubbles", *Langmuir*, vol. 35, no. 31, pp. 10 014–10 024, 2019. DOI: 10.1021/acs.langmuir.8b02516.

[231] G. Chen, L. Yang, L. Zhong, S. Kutty, Y. Wang, K. Cui, J. Xiu, S. Cao, Q. Huang, W. Liao, Y. Liao, J. Wu, W. Zhang, and J. Bin, "Delivery of Hydrogen Sulfide by Ultrasound Targeted Microbubble Destruction Attenuates Myocardial Ischemia-reperfusion Injury", *Scientific Reports*, vol. 6, no. 1, p. 30 643, 2016. DOI: 10.1038/srep30643.

[232] D. C. Steinl, L. Xu, A. Ochoa-Espinosa, M. Punjabi, and B. A. Kaufmann, "Non-invasive contrast enhanced ultrasound molecular imaging of inflammation in autoimmune myocarditis for prediction of left ventricular fibrosis and remodeling", *PLoS ONE*, vol. 14, no. 10, V. Lionetti, Ed., e0224377, 2019. DOI: 10.1371/journal.pone.0224377.

[233] A. S. Shaw, "Lipid rafts: now you see them, now you don't", *Nature Immunology*, vol. 7, no. 11, pp. 1139–1142, 2006. DOI: 10.1038/ni1405.

[234] V. Daeichin, T. van Rooij, I. Skachkov, B. Ergin, P. A. C. Specht, A. Lima, C. Ince, J. G. Bosch, A. F. W. van der Steen, N. de Jong, and K. Kooiman, "Microbubble Composition and Preparation for High-Frequency Contrast-Enhanced Ultrasound Imaging: In Vitro and In Vivo Evaluation", *IEEE Transactions on Ultrasonics, Ferroelectrics, and Frequency Control*, vol. 64, no. 3, pp. 555–567, 2017. DOI: 10.1109/TUFFC.2016.2640342.

[235] A. Blume, "Lipids at the air–water interface", *ChemTexts*, vol. 4, no. 1, p. 3, 2018. DOI: 10.1007/s40828-018-0058-z.

[236] E. Hosgor, T. Kucuk, I. N. Oksal, and D. B. Kaymak, "Design and control of distillation processes for methanol–chloroform separation", *Computers & Chemical Engineering*, vol. 67, pp. 166–177, 2014. DOI: 10.1016/j.compchemeng.2014.03.026.

[237] S. Hell and E. H. Stelzer, "Fundamental improvement of resolution with a 4Pi-confocal fluorescence microscope using two-photon excitation", *Optics Communications*, vol. 93, no. 5-6, pp. 277–282, 1992. DOI: 10.1016/0030-4018(92)90185-T.

[238] T. R. Baekmark, G. Elender, D. D. Lasic, and E. Sackmann, "Conformational Transitions of Mixed Monolayers of Phospholipids and Polyethylene Oxide Lipopolymers and Interaction Forces with Solid Surfaces", *Langmuir*, vol. 11, no. 10, pp. 3975–3987, 1995. DOI: 10.1021/la00010a058.

[239] H. Hussain, A. Kerth, A. Blume, and J. Kressler, "Amphiphilic Block Copolymers of Poly(ethylene oxide) and Poly(perfluorohexylethyl methacrylate) at the Water Surface and Their Penetration into the Lipid Monolayer", *The Journal of Physical Chemistry B*, vol. 108, no. 28, pp. 9962–9969, 2004. DOI: 10.1021/jp0495702.

[240] T. R. Baekmark, T. Wiesenthal, P. Kuhn, A. Albersdörfer, O. Nuyken, and R. Merkel, "A Systematic Infrared Reflection-Absorption Spectroscopy and Film Balance Study of the Phase Behavior of Lipopolymer Monolayers at the Air-Water Interface", *Langmuir*, vol. 15, no. 10, pp. 3616–3626, 1999. DOI: 10.1021/la981360r.

[241] R. H. Abou-Saleh, M. Swain, S. D. Evans, and N. H. Thomson, "Poly(ethylene glycol) Lipid-Shelled Microbubbles: Abundance, Stability, and Mechanical Properties", *Langmuir*, vol. 30, no. 19, pp. 5557–5563, 2014. DOI: 10.1021/la404804u.

[242] C. Theiss and U. Holzgrabe, "Characterization of polydisperse macrogols and macrogol-based excipients via HPLC and charged aerosol detection", *Journal of Pharmaceutical and Biomedical Analysis*, vol. 160, pp. 212–221, 2018. DOI: 10.1016/j.jpba.2018.07.043.

[243] R. H. Abou-Saleh, J. R. McLaughlan, R. J. Bushby, B. R. Johnson, S. Freear, S. D. Evans, and N. H. Thomson, "Molecular Effects of Glycerol on Lipid Monolayers at the Gas–Liquid Interface: Impact on Microbubble Physical and Mechanical Properties", *Langmuir*, vol. 35, no. 31, pp. 10 097–10 105, 2019. DOI: 10.1021/acs.langmuir.8b04130.

[244] H. McConnell, "Structures And Transitions In Lipid Monolayers At The Air-Water Interface", *Annual Review of Physical Chemistry*, vol. 42, no. 1, pp. 171–195, 1991. DOI: 10.1146/annurev.physchem.42.1.171.

[245] P. Scholtysek, Z. Li, J. Kressler, and A. Blume, "Interactions of DPPC with Semitelechelic Poly(glycerol methacrylate)s with Perfluoroalkyl End Groups", *Langmuir*, vol. 28, no. 44, pp. 15 651–15 662, 2012. DOI: 10.1021/la3028226.

[246] G. W. Feigenson, "Phase behavior of lipid mixtures", *Nature Chemical Biology*, vol. 2, no. 11, pp. 560–563, 2006. DOI: 10.1038/nchembio1106-560.

[247] E. Rufeil-Fiori, N. Wilke, and A. J. Banchio, "Dipolar interactions between domains in lipid monolayers at the air–water interface", *Soft Matter*, vol. 12, no. 21, pp. 4769–4777, 2016. DOI: 10.1039/C5SM02862K.

[248] D. Andelman, F. Broçhard, and J. Joanny, "Phase transitions in Langmuir monolayers of polar molecules", *The Journal of Chemical Physics*, vol. 86, no. 6, pp. 3673–3681, 1987. DOI: 10.1063/1.451970.

[249] K. Tanwir and V. Tsoukanova, "Lateral Distribution of a Poly(ethylene glycol)-Grafted Phospholipid in Phosphocholine Monolayers Studied by Epifluorescence Microscopy", *Langmuir*, vol. 24, no. 24, pp. 14 078–14 087, 2008. DOI: 10.1021/la802205y.

[250] M. L. Mitchell and R. A. Dluhy, "In situ FT-IR investigation of phospholipid monolayer phase transitions at the air water interface", *Journal of the American Chemical Society*, vol. 110, no. 3, pp. 712–718, 1988. DOI: 10.1021/ja00211a008.

[251] R. D. Hunt, M. L. Mitchell, and R. A. Dluhy, "The interfacial structure of phospholipid monolayer films: an infrared reflectance study", *Journal of Molecular Structure*, vol. 214, pp. 93–109, 1989. DOI: 10.1016/0022-2860(89)80007-9.

[252] A. Blume and A. Kerth, "Peptide and protein binding to lipid monolayers studied by FT-IRRA spectroscopy", *Biochimica et Biophysica Acta (BBA) - Biomembranes*, vol. 1828, no. 10, pp. 2294–2305, 2013. DOI: 10.1016/j.bbamem.2013.04.014.

[253] D. Shi, X. Liu, C. Counil, and M. P. Krafft, "Fluorocarbon Exposure Mode Markedly Affects Phospholipid Monolayer Behavior at the Gas/Liquid Interface: Impact on Size and Stability of Microbubbles", *Langmuir*, vol. 35, no. 31, pp. 10 025–10 033, 2019. DOI: 10.1021/acs.langmuir.8b03546.

[254] R. H. Abou-Saleh, S. A. Peyman, B. R. G. Johnson, G. Marston, N. Ingram, R. Bushby, P. L. Coletta, A. F. Markham, and S. D. Evans, "The influence of intercalating perfluorohexane into lipid shells on nano and microbubble stability", *Soft Matter*, vol. 12, no. 34, pp. 7223–7230, 2016. DOI: 10.1039/C6SM00956E.

[255] J. H. Crowe, M. A. Whittam, D. Chapman, and L. M. Crowe, "Interactions of phospholipid monolayers with carbohydrates", *Biochimica et Biophysica Acta (BBA) - Biomembranes*, vol. 769, no. 1, pp. 151–159, 1984. DOI: 10.1016/0005-2736(84)90018-X.

[256] K. W. Ferrara, M. A. Borden, and H. Zhang, "Lipid-Shelled Vehicles: Engineering for Ultrasound Molecular Imaging and Drug Delivery", *Accounts of Chemical Research*, vol. 42, no. 7, pp. 881–892, 2009. DOI: 10.1021/ar8002442.

[257] S. R. Sirsi and M. A. Borden, "Microbubble compositions, properties and biomedical applications", *Bubble Science, Engineering & Technology*, vol. 1, no. 1-2, pp. 3–17, 2009. DOI: 10.1179/175889709X446507.

[258] A. L. Klibanov, *Contrast Agents II*, W. Krause, Ed., ser. Topics in Current Chemistry. Berlin, Heidelberg: Springer Berlin Heidelberg, 2002, vol. 222, pp. 73–106. DOI: 10.1007/3-540-46009-8.

[259] S. Lee, D. H. Kim, and D. Needham, "Equilibrium and Dynamic Interfacial Tension Measurements at Microscopic Interfaces Using a Micropipet Technique. 1. A New Method for Determination of Interfacial Tension", *Langmuir*, vol. 17, no. 18, pp. 5537–5543, 2001. DOI: 10.1021/la0103259.

[260] B. L. Helfield, B. Y. C. Leung, and D. E. Goertz, "The effect of boundary proximity on the response of individual ultrasound contrast agent microbubbles", *Physics in Medicine and Biology*, vol. 59, no. 7, pp. 1721–1745, 2014. DOI: 10.1088/0031-9155/59/7/1721.

[261] Y. Liu, E. Gill, and Y. Y. Shery Huang, "Microfluidic on-chip biomimicry for 3D cell culture: a fit-for-purpose investigation from the end user standpoint", *Future Science OA*, vol. 3, FSO173, 2017. DOI: 10.4155/fsoa-2016-0084.

[262] F. Pampaloni, E. G. Reynaud, and E. H. K. Stelzer, "The third dimension bridges the gap between cell culture and live tissue", *Nature Reviews Molecular Cell Biology*, vol. 8, no. 10, pp. 839–845, 2007. DOI: 10.1038/nrm2236.

[263] T. G. Walsh, R. P. Murphy, P. Fitzpatrick, K. D. Rochfort, A. F. Guinan, A. Murphy, and P. M. Cummins, "Stabilization of brain microvascular endothelial barrier function by shear stress involves VE-cadherin signaling leading to modulation of pTyr-occludin levels", *Journal of Cellular Physiology*, vol. 226, no. 11, pp. 3053–3063, 2011. DOI: 10.1002/jcp.22655.

[264] A. Yudina, M. De Smet, M. Lepetit-Coiffé, S. Langereis, L. Van Ruijssevelt, P. Smirnov, V. Bouchaud, P. Voisin, H. Grüll, and C. T. Moonen, "Ultrasound-mediated intracellular drug delivery using microbubbles and temperature-sensitive liposomes", *Journal of Controlled Release*, vol. 155, no. 3, pp. 442–448, 2011. DOI: 10.1016/j.jconrel.2011.06.006.

[265] D. Carugo, J. Owen, C. Crake, J. Y. Lee, and E. Stride, "Biologically and Acoustically Compatible Chamber for Studying Ultrasound-Mediated Delivery of Therapeutic Compounds", *Ultrasound in Medicine & Biology*, vol. 41, no. 7, pp. 1927–1937, 2015. DOI: 10.1016/j.ultrasmedbio.2015.03.020.

[266] V. van Duinen, S. J. Trietsch, J. Joore, P. Vulto, and T. Hankemeier, "Microfluidic 3D cell culture: From tools to tissue models", *Current Opinion in Biotechnology*, vol. 35, pp. 118–126, 2015. DOI: 10.1016/j.copbio.2015.05.002.

[267] S. J. Trietsch, G. D. Israëls, J. Joore, T. Hankemeier, and P. Vulto, "Microfluidic titer plate for stratified 3D cell culture", *Lab on a Chip*, vol. 13, no. 18, p. 3548, 2013. DOI: 10.1039/c3lc50210d.

[268] P. Vulto, S. Podszun, P. Meyer, C. Hermann, A. Manz, and G. A. Urban, "Phaseguides: A paradigm shift in microfluidic priming and emptying", *Lab on a Chip*, vol. 11, no. 9, pp. 1596–1602, 2011. DOI: 10.1039/c0lc00643b.

[269] N. R. Wevers, R. van Vught, K. J. Wilschut, A. Nicolas, C. Chiang, H. L. Lanz, S. J. Trietsch, J. Joore, and P. Vulto, "High-throughput compound evaluation on 3D networks of neurons and glia in a microfluidic platform", *Scientific Reports*, vol. 6, no. December, p. 38 856, 2016. DOI: 10.1038/srep38856.

[270] S. J. Trietsch, E. Naumovska, D. Kurek, M. C. Setyawati, M. K. Vormann, K. J. Wilschut, H. L. Lanz, A. Nicolas, C. P. Ng, J. Joore, S. Kustermann, A. Roth, T. Hankemeier, A. Moisan, and P. Vulto, "Membrane-free culture and real-time barrier integrity assessment of perfused intestinal epithelium tubes", *Nature Communications*, vol. 8, no. 1, p. 262, 2017. DOI: 10.1038/s41467-017-00259-3.

[271] M. Jang, P. Neuzil, T. Volk, A. Manz, and A. Kleber, "On-chip three-dimensional cell culture in phaseguides improves hepatocyte functions in vitro", *Biomicrofluidics*, vol. 9, no. 3, p. 34 113, 2015. DOI: 10.1063/1.4922863.

[272] M. Overvelde, V. Garbin, J. Sijl, B. Dollet, N. de Jong, D. Lohse, and M. Versluis, "Nonlinear Shell Behavior of Phospholipid-Coated Microbubbles", *Ultrasound in Medicine & Biology*, vol. 36, no. 12, pp. 2080–2092, 2010. DOI: 10.1016/j.ultrasmedbio.2010.08.015.

[273] T. Segers, L. de Rond, N. de Jong, M. Borden, and M. Versluis, "Stability of Monodisperse Phospholipid-Coated Microbubbles Formed by Flow-Focusing at High Production Rates", *Langmuir*, vol. 32, no. 16, pp. 3937–3944, 2016. DOI: 10.1021/acs.langmuir.6b00616.

[274] S. Hilgenfeldt, D. Lohse, and M. Zomack, "Response of bubbles to diagnostic ultrasound: A unifying theoretical approach", *European Physical Journal B*, vol. 4, no. 2, pp. 247–255, 1998. DOI: 10.1007/s100510050375.

[275] MatWeb. (). Schott D263 Thin Borosilicate Glass. Accessed 12 April 2017, [Online]. Available: http://www.matweb.com/search/datasheettext.aspx?matguid=8df9f3e0106d43818ebe1862e76a1107.

[276] D. Vaughn and J. Mould, *PZFlex Time Domain Finite Element Analysis Package*. CA, USA: PZFlex LLC, 2001.

[277] W. Xia, D. Piras, J. C. G. van Hespen, W. Steenbergen, and S. Manohar, "A new acoustic lens material for large area detectors in photoacoustic breast tomography", *Photoacoustics*, vol. 1, no. 2, pp. 9–18, 2013. DOI: 10.1016/j.pacs.2013.05.001.

[278] G. Kino, *Acoustic Waves: Devices, Imaging, and Analog Signal Processing*. 1987, vol. 100, p. 103.

[279] A. Rahim, S. L. Taylor, N. L. Bush, G. R. ter Haar, J. C. Bamber, and C. D. Porter, "Physical parameters affecting ultrasound/microbubble-mediated gene delivery efficiency in vitro", *Ultrasound in Medicine & Biology*, vol. 32, no. 8, pp. 1269–1279, 2006. DOI: 10.1016/j.ultrasmedbio.2006.04.014.

[280] K. Hensel, M. P. Mienkina, and G. Schmitz, "Analysis of Ultrasound Fields in Cell Culture Wells for In Vitro Ultrasound Therapy Experiments", *Ultrasound in Medicine & Biology*, vol. 37, no. 12, pp. 2105–2115, 2011. DOI: 10.1016/j.ultrasmedbio.2011.09.007.

[281] K. Kooiman, M. Emmer, M. Foppen-Harteveld, A. Van Wamel, and N. de Jong, "Increasing the endothelial layer permeability through ultrasound-activated microbubbles", *IEEE Transactions on Biomedical Engineering*, vol. 57, no. 1, pp. 29–32, 2010. DOI: 10.1109/TBME.2009.2030335.

[282] T.-Y. Wang, K. Wilson, S. Machtaler, and J. Willmann, "Ultrasound and Microbubble Guided Drug Delivery: Mechanistic Understanding and Clinical Implications", *Current Pharmaceutical Biotechnology*, vol. 14, no. 8, pp. 743–752, 2014. DOI: 10.2174/1389201014666131226114611.

[283] N. N. Salama, N. D. Eddington, and A. Fasano, "Tight junction modulation and its relationship to drug delivery", *Advanced Drug Delivery Reviews*, vol. 58, no. 1, pp. 15–28, 2006. DOI: 10.1016/j.addr.2006.01.003.

[284] M. A. Deli, "Potential use of tight junction modulators to reversibly open membranous barriers and improve drug delivery", *Biochimica et Biophysica Acta - Biomembranes*, vol. 1788, no. 4, pp. 892–910, 2009. DOI: 10.1016/j.bbamem.2008.09.016.

[285] V. Van Duinen, A. Van Den Heuvel, S. J. Trietsch, H. L. Lanz, J. M. Van Gils, A. J. Van Zonneveld, P. Vulto, and T. Hankemeier, "96 Perfusable Blood Vessels To Study Vascular Permeability in Vitro", *Scientific Reports*, vol. 7, no. 1, pp. 1–11, 2017. DOI: 10.1038/s41598-017-14716-y.

[286] V. van Duinen, D. Zhu, C. Ramakers, A. J. van Zonneveld, P. Vulto, and T. Hankemeier, "Perfused 3D angiogenic sprouting in a high-throughput in vitro platform.", eng, *Angiogenesis*, vol. 22, no. 1, pp. 157–165, 2019. DOI: 10.1007/s10456-018-9647-0.

[287] Y. C. Park, C. Zhang, S. Kim, G. Mohamedi, C. Beigie, J. O. Nagy, R. G. Holt, R. O. Cleveland, N. L. Jeon, and J. Y. Wong, "Microvessels-on-a-Chip to Assess Targeted Ultrasound-Assisted Drug Delivery", *ACS Applied Materials & Interfaces*, vol. 8, no. 46, pp. 31 541–31 549, 2016. DOI: 10.1021/acsami.6b09071.

[288] E. W. Ades, F. J. Candal, R. A. Swerlick, V. G. George, S. Summers, D. C. Bosse, and T. J. Lawley, "HMEC-1: Establishment of an Immortalized Human Microvascular Endothelial Cell Line", *Journal of Investigative Dermatology*, vol. 99, no. 6, pp. 683–690, 1992. DOI: 10.1111/1523-1747.ep12613748.

[289] W. Yuan, Y. Lv, M. Zeng, and B. M. Fu, "Non-invasive measurement of solute permeability in cerebral microvessels of the rat", *Microvascular Research*, vol. 77, no. 2, pp. 166–173, 2009. DOI: 10.1016/j.mvr.2008.08.004.

[290] G. M. Price, K. H. Wong, J. G. Truslow, A. D. Leung, C. Acharya, and J. Tien, "Effect of mechanical factors on the function of engineered human blood microvessels in microfluidic collagen gels", *Biomaterials*, vol. 31, no. 24, pp. 6182–6189, 2010. DOI: 10.1016/j.biomaterials.2010.04.041.

[291] P. J. Frinking, I. Tardy, M. Théraulaz, M. Arditi, J. Powers, S. Pochon, and F. Tranquart, "Effects of Acoustic Radiation Force on the Binding Efficiency of BR55, a VEGFR2-Specific Ultrasound Contrast Agent", *Ultrasound in Medicine & Biology*, vol. 38, no. 8, pp. 1460–1469, 2012. DOI: 10.1016/j.ultrasmedbio.2012.03.018.

[292] S. Turco, I. Tardy, P. Frinking, H. Wijkstra, and M. Mischi, "Quantitative ultrasound molecular imaging by modeling the binding kinetics of targeted contrast agent", *Physics in Medicine and Biology*, vol. 62, no. 6, pp. 2449–2464, 2017. DOI: 10.1088/1361-6560/aa5e9a.

[293] P. Marmottant, M. Versluis, N. de Jong, S. Hilgenfeldt, and D. Lohse, "High-speed imaging of an ultrasound-driven bubble in contact with a wall: "Narcissus" effect and resolved acoustic streaming", *Experiments in Fluids*, vol. 41, no. 2, pp. 147–153, 2006. DOI: 10.1007/s00348-005-0080-y.

[294] A. A. Doinikov, S. Zhao, and P. A. Dayton, "Modeling of the acoustic response from contrast agent microbubbles near a rigid wall", *Ultrasonics*, vol. 49, no. 2, pp. 195–201, 2009. DOI: 10.1016/j.ultras.2008.07.017.

[295] P. Yan, K.-J. Chen, J. Wu, L. Sun, H.-W. Sung, R. D. Weisel, J. Xie, and R.-K. Li, "The use of MMP2 antibody-conjugated cationic microbubble to target the ischemic myocardium, enhance Timp3 gene transfection and improve cardiac function", *Biomaterials*, vol. 35, no. 3, pp. 1063–1073, 2014. DOI: 10.1016/j.biomaterials.2013.10.043.

[296] W.-H. Shentu, C.-X. Yan, C.-M. Liu, R.-X. Qi, Y. Wang, Z.-X. Huang, L.-M. Zhou, and X.-D. You, "Use of cationic microbubbles targeted to P-selectin to improve ultrasound-mediated gene transfection of hVEGF165 to the ischemic myocardium", eng, *Journal of Zhejiang University-SCIENCE B*, vol. 19, no. 9, pp. 699–707, 2018. DOI: 10.1631/jzus.B1700298.

[297] Q. Deng, B. Hu, S. Cao, H.-N. Song, J.-L. Chen, and Q. Zhou, "Improving the efficacy of therapeutic angiogenesis by UTMD-mediated Ang-1 gene delivery to the infarcted myocardium", eng, *International Journal of Molecular Medicine*, vol. 36, no. 2, pp. 335–344, 2015. DOI: 10.3892/ijmm.2015.2226.

[298] J. E. Hall, *Guyton and Hall textbook of medical physiology e-Book*. Elsevier Health Sciences, 2015.

[299] I. Skachkov, Y. Luan, S. T. van Tiel, A. F. W. van der Steen, N. de Jong, M. R. Bernsen, and K. Kooiman, "SPIO labeling of endothelial cells using ultrasound and targeted microbubbles at diagnostic pressures", *PLoS ONE*, vol. 13, no. 9, C. E. Hagemeyer, Ed., e0204354, 2018. DOI: 10.1371/journal.pone.0204354.

[300] L. Munaron, "Intracellular Calcium, Endothelial Cells and Angiogenesis", eng, *Recent Patents on Anti-Cancer Drug Discovery*, vol. 1, no. 1, pp. 105–119, 2006. DOI: 10.2174/157489206775246502.

[301] Y. Wang, Y. Li, K. Yan, L. Shen, W. Yang, J. Gong, and K. Ding, "Clinical study of ultrasound and microbubbles for enhancing chemotherapeutic sensitivity of malignant tumors in digestive system", eng, *Chinese Journal of Cancer Research*, vol. 30, no. 5, pp. 553–563, 2018. DOI: 10.21147/j.issn.1000-9604.2018.05.09.

[302] A. Carpentier, M. Canney, A. Vignot, V. Reina, K. Beccaria, C. Horodyckid, C. Karachi, D. Leclercq, C. Lafon, J.-Y. Chapelon, L. Capelle, P. Cornu, M. Sanson, K. Hoang-Xuan, J.-Y. Delattre, and A. Idbaih, "Clinical trial of blood-brain barrier disruption by pulsed ultrasound", *Science Translational Medicine*, vol. 8, no. 343, 343re2–343re2, 2016. DOI: 10.1126/scitranslmed.aaf6086.

[303] J. J. Choi, R. C. Carlisle, C. Coviello, L. Seymour, and C. C. Coussios, "Non-invasive and real-time passive acoustic mapping of ultrasound-mediated drug delivery", *Physics in Medicine and Biology*, vol. 59, no. 17, pp. 4861–4877, 2014. DOI: 10.1088/0031-9155/59/17/4861.

[304] M. A. O'Reilly and K. Hynynen, "Blood-Brain Barrier: Real-time Feedback-controlled Focused Ultrasound Disruption by Using an Acoustic Emissions–based Controller", *Radiology*, vol. 263, no. 1, pp. 96–106, 2012. DOI: 10.1148/radiol.11111417.

[305] Y. Huang, R. Alkins, M. L. Schwartz, and K. Hynynen, "Opening the Blood-Brain Barrier with MR Imaging–guided Focused Ultrasound: Preclinical Testing on a Trans–Human Skull Porcine Model", *Radiology*, vol. 282, no. 1, pp. 123–130, 2016. DOI: 10.1148/radiol.2016152154.

[306] D. McMahon and K. Hynynen, "Acute Inflammatory Response Following Increased Blood-Brain Barrier Permeability Induced by Focused Ultrasound is Dependent on Microbubble Dose", eng, *Theranostics*, vol. 7, no. 16, pp. 3989–4000, 2017. DOI: 10.7150/thno.21630.

[307] S. Pochon, I. Tardy, P. Bussat, T. Bettinger, J. Brochot, M. von Wronski, L. Passantino, and M. Schneider, "BR55: A Lipopeptide-Based VEGFR2-Targeted Ultrasound Contrast Agent for Molecular Imaging of Angiogenesis", *Investigative Radiology*, vol. 45, no. 2, pp. 89–95, 2010. DOI: 10.1097/RLI.0b013e3181c5927c.

Summary

Local drug delivery is essential to effectively treat diseases and reduce side effects in the rest of the body. After intravenous administration, drugs circulate through the bloodstream and are delivered to the entire body. In addition, the vascular endothelium forms an important barrier, so only a small percentage of the drugs manage to leave the vascular system and actually reach the diseased tissue. However, drug delivery can be locally enhanced with ultrasound in combination with microscopically small gas bubbles (1 - 10 μm in diameter). These gas bubbles are encased in a layer of fat and are known as microbubbles. The incoming ultrasound pressure wave causes microbubbles to vibrate (oscillate). Upon oscillation, microbubbles can very locally stimulate drug release or even cause cell death. In addition, microbubbles are also very effective in reflecting ultrasound. They have been used in the clinic for decades as contrast agents for diagnostic ultrasound imaging to visualize blood flow. In **Chapter 1** we introduce how microbubbles are used for diagnostic and therapeutic applications. We explain how oscillating microbubbles are studied and which drug delivery pathways can occur. We know that an oscillating microbubble can create a pore in the cell membrane for intracellular delivery (sonoporation), it can open the junctions between cells for drug extravasation, but it can also stimulate active drug uptake via endocytosis. However, the underlying biological and physical mechanisms are still poorly understood. To get therapeutic microbubbles to the clinic, it is essential to better understand how a microbubble should oscillate to enhance drug delivery.

Microbubbles can bind to specific biomarkers on a cell by adding certain molecules to their shell. By targeting microbubbles to diseased tissue, ultrasound can be used for molecular imaging. In **Chapter 2** we studied the acoustic response (oscillation) of bound and non-bound microbubbles, to improve the specificity of molecular imaging. We identified acoustic parameters that distinguished bound from non-bound microbubbles other at low pressures, but showed that it is more challenging to do so at clinically relevant pressures. Next, the effect of oscillating bound and non-bound microbubbles on human endothelial cells was compared in **Chapter 3**. The displacement of microbubbles proved to be crucial for the survival of a cell after sonoporation. When a microbubble did not displace and therefore continuously oscillated at the same place, it caused large cell membrane pores that remained open. This leads to cell death. To keep the cell alive after sonoporation, the microbubble had to oscillate for a shorter time or displace across the cell membrane.

This thesis is based on *in vitro* work, that is, biological studies conducted under artificial and controlled laboratory conditions in special cell culture systems. To study the microbubble–cell interaction *in vitro,* in **Chapter 4** we assessed whether a CLINIcell was compatible with both microscopy and ultrasound. The microbubble oscillation was visualized with the unique Brandaris 128 ultra-high-speed camera. This camera can record up to 25 million frames per second, which is necessary to resolve the ultra-fast oscillation of microbubbles. Since microbubbles oscillated in a controlled manner in the CLINIcell, it turned out to be an excellent 2D cell culture system to study the microbubble–cell interaction. In order to actually visualize the microbubble–cell interaction, we developed a novel and unique optical imaging system in **Chapter 5**. The Brandaris 128 ultra-high-speed camera was coupled to a custom-built confocal microscope. For the first time, the microbubble–cell interaction could be simultaneously investigated at nanosecond and nanometer resolution.

In **Chapter 6 & 7**, the novel optical imaging system demonstrated that sonoporation of an endothelial cell occurred when the microbubble grew more than 0.7 μm during oscillation (radial excursion). In addition, sonoporation always caused a rise in the intracellular calcium (Ca_i^{2+}) concentration, as shown in **Chapter 6**. Fluctuations in Ca_i^{2+} are a universal cellular messenger and play an important role in, for example, endocytosis, integrity of intercellular connections, membrane repair after pore formation, and cell division. An irreversible change in the Ca_i^{2+} concentration correlated with large pores that remained open for more than 120 s, and therefore irreversible cell damage. This occurred when microbubbles had a radial excursion of > 1.0 μm. Remarkably, the Ca_i^{2+} fluctuations also propagated to neighboring cells. This phenomenon is known as a *calcium wave* and proved that a single microbubble can have an impressive impact on multiple cells at the same time. Upon extreme Ca_i^{2+} fluctuations, the junctions between cells opened more often. This has great potential to achieve drug extravasation from the vascular system towards the underlying diseased tissue. In **Chapter 7** we further explored this opening of cell-cell contacts. For the first time, we demonstrated that cell-cell contacts only opened after sonoporation and that the microbubble did not have to be on the cell edge. Apparently, the intercellular junctions opened in response to sonoporation, and not as an independent drug delivery pathway. Moreover, the initial state of the cells was crucial for the cellular response. When a cell was fully attached to its neighboring cells, it was much harder for the oscillating microbubble to open the junctions. This emphasized the importance of a clinically relevant cell culture model.

The oscillation of a microbubble is variable. Hence, one microbubble will stimulate drug delivery, but the other microbubble will not. To make microbubble-mediated drug delivery predictable and safe, we need better control over microbubbles. That is why we want to better understand what the microbubble fatty shell (lipid

coating) looks like. In **Chapter 8** the physicochemical properties of the microbubble coating were investigated. The lipid microstructure in the coating differed per microbubble, a possible explanation for the variable acoustic response. Different lipid compositions and production methods were tested. We achieved a microbubble with a homogeneous ligand distribution, meaning it had a uniform distribution of the molecule that can bind to the biomarkers on cells.

In **Chapter 9 & 10** we introduced the OrganoPlate™. With the help of this 3D cell culture platform, a more realistic *in vitro* model can be created that better simulates the physiologic situation. First, in **Chapter 9** we assessed whether the OrganoPlate was compatible with ultrasound. The incoming ultrasound field was simulated with a mathematical finite-element model. Using the Brandaris 128 ultra-high-speed camera we found that microbubbles in the microfluidic channels oscillated in a controlled manner. Then, a cell culture method was developed in **Chapter 10** to actually grow microvessel using human endothelial cells in the OrganoPlate. The microvessels achieved barrier integrity. This demonstrated the potential of the OrganoPlate as a 3D *in vitro* platform to investigate drug extravasation upon microbubble oscillation.

Finally, **Chapter 11** discusses the knowledge gained in this thesis on the underlying mechanisms of microbubble-mediated drug delivery. There are certainly still challenges to unravel, but microbubbles have a clear potential for successful clinical translation.

Samenvatting

Lokale medicijnafgifte is essentieel om effectief ziektes te behandelen en bijwerkingen in de rest van het lichaam te beperken. Bij intraveneuze toediening circuleren medicijnen door de bloedbaan en worden zo door het hele lichaam afgegeven. Bovendien vormt het vasculaire endotheel een belangrijke barrière, dus slaagt maar een klein percentage van de medicijnen erin om het vaatstelsel te verlaten en daadwerkelijk het zieke weefsel te bereiken. Medicijnafgifte kan lokaal worden gestimuleerd door ultrageluid in combinatie met microscopisch kleine gasbelletjes (1 – 10 µm in diameter). Deze gasbelletjes zijn ingekapseld in een laagje vet en noemen we microbellen. Door de inkomende ultrageluidsgolf gaan microbellen trillen (oscilleren) en kunnen ze zeer lokaal medicijnafgifte stimuleren of zelfs celdood veroorzaken. Daarnaast zijn microbellen ook erg effectief in het reflecteren van ultrageluid. Ze worden al tientallen jaren gebruikt in de kliniek als contrastmiddelen voor diagnostische echografie om de bloedstroming in beeld te brengen. In **Hoofdstuk 1** introduceren we hoe microbellen worden gebruikt voor diagnostische en therapeutische toepassingen. We leggen uit hoe oscillerende microbellen bestudeerd worden en welke medicijnroutes er kunnen plaatsvinden. Het is namelijk bekend dat een oscillerende microbel een porie kan creëren in de celmembraan voor intracellulaire opname (sonoporatie), de verbindingen tussen cellen kan verbreken voor medicijn extravasatie en er ook voor kan zorgen dat een cel medicijnen actief opneemt via endocytose. Echter worden de onderliggende biologische en fysische mechanismen nog slecht begrepen. Om therapie met microbellen naar de kliniek te krijgen is het van essentieel belang om beter te begrijpen hoe een microbel moet oscilleren om medicijnafgifte te stimuleren.

Door bepaalde moleculen aan de vetschil toe te voegen kunnen microbellen doelgericht gebonden worden aan specifieke biomarkers op cellen. Door microbellen te laten plakken aan ziek weefsel kan echografie gebruikt worden voor moleculaire beeldvorming. In **Hoofdstuk 2** bestudeerden we de akoestische response (oscillatie) van gebonden en niet gebonden microbellen om de specificiteit van moleculaire beeldvorming verbeteren. We identificeerde akoestische parameters die gebonden en niet gebonden microbellen van elkaar konden onderscheiden bij lage drukken, en toonden aan dat het uitdagend is om dit ook te doen op een hogere en klinisch relevante druk. Vervolgens vergeleken we in **Hoofdstuk 3** het effect van oscillerende gebonden en niet gebonden microbellen op humane endotheelcellen. De verplaatsing van microbellen bleek van groot belang voor de overlevingskans van een cel na sonoporatie. Wanneer een microbel zich niet verplaatste en daardoor voortdurend

op dezelfde plek bleef oscilleren, veroorzaakte dat grote celmembraan poriën die open bleven staan. Dit leidt tot celdood. Om de cel in leven te houden na sonoporatie, moest de microbel korter oscilleren of zich verplaatsen over de celmembraan.

Deze thesis is gebaseerd op *in vitro* werk, oftewel, biologische studies die worden uitgevoerd onder kunstmatige en gecontroleerde laboratorium omstandigheden in speciale celkweek systemen. Om de microbel–cel interactie *in vitro* te bestuderen, onderzochten we in **Hoofdstuk 4** of een CLINIcell compatibel was met zowel microscopie als ultrageluid. De oscillatie van de microbellen werd bekeken met de unieke Brandaris 128 ultrahogesnelheidscamera. Deze camera kan 25 miljoen beelden per seconde opnemen, wat noodzakelijk is om de ultrasnelle oscillatie van microbellen te filmen. Aangezien de microbellen gecontroleerd oscilleerde in de CLINIcell, bleek het een uitstekend 2D celkweek systeem om de microbel–cel interactie te bestuderen. Om die microbel–cel interactie ook daadwerkelijk in beeld te kunnen brengen, ontwikkelden we in **Hoofdstuk 5** een zeer geavanceerd en uniek optisch systeem. De Brandaris 128 ultrahogesnelheidscamera werd gekoppeld aan een op maat gemaakte confocale microscoop. Eindelijk kon de microbel–cel interactie tegelijkertijd op nanoseconde en nanometer resolutie onderzocht worden.

In **Hoofdstuk 6 & 7** werd met het nieuwe optische systeem aangetoond dat sonoporatie van een endotheel cel plaatsvond wanneer de microbel meer dan 0.7 μm groter werd tijdens oscillatie (radiale excursie). Bovendien veroorzaakte sonoporatie altijd een verhoogde intracellulaire calcium (Ca_i^{2+}) concentratie, zoals aangetoond in **Hoofdstuk 6**. Schommelingen in de Ca_i^{2+} concentratie zijn een universeel cellulair communicatiemechanisme en spelen een belangrijke rol in bijvoorbeeld endocytosis, integriteit van intercellulaire verbindingen, membraan herstel na porie formatie en celdeling. Een onomkeerbare verandering in de Ca_i^{2+} concentratie correleerde met grote poriën die langer dan 120 s openbleven, en dus onherstelbare cel schade. Dit werd veroorzaakt als de microbel > 1.0 μm groter werd tijdens oscillatie. Opmerkelijk was hoe de Ca_i^{2+} schommeling zich ook verspreidde naar de omliggende cellen. Dit fenomeen staat bekend als een *calcium golf* en toonde aan dat een enkele microbel een indrukwekkende impact kan hebben op meerdere cellen tegelijk. Bij extreme Ca_i^{2+} schommelingen zagen we dat de verbindingen tussen cellen vaker opengingen. Dit is zeer veelbelovend om medicijnen uit het vaatstelsel te krijgen, naar het achterliggende zieke weefsel. In **Hoofdstuk 7** verdiepten we ons verder in deze opening van cel-cel contacten. Voor het eerst toonden we aan dat cel-cel contacten alleen opengaan na sonoporatie en dat de microbel daarvoor niet op de rand van de cel hoeft te liggen. Blijkbaar gingen de verbindingen tussen cellen open als reactie op sonoporatie, en is het dus geen onafhankelijke medicijnroute. Bovendien bleek de initiële staat van de verbindingen tussen de cellen cruciaal voor de cellulaire respons. Wanneer een cel volledig verbonden was met zijn omliggende cellen was het veel lastiger voor de

oscillerende microbel om die verbindingen open te krijgen. Dit benadrukte het belang van een klinisch relevant celkweek model.

De oscillatie van een microbel is nog zeer variabel. Daarom zal de ene microbel wel medicijnafgifte stimuleren, maar de andere microbel niet. Om microbeltherapie voorspelbaarder en veiliger te maken, moeten we meer controle krijgen over de microbel. Daarom willen we beter begrijpen hoe de vetschil, ofwel lipide coating, van de microbel eruitziet. In **Hoofdstuk 8** werden de fysicochemische eigenschappen van de microbel coating onderzocht. De lipide microstructuur in de coating verschilde per microbel, een mogelijke verklaring voor de variabelle akoestische response. Verschillende lipide composities en productiemethoden werden getest. We bereikten een microbel met een homogene ligand distributie, ofwel met een uniforme verdeling van het molecuul dat kan binden aan de biomarkers van cellen.

In **Hoofdstuk 9 & 10** presenteerden we de OrganoPlate™. Met behulp van dit 3D celkweek systeem kan een realistischer *in vitro* model gecreëerd worden die de fysiologie situatie in het lichaam beter nabootst. We kunnen namelijk bloedvaten kweken in de microscopische kanaaltjes van de OrganoPlate. Ten eerste beoordeelden we in **Hoofdstuk 9** of de OrganoPlate wel compatibel was met ultrageluid. Het inkomende ultrageluid veld werd gesimuleerd. Met de Brandaris 128 ultrahogesnelheidscamera zagen we dat microbellen op een gecontroleerde manier oscilleerden in de kanaaltjes van de OrganoPlate. Vervolgens ontwikkelden we in **Hoofdstuk 10** een protocol om ook daadwerkelijk bloedvaten te kweken in de OrganoPlate met humane endotheel cellen. Aangezien de bloedvaten een barrière vormden, bleek de OrganoPlate een uitstekend *in vitro* systeem om medicijn extravasatie door oscillerende microbellen te onderzoeken.

Tenslotte bediscussieert **Hoofdstuk 11** de behaalde resultaten in dit proefschrift. Ook besteden we aandacht aan de uitdagingen en toekomstige perspectieven van lokale medicijnafgifte met behulp van ultrageluid en microbellen, met oog op een succesvolle klinische translatie.

Publications and Presentations

PEER-REVIEWED PAPERS

Inés Beekers, Frits Mastik, Robert Beurskens, Phoei Ying Tang, Merel Vegter, Antonius F. W. van der Steen, Nico de Jong, Martin D. Verweij, and Klazina Kooiman, "High-resolution imaging of oscillating microbubbles inducing intracellular calcium fluctuations", *Ultrasound in Medicine & Biology*, 2020.

Inés Beekers, Merel Vegter, Kirby R. Lattwein, Frits Mastik, Robert Beurskens, Antonius F. W. van der Steen, Nico de Jong, Martin D. Verweij, and Klazina Kooiman, "Opening of endothelial cell-cell contacts due to sonoporation imaged with combined confocal microscopy and Brandaris 128", *Journal of Controlled Release*, vol. 322, pp. 426-438, 2020.

Simone A. G. Langeveld, Christian Schwieger, **Inés Beekers**, Jacob Blaffert, Tom van Rooij, Alfred Blume, and Klazina Kooiman, "Ligand distribution and lipid phase behavior in phospholipid-coated microbubbles and monolayers", *Langmuir*, vol. 36, no. 12, pp. 3221-3233, 2020.

Inés Beekers, Kirby R. Lattwein, Joop J. P. Kouijzer, Simone A. G. Langeveld, Merel Vegter, Robert Beurskens, Frits Mastik, Rogier Verduyn Lunel, Emma Verver, Antonius F. W. van der Steen, Nico de Jong, and Klazina Kooiman, "Combined Confocal Microscope and Brandaris 128 Ultra-High-Speed Camera", *Ultrasound in Medicine & Biology*, vol. 45, no. 9, pp. 2575-2582, 2019.

Inés Beekers, Tom van Rooij, Antonius F. W. van der Steen, Nico de Jong, Martin D. Verweij, and Klazina Kooiman, "Acoustic Characterization of the CLINIcell for Ultrasound Contrast Agent Studies", *IEEE Transactions on Ultrasonics, Ferroelectrics, and Frequency Control*, vol. 66, no. 1, pp. 244-246, 2019.

Inés Beekers, Tom van Rooij, Martin D. Verweij, Michel Versluis, Nico de Jong, Sebastiaan J. Trietsch, and Klazina Kooiman, "Acoustic Characterization of a Vessel-on-a-Chip Microfluidic System for Ultrasound-Mediated Drug Delivery", *IEEE Transactions on Ultrasonics, Ferroelectrics, and Frequency Control*, vol. 65, no. 4, pp. 570-581, 2018.

Tom van Rooij, **Inés Beekers**, Kirby R. Lattwein, Antonius F. W. van der Steen, Nico de Jong, and Klazina Kooiman, "Vibrational Responses of Bound and Nonbound Targeted Lipid-Coated Single Microbubbles", *IEEE Transactions on Ultrasonics, Ferroelectrics, and Frequency Control*, vol. 64, no. 5, pp. 785-797, 2017.

Tom van Rooij, Ilya Skachkov, **Inés Beekers**, Kirby. R. Lattwein, Jason D. Voorneveld, Tom J. Kokhuis, Deep Bera, Ying Luan, Antonius F. W. van der Steen, Nico de Jong, and Klazina Kooiman, "Viability of endothelial cells after ultrasound-mediated sonoporation: Influence of targeting, oscillation, and displacement of microbubbles", *Journal of Controlled Release*, vol. 238, pp. 197–211, 2016.

PUBLISHED CONFERENCE ABSTRACTS

(Presenter underlined)

Inés Beekers, Merel Vegter, Kirby R. Lattwein, Frits Mastik, Robert Beurskens, Antonius F. W. van der Steen, Martin D. Verweij, Nico de Jong, Klazina Kooiman, "Targeted microbubble opening of cell-cell junctions for vascular drug delivery elucidated with combined confocal microscopy and Brandaris 128 imaging", Joined Acoustical Society of America and Canadian Acoustics Association Meeting, Victoria, Canada, *The Journal of the Acoustical Society of America*, vol. 144, pp. 1824, 2018.

Simone A.G. Langeveld, **Inés Beekers**, Antonius F. W. van der Steen, Nico de Jong, Klazina Kooiman, "Phospholipid-coated microbubbles: Controlling response to ultrasound", Joined Acoustical Society of America and Canadian Acoustics Association Meeting, Victoria, Canada, *The Journal of the Acoustical Society of America*, vol. 144, pp. 1825, 2018.

Inés Beekers, Tom van Rooij, Martin D. Verweij, Michel A. Versluis, Nico de Jong, Sebastiaan J. Trietsch, Klazina Kooiman, "The use of a novel microfluidics system for *in vitro* ultrasound-mediated drug delivery", Joined Acoustical Society of America and European Acoustics Association Meeting, Boston, USA, *The Journal of the Acoustical Society of America*, vol. 141, pp. 4012, 2017.

CONFERENCE PRESENTATIONS

(Presenter underlined)

Inés Beekers, Phoei Ying Tang, Merel Vegter, Frits Mastik, Robert Beurskens, Antonius F. W. van der Steen, Martin D. Verweij, Nico de Jong, Klazina Kooiman, "Intracellular calcium fluctuations due to sonoporation in microbubble-mediated drug delivery imaged at high temporal and spatial resolution", IEEE International Ultrasonics Symposium 2019, Glasgow, Scotland, 6-9 Oct 2019 (oral).

Kirby R. Lattwein, **Inés Beekers**, Tom van Rooij, Joop J.P. Kouijzer, Antonius F. W. van der Steen, Nico de Jong, Willem J. B. van Wamel, Klazina Kooiman, "Bacteria in biofilms sonoporated by vibrating microbubbles", IEEE International Ultrasonics Symposium 2019, Glasgow, Scotland, 6-9 Oct 2019 (oral).

Simone A. G. Langeveld, Christian Schwieger, **Inés Beekers**, Tom van Rooij, Alfred Blume, Klazina Kooiman, "Phospholipid-coated microbubbles: lipid phase and ligand distribution", 6th International Symposium on Phospholipids in Pharmaceutical Research, Heidelberg, Germany, 9-10 Sept 2019 (poster).

Joop J. P. Kouijzer, Kirby R. Lattwein, **Inés Beekers**, Nico de Jong, Antonius F.W. van der Steen, Alexander L. Klibanov, Willem J. B. van Wamel, Klazina Kooiman, "Vancomycin-targeted microbubbles as a novel treatment of Staphylococcus aureus biofilms", Microbubble Symposium, Leeds, England, 8-9 July 2019 (pitch & poster).

Inés Beekers, Merel Vegter, Kirby R. Lattwein, Frits Mastik, Robert Beurskens, Antonius F. W. van der Steen, Martin D. Verweij, Nico de Jong, Klazina Kooiman, "Microbubble-mediated drug delivery revealed at nanometer and nanosecond resolution", Innovation for Health, Rotterdam, the Netherlands, 14 Feb 2019 (oral & poster).

Inés Beekers, Phoei Ying Tang, Merel Vegter, Frits Mastik, Robert Beurskens, Antonius F. W. van der Steen, Martin D. Verweij, Nico de Jong, Klazina Kooiman, "Cellular calcium during microbubble-mediated drug delivery revealed with combined confocal microscopy and Brandaris 128 imaging", 24st European symposium on Ultrasound Contrast Imaging, Rotterdam, the Netherlands, 17-18 Jan 2019 (oral).

Joop J. P. Kouijzer, Kirby R. Lattwein, **Inés Beekers**, Nico de Jong, Antonius F. W. van der Steen, Alexander L. Klibanov, Willem J. B. van Wamel, Klazina Kooiman, "Targeted microbubbles as a novel therapy for *Staphylococcus aureus* biofilms on cardiac devices", 24st European symposium on Ultrasound Contrast Imaging, Rotterdam, the Netherlands, 17-18 Jan 2019 (poster).

Simone A. G. Langeveld, **Inés Beekers**, Antonius F. W. van der Steen, Nico de Jong, Klazina Kooiman, "Lipid coating structure and acoustic response of ultrasound contrast agents containing cholesterol", 24st European symposium on Ultrasound Contrast Imaging, Rotterdam, the Netherlands, 17-18 Jan 2019 (poster).

Inés Beekers, Merel Vegter, Kirby R. Lattwein, Frits Mastik, Robert Beurskens, Antonius F. W. van der Steen, Martin D. Verweij, Nico de Jong, Klazina Kooiman, "Targeted microbubble opening of cell-cell junctions for vascular drug delivery elucidated with combined confocal microscopy and Brandaris 128 imaging", 176th Meeting Acoustical Society of America, Victoria, Canada, 5-9 Nov 2018.

Simone A. G. Langeveld, **Inés Beekers**, Antonius F. W. van der Steen, Nico de Jong, Klazina Kooiman, "Phospholipid-coated microbubbles: Controlling response to ultrasound", 176th Meeting Acoustical Society of America, Victoria, Canada, 5-9 Nov 2018.

Inés Beekers, Merel Vegter, Kirby R. Lattwein, Frits Mastik, Robert Beurskens, Antonius F. W. van der Steen, Martin D. Verweij, Nico de Jong, Klazina Kooiman, "Targeted microbubble-cell interactions elucidated with combined confocal microscopy and Brandaris 128 ultra-high speed imaging", IEEE International Ultrasonics Symposium 2018, Kobe, Japan, 22-25 Oct 2018 (oral).

Simone A.G. Langeveld, **Inés Beekers**, Antonius F. W. van der Steen, Nico de Jong, Klazina Kooiman, "Chemical and acoustic characterization of a novel ultrasound contrast agent", IEEE International Ultrasonics Symposium 2018, Kobe, Japan, 22-25 Oct 2018 (oral).

Inés Beekers, Merel Vegter, Phoei Ying Tang, Frits Mastik, Robert Beurskens, Antonius F. W. van der Steen, Martin D. Verweij, Nico de Jong, Klazina Kooiman, "Cellular calcium during sonoporation revealed with combined confocal microscopy and Brandaris 128", Microbubble Symposium, Leeds, England, 16-17 July 2018 (pitch & poster).

Simone A.G. Langeveld, **Inés Beekers**, Antonius F. W. van der Steen, Nico de Jong, Klazina Kooiman, "Ligand and lipid phase distribution of phospholipid-coated microbubbles", Microbubble Symposium, Leeds, England, 16-17 July 2018 (pitch & poster).

Inés Beekers, Merel Vegter, Kirby R. Lattwein, Frits Mastik, Robert Beurskens, Rogier Verduyn Lunel, Antonius F. W. van der Steen, Nico de Jong, Klazina Kooiman, "Microbubble–cell interactions revealed with combined confocal microscopy and Brandaris 128 ultra-high speed imaging", 23st European symposium on Ultrasound Contrast Imaging, Rotterdam, the Netherlands, 18-19 Jan 2018 (oral & poster).

Simone A. G. Langeveld, **Inés Beekers**, Klazina Kooiman, "Theranostic phospholipid-coated ultrasound contrast agents: response on demand", 5th International Symposium on Phospholipids in Pharmaceutical Research, Heidelberg, Germany, 18-19 Sept 2017 (poster).

Emma Kanbar, **Inés Beekers**, Tom van Rooij, Nico de Jong, Klazina Kooiman, Ayache Bouakaz, "Enhanced subharmonic emission of single microbubbles by acoustic deflation", IEEE International Ultrasonics Symposium 2017, Washington, USA, 6-9 Sept 2017 (oral).

Inés Beekers, Tom van Rooij, Martin D. Verweij, Michel Versluis, Nico de Jong, Sebastiaan J. Trietsch, Klazina Kooiman, "The use of a novel microfluidics system for *in vitro* ultrasound-mediated drug delivery", Acoustics '17, Acoustical Society of America, Boston, United States, 25-29 June 2017 (oral & poster).

Inés Beekers, Tom van Rooij, Martin D. Verweij, Michel Versluis, Nico de Jong, Sebastiaan J. Trietsch, Klazina Kooiman, "A vessel-on-a-chip model to elucidate the mechanisms involved in microbubble-mediated drug delivery", 7th European Cell Mechanics Meeting, Windermere, England, 21-23 June 2017 (poster).

Inés Beekers, Tom van Rooij, Martin D. Verweij, Michel Versluis, Nico de Jong, Sebastiaan J. Trietsch, Klazina Kooiman, "A novel microfluidics system for *in vitro* ultrasound-enhanced drug delivery: acoustic characterization", Dutch Biomedical Engineering Conference 2017, Egmond aan Zee, the Netherlands, 26-27 Jan 2017 (oral).

Inés Beekers, Tom van Rooij, Martin D. Verweij, Michel Versluis, Nico de Jong, Sebastiaan J. Trietsch, Klazina Kooiman, "Wave propagation in the OrganoPlate™ for *in vitro* ultrasound-mediated drug delivery", 22st European symposium on Ultrasound Contrast Imaging, Rotterdam, the Netherlands, 19-20 Jan 2017 (poster).

Inés Beekers, Shreyas B. Raghunathan, Tom van Rooij, Verya Daeichin, Nico de Jong, Klazina Kooiman, Sebastiaan J. Trietsch, "Wave propagation in a novel microfluidics system for *in vitro* ultrasound-enhanced drug delivery", IEEE International Ultrasonics Symposium 2016, Tours, France, 18-21 Sept 2016 (poster).

Tom van Rooij, Ilya Skachkov, **Inés Beekers**, Kirby R. Lattwein, Jason D. Voorneveld, Tom J.A. Kokhuis, Deep Bera, Ying Luan, Antonius F.W. van der Steen, Nico de Jong, Klazina Kooiman, "Bubble-cell interactions for endothelial sonoporation at long pulses using targeted and non-targeted microbubbles", IEEE International Ultrasonics Symposium 2016, Tours, France, 18-21 Sept 2016 (oral).

Tom van Rooij, Ilya Skachkov, **Inés Beekers**, Kirby R. Lattwein, Jason D. Voorneveld, Tom J.A. Kokhuis, Deep Bera, Ying Luan, Antonius F.W. van der Steen, Nico de Jong, Klazina Kooiman, "Viability of endothelial cells after ultrasound-mediated sonoporation", 31st Bubble Conference 2016, Chicago, Illinois, USA, 10-12 Sept 2016 (oral).

Inés Beekers, Shreyas B. Raghunathan, Tom van Rooij, Verya Daeichin, Nico de Jong, Klazina Kooiman, Sebastiaan J. Trietsch, "Acoustic characterization of a novel microfluidics system for *in vitro* ultrasound-mediated drug delivery", NanoCity 2016, Amsterdam, the Netherlands, 21 June 2016 (oral & poster).

Inés Beekers, Shreyas B. Raghunathan, Tom van Rooij, Verya Daeichin, Nico de Jong, Klazina Kooiman, Sebastiaan J. Trietsch, "Acoustic characterization of a novel cell culture platform for ultrasound-mediated drug delivery", 21st European symposium on Ultrasound Contrast Imaging, Rotterdam, the Netherlands, 21-22 Jan 2016 (poster).

SCIENTIFIC AWARDS

Acoustical Society of America Student Transportation Subsidy for an oral presentation at the Joined Acoustical Society of America and Canadian Acoustics Association Meeting, Victoria, Canada, 2018.

IEEE Student travel support for an oral presentation at the International Ultrasonics Symposium in Kobe, Japan, 2018.

Second prize for best poster presentation during Microbubble Symposium, Leeds, England, 2018.

Acoustical Society of America Student Transportation Subsidy for an oral presentation at the Joined Acoustical Society of America and European Acoustics Association Meeting, Boston, USA, 2017.

Third prize for best poster and pitch during the National Event on Nanotechnology - Nanocity, Amsterdam, the Netherlands, 2016.

First prize for best poster presentation during 21st European Symposium on Ultrasound Contrast Imaging, Rotterdam, the Netherlands, 2016.

Second prize of the Dutch Physics Society (NNV) for BSc thesis on "Identification of tumor vasculature with ultrasound imaging" at FYSICA, Leiden, the Netherlands, 2014.

SUPERVISED ACADEMIC REPORTS

Cheryl Mok, "Microbubble- and ultrasound-mediated drug delivery", report of MSc traineeship, Erasmus University Medical Center Rotterdam, the Netherlands, 2019.

Phoei Ying Tang, "OrganoPlate cell culture optimization for growing leak tight microvessels", report of HBO traineeship, Rotterdam University of Applied Sciences, the Netherlands, 2018.

Merel Vegter, "Bel-cel interactie bij medicijn levering", report of MBO traineeship, Techniek College Rotterdam, the Netherlands, 2018.

Lizzy van den Bosch, "Wat is kracht van bellen in de medische wetenschap?", report of final high school project, Lentiz Reviuslyceum in Maassluis, the Netherlands, 2018.

Adeline Visser, "Trespassing the brain's greatest barrier", report of final high school project, Stedelijk Dalton Lyceum in Dordrecht, the Netherlands, 2017.
With this project she won a NexTecH scholarship in 2019 for four years (€8400) to study Biomedical Engineering at Eindhoven University of Technology.

Jasper Dijkstra, “Quantifying the acoustic influence of glass layers in the OrganoPlate”, report of BSc thesis, TU Delft, the Netherlands, 2017.

Tesse van der Akker and Saskia Vink, “Bubble behaviour”, report of final high school project, Maurick College in Vught, the Netherlands, 2017.

PhD Portofolio

Conferences	Year	ECTS
21st European Symposium on Ultrasound Contrast Imaging *Rotterdam, the Netherlands*	2016	1.1
NanoCity *Amsterdam, the Netherlands*	2016	1.8
IEEE IUS *Tours, France*	2016	1.4
22nd European Symposium on Ultrasound Contrast Imaging *Rotterdam, the Netherlands*	2017	1.1
Dutch BioMedical Engineering Conference *Egmond aan Zee, the Netherlands*	2017	1.6
7th European Cell Mechanics Meeting *Windermere, England*	2017	1.1
Acoustical Society of America *Boston, United States*	2017	2.4
23rd European Symposium on Ultrasound Contrast Imaging *Rotterdam, the Netherlands*	2018	1.6
Microbubble Symposium *Leeds, England*	2018	1.1
IEEE IUS *Kobe, Japan*	2018	2.1
Acoustical Society of America *Victoria, Canada*	2018	2.1
24th European Symposium on Ultrasound Contrast Imaging *Rotterdam, the Netherlands*	2019	1.6
Innovation for Health *Rotterdam, the Netherlands*	2019	0.8
IEEE IUS *Glasgow, Scotland*	2019	2.1

Courses	Year	ECTS
The Physics of Biological Systems Summer School *Nicolas Cabrera Institute, Spain*	2016	1.5
Ultrasonic Therapy *IEEE IUS Tours, France*	2016	0.15
Ultrasound Vector Velocity Imaging *IEEE IUS Tours, France*	2016	0.15
Computational Fluid Dynamics *Delft University of Technology, the Netherlands*	2016	2.0
Functional Imaging and Super Resolution *Optical Imaging Center Erasmus MC, the Netherlands*	2016	1.5
Zeiss Confocal Microscopy Course *Optical Imaging Center Erasmus MC, the Netherlands*	2017	0.2
Computational Mechanics of Tissues and Cells *Delft University of Technology, the Netherlands*	2017	2.0
Basic Introduction Course on SPSS *Erasmus MC, the Netherlands*	2017	1.0
Biomedical English Writing and Communication *Erasmus MC, the Netherlands*	2018	3.0
Leeds Thundar Workshop *Leeds Microbubble Consortium, England*	2018	0.3
Microbubbles and Nanodroplets for Biomedical Ultrasound Applications: Design Principles and Methods *IEEE IUS Kobe, Japan*	2018	0.15
Scientific Integrity *Erasmus MC, the Netherlands*	2019	0.3
Ultrafast Ultrasound Imaging *IEEE IUS Glasgow, Scotland*	2019	0.15

Scientific Meetings	**Year**	**ECTS**
NVMU meeting *Delft University of Technology, Delft*	2017	0.5
PhD Day *Erasmus MC, Rotterdam*	2017	0.2
hDMT vessel-on-a-chip consortium *LUMC, Leiden*	2017	0.5
Unveil of Brandaris 128 and Confocal Microscope *Erasmus MC, Rotterdam*	2018	0.3
ACE Molecular Cellular Imaging *Erasmus MC, Rotterdam*	2018	0.1
COEUR Day *Erasmus MC, Rotterdam*	2019	0.3

Supervision	**Year**	**ECTS**
Profielwerkstuk - Tesse van der Akker & Saskia Vink *Erasmus MC, Rotterdam*	2017	1.4
BSc thesis co-supervision - Jasper Dijkstra *Applied Physics, Delft University of Technology*	2017	0.5
MBO internship - Merel Vegter *Biotechnologie, Techniek College Rotterdam*	2017 2018	2.8
HBO internship - Phoei Ying Tang *Biology and Medical Laboratory Research,* *Rotterdam University of Applied Sciences*	2018	1.1
MSc internship - Cheryl Mok *Infection and Immunity, Erasmus MC*	2019	0.9
	Total	**42.9**

Acknowledgements

I made it! Here I am, at the end of my thesis. The freedom is a bit surreal while stuck at home, banned from the office and any social activities due to Covid-19. On the positive side, I think this is the most effective way to realize how grateful I am to have been surrounded by amazing colleagues, friends, and family during the last 4 years. Having to decide on an order of acknowledging is hopeless. I would have preferred making individual copies for each of you, with a personal dedication. Disclaimer: this 'thank you' was written during severe social withdrawal.

Dear **Klazina**, all of this wouldn't have been possible if you hadn't hired me as your PhD student. Thank you for the opportunity and, most importantly, for guiding my through the PhD journey. You created a warm and safe nest and coached me along this rollercoaster. Your love for science is truly inspiring. You remind me to celebrate every little step of progress, instead of only worrying about everything that is still to come. I admire your patience and attention to detail. You definitely passed on to me your talent for enormous and colourful Excel sheets, planning out experimental days down to toilet and lunch breaks. I'm grateful you taught me to not be defeated by (extremely) challenging experiments. You got me into the cell culture lab and we'll never know for sure, but I believe that your golden-tip to talk to cells to keep them happy has saved me from many troubles. I've truly enjoyed our discussions, talking about cells as if we know what they are feeling, and always joining forces of biology and engineering to unravel mysteries. Your caring personality has created a lovely safe place for the bubble-family and I hope you'll keep feeding it with chocolate and home grown vegetables. I will miss your endless positive energy.

Nico, thank you for taking me along into the physics of the bubble-world. I'm grateful for your guidance and all the fruitful discussions, always leaving me with even more new ideas to try and things to figure out. I'm so glad to have had you as my mentor during this PhD. You've taught me that there is always an explanation, one just needs to take the time to find it. I've often had to remind myself that it's ok that you will always know some bubble fact or issue I don't, after all, you've been dealing with bubbles longer than I've been with life. Your busy schedule and double-agenda have taught me to make meetings more efficient. I hereby apologize for all those times I impatiently waited by your office door and continued presenting data although you already had your jacket on, because you really had to go. I've honestly suggested hanging 'wanted'-posters around the office. I hope it's just a reminder of how valuable you are. Thank you for patience, your enthusiasm, and your inspiring confidence.

I want to thank you, **Martin**, for introducing me to science and to this PhD. I started on a bachelor's project with you at the TU Delft and since then I've enjoyed working together. You've always managed to trigger my curiosity for solving the puzzles science throws at us. I once told you: 'I feel like every time I try to answer a question, instead of an answer, I just find more questions'. And you told me I had just quite accurately described research. Over the years I've learned to appreciate that. Thank you for wanting to join as a co-promotor, for all the meetings, and for your valuable opinion on content, text, and appearance. Cells are a bit of a mystery to both of us, but I'm glad you helped me think of them in terms of numbers and equations.

Ton, thank you for giving me the opportunity to learn, grow, explore, and spread my wings in this welcoming and thriving lab environment. I'm very grateful for your support, especially during the last critical phase, and for your concern about ambitious planning and maintaining a bit of mental health. The frequent informal check-ups towards the end made me feel supported, although they were maybe just due to the increasing amount of candy at my desk. By suggesting the proposition 'Good PhD's make bad housewives' I gave you a very untainted view of my household during the last months of my PhD, but I can assure you that quarantine has changed that. Dear Ton, you're a great *opperhoofd* to the BME family.

Dear bubbly-bubbles, I wish to pop a bottle of bubbles with all of you as soon as we can to celebrate my thesis! Dear **Kirby**, my partner in crime. Thank you for your warm welcome in the bubble-group by teaming up against Tommie. I already miss our nights at the lab. You are the only one left that remembers the pain of using a blurry AxioCam, so will you do me a favour and remind the newcomers how wonderful the confocal is? Thank you for celebrating with me on so many occasions: drinks at the Witte Aap, dinners in Boston, beers in the lab, wine in the lab, sugar-boosts at Starbucks, and many AH-to-go cappuccino's. Also, I'm very grateful to have shared with you all those ventilation sessions and frustrations. You and my grocery store drawer helped us through rough times. Oh, and you've always said that spending time with a two-year old is the best birth control there is. I think your sweet little **Julia** is a very bad example for that. My dear paranymph, I look forward to celebrating my thesis with you in a better future. After Tom left us, we were relieved another man joined our team. **Joop**, although Kirby and I asked for a blond with blue eyes, you turned out to be a pretty fine colleague too. Dear metro-man, you even became a good friend. Thank you for all the distractions with stress-balls flying around, push-ups on the 'clean' office floor, AD news updates, and for your passion for baking and the continuous feeding: chocolate, cookies, cake, candy, eiersalade, stokbroden, zalm-stoom maaltijden, hot coffee, cold coffee, lot's of coffee. Without your tosti-ijzer, the end of my PhD would have sucked. Oh, and thanks for letting me try to push the Brandaris-daddy duties on you. I'm grateful for your support, for all the fun we've had, and for all the times you have tried to remind me I can have a life after 5 pm. I'm still amazed at how well

you handle the high levels of oestrogen in the trench. Dear **Simone**, I will never forget our great trip around the world. I hope I finally have some time now to make a photo album of our Japan-Canada adventure, from work to nature to karaoke. We've spend many hours in the lab together and I'm sorry Brandaris wasn't always nice to you, but I hope some of the Matlab scripts have made up for lost time. Thank you for your Lama motivational quotes, for reminding me we are just human and sometimes need a mental break, and for all those times you let me ramble on about data analysis. You started your PhD amazed at my burger-points and trying to convince me I was young and should party, but today you're enjoying your huisje-boompje-beestje life too. Stay strong, stay hopeful. Once you reach the end, you'll almost forget about the struggles along the way. Oh and remember, if you need a break, McDonalds will always be there for you. Thank you **Bram**, for all the enthusiasm, motivational high-fives, and energy you bring into the lab. While my positivity was quickly draining towards the end, it was an eye-opener to realize that I probably once started as hopeful as you and wanted to finish like that too. Thank you for making sure I kept my head up. I hope I'm not too hard on you when reality crushes your dreams about easy experiments. I look forward to share more lab time together, help you onto the right OrganoPlate-path, and make the start of your PhD as fruitful as possible. Dear **Mariël**, thank you for joining our team and taking over with your great organisational skills. You have no idea how good it feels to see the lab labelled and cleaner than ever. Please send me a picture if you manage to do the same with Klazina's desk. I'm glad to know the lab is in such good hands, I can let go in peace now. **Reza**, welcome to the bubble-family. I hope you'll enjoy your time here as much as I did.

To all my bubbly-students, thank you for your commitment, the extremely long hours in the Brandaris lab, and together enjoying the scheduled AH-to-go bezoekjes during experiments. Lieve **Merel**, I hope you realize what an important turning point you were in my PhD, you got me through all those cell culture and lab hours. But it wasn't just sharing a workload, we had so much fun together. From blasting Lil Kleine in the late evenings, to Lingo or Kinderen voor Kinderen's groen-groen when switching to the GFP channel, to mourning together and cheering each other up with zure cadillacs or kaasstengels. I'm grateful for all those times you motivated me to keep going, telling me: 'when I get back from holidays, that OrganoPlate paper is finished!' or 'he, come on, we can do at least 4 CLINIcells a day'. Although you left the lab, we definitely never stopped having fun together: game nights, outdoor bbq's, cactus parties, jenever bar visits, assuring me the Maasstunnel is the safest part of my cycle home, snapchat-streaks, and so much more. I truly wish you could be standing next to me as my paranymph during my defense, but I'm sure we'll find a way to make up for it. What once was my intern, turned into a wonderful friend. **Phoei Ying**, I'm glad we shared a passion for illustrator schematics. Thank you for all your help and support, and for bringing me chocolate after setbacks. Dear **Cheryl**, thank you for staying so

strong through the OrganoPlate project, that was definitely not an easy task. I admire your perseverance and kindness. Thank you for sharing a passion in paper-goodies and for the extra big box of zure autodrop.

Dear **Tom**, the role model that was building Lego at his desk the day before his deadline. Thank you for letting me join forces on your publications when I started. Everything you taught me has been so valuable along the way, from the importance of illustrator to managing supervisors. You tried your best at warning me to never do cell culture and learning to say no, I've been truly sorry for not listening to you many times. Thank you for your happiness, support, and passiebloemen, even to this day. **Sara**, you were such a great desk neighbour. Thank you for your kindness and the smell of nice food. With a bit more time we would have made those stubborn droplets pop.

Dear **Robert**, thank you for every troubleshoot session, every fix, every cable, every speculaasje, every time you send me home, every bit of advice about tools and Marktplaats, and all the stories, jokes, mood-boosters, and *doe geen domme dingen* warnings. With your help, every experimental set-up appears feasible and there seems to be a solution to every problem. I'm glad you taught me your wise RTFM (read the fucking manual) and ANNA (alles nagaan, niets aannemen) principles. Dolores Inés is grateful for everything you did for her and still owes you and Hanneke a dinner at BeyMen. For all those PhD's that follow: when you start predicting which joke Robert will tell, the time has come to finish your thesis. **Frits**, the Brandaris guru. I can't imagine how I would have made it through without your wiliness to help, to fix every inexplicable Brandaris issue, and to make me understand the beast piece-by-piece. I admire your elegant coding and patient debugging. Thank you for keeping the Brandaris alive. **Michiel**, I've been amazed by every smart design you make based on our troubles and ideas. Thank you for all the hours you've put into understanding what we need and for all the parts you have made, adjusted, and altered. Together with **Geert** and the rest of the team, you make the 19^{th} floor indispensable. **Gerard**, thank you for always making sure I had what I needed, from replacements for exploding laptop batteries, to saving crashed computers, to Matlab licenses. **Sharon**, thank you for placing the countless orders, rushing through the spoed-bestellingen, finding unfindable products, and all your battles with PSA.

I apologize to the inhabitants of the coffee-machine trench for all the distraction I've caused, but I'm very grateful I (almost) always felt welcome to chat, gossip, catch-up, and blow off some steam. Dear **Lana**, I can't imagine working somewhere without having you around. I'm glad I listened to you and stayed around after my PhD, at least to complete our 10-year anniversary. Thank you for always being there, listening, and knowing how to snap me out of a downwards spiral. I'm grateful that I can always count on you for advice and your honest and valuable opinion. Your can-do attitude has kept me going more than once and I aspire to achieve your efficiency. Oh, and if you check carefully, I actually met your request and mention you in three paragraphs. You truly

deserve them. **Jason**, although you are often inaccessible while hidden behind your screens and headphones, when you hear *snoepjes* you are suddenly there. I'm grateful I also know the caring and fun out-of-office version and that you worry about my utility bills in Corona-times. You and **Jenna** have become beloved friends. Thank you for all the fun we have had, always making me feel welcome and supported, and for letting me dream of getting little **Juniper** on a horse. **Gonzalo**, verte leyendo el País en la oficina me ha hecho sentir como en casa. Thank you for reminding me to not forget my physics and for taking care of Joop, he really needed a bromance. Hold on tight, you'll make it through the PhD rollercoaster. I hope Corona gives you back your man-bun. Dear **Jorinde**, it has been great to see you thrive on what once was my MSc thesis and that you even put the project into the hands of a professional illustrator. Thank you for always transmitting me the *het komt uiteindelijk wel goed*-vibe. **Rik**, thank you for you compassion during the last months by double-checking if I actually went home at all the night before. **Hans**, thank you for letting us invade your office for all those meetings, I hope that one day I master your art of not getting distracted.

Eline, thank you for all those times you came over from the other side. You and your empty Pluk mug were a daily (or hourly) beloved visitor. Thank you for checking up on me so often, for every AH-to-go maaltijd, for cheering me up, for helping me eat my vieze gezonde koekjes, and for every feitje, you really are a walking Wikipedia. *Hard voor weinig, maar nooit chagrijnig.* Nou bijna nooit dan, want even lekker ventileren geeft toch wel de beste opkikker. You're one of a kind: a doctor with nerdy Matlab talents and great at cooking steak in illustrator. Dear **Mirjam**, you have been an esteemed frequent visitor too. I'm grateful for all the talks, sharing our ups and downs, and thank you for the daily checks after submitting my paper. Unfortunately, we both know it can be a rocky road. I'm glad you helped to keep my mental health on track with your advice and great ability to put things in perspective.

Sophinese, you have such a kind heart and you could always tell when I needed a hug. It wasn't after I also started my postdoc that I understood why you were still spending evenings in the lab after your PhD. I admire how passionate you are about work and the joy it gives you to get a nice signal. **Astrid**, I'm amazed at how well you handle your life-work balance, or at least, of the relaxed impression you always give. **Nuria**, thank you for motivating me to keep going to the gym. **Eric**, I'm happy to see you with a haircut, since it means you also finished your thesis. **Ayla**, thanks for setting a shining example of how to succeed during and after your PhD. **Pieter**, thanks for your confidence in me from day one. **Verya**, thank you for taking me under your wings during my first lab experience as a student and good luck with the miniature Brandaris.

A special note to all final countdown warriors: Hang in there, you can do this! I promise, listen to Roosvicee: *Het komt wel goed, schatje.*

Finally, I want to thank the entire BME family for making me feel at home in the department. I felt like your doors were always open for help, advice, or support. Lunch downstairs, tosti's in the office, BME presentations, conferences, labuitjes, chats in the hallway, and elevator rides. I am grateful for all the time spend with you.

A thank you to the departments of Experimental Cardiology and Experimental Anesthesiology from the Erasmus MC, for their friendly help and sharing their already crowded ML-1 lab with us. **Lau**, thank you for always keeping the labs in shape and the liquid nitrogen stocked; **Marielle**, thank you for welcoming and familiarizing us with the lab; **Maarten**, thank you for your efforts to help us out with leaky cells.

I also want to thank the Optical Imaging Center of the Erasmus MC, for the excellent training and making sure the facilities are always in great conditions. **Gert van Cappellen**, thank you for advising us along the way with our imaging system purchase, calibrations, and challenging samples.

Thank you to all from Nikon Instruments that made the Brandaris-Confocal system possible. I'm glad we got to celebrate this successful achievement together during the unveil. **Rogier Verduyn Lunel**, thank you for figuring out how to cut a microscope in half without killing it, for all those hours spend in in the lab coupling the system, for your patience in teaching us and making the hours fly by, and for never giving up on the challenges that came along. You are an inspiring hands-on problem solver and I'm very grateful I got to work with you on this project. Without you we wouldn't have the amazing system we have today. **Emma Verver**, thank you for your caring support along the way and for looking for answers to all those burning questions and worries. **Alessandra Scarpellini**, thank you for the early stage brainstorming that converted ideas into a tangible project.

To the organ-on-a-chip team from Mimetas, thank you for the collaboration on this challenging project. I'm glad I got to peak behind the scenes during my internship and that we continued working together throughout my PhD. Special thanks to all of you that made the adapted OrganoPlate design feasible. **Bas Trietsch**, thank you for all the discussions and support to get us onto a leaktight path. **Kristina Bishard**, **Angelique van den Heuvel**, and **Dorota Kurek**, thank you for your trainings and elaborate efforts in protocol optimization.

Thank you **Michel Versluis**, for your help on getting the microbubble-physics right, for your guidance, and for making me feel welcome in Twente by even attempting to find housing for my horse. I wish there would have been more time, but apparently the Brandaris kept me too busy. **Guillaume Lajoinie**, thank you for sharing the beast.

Thank you **Ine Lentacker**, for your encouragement to keep trying despite challenging biology and for the shared time in Boston. A part from your science, I'm also inspired by your sewing skills on Instagram. **Chrit Moonen** and **Hanneke van Laarhoven**, thank you for your constructive feedback and for keeping an eye on the project. **Ayache Bouakaz** and **Emma Kanbar**, thank you for the collaboration. It was a pleasure to work with you and teaching the Brandaris to someone for the first time, taught me even more.

Dear **Bas**, **Joep**, **Lana**, **Liesbeth**, and your lovely plus one's, thank you for the dinners, games, and housewarming and birthday parties. I'm glad we stayed in touch with our TU Delft roots despite us spreading over the country and splitting into academia and industry. I hope we keep the *Master is vet onmogelijk* of *was eigenlijk wel redelijk doenbaar* club thriving. Dear **Miranda**, **Dennis**, and **Anouk**, I wish we could go back in time and spend some days driving around in Catalunya. I hereby promise I will do a better job at making time for you. Jullie hebben sowieso nog kaasfondue en een Efteling uitje van me tegoed.

Karlien, thank you for welcoming me in Rotterdam by literally giving me a place to feel at home. Although we will probably never stop worrying, deep down we both know that in the end, everything will be fine. Dear **Kirsten**, we shared the same PhD timeline battle and I hope you also get to celebrate in a better future, because you truly deserve it. Now that we are free, I hope we can plan another getaway to the sun once the world lets us. Maybe, together with **Sophie**, we can finally reunite the *minor meisjes* under some palm trees.

Thank you **Ganesh**, for making sure to get me out of the office and clear my head at the end of the day. Thank you for the adventure we had together.

Gràcies **Laura**, **Ester**, i **Miós** per la vostra infinita alegria, per tots els missatges d'ànims i entreteniment, pel vostre carinyo, i per sempre rebre'm amb els braços ben oberts. **Enara**, gràcies per totes les postals, per la teva confiança en mi al començar i durant aquesta aventura a Holanda, i per fer-me sentir sempre benvinguda a la preciosa Costa Brava. Catalunya, espero que mai deixis de formar part de mi.

Lieve **Martin** en **Greetje**, bedankt voor jullie vertrouwen in mij en jullie enthusiasme over alles wat er nog komen gaat. Het is fijn geweest om samen het uitzicht over de Maas te delen en naar jullie te kunnen zwaaien vanaf kantoor.

Lieve **Opa** en **Oma**, ik ben straks echt doktor, jammer genoeg niet zo'n dokter die jullie beter had kunnen maken, maar wel zo eentje waar jullie trots op zouden zijn. Ik koester onze herinneringen, het oog voor detail waarmee de prachtigste klus projecten ontstonden, de groene vingers, de liefdevolle nuchterheid, en de geur van worstenbroodjes en Oma-soep.

Lieve **Momo**, bedankt dat je in mij gelooft en ook mij doet geloven dat ik alle beren aankan die ik op de weg zie. Ik ben je dankbaar voor de talloze uren die je naar me hebt geluisterd terwijl ik ratelde over mijn PhD en voor alle keren dat je me geruststelde als ik weer eens de controle kwijt was. Je weet altijd hoe je een glimlach op mijn gezicht kan toveren. Je koestert me voor wie ik ben en herinnert me eraan om te genieten van de kleine (en grote) dingen in het leven. Ik ben blij dat we elkaar vonden in onze passie voor werk, en dat we net zo'n goed team zijn in samen leven en in samen elkaar de vrijheid geven om onszelf te zijn. Ik vond een veilige plek in je armen en ik kan niet wachten om onze toekomst samen te ontdekken. Ik hou één keer meer van jou.

Lieve **Joke** en **Dalien**, bedankt dat jullie altijd voor me klaar stonden, ondanks dat jullie vaak niet begrepen waarom ik al die uren in werk stopte of waarom ik het niet los kon laten terwijl ik er bijna aan onderdoor ging. Bij het zien van dit proefschrift snappen jullie misschien nog niet waarom, maar in ieder geval wel waar al die tijd in is gaan zitten. Dank voor jullie onvoorwaardelijke liefde, voor de hapjes eten, de opvang met me kapotte knieën, de kopjes koffie, de wijze woorden, en altijd het beste met me voor hebben. **Félix**, broertje-lief, bedankt voor je schaterende lach, voor de altijd verassende twist die je aan het leven geeft, en voor je telefoontjes op de woensdag avond. Het is zo fijn geweest om jullie drietjes ietsje dichterbij te hebben. Maar tegelijkertijd, mis ik onze *cafès amb llet* op de veranda in Can Sargantana. Bedankt voor het creëren van een thuis dat mij de kans gaf om zover te komen. Us estimo.

Dankjewel. Gràcies. Thank you.

About the author

Dalien Inés Beekers was born on September 12th, 1992 in Hillegom, the Netherlands. At the age of nine she moved to Girona, Spain, and completed secondary school in Catalan and Spanish. She relocated to Delft in the Netherlands in 2010 to start university. In 2013, she graduated with honours (*cum laude*) from her Bachelors in Applied Physics at the Delft University of Technology. At the same university she received the Masters degree in Applied Physics in 2015, specializing in medical imaging and acoustical wavefield modeling. During her Masters she investigated neonatal brain perfusion imaging using ultrasound at the Department of Imaging Physics at the Delft University of Technology.

In 2015, Inés joined the Biomedical Engineering Department at the Erasmus University Medical Center, where she started her PhD on a project titled 'Treatment in sight through sound'. The project focussed on unraveling the biological and physical mechanisms involved in microbubble-mediated drug delivery using ultrasound. During her PhD she was involved in novel technological developments, worked with advanced biological systems, and pursued image analysis and coding challenges. Currently, Inés is working as a postdoctoral researcher at the Erasmus University Medical Center Rotterdam, continuing the pursuit into the underlying mechanisms of microbubble-mediated drug delivery.